Fluorescent sensors for the small GTPase switch

Dissertation

zur Erlangung des akademischen Grades
eines Doktors der Naturwissenschaften
der Fakultät Chemie an der Technischen Universität Dortmund

angefertigt am
Max-Planck-Institut für molekulare Physiologie
Dortmund

vorgelegt von
Dipl.-Chem. Stephanie Voß

2017

This thesis was prepared between December 2011 and January 2017 under the supervision of Dr. Yaowen Wu and Prof. Roger S. Goody at the Max Planck Institute of Molecular Physiology.

1. Examiner: Prof. Dr. Roger S. Goody
2. Examiner: Prof. Dr. Roland Winter

Results and methodologies presented in this thesis contributed to the following peer-reviewed publications:

Voss, S., Kruger, D.M., Koch, O. & Wu, Y.W. Spatiotemporal imaging of small GTPases activity in live cells. *Proc Natl Acad Sci U S A* **113**, 14348-14353 (2016).

Voss, S., Klewer, L. & Wu, Y.W. Chemically induced dimerization: reversible and spatiotemporal control of protein function in cells. *Curr Opin Chem Biol* **28**, 194-201 (2015).

Voss, S., Zhao, L., Chen, X., Gerhard, F. & Wu, Y.W. Generation of an intramolecular three-color fluorescence resonance energy transfer probe by site-specific protein labeling. *J Pept Sci* **20**, 115-20 (2014).

Liu, P., Calderon, A., Konstantinidis, G., Hou, J., Voss, S., Chen, X., Li, F., Banerjee, S., Hoffmann, J.E., Theiss, C., Dehmelt, L. & Wu, Y.W. A bioorthogonal small-molecule-switch system for controlling protein function in live cells. *Angew Chem Int Ed Engl* **53**, 10049-55 (2014).

Voss, S. & Wu, Y.W. Tandem orthogonal chemically induced dimerization. *Chembiochem* **14**, 1525-7 (2013).

Contents

Abbreviations

APD	Avalanche photodiode
AT	Affinity tag
COS	CV-1 in Origin carrying the SV40 genetic material
DMSO	Dimethyl sulfoxide
DNA	Desoxyribonucleic acid
DTE	Dithioerythritol
DTT	Dithiothreitol
E. Coli	*Escherichia coli*
EDTA	N,N,N`,N`-Ethylenediaminetetraacetic acid
EGF	Epidermal growth factor
ER	Endoplasmic reticulum
FBS	Fetal bovine serum
FLIM	Fluorescence lifetime imaging microscopy
FRAP	Fluorescence recovery after photobleaching
FRET	Förster resonance energy transfer
GAP	GTPase activating protein
GDF	GDI dissociation factor
GDI	Guanosine nucleotide dissociation inhibitor
GDP	Guanosine diphosphate
GEF	Guanine nucleotide exchange factor
GFP	Green fluorscent protein
GppNHp	Guanosine-5'-(β-γ-imido)triphosphate
GTP	Guanosine-5'-triphosphate
HeLa	Henrietta Lacks
HEPES	4-(2-Hydroxyethyl)-piperazine-1-ethanesulfonic acid
His-tag	Polyhistidine-tag
HPLC	High-performance liquid chromatography
IANBD	N,N'-Dimethyl-N-(iodoacetyl)-N'-(7-nitrobenz-2-oxa-1,3-diazol-4-yl)ethylenediamine
IPTG	Isopropyl β-D-1-thiogalactopyranoside
LB-medium	Lysogeny broth-medium
LC-ESI-MS	Liquid chromatography-electrospray ionization mass spectrometry
LMW	low molecular weight
mant	2'-/3'-O-(N'-Methylanthraniloyl)

Abbreviations

MBP	Maltose-binding protein
MDCK	Madin-Darby Canine Kidney
MESNA	Sodium 2-mercaptoethanesulfonate
MPAA	4-Mercaptophenylacetic acid
MWCO	molecular weight cut off
NCL	Native chemical ligation
NTA	Nitrilotriacetic acid
OD	Optical density
paGFP	photoactivatable GFP
PBS	Phosphate-buffered saline
PCR	Polymerase chain reaction
PDB	Protein Data Bank
PMSF	Phenylmethanesulfonyl fluoride
R_0	Förster radius
Raichu	Ras and interacting protein chimaeric unit
REP	Rab escort protein
ROI	Region of interest
rpm	Revolutions per minute

Amino acids and nucleobases were referred to as their respective one-letter or three-letter codes in compliance with the recommendations of the International Union of Pure and Applied Chemistry (IUPAC) and the International Union of Biochemistry and Molecular Biology (IUB).

Zusammenfassung

Kleine GTPasen regulieren eine Vielzahl an hoch dynamischen Prozessen, welche von Signaltransduktion und Cytoskelettorganisation bis zum nuklearen und vesikulären Transport reichen. Sie erfüllen ihre regulatorische Rolle indem Sie als molekulare Schalter agieren, die zwischen einer aktiven, GTP-gebunden Form und einer inaktiven, GDP-gebundenen Form hin- und herwechseln. Der Wechsel zwischen der aktiven und der inaktiven Form geht mit einer Konformationsänderung der Proteinstruktur einher und wird durch GTPase-aktivierende Proteine (GAPs) und Guaninnukleotidaustauschfaktoren (GEFs) gesteuert. Zudem weisen die meisten GTPasen eine charakteristische subzelluläre Lokalisation auf und zirkulieren zwischen verschiedenen Zellkompartimenten.

Aufgrund ihrer Schlüsselrolle in komplexen zellulären Vorgängen sind GTPasen ein beliebtes Ziel für die Entwicklung von Biosensoren, die einen Einblick in die zeitlichen und räumlichen Aspekte ihrer Aktivität ermöglichen. Die meisten der bisher etablieren Sensoren basieren auf der spezifischen Bindung einer modifizierten Effektordomäne an die aktivierte GTPase. Ein Nachteil dieser Strategie ist, dass zunächst für jede GTPase eine passende Effektordomäne identifiziert und optimiert werden muss und daher einmal etablierte Sensoren nicht einfach auf andere GTPasen übertragen werden können. Zudem erfordern konventionelle Sensorkonstrukte häufig die Modifikation der Proteintermini, was die native Lokalisation der GTPase beeinträchtigen kann.

Im Rahmen dieser Arbeit wurde ein neuartiger Ansatz zur Entwicklung von GTPase-Sensoren verfolgt, der auf alle GTPasen übertragbar ist und nur eine minimale Modifikation der Proteine erfordert. Der Sensor basiert auf einem intramolekularen Förster-Resonanzenergietransfer (FRET) Paar, das es ermöglicht die Konformationsänderung der GTPase im Zuge des Nukleotidaustausches direkt auszulesen. Das Sensordesign wurde zunächst auf Rab1 und später auf KRas angewandt.

Der Erhalt der nativen Funktionalität von Rab1 im Sensorkonstrukt wurde zunächst durch die eingehende Charakterisierung der Interaktion mit dem GEF DrrA, dem GAP TBC1D20 und den Effektorproteinen OCRL und LidA überprüft. Anschließend wurde in Zellstudien der Anteil an aktivem Rab1 im Cytoplasma und am Golgi quantifiziert. Der für KRas entwickelte Sensor offenbarte ein polarisiertes Aktivitätsprofil von KRas in COS7 Zellen mit geringerer Aktivität an der freien Zellkante. Zudem zeigte der KRas Sensor, dass EGF-Stimulation zu einem globalen Anstieg der intrazellulären KRas-Aktivität führt.

Ergänzend wurde der dynamische Austausch von Rab1 zwischen Cytoplasma und Golgi durch *Fluorescence Recovery after Photobleaching* (FRAP)-Studien und Experimente mit photoaktivierbarem GFP quantifiziert. Die Versuche weisen darauf hin, dass der Übergang von Rab1 zwischen Cytoplasma und Golgimembran eng mit der Fähigkeit verknüpft ist zwischen aktivem und inaktivem Zustand zu wechseln.

Abstract

Small GTPases regulate a variety of highly dynamic biological processes ranging from signal transduction, cytoskeleton rearrangement and gene expression to nuclear and vesicular transport. They exert their regulatory role by acting as molecular switches, cycling between an active GTP-bound and an inactive GDP-bound form. The switching between the active and the inactive state involves distinct conformational changes in the GTPase structure and is tightly regulated by guanine nucleotide exchange factors (GEFs) and GTPase-activating proteins (GAPs). Most small GTPases exhibit a characteristic subcellular localization and cycle between different cellular compartments. This spatial cycle constitutes an additional level of regulation.

Due to their key role in highly dynamic processes, GTPases have been a popular target for the development of biosensors that provide insight into the spatiotemporal aspects of their functioning. Most GTPase sensors rely on an indirect signal read out, generated through binding of an engineered effector domain to the activated, GTP-bound GTPase. However, the versatility of this approach is limited. It requires a suitable effector domain, which has to be identified and optimized for each target GTPase. Moreover, these conventional sensor designs often involve modification of the protein's termini, affecting native GTPase functioning and localization.

In the course of this thesis a new GTPase activation sensor that avoids the aforementioned drawbacks of conventional designs was established. By employing Förster energy transfer (FRET) between a N-terminal fluorescent protein and an organic dye, the intrinsic conformational change of the GTPase-fold can be used as the primary indicator for GTPase activation. The sensor design was first applied to Rab1 and later extended to KRas.

Retained native behavior and sensitivity of Rab1 in the sensor constructs was assessed by monitoring their interaction with GEFs, GAPs and effector proteins. In cellular studies, using fluorescence lifetime imaging microscopy (FLIM), the ratio of active to inactive Rab1 in the cytoplasm and on the Golgi was quantified. Rab1 was found to be mostly active in the cytoplasm and largely inactive when localized on the Golgi, suggesting that the Golgi organelle serves as the terminal of the Rab1 functional cycle. The KRas sensor revealed polarized KRas activity at the plasma membrane with lower KRas activity at the cell edges. Upon EGF-stimulation the sensor indicated a global increase in activated KRas.

The work based on the GTPase activation sensor in this thesis is complemented with an analysis of the dynamics of Rab1 trafficking between the cytoplasmic pool and the Golgi organelle. Using fluorescence recovery after photobleaching (FRAP) and photoactivation experiments, the effect of impaired Rab1 function on Rab1's spatial cycling was assessed. These experiments indicate, that the ability to cycle between its active and inactive state is essential for sustained Rab1 trafficking between cytoplasm and Golgi.

1 Introduction

1.1 Small GTPase function and cycle

The small GTPases of the Ras superfamily are responsible for the regulation of a variety of biological processes ranging from signal transduction, gene expression, cytoskeletal organization and cell motility to nuclear and membrane trafficking.[1]

Based on their specific structure and function the members of the Ras superfamily can be assigned to five different subfamilies: the Ras, Rho/Rac/Cdc42, Rab, Ran and Sar/Arf family. The Ras family proteins are involved in signal transduction, gene expression, cell proliferation and differentiation. Due to their role in these critical signaling pathways they play a substantial part in human oncogenesis.[2] Rho proteins are key regulators of the cytoskeletal actin organization, cell cycle progression and gene expression. Thus, members of this family are involved in the regulation of cell polarity, movement, shape, and cell-cell and cell-matrix interactions.[3] The Rab proteins constitute the largest of the five subfamilies with over 60 identified members in humans.[4] Rab GTPases are involved in all stages of vesicular transport and regulate endocytic and secretory trafficking.[5] The only member of the Ran family is the most abundant small GTPase in cells. Ran GTPase is involved in import and export of nuclear cargo[6] as well as the mitotic spindle assembly, DNA replication and assembly of the nuclear envelope.[7] Like Rab proteins, the members of the Sar/Arf family are involved in the organization of vesicular transport. More specifically they regulate vesicle budding, coat assembly and cargo sorting.[8]

All small GTPases feature a conserved, approximately 20 kDa guanosine nucleotide binding-domain that governs the proteins activation state by binding to either GDP or GTP. The so called 'G-domain' is unique for this superfamily and exerts the proteins regulatory role by acting as a molecular switch, cycling between the active GTP-bound and the inactive GDP-bound form.[9] This cycling is an earmark of the GTPase's functional mode and is tightly regulated by guanine nucleotide exchange factors (GEFs) and GTPase-activating proteins (GAPs) (Figure 1-1).[10,11] Only in the GTP-bound form the small GTPases can bind to effector proteins to activate downstream signaling.[1]

GEFs catalyze the reversible exchange of the bound nucleotide by forming a stable nucleotide free complex with the GTPase.[12] Because most GTPases bind GDP and GTP with similar affinity [13], nucleotide binding after GEF complex formation largely depends on the surrounding nucleotide concentration. In cells, GTP is generally present in a ten-fold higher concentration than GDP ([GTP] = 0.3-0.5 mM; [GDP] = 0.03-0.06 mM)[14], thus GEF-mediated nucleotide exchange typically leads to the formation of the activated GTP-bound GTPase.

Deactivation can occur through the slow intrinsic GTPase activity that leads to hydrolysis of the bound GTP to GDP. However, in most cases the inherent hydrolysis rate is not sufficient to effectively silence

downstream signaling by the GTP-bound protein.[15] GAPs facilitate coordinated deactivation by accelerating the slow intrinsic hydrolysis.[11] The transition between the two nucleotide configurations involves structural changes in the so-called 'switch regions' of the proteins.[12] The structural basis of this switching mechanism is discussed in more detail in section 1.1.1.

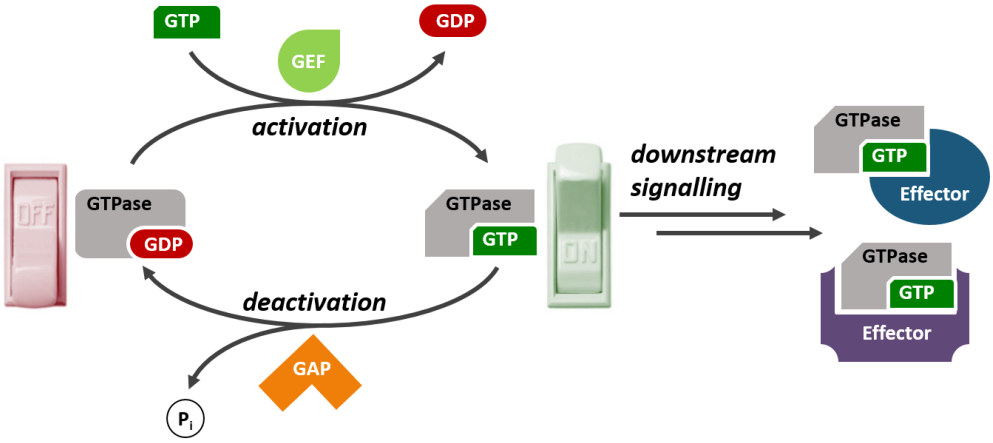

Figure 1-1: Small GTPases activation and deactivation cycle.
Inactive, GDP-bound GTPase is converted through GEF-mediated nucleotide exchange, to the active, GTP-bound form. The active GTPase can then bind to effector proteins and initiate downstream signaling. Deactivation is facilitated through GAP-induced GTP hydrolysis.

1.1.1 Structural basis for small GTPase functioning and regulation

The structural basis for the functioning of the small GTPases as molecular switches is centered around the conserved G-domain that facilitates binding to the guanosine nucleotides GDP and GTP. The conformational difference between the two nucleotide states are the decisive factor for specific effector binding and subsequent downstream signaling. In this section the structure-function relationship of the G-domain, the nucleotide dependent conformational changes in the GTPase-fold and the structural basis of GTPases regulation by GEFs and GAPs will be discussed.

The G-domain

The small GTPase fold was first described for the protein HRas and features a central 6-stranded mixed β-sheet surrounded by 5 α-helices.[16,17] Guanine nucleotide binding and hydrolysis is conveyed through five conserved sequence motifs (G1-G5) located in the loop regions connecting the β-sheets and α-helices (Figure 1-2).

The G1-motif (GxxxxGKS/T), also termed Walker A motif[18] or P-loop, is a glycine-rich loop that binds to the nucleotides phosphates and a Mg^{2+} located in the binding pocket. The GTPase backbone nitrogen atoms interact with the negatively charged α- and β-phosphate groups of the bound nucleotide. The side chain amino group of the conserved lysine contacts the oxygen atoms of the nucleotide phosphates (β-phosphate for GDP, β- and γ-phosphate for GTP).

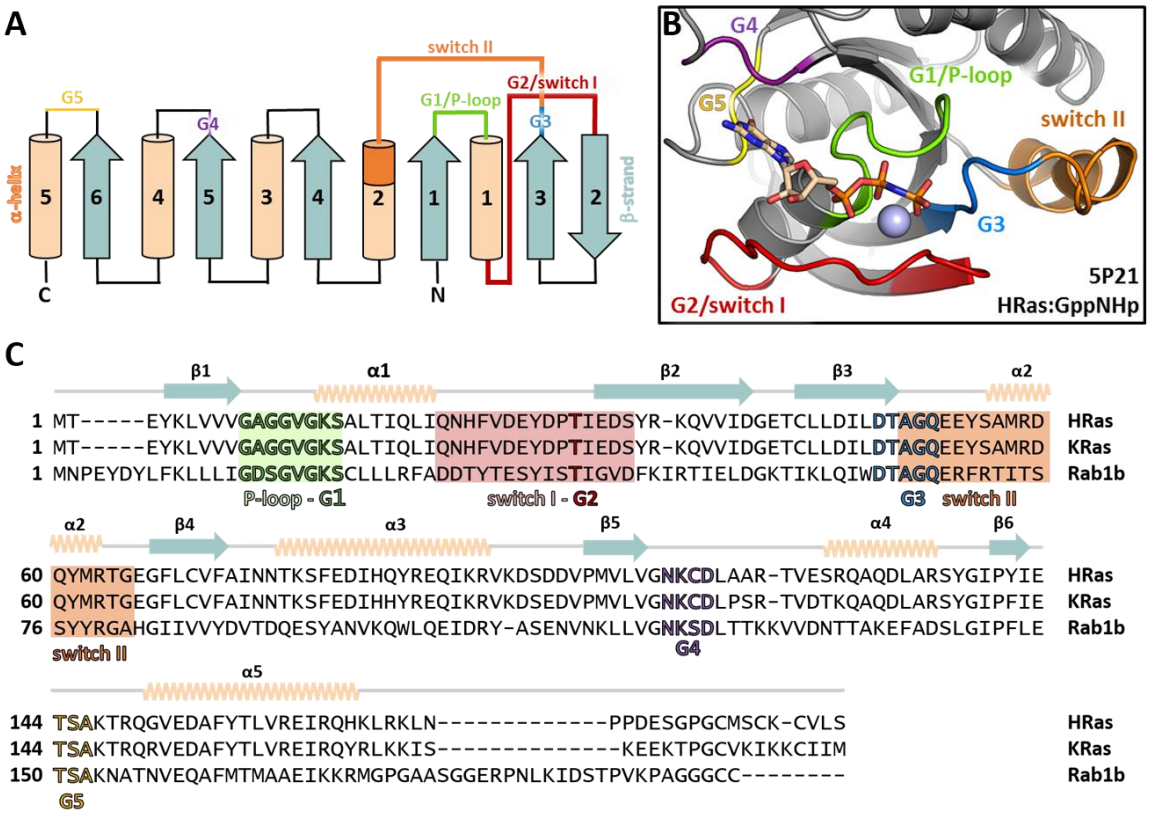

Figure 1-2: G-domain topology, structure and sequence based on HRas (PDB ID: 5P21)/KRas/Rab1b.
HRas was the first small G-domain protein to be characterized.[16,17] Rab1b and KRas were chosen as they are central to the work described in this thesis. **(A)** Topology diagram of the G-domain[9] with β-sheets and α-helices colored in light blue and orange, respectively. The G-motifs and switch regions are labeled and colored as follows: G1/P-loop in green, G2/switch I in red, G3 in blue, switch II in orange, G4 in purple and G5 in yellow. **(B)** Crystal structure of HRas: GppNHp (PDB ID:5P21) with the G-domain motifs highlighted in the same color scheme as in (A). Mg^{2+} is shown as a sphere in light purple. The bound guanine nucleotide is depicted in beige with atoms highlighted in red (oxygen), blue (nitrogen) and orange (phosphorous). **(C)** Sequence alignment of HRas, KRas and Rab1b. The G-motifs and switch regions are colored in the same scheme as described in (A). Conserved residues are highlighted in bold outlined letters.

The hydroxyl group of the serine/threonine, contacts the β-phosphate oxygen and coordinates the Mg^{2+} in the nucleotide binding pocket. Due to the two conserved glycine residues, the P-loop features a highly defined and rigid conformation, that is preserved throughout GTP hydrolysis. Together with the G4 and G5, G1 mediates the high binding affinity of the small GTPases towards the guanine nucleotides.[19] The G2-motif, is located in the switch I region, one of the two regions of the protein fold that undergo significant conformational changes upon nucleotide exchange. This motif features a highly conserved Threonine (T35 in HRas) that senses the presence of the γ-phosphate when GTP is bound and contacts the Mg^{2+} located in the binding pocket. G3 (DxxGQ) lies in 'switch II', the second region that changes its conformation and flexibility most considerably depending on the bound nucleotide. Besides a glycine (G60 in HRas) the switch II region itself does not feature a conserved sequence motif. Similar to switch I, switch II senses the γ-phosphate of the bound nucleotide. G3 is often involved in effector binding, interaction with GEFs and GAP-induced GTP-hydrolysis. G4 ((N/T)KxD) and the less conserved G5 motifs are mainly involved in sensing

of the guanine base and thus are responsible for discriminating against other nucleotides such as ATP.[20] Attached to the G-domain is a hypervariable C-terminus that can be posttranslationally modified with isoprenyl- or palmitoyl moieties. These lipophilic anchors facilitate membrane attachment of the small GTPases. In case of some members of the Arf family, membrane interaction is mediated by a myristoylated N-terminus.[21,22]

Small GTPases as molecular switches – structural changes upon nucleotide exchange

The basis of small GTPases functioning as molecular switches are the conformational differences between their GDP and their GTP-bound state. The structural changes associated with the exchange of GTP to GDP can be described by a "loaded-spring mechanism".[12] The conformational changes are mostly limited to the G2/switch I and G3/switch II region of the G-domain.[23] In the active, GTP-bound configuration, the additional interactions with the γ-phosphate force the switch I and switch II regions into a position close to the nucleotide. The main contacts contributing to this active conformation are formed through hydrogen bonds between the γ-phosphate of GTP with the side chain hydroxyl group of the conserved Threonine residue in the G1/switch I motif (T35 in HRas) and the backbone nitrogen of the glycine in the switch II region (G60 in HRas).[16,17] The conformation induced through these interactions allows for high affinity effector binding. When these contacts are missing, e.g. when the GTPase is bound to GDP, the switch regions become more flexible and disordered.

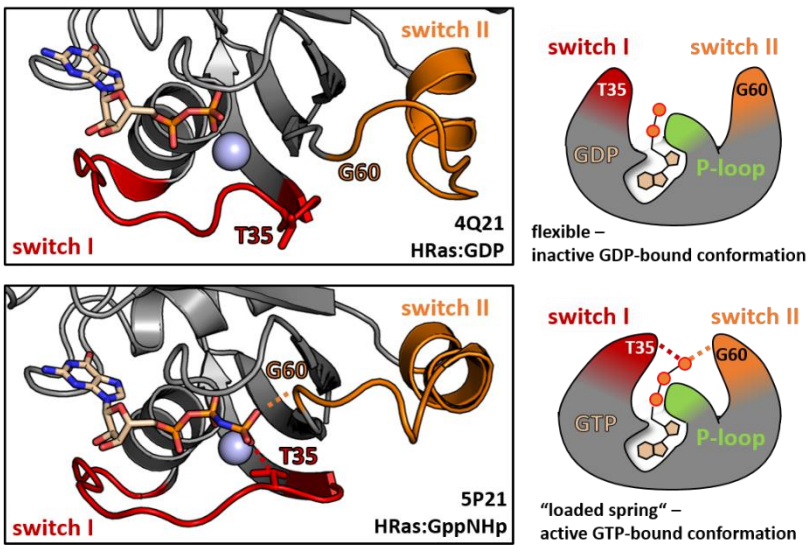

Figure 1-3: "Loaded-spring mechanism"[12] of the small GTPase switch.
Conformational changes in the small GTPase structure are most distinct in the switch I (red) and switch II (orange) region of the G-domain.
In the active GTP-bound configuration the γ-phosphate of the nucleotide interacts with main-chain atoms of a highly conserved Threonine (T35 in HRas) in switch I and a glycine (G60 in HRas) in switch II. When GTP is hydrolyzed the hydrogen bonds are released and the switch I and II regions relax into a more flexible conformation.

This structurally relaxed state is evidenced by numerous crystal structures of GDP-bound GTPases lacking well-defined density in the switch regions[24] and NMR-based studies that show intrinsic mobility in these areas.[25] The loss in structural definition is the cause for effector binding becoming less favorable. The binding enthalpy has to compensate the reduction in entropy caused by restricting the flexible switch regions to the fixed conformation in the GTPase:effector complex. It should be noted that, even in the GTP-

bound state the switch regions remain slightly flexible and are not completely locked in a defined conformation. It has been shown by H-[26,27] and P-NMR[28,29], as well as EPR[30,31] and FTIR-studies[32] that the active, GTP-/GppNHp-bound GTPase features distinguishable conformational sub-states.

In case of the members of the Arf and Ran family, the general assignment of the GDP-bound form as an open and undefined conformation has to be qualified. In this case the switch I changes its position and secondary structure when bound to GDP to form an additional β-strand extending the central β-sheet. Thus, their switch regions are in a fixed conformation when bound to GDP, albeit different from the GTP-bound structure.[33,34]

Regulation by GEFs/GAPs

In their nature of molecular switches, small GTPases alternate between the inactive, GDP-bound and the active, GTP-bound configuration. Due to their low rate of spontaneous nucleotide release[15,35] and the slow intrinsic GTP hydrolysis[15], the proteins generally remain in their respective activation state until they encounter one of their regulatory partners, GEF and GAP proteins. The tight regulation of GTPase switching through the interaction with GEFs and GAPs is crucial to achieve the level of spatiotemporal control required to govern such diverse cellular processes as observed for the members of the Ras superfamily.[11]

GTPase activation by GEFs

Small GTPases exhibit high affinity binding (nano to picomolar range) to either guanine nucleotide (GDP/GTP).[15,35] As a consequence, once the nucleotide:GTPase complex is formed, the dissociation of the nucleotide is very slow. The rate of spontaneous nucleotide exchange is too low to be relevant for GTPases governed signaling (ranging from $t_{1/2,\,Rho} \approx 1$ h[36] to $t_{1/2,\,Ran} \approx 13$ h[13]). Thus, efficient GTPase activation requires a catalyst to accelerate the slow intrinsic nucleotide exchange.

Numerous structural studies of GTPase-GEF pairs illustrate that the catalytic domains of different GEF families are structurally unrelated, but function through the common mechanism of accelerating the nucleotide release through distorting the GTPase nucleotide binding site.[10,11] Typically, the conformational changes are restricted to the switch I, switch II regions and the P-loop of the GTPase. As described previously, these regions form the primary contacts with the nucleotide's phosphate groups and the Mg^{2+} in the interaction site, thus mediating the high affinity binding of the guanine nucleotide. Perturbation of these crucial interaction sites reduces the affinity of the GTPases towards the bound nucleotide and leads to its subsequent release.

On the molecular level, crystal structures of nucleotide-free GTPase:GEF complexes revealed that a common feature is the displacement of the flexible switch I region from the nucleotide-binding site (Figure 1-4). Furthermore, GEFs form extensive interactions with the switch II region of the small GTPase, likely in order to compensate the loss in structural stability upon nucleotide release.

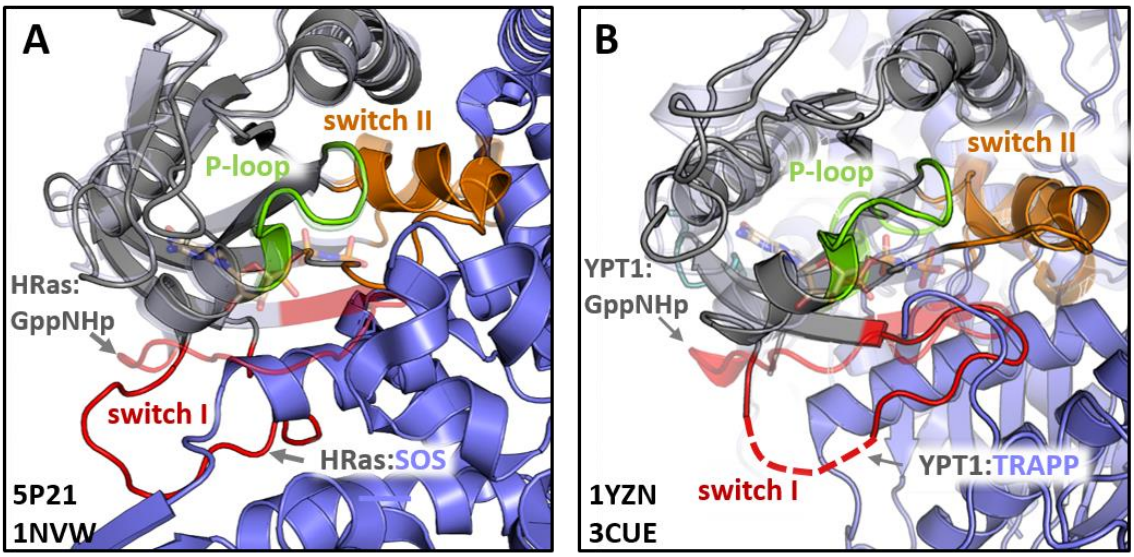

Figure 1-4: Binding of GEF distorts the nucleotide binding site.
Overlay of the complex structures of the nucleotide-free GTPase:GEF complexes, **(A)** HRas:SOS (PDB ID: 1NVW) and **(B)** YPT1:TRAPP (PDB ID: 3CUE) with the respective GppNHp-bound structures of HRas (PDB ID: 5P21) and YPT1 (PDB ID: 1YZN) (displayed in the same color scheme but semitransparent). In complex with the GEF, the switch I (red) is displaced from the nucleotide binding site. The switch II (orange) structure is stabilized by the GTPase:GEF interaction.

GEF-mediated nucleotide exchange can be described through a succession of multiple reversible association and dissociations steps.[11,13,37] In the initial stage, a low-affinity ternary GDP:GTPase:GEF-complex is formed that leads to the release of the bound nucleotide. Subsequently, a new nucleotide can bind, weakening the nucleotide-free GTPase:GEF-complex. Finally, the newly associated nucleotide allows for the dissociation of the GEF from the GTPase:GEF complex to complete the nucleotide exchange. As the affinity of the GTPase:GEF complex towards GDP and GTP is comparable[13,38], the nature of the newly bound nucleotide depends largely on the local GDP and GTP concentration. In the cellular context the concentration of GTP is usually 10-fold higher than GDP[14], thus GEF-mediated nucleotide exchange *in vivo* typically leads to the formation of the active, GTP-bound GTPase.

GTPase deactivation by GAPs

The intrinsic GTP hydrolysis rate is too slow to efficiently silence GTPase signaling. In order to effectively deactivate small GTPase signaling, the intrinsic GTPase activity is accelerated through interaction with GAP proteins. The first two GTPase-GAP pairs that were characterized on a structural and mechanistic level are HRas:RasGAP[39] and Cdc42:RhoGAP[40]. In these studies the GDP-bound GTPase:GAP complex is stabilized by AlF_3, mimicking the transition state of the GTP hydrolysis.

GAPs primarily interact with the switch I and switch II regions of the GTPase. In contrast to their regulatory counterpart, GAPs do not convey their function by inducing large structural changes in these regions. The enhanced GTP hydrolysis activity is based on the GAPs ability to: (1) counterbalance the negative charges of the transition state and (2) activate/position a water molecule for nucleophilic attack at the γ-phosphate.

Analogous to GEFs, GAPs are structurally diverse and the aforementioned requirements for induced GTP hydrolysis are met through different molecular mechanism depending on the specific GTPase and its cognate GAP (Figure 1-5).

In the HRas:RasGAP complex the GAP domain inserts an "arginine finger" at the nucleotide binding site that counters the partial negative charges and positions the conserved glutamine residue (Q61 in HRas) of the G3 (DxxGQ) motif/switch II to activate a water molecule for the nucleophilic attack on the γ-phosphate (Figure 1-5 A). The same combination of charge stabilization and water activation is found for Rab GTPases and their cognate TBC-domain containing GAPs. However, in this case the positioning and activation of the water molecule is mediated by a glutamine residue provided by the GAP instead of the switch II glutamine of the Rab protein(Figure 1-5 B).

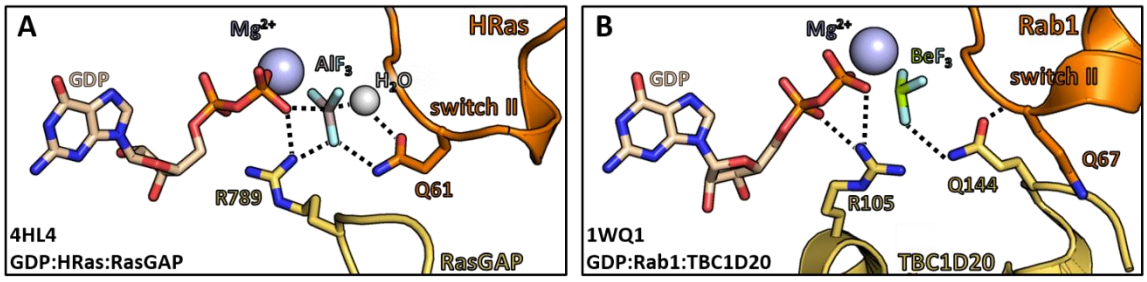

Figure 1-5: Molecular mechanism of the GAP-stimulated GTP hydrolysis HRas:RasGAP (PDB ID: 4HL4) and Rab1:TBC1D20 (1WQ1).
(A) The HRas:RasGAP mechanism features a arginine finger and the GTPase switch II glutamine.[39] **(B)** Rab1:TBC1D20 employs a GAP arginine finger and a GAP domain a glutamine, while the switch II glutamine is contacting the GAP domain.[41]

It is important to keep in mind that for some small GTPase-GAP pairs, the often utilized "dominant-active" switch II glutamine mutants do not necessarily completely abolish GAP induced GTP-hydrolysis (e.g. Rab33/RUTBC1[42], Rab5/RUTBC3[43] and Rab1/TBC1D20[41]). The use of these constitutively active/inactive small GTPase mutants becomes even more problematic when considering the involvement of some of these critical residues in both GEF-mediated activation and GAP-mediated deactivation.[43]

In RapGAP and RanGAP-induced GTP hydrolysis, a different combination of residues is involved. Both GAPs utilize a switch I tyrosine and different second residues for water activation and positioning. RapGAP provides an asparagine from its GAP domain[44], whereas RanGAP exploits the GTPase's conserved switch II glutamine residue[45] similar to the mechanism described for HRas:RasGAP.

1.1.2 The Rab subfamily and their role in vesicular transport

With over 60 identified members in humans, Rab proteins constitute the largest branch of the Ras superfamily of small GTPases.[46] The term Rab originates from **Ra**s-related in **b**rain, as mammalian Rab proteins were first discovered in a rat brain DNA library.[47]

Besides sharing the conserved motifs of the G-domain, Rab proteins feature five additional conserved sequence motifs that distinguish them from other members of the Ras superfamily.[48] These Rab family motifs (RabF1-RabF5) were identified through sequence alignment and are located in or around the switch and interswitch regions. Rab proteins can further be grouped into subfamilies based on four Rab subfamily-conserved sequences (RabSF1-RabSF4). The RabSF motifs are believed to convey the proteins specificity towards their respective GEFs, GAPs and effector proteins while the RabF motifs are thought to be mainly responsible for the discrimination of the active/inactive state and/or involved in binding to universal regulators such as Rab escort protein (REP) and GDP dissociation inhibitor (GDI). The largest heterogeneity between Rab structures can be found in their switch domains and the loop between the third α-helix and the fifth β-sheet, close to switch II and likely mediates effector specificity.[49,50]

The greatest divergence in primary sequence is displayed by the ~30-40 amino acid long hypervariable region at the proteins C-termini. This region is primarily unstructured and plays an important role in targeting Rab proteins to specific subcellular locations.[51,52] It is, however, not the sole decisive factor. Membrane targeting is also mediated through several other factors such as other regions of the protein[53] and the interaction with GEFs, GAPs and effector proteins.[53-58] Generally, Rab membrane attachment is facilitated through the posttranslational modification of one or two cysteines at the proteins C-terminus with geranylgeranyl moieties. Unlike members of the Ras and Rho family, Rabs do not share a consensus prenylation motif. Most common are the C-terminal amino acid sequences XXCC, XCXC and CCXX with other permutations occurring as well. Specificity for geranylgeranylation is exerted through an additional protein factor, REP. Newly synthesized, unmodified GDP-bound Rab associates to REP, which in turn presents the Rab to RabGGTase.[59] The RabGGTase then covalently attaches (two) geranylgeranyl groups at the C-terminal cysteines of Rab.[60] After dissociation from the complex, REP is assumed to deliver the modified protein to its specific target membrane.[61] REP binds the unprenylated as well as the lipidated protein with high affinity.[62] In contrast, the structurally and functionally closely related GDI binds to the geranylgeranylated Rab with high affinity and only poorly to the unprenylated protein. Thus, both proteins fulfill distinctive roles in Rab regulation. While REP facilitates Rab prenylation by RabGGTase, GDI's main function is the extraction of prenylated Rab proteins from membranes. The affinity of GDI towards Rab is reduced by three orders of magnitude when GDP is exchanged for GTP.[63] Hence, Rab activation is believed to stabilize membrane attachment by impeding GDI-mediated membrane extraction. Because of the high affinity of GDI towards prenylated Rab[63,64] it has been speculated that an additional factor, termed GDI dissociation factor (GDF), is necessary to assist in releasing and targeting the GDI-bound Rab to a specific membrane. So far only

Pra1/Yip3 (in yeast), has displayed genuine GDF activity by catalyzing the dissociation of Rab:GDI complexes.[65,66] However, the exact mechanisms of how GDI is displaced by this GDF remains unclear.

The cycling of Rab between different membrane compartment is linked to its interaction with GEFs, GAPs and effector proteins. A more detailed description of how Rab activation and deactivation is connected to the Rab proteins spatial cycle in vesicular transport is given in Figure 1-6.

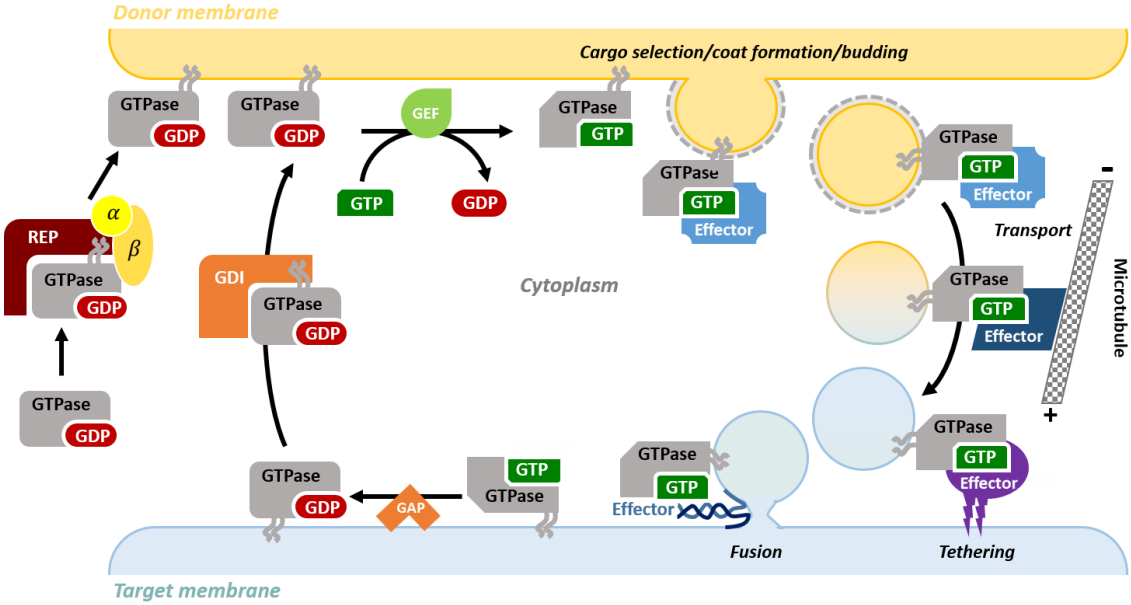

Figure 1-6: Rab cycling regulates vesicular transport.
Newly synthesized Rab binds to REP, which then presents the protein to RabGGTase (a heterodimer consisting of an α and a β–subunit) for prenylation at its C-terminus. Subsequently, REP delivers the now prenylated Rab to its target membrane. Following membrane attachment at the donor membrane, GEFs facilitate activation of the Rab protein through GDP to GTP exchange. The GTP-bound Rab can now bind to effector proteins that are involved in vesicle budding and cargo selection and initiate vesicular transport. After the vesicle is transported to the target compartment, Rab proteins recruit tethering factors, SNAREs, and other effectors involved in docking and fusion. After fusion with the acceptor membrane, the Rab protein is deactivated through interaction with GAPs that accelerate the intrinsic GTP hydrolysis. Following deactivation, the Rab can be extracted from the membrane through the solubilization factor GDI. From the cytosol the Rab protein can re-enter the spatial cycle through delivery to the donor membrane.

Rab activity is regulated through interacting with GEFs and GAPs. The number of characterized Rab GEFs is relatively small, when compared to the over 60 identified proteins of the Rab family. Rab GEFs show a high diversity in their primary and tertiary structure and hence cannot be easily identified by sequence analysis.[10] Available structures of Rab:GEF complexes (YPT1:TRAPP[67] (yeast homolog of Rab1:TRAPP), Sec4:Sec2[68] (yeast homolog of Rab8:Rabin8), Rab21:Rabex-5[69], Rab35:DENND1B[70] and Rab1:DrrA[71]) indicate that the general mechanism of GEF-mediated Rab activation is similar to the one observed for other small GTPase families (1.1.1). The nucleotide/Mg^{2+}-binding site is deformed through direct insertion of residues from the GEF domain or indirect conformational change upon binding to the GEF, ultimately resulting in displacement of the bound nucleotide.[11] Rab GEFs can be divided into a number of discrete families with the Vps9 family[72] and DENN domain-containing GEFs[73] being the largest. Other GEFs are comprised of two or more subunits such as the multisubunit TRAPP complex that specifically interacts with Rab1/YPT1 and also acts as a vesicle

tethering complex.[67,74-76] Another notable Rab GEF is DrrA, the first identified bacterial GEF from the organism *Legionella pneumophila* with highly specific nucleotide exchange activity towards Rab1.[71,77,78] Recent studies demonstrate that GEFs are important factors in Rab membrane targeting. Ectopic mislocalization of a GEF leads to mistargeting of its cognate Rab to the same membrane compartment.[54]

In contrast to the diversity of the catalytic motifs of Rab GEFs, most known Rab GAPs share a conserved catalytic TBC (Tre2/Bub2/Cdc16) domain. Like GAPs for members of the Ras and Rho family, Rab GAPs feature a conserved catalytic arginine finger and were believed to induce GTP hydrolysis through a similar mechanism. However, structures of the transition state of Rab33:Gyp1[79] and Rab1:TBC1D20[41] revealed that instead of utilizing the conserved glutamine residue of the G3 (DXXGQ) motif, Rab GAPs insert a glutamine from their GAP domain to activate the attacking water molecule (Figure 1-5).

The Rab activation/deactivation cycle is directly linked to Rab membrane localization and their interaction with effector proteins.[80,81] Effectors are defined as proteins that specifically interact with the active, GTP-bound form of the small GTPase. While some effectors bind specifically to only one Rab, other effectors can bind to multiple members of the Rab family[82,83] and some Rabs can bind to a multitude of effector proteins.[84] Through their interaction with diverse effector proteins, Rabs are involved in all steps of vesicular transport. This includes vesicle budding and cargo selection, motility as well as vesicle tethering and fusion of transport vesicle with their target membrane.

Examples for Rab proteins that are involved in cargo selection during vesicle formation include Rab5, Rab7 and Rab9. Rab5 and Rab7 are required for the recruitment of the Vps26-Vps19-Vps35 trimer complex which, as part of the retromer complex, is responsible for cargo selection.[85,86] Rab9 enhances the interaction between its effector protein TIP47 and the mannose-6-phosphate receptor during vesicle formation, thereby facilitating recycling from the endosome to the trans-Golgi network.[87,88]

Besides cargo selection, Rab proteins take part in the regulation of the vesicular movement. In mammalian cells vesicular trafficking often relies on motor proteins that move along microtubules. Rabs have been shown to regulate traffic in either microtubule transport direction by interacting with members of the kinesin and dynein family. Rab6 for instance, directly interacts with Rabkinesin-6 to facilitate intra-Golgi transport.[89,90] Another example is Rab7 which regulates trafficking between late endosomes and lysosomes by recruiting the dynein-dynactin motor complex through interacting with Rab-interacting lysosomal protein (RILP).[91,92]

Most transport pathways require tethering prior to vesicle fusion. This initial recognition ensures proper association of cargo and target membrane. Tethering factors can be divided into two categories: long coiled-coiled tethers and multisubunit protein complexes. Effectors of Rab proteins can be found in both categories. Notable members of the coiled-coil tethers are the family of Golgins. This includes p115, giantin and GM130, that all have been linked to Rab1 and its effectors. Rab1 is essential for the assembly of the accessory factors that tether ER-derived vesicles to the Golgi membrane. p115 is a homodimer that binds

to GM130 (localized at the *cis*-Golgi) and giantin (localized at COPI vesicles) through its coiled-coil tail while associating to Rab1 through its globular head domain.[56,93-95] GM130 localization to the *cis*-Golgi is mediated through the interaction with the Rab1 effector GRASP65. This interaction regulates tethering of COPII vesicles at the *cis*-Golgi.[94,96] The Rab1 effector p115 has also been shown to interact with SNARE proteins, the driving force for vesicular fusion.[97,98] Among the multisubunit complexes involved in vesicle tethering are the TRAPP complexes, which are critical for endoplasmic reticulum (ER) to Golgi transport in yeast and mammalian cells.[74] In contrast to other tether complexes, the TRAPP complexes do not function as effector proteins but act as GEFs towards Rab1/YPT1. In yeast, two TRAPP complexes have been described that regulate two aspects of the ER-Golgi transport[76], while in mammalian cells, only one TRAPP complex has been identified so far.[74] The function of the TRAPP complexes as tethers can be derived from their interactions with Sec23 and the SNARE proteins Bet1, Sed5 and Sec22, as well as its GEF activity towards Rab1, that leads to the recruitment to the aforementioned coiled-coil tethering factors. Sec23, a subunit of the COPII coat, has been shown to interact with the Bet3 subunit of the TRAPP complex.[99] Bet3 has also been implicated to interact with the SNARE proteins Bet1, Sed5 and Sec22, that are involved in ER to Golgi trafficking.[76,100]

Other large multisubunit tether complexes include COG (conserved oligomeric Golgi; endosome-Golgi and intra-Golgi transport), exocyst (Golgi-plasma membrane transport), HOPS (homotypic fusion and vacuole protein sorting; vacuole-vacuole and endosome-vacuole transport), CORVET (class C core vacuole/endosome tethering; endosome-Golgi transport), Dsl1 (dependence on Sly1, Golgi-ER transport) and GARP (Golgi-associated retrograde protein; recycling from endosome to Golgi).[46,101,102]

The final step of vesicular trafficking is fusion of the transport vesicle with the target membrane. Rabs are involved in this process by either directly interacting with the SNARE proteins or indirectly through interaction with proteins that regulate SNARE function. Examples for Rab proteins involved in regulation of vesicular fusion are Sec4 (the yeast analogue of Rab8) and Rab5. Sec4 is involved in the final stage of the secretory pathway and has been shown to interact with Sro7, which interacts with Sec9 and regulates SNARE function.[103] Rab5 is important for targeting endosomal traffic towards lysosomes. Its effectors EEA1 and rabenosyn-5 interact with the SNARE protein syntaxin-6 and VPS45, respectively.[104,105]

1.1.3 The Ras subfamily and their role in signal transduction and cancer

The term Ras originates from **Ra**t **s**arcoma, as Ras genes were initially discovered in studies of cancer-causing viruses in rats.[106,107] In humans, the three Ras genes encode four highly homologous Ras proteins: HRas (Harvey-Ras, first discovered by Jennifer Harvey[106]), NRas (first identified in human neuroblastoma cells[108,109]) and two KRas isoforms (Kirsten-Ras, first discovered by Werner Kirsten[107]). The two KRas proteins result from two alternative splice variants and are termed KRas4a and KRas4b. All four Ras proteins feature an exceptionally high sequence similarity within the G-domain. Their lipidated C-terminal hypervariable region however, is different for each isoform and critical for the proteins specific membrane localization and subsequent activation.

The lipid moieties are introduced through a series of posttranslational modification. All isoforms are initially farnesylated at the C-terminal cysteine residue followed by cleavage of the last three amino acids (-AAX) of the -CAAX box motif and transformation of the C-terminal carboxyl into a methyl ester (Figure 1-7 A). While HRas, NRas and KRas4a are additionally modified with one or two palmitoyl groups that further stabilize attachment to endomembranes, KRas4b features a polybasic lysine stretch that mediates association to the negatively charged plasma membrane (Figure 1-7 B).

Ras proteins play a crucial role in the regulation of cell proliferation, differentiation and survival. They are vital to a number of important cellular signaling pathways such as the RAF-MEK-ERK[110-112] and the PI3K-AKT-mTor[113,114] pathway. Commonly, Ras signaling is initiated through recruitment of the cognate Ras GEFs to the specific Ras membrane localization sites. Following GEF mediated GDP to GTP exchange, the activated Ras protein can bind to its respective effector proteins, thereby triggering downstream signaling. A classic example of this mechanism is the activation of KRas through translocation of the son of sevenless (SOS) homologue 1 and 2 to the plasma membrane (Figure 1-7 C).[115,116]

As a consequence of their role as central signaling nodes, Ras mutations that lead to protein hyper activation, e.g. through impairment of the intrinsic or GAP-mediated GTP hydrolysis, are among the most common mutations found in tumors. The sites most frequently affected are the conserved residues G12/G13 in the G1 and Q61 in the G3 motif of the G-domain (Figure 1-2 C).

Mutation at G12 or G13, leads to steric occlusion of the insertion site of the GAP arginine finger and prevents the correct orientation of the residues involved in GTP hydrolysis in the Ras:GAP complex.[39] Mutation at the critical Q61 residue interferes with the positioning of the activated H_2O molecule (Figure 1-5 A) that is required for GTP hydrolysis.[117]

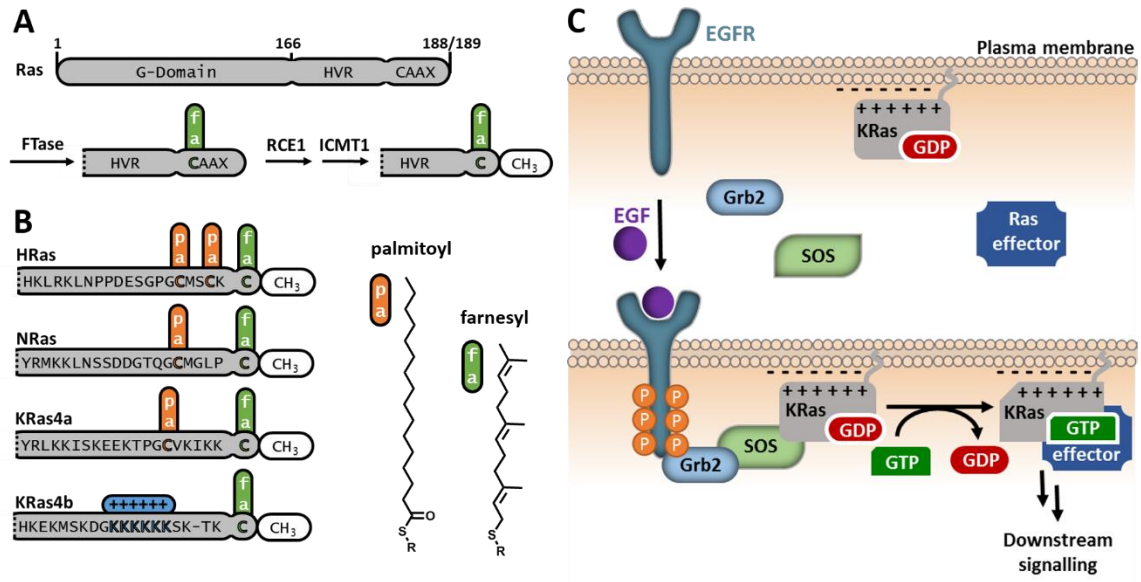

Figure 1-7: Posttranslational processing of Ras isoforms[118] and Grb2-mediated EGF-induced Ras activation[116].
(A) All Ras isoforms are farnesylated at their C-terminal cysteine by farnesyltransferase (FTase). Subsequently Ras-converting enzyme 1 (RCE1) cleaves the three –AAX residues of the farnesylated –CAAX motif and isoprenylcysteine carboxylmethyltransferase 1 (ICMT1) converts the C-terminal carboxyl-moiety into a methyl ester. **(B)** Left: Posttranslational C-terminal modifications for the four Ras isoforms. Palmitoylation is indicated in orange, farnesylation in green and the positively charged polylysine stretch of the KRas4b isoform in blue. Right: Structures of the lipophilic moieties. **(C)** Mediated by its farnesylated C-terminus in combination with its positively charged polylysine tail, Ras localizes to the negatively charged plasma membrane. The GEF son of sevenless (SOS) and the adaptor protein growth factor receptor-bound protein 2 (Grb2) are localized in the cytosol. Upon stimulation, e.g. by EGF, the EGF receptor (EGFR) is phosphorylated leading to binding of Grb2. Grb2 in turn recruits SOS to the plasma membrane, prompting Ras activation through GEF-mediated GDP to GTP exchange. The GTP-bound Ras protein can then bind to effector proteins, activating downstream signaling.

These constitutively active Ras mutations are powerful cancer drivers and thus high-profile targets for drug development.[119-121] However, due to a combination of the high affinity towards its native substrates (GDP/GTP), the lack of alternative accessible binding sites, redundancy and feedback loops in Ras-mediated signaling and the high similarity within the small GTPase family, drugs that directly target Ras remain ineffective to the extent that the proteins have been denoted “undruggable” by conventional approaches.[118,121,122]. While mutations in each of the isoforms can lead to cancer, different tumor types are associated with individual Ras isoforms and mutations in KRas are by far the most common found in human cancer.[2,123] New approaches such as specific and covalent targeting of the aforementioned hyperactive KRas mutants[124,125] or interference with the KRas-PDEδ interaction[126], has led to a resurgence in the effort to directly target Ras signaling recently.[121,122,127]

1.2 Fluorescence as a tool to study dynamic processes

Fluorescence microscopy is one of the few techniques that is able to reach the spatial and temporal resolution necessary to observe the highly dynamic functioning of proteins in cells. It allows for the simultaneous observation of multiple components and is largely noninvasive.

When used in combination with FRET it is exceptionally well-suited to reliably observe and quantify protein interactions. Specialized fluorescent biosensors can facilitate the direct observation of protein functioning in the cellular environment. Furthermore, other advanced techniques such as fluorescence recovery after photobleaching and photo activatable fluorescent proteins can be used to assess protein mobility and diffusion within cells.

1.2.1 Förster Resonance Energy Transfer (FRET)

Luminescence is the emission of light that is associated with the return of a molecule from an electronically excited state to its ground state. Depending on the nature of the excited state, this process can be categorized as fluorescence or phosphorescence. In fluorescence the molecule (fluorophore) relaxes from an excited singlet state. This spin allowed transition occurs rapidly and typically proceed within less than 10 ns. In contrast, emission in phosphorescence is slow (~10^{-4} - 10^{2} s) as the molecule relaxes from an excited triplet state, a spin forbidden transition.

The term fluorescence was coined by George Stokes in 1852.[128] Two important characteristics of this process are the fluorescence lifetime and the quantum yield. The quantum yield is the ratio of photons emitted to the number of photons absorbed during excitation of the fluorophore. The fluorescence lifetime of the excited state is the average time the molecule remains in the excited state until it relaxes to the ground state. The depopulation of the excited state can occur through radiative and non-radiative processes. One of these non-radiative processes is the Förster resonance energy transfer (FRET), termed after Theodor Förster who first described the phenomenon in 1940.[129]

In general terms FRET can occur when the emission spectrum of the fluorophore (donor) overlaps with the absorption spectrum of another molecule (acceptor) that is in close proximity (Figure 1-8). The energy transfer occurs through coupling of the respective dipoles and thus does not involve the emission/absorption of a photon, it is radiationless. The extent of the energy transfer depends on the distance of the involved donor and acceptor molecules (typically 1-10 nm), their relative orientation and the spectral overlap of their emission/absorption spectra. The exceptional spatial sensitivity of FRET is the main reason for its widespread application in molecular biology. The typical FRET range (< 10 nm) is in line with the size of biomolecules and below the optical resolution limit.

Any process that influences relative distance/orientation of the two dipoles will affect the energy transfer rate and thus can be assessed by fluorescence spectroscopic methods. Consequently, FRET has been

extensively used to observe protein-protein interactions or to monitor conformational changes within proteins.

More precisely the spatial sensitivity of the FRET can be derived from the following relations. The rate of energy transfer k_{FRET} is given by Eq. 1-1:

$$k_{FRET} = \frac{1}{\tau_D}\left(\frac{R_o}{r}\right)^6 \qquad \textbf{Eq. 1-1}$$

and closely related to the FRET efficiency (E_{FRET}). Here τ_D is the average lifetime of the excited state of the donor in absence of a FRET acceptor, R_0 is the Förster radius, the distance where the transfer efficiency E_{FRET} is 50 %, and r is the distance between the donor fluorophore and the acceptor.

E_{FRET} is a quantitative measure of the ratio of photons that are transferred through FRET to the total amount of photons absorbed by the donor fluorophore and defined as:

$$E_{FRET} = \frac{k_{FRET}}{\frac{1}{\tau_D} + k_{FRET}} \text{ using Eq. 1-1 it follows } E_{FRET} = \frac{1}{1+\left(\frac{r}{R_0}\right)^6} \qquad \textbf{Eq. 1-2}$$

The strong dependence of the FRET efficiency from the donor-acceptor distance, is the reason for its spatial resolution, especially close to R_0 (Figure 1-8 B).

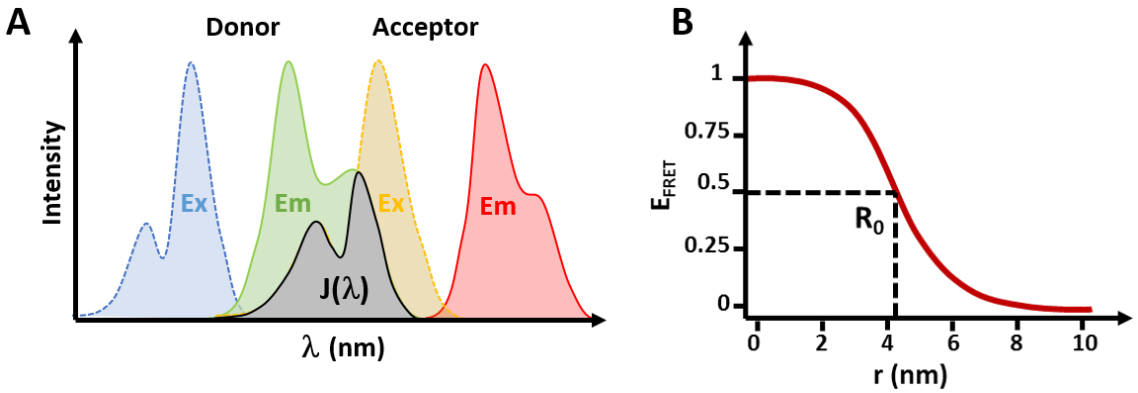

Figure 1-8: Factors in FRET efficiency. Spectral overlap integral and donor-acceptor distance.
(A) Spectral overlap integral J(λ) between the donor emission and the acceptor absorption spectrum. **(B)** Dependency of the FRET efficiency from the donor-acceptor distance**.** R_0 marks where the FRET efficiency is 50 %.

R_0 can be obtained from the following relation:

$$R_0^6 = 8.79 \cdot 10^{23} \cdot \frac{\kappa^2 \cdot Q_D \cdot J(\lambda)}{n^4} \qquad \textbf{Eq. 1-3}$$

n is the refractive index of the surrounding medium, Q_D is the fluorescence quantum yield of the donor dye, κ^2 is the dipole orientation factor and J(λ) is the overlap integral of the donor emission and acceptor excitation integrated over the wavelengths λ. The overlap integral J(λ) depends on the spectral overlap of the donor emission and acceptor excitation spectrum and is determined by the chosen fluorophores (Figure 1-8 A).

The sensitivity towards the relative orientation of the donor acceptor dipoles is founded in κ^2 and can be quantified using Eq. 1-4:

$$\kappa^2 = (\cos\theta_{DA} - 3\cos\theta_D \cos\theta_A)^2 \qquad \textbf{Eq. 1-4}$$

θ_{DA} is the angle between the emission dipole of the donor and the absorption dipole of the acceptor (Figure 1-9). θ_D and θ_A are the angles between these dipoles and the vector joining the donor and the acceptor dipoles. The value of κ^2 can range between 0 to 4. For most approaches a value of 2/3 is assumed based on averaging the donor and acceptor orientations for freely rotating dyes. However, this approximation may be inappropriate for FRET pairs that are constricted in their rotational freedom.

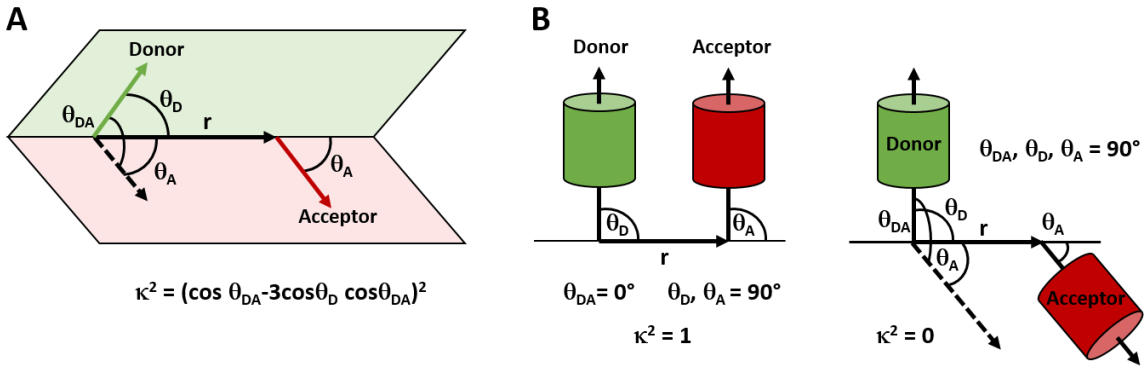

Figure 1-9: Factors in FRET efficiency. Orientation factor κ^2.
(A) The factors determining the value of κ^2 are the angles between the transitioning dipoles of the donor emission and the acceptor absorption and their joining vector. **(B)** Depending on the relative orientation κ^2 can range between 0 to 4. When the transitioning dipoles of the FRET donor and acceptor are parallel, κ^2 has the value 1. When the transitioning dipoles are orthogonal, κ^2 has the value 0 and no FRET occurs. A value of 4 is reached when the dipoles are collinear.

1.2.2 FRET imaging by Fluorescence Lifetime Imaging Microscopy (FLIM)

FRET can be assessed by several imaging techniques such as acceptor photobleaching, fluorescence polarization, sensitized emission and fluorescence lifetime imaging. The advantage of using fluorescence lifetime based FRET quantification is that it is based on an intrinsic molecular property and thus independent of the concentration of the involved fluorophores. Furthermore, FLIM analysis does not suffer from artifacts commonly encountered when using sensitized emission approaches, such as signal cross contamination through acceptor spectral bleed through and cross-talk.[130] These traits make FLIM a powerful tool for mapping FRET quantitatively *in vivo*.

The fluorescence lifetime τ is defined as the average time that a fluorophore remains in its excited state before returning to its ground state and is the key parameter characterizing the fluorescence decay. The intensity decay of the excited fluorophore population can be expressed as:

$$I(t) = I_0 \cdot e^{-1/\tau} \qquad \textbf{Eq. 1-5}$$

Here I_0 is the initial intensity directly after excitation. The fluorescence lifetime is determined by the rate constants of the processes contributing to fluorophore relaxation from the excited state:

$$\tau_D = \frac{1}{k_r + k_{nr}}, \text{ with FRET } \tau_{DA} = \frac{1}{k_r + k_{nr} + k_{FRET}} \qquad \textbf{Eq. 1-6}$$

k_r and k_{nr} are the rate constants for radiative and non-radiative deactivation, respectively. τ_D is the fluorescence lifetime of the donor in the absence of the acceptor and τ_{DA} is the fluorescence lifetime in the presence of the FRET acceptor. The radiative rate constant is determined by the spectroscopic properties of the fluorophore and the refractive index of the surrounding medium.[131] The non-radiative rate constant depends on the local environment of the fluorophore such as pH and ion concentration and includes the rates for vibrational relaxation and intersystem crossing. FRET contributes an additional channel of excited state depopulation (k_{FRET}) and therefore reduces its average fluorescence lifetime of the donor fluorophore. From this drop in fluorescence lifetime, the efficiency of FRET can be determined using Eq. 1-7:

$$E_{FRET} = 1 - \frac{\tau_{DA}}{\tau_D} \qquad \textbf{Eq. 1-7}$$

There are two standard approaches to fluorescence lifetime imaging: time-domain and frequency-domain FLIM. In this thesis, time-correlated single photon counting (TCSPC) was used to determine the lifetime of a FRET based biosensor.

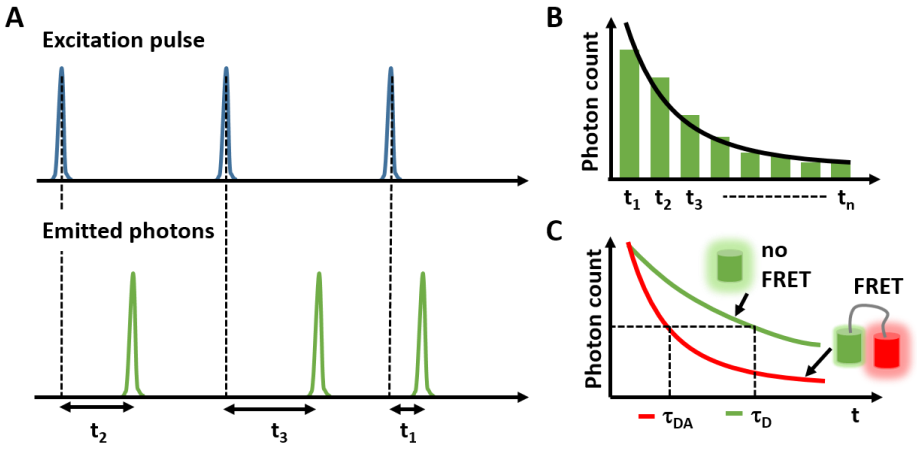

Figure 1-10: Principle of TCSPC-FLIM.
(A) A short, intense excitation pulse excites the fluorophore population. After excitation the arrival time of the subsequently emitted photons is measured. **(B)** The photon arrival times are binned and the histogram of the number of photons over the time after the excitation pulse yields the fluorescence decay curve. **(C)** The average fluorescence lifetime is reduced through FRET.

The general principle of TCSPC is based on detecting the arrival times of emitted photons after simultaneously excitation of the whole fluorophore population. Excitation is typically achieved by a short, intense laser pulse. The excitation pulse starts the photon timing and is subsequently stopped upon arrival of an emitted photon at a detector, e.g. an avalanche photodiode (APD). The excitation-emission cycle is repeated and the detected arrival times are sorted into time bins, amounting to the fluorescence decay curve of the fluorescent species. The obtained histogram can then be fitted with a (multi)-exponential curve.

For fluorophores exhibiting single exponential decay kinetics and if the population of the excited fluorophore is homogenous, the decay kinetics can be described by a single exponential function. If a fraction of the fluorophore population undergoes FRET, the decay curve features a second lifetime component that can be quantified by fitting the obtained histograms with a multi-exponential model.

1.2.3 Protein dynamics resolved by photobleaching and photoactivation

When using standard fluorescence microscopy, only the steady state distribution of a fluorescently tagged protein can be observed. By photobleaching or –activation of a defined subcellular compartment, a specific protein pool can be selected and its redistribution over time can then be monitored by time-lapse imaging. This allows the observation and quantification of a proteins kinetic behavior, such as association and dissociation from membranes, binding to interaction partners or diffusion inside and in between different cellular compartments.

Fluorescence recovery after photobleaching (FRAP)

Established almost 40 years ago, FRAP was developed to examine the lateral diffusion properties of molecules in living cells.[132-135] For a typical FRAP experiment the fluorophores in a specific region of interest (ROI) are bleached through irradiation with a high intensity laser beam. The subsequent recovery of the fluorescence intensity is then followed by time-lapse imaging. The time-course of a representative FRAP experiment is depicted in Figure 1-11.

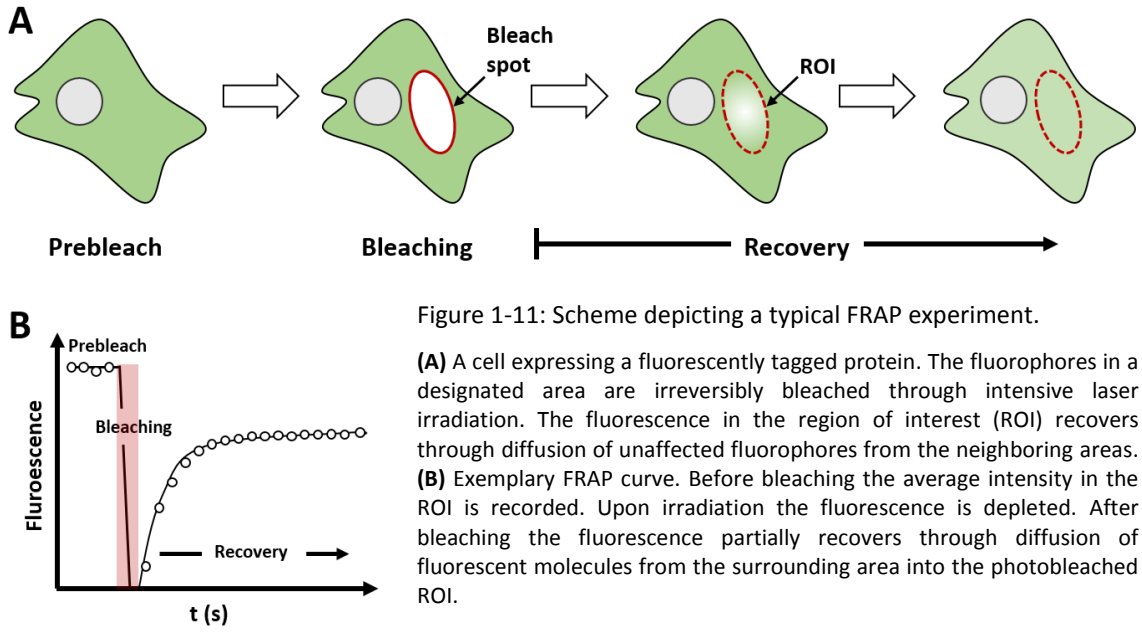

Figure 1-11: Scheme depicting a typical FRAP experiment.

(A) A cell expressing a fluorescently tagged protein. The fluorophores in a designated area are irreversibly bleached through intensive laser irradiation. The fluorescence in the region of interest (ROI) recovers through diffusion of unaffected fluorophores from the neighboring areas. **(B)** Exemplary FRAP curve. Before bleaching the average intensity in the ROI is recorded. Upon irradiation the fluorescence is depleted. After bleaching the fluorescence partially recovers through diffusion of fluorescent molecules from the surrounding area into the photobleached ROI.

Depending on the nature of the fluorescently labeled molecule and the bleached region the observed recovery can originate from diffusion, association and dissociation or transport processes. Thus,

quantitative analysis of the recovery curve contains information regarding the kinetic parameters of the movement of the labeled molecule and can be employed to determine the diffusion constants and transport rates of proteins.

FRAP has been used to study protein dynamics in the cytoplasm, nucleus and other cell organelles such as mitochondria, Golgi and the ER.[136] Furthermore photobleaching has been used to analyze the dynamics of protein trafficking.[137-140]

Fluorescence localization after photoactivation (FLAP)

Photoactivation experiments can be used to complement FRAP measurements. The most commonly used photoactivatable fluorescent protein is photoactivatable GFP (paGFP).[141] Before activation paGFP displays only very low fluorescence at typical GFP imaging settings. Upon intense UV irradiation the chromophore undergoes irreversible photoconversion, changing its spectral properties and leading to a more than 100-fold increase in fluorescence.

The procedure of a typical photoactivation experiments is similar to the previously described FRAP setup. Instead of a bleaching step, a fluorophore population is activated at a predefined ROI through irradiation at a specific wavelength (usually in the UV range) and the subsequent depletion from this area and/or the resulting increase in fluorescence at a different site is monitored (Figure 1-12).

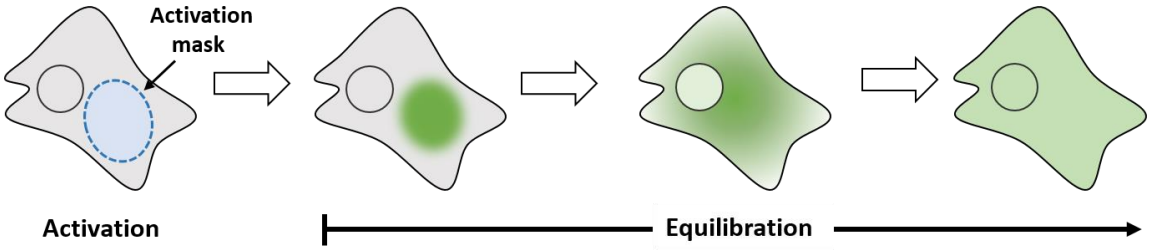

Figure 1-12: Scheme depicting a typical FLAP experiment.
Before photoactivation cells expressing a paGFP-tagged protein display negligible fluorescence. After irradiation with the appropriate wavelength, the fluorophores in the exposed area show a marked increase in fluorescence. Subsequently, the fluorophores diffuse through the cytoplasm and later into the cell nucleus.

In contrast to photobleaching, newly synthesized protein that is generated over the course of the measurement does not affect photoactivation experiments. Like FRAP, photoactivation can be utilized to examine protein kinetics and determine properties such as the diffusion coefficient or the residence time of a protein at a specific organelle.

1.3 Small GTPase biosensors

Due to their involvement in a plethora of highly dynamic processes, small GTPases have been among the first targets for biosensor development. GTPase biosensors are primarily focused on spatially resolving GTPase activation in cells.[142]

The common methodology of most GTPase sensors is based on utilizing effector domains as affinity tags. These tags report on GTPase activation through specifically binding to the GTP-bound protein. This concept was first exploited in a bimolecular FRET biosensor to visualize Rac1 activity in cells[143] and is derived from biochemical assays used to quantify GTPase activity in cell lysates.[144] In this approach, a fluorescently labeled affinity tag, based on the p21-activated kinase 1 (Pak1) effector domain, binds to activated GFP-tagged Rac1, bringing the two fluorophores in close proximity to generate a FRET signal read out at locations of high Rac1 activity.(Figure 1-13 A).

A different bimolecular sensor design that does not rely on FRET, is the translocation sensor strategy. In this case, the read out is generated by fluorescently labeled effector domains that bind and enrich at sites with a high concentration of active, GTP-bound GTPase (Figure 1-13 B). This methodology also allows for the observation of endogenous GTPase activity.[145-148]

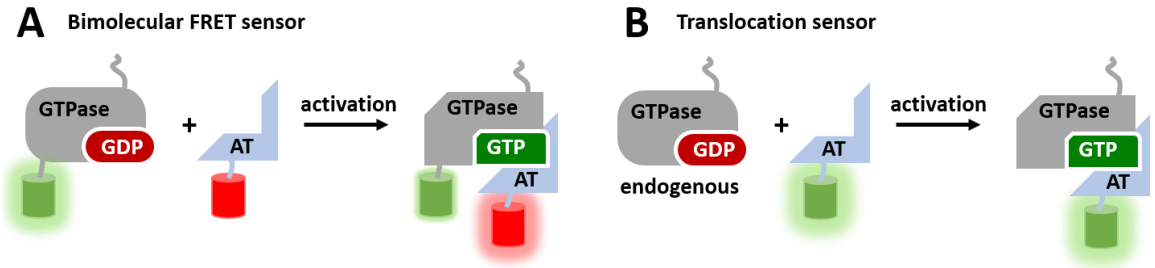

Figure 1-13: Bimolecular sensor approaches.
(A) Bimolecular FRET sensor. Binding of the fluorescently labeled affinity tag (AT) to the activated, labeled GTPase leads to FRET. **(B)** Translocation sensor. A labeled AT locates to the sites of high GTPase activity through specific interaction with the active GTPase.

These dual-chain approaches, where the affinity-tag and the GTPase are located in two separate molecules, were later complemented by single-chain FRET constructs that can be purely genetically encoded. The first of these small GTPase single-chain FRET sensors was developed to monitor Rap1 and HRas activation in cells.[149] In this case, the GTPase and the affinity tag are directly linked and sandwiched between two fluorescent proteins. Upon binding of the affinity tag to the activated, GTP-bound GTPase, the two fluorescent proteins are brought in close proximity and form an efficient FRET pair. This sensor principle is also referred to as “Ras and interacting protein chimaeric unit” (Raichu) sensors and variations have been applied to multiple other small GTPases, including members of the Rho[150-154], Ras[149,155], Rab[156,157], and the Ran family[158] (Figure 1-14).

Both approaches have specific advantages and weaknesses. Dual-chain designs are more accessible as they only require optimization of one component, while single-chain constructs have to be optimized for their linker regions, topology and relative orientation.[157,159,160]

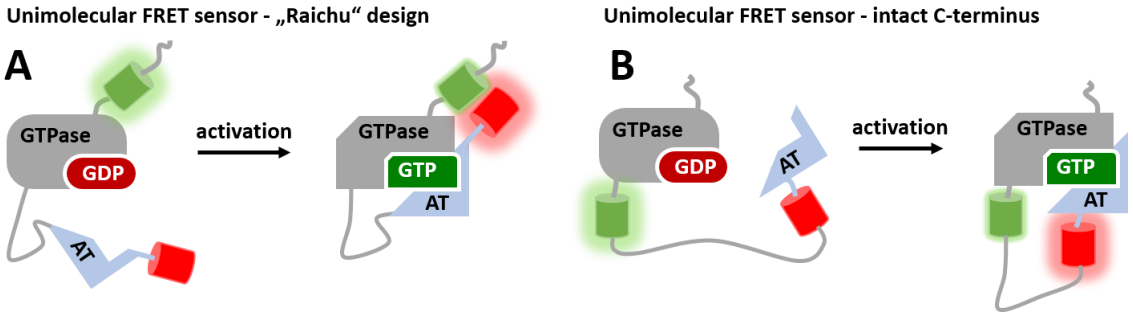

Figure 1-14: Unimolecular FRET sensors.
(A) “Raichu” sensor design that sandwiches the GTPase and the affinity tag (AT) between two fluorescent proteins. Upon activation the fluorescent proteins are brought in close proximity resulting in FRET. **(B)** A variation of the unimolecular FRET sensor design that preserves the GTPase’s C-terminus. The C-terminal region is often critical for native membrane localization.

Furthermore, dual chain constructs usually allow for a higher dynamic range as they do not exhibit the basal FRET-signal on their off state as often the case for single-chain constructs. However, ratiometric imaging of these dual chain constructs is susceptible to artifacts that can arise from inhomogeneous cellular distribution of the two sensory units or differences in their expression levels. For single chain constructs the distribution and concentration of the two fluorophores is identical by design. However, in this case inhomogeneous bleaching of the two fluorophores can be problematic for FRET quantification. The impact of the sensor designs on the endogenous interactions has to be considered as well. For the single chain design, binding of the intramolecular affinity tag competes with the endogenous interaction partners of the GTPase, e.g. GEFs, GAPs and GDI. In dual chain sensors the affinity tag can be outcompeted by the endogenous effector proteins, leading to a false “inactive” signal.

Membrane localization is another important aspect of GTPase signaling. Small GTPases membrane interaction is generally mediated through lipid moieties that are posttranslationally attached to the proteins C-terminal region. Thus, single chain sensors, where the GTPase is positioned in the interior of the chain, often lack the native membrane localization signal[161] or have to be artificially anchored to the membrane[149,151,152], e.g. through appending a –CAAX motif.

A FRET-based approach that reports on endogenous GTPase activity employs affinity tags with two fluorescent proteins attached. In this case, binding to the activated endogenous GTPase leads to a change in the relative position of the fluorescent proteins and thus to a change in the observed FRET signal (Figure 1-15).[158,162,163]

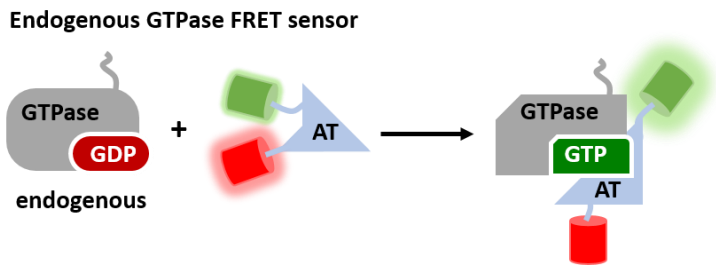

Figure 1-15: FRET sensor for endogenous GTPase activity.
A unimolecular FRET probe that reports on the endogenous GTPase activity. Upon binding of the affinity domain (AT) to the GTPase, the position/orientation of the two attached fluorescent proteins is distorted, leading to a change in FRET signal.

Another group of sensors utilizes environment sensitive dyes to report on small GTPase activity. In one of these approaches the read out is generated through a solvatochromic dye attached to an affinity tag.[164-166] The tag binds to the activated GTPase, changing the dye's local environment resulting in a change in fluorescence signal.

In a different methodology the GTPase is directly labeled with the environment-sensitive dye. The conformational changes of the GTPase upon nucleotide exchange and effector binding lead to a changed local environment that surrounds the dye. So far the latter method has been restricted to *in vitro* measurements.

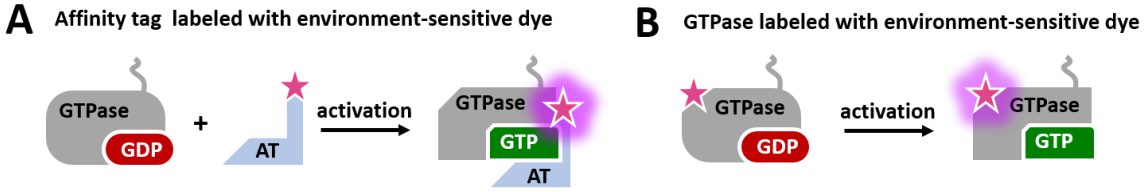

Figure 1-16: GTPase Biosensors based on environment-sensitive dyes.
(A) The GTPase affinity tag (AT) is labeled with a solvatochromic dye that changes its fluorescence due to a change in local environment upon binding to the activated GTPase. **(B)** The GTPase is labeled with an environment-sensitive dye. Nucleotide exchange leads to changes in the local dye environment and thus a change in fluorescence signal.

Recently, a novel small GTPase biosensor has been described that reports on the GTPase-GDI interaction.[167] For this purpose, the GTPase is equipped with two fluorescent proteins that form a FRET antenna. Upon binding to GDI, the relative position of the two fluorophores is altered, which in turn leads to a change in FRET signal. This probe can be used in combination with traditional GTPase activations sensors to examine the interdependence of GDI and GEF/GAP-mediated GTPase regulation.

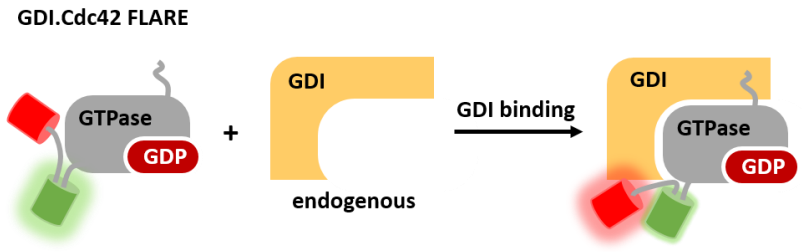

Figure 1-17: Sensor for endogenous GDI interaction.
A unimolecular FRET probe that reports on the endogenous GTPase-GDI interaction. Binding of the GTPase to GDI leads to change in relative orientation of the two attached fluorescent proteins and thus to a change in the FRET signal.

2 Materials and methods

2.1 Materials

2.1.1 Chemicals

Chemicals used in this thesis are listed below (Table 2-1).

Table 2-1: Used chemicals.

Chemical	Supplier
2'/3'-O-(N-methyl-anthraniloyl)-guanosin-5'-diphosphate	Jena Bioscience (Jena, Germany)
2-Propanol	Sigma-Aldrich (Munich, Germany)
4-(2-hydroxyethyl)-1-piperazineethanesulfonic acid	Gerbu (Gaiberg, Germany)
4-Mercaptophenylacetic acid	Sigma-Aldrich (Munich, Germany)
Acetic acid	Merck (Darmstadt, Germany)
Acetone	JT Baker (Deventer, Netherlands)
Acetonitrile	JT Baker (Deventer, Netherlands)
Acrylamid 4K-solution (30 %, Mix 37.5 : 1)	Applichem (Darmstadt, Germany)
Agarose	Invitrogen (Darmstadt, Germany)
Alexa Fluor 594 C5 maleimide	Thermo Fisher Scientific (Waltham, USA)
Ampicillin	Serva (Heidelberg, Germany)
Bovine serum albumine	Sigma-Aldrich (Munich, Germany)
Bradford reagent	Bio-Rad (Munich, Gernamy)
Bromphenol blue Serva	Serva (Heidelberg, Germany)
Carbenicillin	Biomol GmbH (Hamburg, Germany)
Chloramphenicol	Merck (Darmstadt, Germany)
Coomassie Brilliant Blue G250+R250	Serva (Heidelberg, Germany)
Dimethylsulfoxide	Fluka - Sigma-Aldrich (Munich, Germany)
Disodium hydrogenphosphate	JT Baker (Deventer, Netherlands)
Dithioerythritol	Gerbu (Gaiberg, Germany)
Dithiothreitol	Gerbu (Gaiberg, Germany)
Dimethyl sulfoxide	Sigma-Aldrich (Munich, Germany)
Ethanol	JT Baker (Deventer, Netherlands)
Ethylenediaminetetraacetic adic	Gerbu (Gaiberg, Germany)
Glycine	Carl Roth GmbH (Karlsruhe, Germany)
Guanosine-5'-β,γ-imidotriphosphate	Sigma-Aldrich (Munich, Germany)
Guanosine diphosphate	Sigma-Aldrich (Munich, Germany)
Guanosine triphosphate	Sigma-Aldrich (Munich, Germany)
Hydrochloric acid	JT Baker (Deventer, Netherlands)
Imidazol	Merck (Darmstadt, Germany)
Isopropyl-β-D-thiogalactopyranoside	Gerbu (Gaiberg, Germany)
Kanamycin	Gerbu (Gaiberg, Germany)
Magnesium chloride	JT Baker (Deventer, Netherlands)

Methanol	Applichem (Darmstadt, Germany)
N,N,N',N'-tetramethylethylenediamine	Carl Roth GmbH (Karlsruhe, Germany)
Phenylmethylsulfonylfluoride	Sigma-Aldrich (Munich, Germany)
Potassium chloride	JT Baker (Deventer, Netherlands)
Potassium dihydrogenphosphate	JT Baker (Deventer, Netherlands)
Potassium hydroxide	JT Baker (Deventer, Netherlands)
RedSafe Nucleic Acid Staining Solution	iNtRON Biotechnology (Sangdaewon-dong, South Korea)
Sodium 2-mercaptoethanesulfonate	Sigma-Aldrich (Munich, Germany)
Sodium chloride	Sigma-Aldrich (Munich, Germany)
Sodium dihydrogenphosphate	JT Baker (Deventer, Netherlands)
Sodium dodecylsulphate	Gerbu (Gaiberg, Germany)
Sodium hydroxide	JT Baker (Deventer, Netherlands)
Tide Fluor 3 maleimide	Aat Bioquest (Sunnyvale, USA)
Tide Fluor 4 maleimide	Aat Bioquest (Sunnyvale, USA)
Tris(2-carboxyethyl)phosphine	Fluka - Sigma-Aldrich (Munich, Germany)
Triton X-100	Sigma-Aldrich (Munich, Germany)
β-mercaptoethanol	Serva (Heidelberg, Germany)

2.1.2 Biomolecular reagents

Biomolecular reagents and kits used in this thesis are listed below (Table 2-2).

Table 2-2: Biomolecular reagents and kits.

Reagent	Supplier
FastAP Thermosensitive Alkaline Phosphatase	Thermo Fisher Scientific (Waltham, USA)
E.Z.N.A. Cycle Pure Kit	Omega Bio-Tek (Norcross, USA)
E.Z.N.A. Gel Extraction Kit	Omega Bio-Tek (Norcross, USA)
E.Z.N.A. Plasmid Midi Kit	Omega Bio-Tek (Norcross, USA)
E.Z.N.A. Plasmid Mini Kit	Omega Bio-Tek (Norcross, USA)
FastDigest restriction enzymes	Thermo Fisher Scientific (Waltham, USA)
Gene Ruler 1 kb DNA Ladder	Fermentas (St. Leon-Rot, Germany)
LMW (low molecular weight) marker	GE Healthcare (Munich, Germany)
Phusion High-Fidelity PCR Master Mix	Finnzymes (Vantaa, Finland)
Protease Inhibitor Cocktail cOmplete ULTRA EDTA-free	Roche Diagnostics (Risch-Rotkreuz, Switzerland)
PreScission Protease	Dortmund Protein Facility MPI of Molecular Physiology (Dortmund, Germany)
QIAprep Spin Miniprep Kit	Qiagen (Hilden, Germany)
REDTaq DNA Polymerase	Sigma-Aldrich (Munich, Germany)
T4 DNA Ligase	Fermentas (St. Leon-Rot, Germany)
TEV-Protease	Dortmund Protein Facility MPI of Molecular Physiology (Dortmund, Germany)
BigDye Terminator v 3.1. Cycle Sequencing Kit	Applied Biosystems (Darmstadt, Germany)

2.1.3 Buffers and solutions

Buffers and solutions used in this thesis are listed below (Table 2-3).

Table 2-3: Buffers and solutions.

Buffer	Composition	Buffer/solution	Composition
PBS buffer	13.7 mM NaCl, 0.27 mM KCl, 10 mM Na_2HPO_4, 2 mM KH_2PO_4, pH 7.4	**SDS stacking gel buffer**	0.5 M Tris-HCl pH 6.8, 0.4 % (w/v) SDS
Buffer A*#	50 mM HEPES pH 8.0, 500 mM LiCl, 2 mM β-mercaptoethanol, 1 mM $MgCl_2$, 10 µM GDP	**SDS resolving gel buffer**	0.5 M Tris-HCl pH 6.8, 0.4 % (w/v) SDS
Buffer B*#	buffer A + 0.5 M imidazol	**SDS running buffer**	25 mM Tris 0.2 M glycine 0.1 % (w/v) SDS
TEV buffer#	50 mM HEPES pH 8.0, 100 mM NaCl, 2 mM β-mercaptoethanol, 10 µM GDP	**4x SDS loading buffer**	200 mM Tris, pH 6.8, 4 % (w/v) SDS, 20 % (w/v) glycerol, 5 % (w/v) 200 mM DTT, 0.2 % (w/v) bromophenol blue
Gel filtration buffer*#	20 mM HEPES pH 7.5, 50 mM NaCl, 2 mM DTE, 1 mM $MgCl_2$, 10 µM GDP	**Coomassie staining solution**	10 % (v/v) acetic acid 40 % (v/v) ethanol 0.1 % (v/v) Coomassie Brilliant Blue R250
Labeling buffer	20 mM HEPES pH 7.5, 20 mM NaCl, 1 mM $MgCl_2$, 10 µM GDP	**SDS destaining solution**	10 % (v/v) acetic acid
Fluorescence buffer	20 mM HEPES pH 7.5, 20 mM NaCl, 1 mM $MgCl_2$, 2 mM DTE	**TAE buffer**	40 mM Tris-HCl pH 8.5, 1 mM EDTA 20 mM acetic acid
NCL buffer	20 mM HEPES pH 7.5, 50 mM NaCl, 1 mM $MgCl_2$, 10 µM GDP, 50 mM MPAA, 20 mM TCEP	**Antibiotic solutions**	125 mg/l ampicillin 34 mg/l chloramphenicol 125 mg/l kanamycin
		5x DNA loading buffer	30 % (w/v) sucrose 20 % (v/v) glycerol 0.2 % (w/v) Orange G

*For protein purification of protein thioester constructs the indicated buffers were used without thiol additives (e.g. DTE, β-mercaptoethanol). # Non-GTPase proteins were purified without GDP and $MgCl_2$.

2.1.4 Cell culture media, additives and reagents

Cell culture media, additives and reagents used in this thesis are listed below (Table 2-4).

Table 2-4: Cell culture media, additives and reagents.

Medium, additive or reagent	Supplier
Dulbecco's phosphate-buffered saline (DPBS)	Thermo Fisher Scientific (Waltham, USA)
Earle's balanced salt solution (EBSS)	Sigma-Aldrich (Munich, Germany)
Fetal bovine serum (FBS)	Thermo Fisher Scientific (Waltham, USA)
GlutaMAX	Thermo Fisher Scientific (Waltham, USA)
Insulin solution, human	Sigma-Aldrich (Munich, Germany)
Minimum essential medium (MEM)	Thermo Fisher Scientific (Waltham, USA)
Clear minimum essential medium (without phenol red)	Thermo Fisher Scientific (Waltham, USA)
Minimum essential medium Non-essential amino acid solution (100×)	Sigma-Aldrich (Munich, Germany)
Opti-MEM	Thermo Fisher Scientific (Waltham, USA)
Sodium pyruvate solution (100 mM)	Sigma-Aldrich (Munich, Germany)
Transfection reagent X-tremeGENE HP DNA	Roche Diagnostic (Risch-Rotkreuz, Switzerland)
Trypsin-EDTA (0,25 %)	Thermo Fisher Scientific (Waltham, USA)

2.1.5 Bacterial strains

Bacterial strains used for plasmid amplification, protein expression (2.3) or transformation of ligation (2.2.4) and site-directed mutagenesis (2.2.1.3) products are listed below (Table 2-5).

Table 2-5: Bacterial strains.

Strain	Genotype	Supplier
***E. coli* XL1-Blue**	recA1 endA1 gyrA96 thi-1 hsdR17 supE44 relA1 lac [F' proAB lacIqZDeltaM15 Tn10 (Tetr)]	Merck (Darmstadt, Germany)
***E. coli* BL21(DE3)**	E. coli B F ompT hsdS(rB mB) dcm+ Tetr gal lambda(DE3) endA Hte	Agilent Technologies (Santa Clara, USA)
***E. coli* BL21-CodonPlus(DE3)-RIL**	E. coli B F ompT hsdS(rB mB) dcm+ Tetr gal lambda(DE3) endA Hte [argU ileY leuW Camr]	Agilent Technologies (Santa Clara, USA)

2.1.6 Eukaryotic cell lines

Cell lines used for transfection (2.6.2), microinjection (2.6.4) and live cell microscopy (2.7) are listed below (Table 2-6).

Table 2-6: Eukaryotic cell lines.

Cell line	Characteristics		ATCC number
HeLa	**organism:** *Homo sapiens* **cell type:** epithelial **culture properties:** adherent	**tissue:** cervix **morphology:** epithelial	CCL-2
COS-7	**organism:** *Cercopithecus aethiops* **cell type:** SV40 transformed **culture properties:** adherent	**tissue:** kidney **morphology:** fibroblast	CRL-1651
MDCK	**organism:** *Canis familiaris* **cell type:** epithelial **culture properties:** adherent	**tissue:** kidney **morphology:** epithelial	CCL-34

2.1.7 Plasmids

Plasmid used for bacterial protein expression (Table 2-7) and mammalian cell transfection (

Table 2-8) are listed below.

Table 2-7: Plasmids for bacterial expression.

Expressed protein	Plasmid	Plasmid source
Rab1b$_{3-174}$	w0294 pMAL Rab1b 3-174 opti	AG Goody, MPI Dortmund
Rab1b$_{3-174}$_G18C	w0836 pMAL Rab1b 3-174 opti G18C	this thesis
Rab1b$_{3-174}$_W102C	w0382 pMAL Rab1b 3-174 opti W102C	this thesis
Rab1b$_{3-174}$_W62C	w0308 pMAL Rab1b 3-174 opti W62C	this thesis
EGFP-Rab1bD2_T34C	w0316 pET19TEV-EGFP-Rab1bD2_T34C	AG Wu, MPI Dortmund
EGFP-Rab1bD2_T34C-thioester	w0722 pTwin EGFP-Rab1bT34C_D2	this thesis
EGFP-Rab1bD2_G18C-thioester	w1049 pTwin EGFP-Rab1bG18C_D2	this thesis
EGFP-Rab1bD2_I41C	w1150 pET-EGFP-Rab1bD2_I41C	this thesis
EGFP-Rab1bD2_S36C	w1151 pTwin_EGFP-Rab1bD2_S36C	this thesis
EGFP-Rab1bD2_T34C	w1273 pET EGFP-Rab1b_T34C_C23S_D2	this thesis
EGFP-Rab1bD2_S36C	w1274 pET EGFP-Rab1b_S36C_C23S_D2	this thesis
EGFP-Rab1bD2_D53C	w1275 pET EGFP-Rab1b_D53C_C23S_D2	this thesis
EGFP-Rab1bD2_G54C	w1276 pET EGFP-Rab1b_G54C_C23S_D2	this thesis
EGFP-Rab1bD2_G54C-thioester	w1301 pTwin EGFP-Rab1b_C23S_G54C	this thesis
EGFP-Rab1bD2_S36C-thioester	w1320 pTwin EGFP-Rab1b_C23S_S36C	this thesis
EGFP-Rab1bD2_D53C-thioester	w1321 pTwin-EGFP-Rab1b_C23S_D53C	this thesis
EGFP-Rab1bD2_W102C-thioester	w1340 pET EGFP-Rab1b_W102C_C23S_D2	this thesis
EGFP-Rab1bD2_G18C-thioester	w1368 pTwin EGFP-Rab1bC23S_G18C_D2	this thesis
EGFP_D11-Rab1bD2_T34C	w1429 pET-EGFP_D11-Rab1bT34C_C23S_D2	this thesis
EGFP_D11-linker-Rab1bD2_T34C	w1430 pET-EGFP_D11-linker-Rab1bT34C_C23S_D2	this thesis
EGFP_D11-Rab1bD2_D53C	w1431 pET-EGFP_D11-Rab1b_D53C_C23S_D2	this thesis
EGFP_D11-linker-Rab1bD2_D53C	w1432 pET-EGFP_D11-linker-Rab1b_D53C_C23S_D2	this thesis
EGFP_D11-Rab1bD2_T34C-thioester	w1532 pTwin EGFPD11-Rab1bC23S_T34C_D2	this thesis
YPT7$_{1-182}$G18C	w1179 pET19mod Ypt7_G18C 1-182	this thesis
EGFP-YPT7$_{1-182}$S34C	w1390 pET-EGFP-YPT7_S34C	this thesis

TBC1D20 $_{1-362}$	w1013 pET19mod TBC1D20 1-362	AG Goody, MPI Dortmund
LidA$_{201-583}$	w1127 LidA_201-583	AG Goody, MPI Dortmund
OCRL$_{539-901}$	w1029 pMAL OCRL opti	AG Goody, MPI Dortmund
EGFP-KRas_C51S_C80L_C118S -thioester	w1589 pTwin EGFP-KRas_cyslight	this thesis
EGFP-KRas_Clight_D30C-thioester	w1564 pTwin EGFP-KRas_cyslight_D30C_DC	this thesis
EGFP-KRas_Clight_E31C -thioester	w1565 pTwin EGFP-KRas_cyslight_E31C_DC	this thesis
EGFP-KRas_Clight_D33C-thioester	w1566 pTwin EGFP-KRas_cyslight_D33C_DC	this thesis
EGFP-KRas_Clight_D47C-thioester	w1567pTwin EGFP-KRas_cyslight_D47C_DC	this thesis
EGFP-KRas_Clight_G48 -thioester	w1568 pTwin EGFP-KRas_cyslight_G48C_DC	this thesis
EGFP-KRas_Clight_Y96 -thioester	w1569 pTwin EGFP-KRas_cyslight_Y96C_DC	this thesis
CitrineD11-KRas_Clight_E31C_DC	w1577 pTwin CitrineD11-KRas_cyslight_E31C_DC	this thesis
EGFPD11-KRas_Clight_E107C-thioester	w1590 pTwin EGFPD11-KRas_cyslight_E107C_DC	this thesis

Table 2-8: Plasmids for mammalian cell transfection.

Expressed protein	Plasmid	Plasmid source
BFP-OCRL	w1277 pTagBFP-OCRL	this thesis
BFP-2xFKBPF37V-DrrA	w1170 pBFP-2xFKBPF37V-Drra	this thesis
EGFP-Rab1b	w0083 pOPINE(n)EGFP-Rab1b	AG Wu, MPI Dortmund
mKate2-giantin	w0599 mKate2-giantin-N1	AG Wu, MPI Dortmund
paGFP-Rab1b	w1319 paGFP-Rab1b	this thesis
paGFP-Rab1b_Q67L	w1609 paGFP-Rab1b_Q67L	this thesis
paGFP-Rab1b_S22N	w1610 paGFP-Rab1b_S22N	this thesis
paGFP-Rab1b_N121I	w1611 paGFP-Rab1b_N1211	this thesis

2.1.8 Columns and other materials

Columns for protein purification and other materials used in this thesis are listed below (Table 2-9).

Table 2-9: Columns and other materials.

Columns and other materials	Supplier
HisTrap HP 5 ml	GE Healthcare (Munich, Germany)
HiLoad 16/600 Superdex 75 pg	GE Healthcare (Munich, Germany)
HiLoad 16/600 Superdex 200 pg	GE Healthcare (Munich, Germany)
HiLoad 26/600 Superdex 75 pg	GE Healthcare (Munich, Germany)
illustra NAP-5 Column	GE Healthcare (Munich, Germany)
Ni-NTA Superflow (25 ml)	Qiagen (Hilden, Germany)
Amicon Ultra-15 (10000 Da MWCO), 30000 Da MWCO, 50000 Da MWCO)	Millipore (Schwalbaach, Germany)
Amicon Ultra-4 (10000 Da MWCO, 30000 Da MWCO, 50000 Da MWCO)	Millipore (Schwalbach, Germany)
Dialysis membranes Spectra/Por 1-4	Carl Roth (Karlsruhe, Germany
Electroporation cuvettes	VWR International (Erlangen, Germany)
Glass bottom dishes 35 mm uncoated	MatTek (Ashland, USA)
Membrane filters mixed cellulose ester 24	VWR International (Erlangen, Germany)
pH-indicator strips pH 5.0 - 10.0	Merck Millipore (Billerica, USA)
Pipette tips (1-10 ml, 20-200 ml, 100-1000 ml)	Nerbe (Winsen/Luhe, Germany)
Rapid-Flow Bottle Top Filter	Nalgene Labware (Roskilde, Denmark)
Safe-Lock Tubes (0.5 ml, 1 ml, 2. 5 ml)	Eppendorf (Hamburg, Germany)
Semi-micro cuvette	Sarstedt (Nümbrecht, Germany)
Serological pipette (5 ml, 10 ml, 25 ml)	Sarstedt (Nümbrecht, Germany)
Tissue culture dish (100 x 20 mm)	Sarstedt (Nümbrecht, Germany)
Reaction Tube (15ml, 50ml)	Sarstedt (Nümbrecht, Germany)
Vivaspin 500 Protein Concentrators (3000 Da MWCO, 10000 Da MWCO, 30000 Da MWCO)	GE Healthcare (Munich, Germany)

2.1.9 Instruments

Microscopes, laser instruments and other equipment used in this thesis are listed below in Table 2-10 and Table 2-11.

Table 2-10: Microscopes, laser and FLIM equipment.

Microscopes and FLIM equipment	Supplier
Leica TCS SP2	Leica Microsystems (Wetzlar, Germany)
Leica TCS SP5	Leica Microsystems (Wetzlar, Germany)
Cube 1162002/AF (405 nm)	Coherent (Santa Clara, USA)
Argon Laser LGK 7872 ML05 (458/488/514 nm)	Lasos (Jena, Germany)
561 DPSS YLK 6120 T02 (561 nm)	Lasos (Jena, Germany)
Koheras White Light Laser (470-670 mn)	NKT Photonics A/S (Birkerød, Denmark)
Olympus FluoView FV1000	Olympus (Tokyo, Japan)
FV5-LD405 (405 nm)	Olympus (Tokyo, Japan)
Argon Laser GLG 3135 (458/488/514 nm)	Showa Optronics (Tokyo, Japan)
561 DPSS 85-YCA-020-230 (561 nm)	Melles Griot (Carlsbad, USA)
PicoHarp 300	PicoQuant (Berlin, Germany)
Single-photon counting avalanche photodiode PDM Series	PicoQuant (Berlin, Germany)

Table 2-11: Instruments and equipment.

Instrument and equipment	Supplier
ÄKTAprime plus	GE Healthcare (Munich, Germany)
Balance CP224S	Sartorius (Göttingen, Germany)
Balance PM480	Mettler (Columbus, USA)
Centrifuge 5415 R	Eppendorf (Hamburg, Germany)
Centrifuge 5424	Eppendorf (Hamburg, Germany)
Centrifuge 5804 R	Eppendorf (Hamburg, Germany)
Centrifuge Avanti J-25	Beckman Coulter (Brea, USA)
Centrifuge avanti J-26XP	Beckman Coulter (Brea, USA)
Dry block heating system QBT	Grant Instruments (Shepreth, UK)
Electrophoresis Apparatus Horizon 58	Life Technologies (Carlsbad, USA)
EPS 301 Power Supply	GE Healthcare (Munich, Germany)
Eppendorf Micro manipulator 5171	Eppendorf (Hamburg, Germany)
Eppendorf Transjector 5246	Eppendorf (Hamburg, Germany)
Finnigan LCQ Advantage Max mass spectrometer	Thermo Fisher Scientific (Waltham, USA)
FluorChem Q imaging system	Alpha Innotech (San Leandro, USA)
FluoroMax-3	Horiba Jobin Yvon (Edison, USA)
High Performance Transilluminators	UVP (Upland, USA)
IKA HS 250 shaker	IKA (Staufen, Germany)
IKA RCT basic	IKA (Staufen, Germany)
Incubator Series ED	Binder (Tuttlingen, Germany)
Incubator shaker Innova 42	Eppendorf (Hamburg, Germany)
Incubator shaker Innova 43	Eppendorf (Hamburg, Germany)

inoLab pH Level 1 pH meter	WTW (Weilheim, Germany)
Microfluidizer M-110S	Microfluidics (Newton, USA)
Microinjection needle puller PD-5	Narishige (Tokyo, Japan)
Milli-Q Water Purification System	Merck Millipore (Billerica, USA)
Nanodrop Micro Volume Fluorospectrophotometer	PeqLab Biotechnology GmbH (Erlangen, Germany)
Peristaltic Pump P-1	Amersham Pharmacia Biotech (Uppsala, Sweden)
Personal Thermocycler	Analytic Jena AG (Jena, Germany)
Pipette PIPETMAN Classic (2 µl, 10 µl, 100 µl, 200 µl, 1000 µl)	Gilson (Middleton, USA)
PowerPAC 300	Biorad (Hercules, USA)
QIAcube	Qiagen (Hilden, Germany
Rotilabo-mini-centrifuge	Carl Roth (Karlsruhe, Germany)
Rotor JA-10	Beckman Coulter (Brea, USA)
Rotor JLA-8.1000	Beckman Coulter (Brea, USA)
Rotor JA-25.50	Beckman Coulter (Brea, USA)
Thermomixer Comfort	Eppendorf (Hamburg, Germany)
Vacuum Diaphragm Pump	Ilmvac (Ilmenau, Germany)
Vortex Genie 2	Scientific Industries (Bohemia, USA)
Water purification system Q-POD	Merck Millipore (Billerica, USA)

2.1.10 Software

Software and programs used in this thesis are listed below (Table 2-12).

Table 2-12: Software and programs.

Software and programs	Supplier
a|e - UV-Vis-IR Spectral Software 1.2	FluorTools (www.fluortools.com)
ChemBioDraw Office 2014	PerkinElmer (Waltham, USA)
EndNote X7	Thomas Reuter (New York, USA)
GraFit 5	Erithacus Software (Horley, UK)
IGOR Pro 6.2	WaveMetrics (Tigard, USA)
ImageJ 1.44p	Wayne Rasband, NIH (Bethesda, USA)
Leica LAS AF Lite 2.6.0	Leica Microsystem (Wetzlar, Germany)
MagTran 1.02	Zhongqi Zhang, Amgen (Thousand Oaks, USA)
MATLAB R2012b	The MathWorks (Natick, USA)
Origin 8.6	OriginLab (Northampton, USA)
PyMOL 1.7.4	Schrödinger (New York, USA)
SnapGene Viewer 2.8.3	GSL Biotech (Chicago, USA)
Xcalibur 1.4 SR1	Thermo Electron (San Jose, USA)

2.2 Biomolecular methods

2.2.1 Polymerase chain reaction (PCR)

Polymerase chain reaction is a method for DNA amplification based on repeated heating and cooling cycles. The cycling program, primer design and reaction composition are adjusted based on the intended purpose of the DNA amplification (e.g. insert amplification, sequencing or colony PCR). PCR protocols used in this thesis are described below.

2.2.1.1 Insert amplification

Table 2-13: PCR for insert amplification.

PCR composition	PCR program		
V_{total} = 50 µl	98 °C	30 s	
25 µl 2x Phusion High-Fidelity PCR Master Mix with	98 °C	10 s	
HF Buffer	50 °C	30 s	x 25-45 cycles (T_m)
+ 2 x 0.5 µl forward and reverse primer (100 µM)	72 °C	30 s	(15-30 s/ 1 kb)
+ 2 µl DNA template with desired insert (1 ng/µl)	72 °C	5 min	
+ H_2O (up to 50 µl)	8 °C	∞	

After completion the PCR product was purified by using the E.Z.N.A. Cycle Pure Kit.

2.2.1.2 Colony PCR

Colony PCR was used after insert ligation to identify bacterial colonies carrying the desired ligation products.

Table 2-14: Colony PCR.

PCR composition	PCR program		
V_{total} = 11 µl	96 °C	120 s	
5 µl Taq DNA Polymerase 2x Master Mix Red	96 °C	30 s	
+ 2 x 1 µl forward and reverse primer (1 µM)	57 °C	30 s	x 25-35 cycles (T_m)
+ 2 µl DNA template (1 ng/µl)	72 °C	90 s	(60 s/ 1 kb)
+ H_2O (up to 10 µl)	72 °C	4 min	
+ 1 µl of bacterial colony suspended in 50 µL H_2O	8 °C	∞	

After completion the PCR products were analyzed by agarose gel electrophoresis (2.2.3).

2.2.1.3 Site-directed mutagenesis

Site-directed mutagenesis was used to introduce specific mutations into a DNA sequence.

Table 2-15: Site-directed mutagenesis.

PCR composition	PCR program		
V_{total} = 50 µl	98 °C	30 s	
25 µl 2x Phusion High-Fidelity PCR Master Mix with HF buffer	98 °C	15 s	
+ 0.5 µl forward Primer containing the desired mutation site (100 µM)	55 °C	30 s	x 29 cycles (T_m)
+ 1 µl DNA template (150-200 ng/µl)	72 °C	4 min	
+ H_2O (up to 50 µl)	72 °C	10 min	
	8 °C	∞	

After completion 2 µl DpnI (Thermo Fisher Scientific) was added and the mixture incubated for at least 1 h at 37 °C to digest remaining template DNA. DpnI was inactivated at 80 °C and 4 µl of the PCR mixture was transformed into competent *E. coli* cells (2.2.5). Successful introduction of the mutation was confirmed by subsequent sequencing (2.2.1.4).

2.2.1.4 Sequencing PCR

Sequencing was used to confirm successful DNA ligation or introduction of site-specific mutations into DNA sequences.

Table 2-16: Sequencing PCR.

PCR composition	PCR program		
V_{total} = 10 µL 500 ng DNA template + 0.5 µl primer (100 µM) + 2 µl BigDye Terminator Mix + 2 µl 5x BigDye Terminator Mix buffer + H_2O (up to 10 µl)	96 °C 96 °C 50 °C 60 °C 8 °C	4 min 10 s 5 s 3 min ∞	x 25 cycles (T_m)

After completion the DNA was precipitated and sequenced by the sequencing facility of the MPI of Molecular Physiology.

2.2.2 Restriction enzyme digestion

For sequence-specific DNA digestion FastDigest enzymes (Thermo Fisher Scientific) were used according to the manufacturer's instructions. For a typical digestion 0.1–1 µg of DNA was mixed with water, 2 µl of 10x FastDigest buffer (Thermo Fisher Scientific) and the restriction enzymes to a total volume of 20 µl or 30 µl. The mixture was incubated at 37 °C until digestion was completed as recommended in the specifications of the specific enzyme. If applicable the enzyme was heat-inactivated. The DNA was purified by using the E.Z.N.A. Cycle Pure Kit (Omega Bio-Tek).

In Order to prevent religation of the cut vector in subsequent ligation, the digested vector DNA was additionally incubated with FastAP Thermosensitive Alkaline Phosphatase (Thermo Fisher Scientific) according to the manufacturer's instructions.

2.2.3 Agarose gel electrophoresis

Agarose gel electrophoresis was used to separate, identify and purify DNA by its size. In this thesis agarose gels with 1 % w/v agarose in TAE buffer mixed with RedSafe Nucleic Acid Staining Solution (iNtRON Biotechnology) were used. For loading the samples on the gel, 3-20 µl DNA sample was mixed with 5x DNA loading buffer. As a reference 7 µl of the size standard Gene Ruler 1 kb DNA (Fermentas) was used. The agarose gels were run at 100 V immersed in TAE buffer. After separation the DNA bands were visualized with the FluorChem Q imaging system (Alpha Innotech) at 302 nm.

For subsequent purification the desired DNA bands were excised from the gel and recovered from the agarose gel by using the E.Z.N.A. Gel Extraction Kit (Omega Bio-Tek).

2.2.4 Ligation

Vector constructs for bacterial or mammalian cell expression were generated through ligation of the desired insert into a linearized vector. The DNA insert was amplified by insert PCR (2.2.1.1), purified using the E.Z.N.A. Cycle Pure Kit and digested with the appropriate restriction enzymes (2.2.2). For the vector about 1 μg of the chosen donor plasmid was digested with the appropriate restriction enzymes (2.2.2) and purified by using the E.Z.N.A. Cycle Pure Kit. Successful insert amplification and DNA digestion was confirmed by agarose gel electrophoresis (2.2.3).

Ligation was performed overnight at 16 °C. A typical ligation mixture with a total volume of 20 μl mixture contained a 3:1 molar ratio of DNA insert to vector, 2 μl 10x T4 DNA Ligase buffer and 1 μl T4 DNA Ligase (1 Weiss unit/μl) as recommended by the manufacturer. After overnight ligation, 4 μl of the ligation mixture were transformed into competent cells (2.2.5), plated overnight on selective medium and single colonies analyzed by colony PCR (2.2.1.2).

2.2.5 Transformation of competent cells

Transformation of competent cells for plasmid amplification, protein expression (4.3) or selection of ligation (4.2.4) and site-directed mutagenesis (4.2.1.3) products was performed as described below.

2.2.5.1 Transformation of chemical competent cells

1-4 μl of plasmid DNA or ligation/site-directed mutagenesis mixture was added to 300 μl chemically competent cells on ice and incubated for 30 min. The cells were heated to 42 °C for 1 min and immediately cooled on ice for 10 min. After addition of 1 ml of LB medium the transformed cells were incubated for 1 h at 37 °C in a shaker at 160 rpm. Finally, the cells were plated on selective medium and incubated overnight at 37 °C.

2.2.5.2 Transformation of electrocompetent cells

1-4 μl of plasmid DNA or ligation/site-directed mutagenesis mixture was added to 80 μl electrocompetent cells on ice and the mixture transferred into a precooled electroporation cuvette. After electroporation at 1.8 kV, 200 Ω and 25 μF, 1 ml LB medium was added and the cells incubated for 30-45 min at 37 °C in a shaker at 160 rpm. Finally, the cells were plated on selective medium and incubated overnight at 37 °C.

2.3 Protein expression and purification

2.3.1 Protein expression

For expression of recombinant proteins the respective plasmid was transformed into *E. coli* BL21(DE3) or *E. coli* BL21-CodonPlus(DE3)-RIL cells (2.1.5), plated on selective medium and inoculated overnight at 37 °C. The colonies were suspended in 5 ml LB medium and added to 5 l LB-medium supplemented with the appropriate selection antibiotic. The cultures were incubated in a shaker at 37 °C and 130-160 rpm until an absorbance of 0.5-0.8 at 600 nm (OD_{600}) was reached. For induction IPTG was added to a final concentration of 0.2 mM and the cultures were further incubated overnight at 22 °C (18 °C for N-terminally His-EGFP-tagged proteins). The cells were harvested by centrifugation using an Avanti J-26XP centrifuge (Beckman Coulter) with a JLA-8.1000 rotor (4000 rpm, 30 min, 4 °C). Finally, the cell pellet was washed with PBS buffer and directly used for protein purification or stored at -80 °C.

2.3.2 Purification of His-tagged proteins

Proteins expressed from a pET or pMAL vector with a N-terminal-His or N-terminal-His-MPB tag were purified as described below.

The bacterial cell pellet was suspended in buffer A (50 mM HEPES pH 8.0, 500 mM LiCl, 2 mM β-mercaptoethanol; for small GTPases additionally: 1 mM $MgCl_2$ and 10 µM GDP) supplemented with cOmplete ULTRA Protease Inhibitor Cocktail (Roche) and 2 mM PMSF. The cells were lysed by passing them through a Microfluidizer (Microfluidics) three times. Insoluble cell fragments were removed by centrifugation in an Avanti J-25 centrifuge (Beckman Coulter) using a JA-25.50 rotor (25000 rpm, 40 min, 10 °C). For specific protein extraction the supernatant was applied to a HisTrap HP (5 ml, GE Healthcare) using an ÄKTAprime plus system (GE Healthcare) after filtration through a Rapid-Flow Bottle Top Filter (Nalgene Labware). Unspecifically bound proteins were removed by a wash step with 4 % buffer B (0.5 M imidazole, 50 mM HEPES pH 8.0, 500 mM LiCl, 2 mM β-mercaptoethanol; for small GTPases additionally: 1 mM $MgCl_2$ and 10 µM GDP). The His-tagged target protein was obtained by fractionated elution with a linear gradient of 100 ml from 4 % to 100 % buffer B. Fractions containing the target protein were identified by measuring the absorption at 280 nm and further analyzed by SDS-PAGE (2.5.1). Protein fractions were pooled and His-tagged TEV-protease was added to remove the affinity-tag. The mixture was dialyzed overnight against Mg^{2+}-free buffer A (50 mM HEPES pH 8.0, 500 mM LiCl, 2 mM β-mercaptoethanol; for small GTPases additionally: 10 µM GDP) at 8° C. The affinity tag, uncleaved protein and TEV-protease were removed in an additional Ni-affinity chromatography step. The protein present in the flow-through was concentrated to 2-5 ml and subjected to size exclusion chromatography on a HiLoad Superdex 75 26/600 or 16/600 gel filtration column (GE Healthcare) using gel filtration buffer (20 mM HEPES pH 7.5, 50 mM NaCl, 2 mM DTE; for small GTPases additionally 1 mM $MgCl_2$ and 10 µM GDP). The fractions containing the target

protein were identified by monitoring absorption at 280 nm and subsequently analyzed by SDS-PAGE. Fractions containing pure protein were pooled, concentrated, frozen in liquid nitrogen and stored at -80 °C.

2.3.3 Purification of small GTPases as thioesters

Proteins expressed from a pTwin vector as a C-terminal-intein fusion proteins were purified as described below.

The bacterial cell pellet was suspended in thiol-free buffer A (50 mM HEPES pH 8.0, 500 mM LiCl; for small GTPases additionally: 1 mM $MgCl_2$ and 10 µM GDP) supplemented with cOmplete ULTRA Protease Inhibitor Cocktail (Roche) and 2 mM PMSF. The cells were lysed by passing them through a Microfluidizer (Microfluidics) three times. Insoluble cell fragments were removed by centrifugation in an Avanti J-25 (Beckman Coulter) with a JA-25.50 rotor (25000 rpm, 40 min, 10 °C) and subsequent filtration through a Rapid-Flow Bottle Top Filter (Nalgene Labware). For specific protein extraction the supernatant was applied to a HisTrap HP (5 ml, GE Healthcare) using a ÄKTAprime plus (GE Healthcare). Nonspecifically bound proteins were eluted with 4 % thiol-free buffer B (0.5 M imidazole, 50 mM HEPES pH 8.0, 500 mM LiCl; for small GTPases additionally: 1 mM $MgCl_2$ and 10 µM GDP). The His-tagged protein was obtained by fractionated elution with a linear gradient of 100 ml from 4 % to 100 % buffer B. Fractions containing the target protein were identified by measuring the absorption at 280 nm, analyzed by SDS-PAGE (2.5.3) and pooled. To the pooled protein, MESNA was added to a final concentration of 0.5 M to generate the protein-MESNA thioester through thiolysis. The mixture was gently stirred overnight at room temperature. The protein solution was diluted with thiol-free buffer 1:5 and the intein tag, uncut protein and impurities containing a His-tag were removed in an additional Ni-affinity chromatography step.

The protein present in the flow-through was concentrated to 2-5 ml and subjected to size exclusion chromatography on a HiLoad Superdex 75 26/600 or 16/600 gel filtration column (GE Healthcare) using MESNA containing gel filtration buffer (20 mM HEPES pH 7.5, 50 mM NaCl, 0.1 M MESNA, 1 mM $MgCl_2$ and 10 µM GDP). The fractions containing the target protein were identified by monitoring absorption at 280 nm and subsequently analyzed by SDS-PAGE. Fractions containing pure protein were pooled, concentrated, frozen in liquid nitrogen and stored at -80 °C.

2.4 Protein chemical methods

2.4.1 Labeling of small GTPases with reactive maleimide dyes

Thiol-reactive dyes carrying a maleimide moiety used in this thesis include Tide Fluor 3, Tide Fluor 4 (AAT Bioquest) and Alexa Fluor 594 C5 (Thermo Fisher Scientific). The dyes were stored and used from a stock solution with a concentration of 10 mM dissolved in DMSO.

For labeling with the acceptor dye, the protein was transferred into thiol-free labeling buffer (20 mM HEPES pH 7.5, 50 mM NaCl, 1 mM $MgCl_2$, 10 µM GDP) using a gravity flow NAP-5 Column (GE Healthcare). The protein concentration was determined and the reactive dye added stepwise to a final molar ratio of 1:1.5 - 1:3. The typical reaction volume was 200-500 µl with a protein concentration of 2-6 mg/ml. The DMSO concentration through dye addition did not exceed 5 % of the total reaction volume. The mixture was flushed with argon, shielded from light and incubated for 30-120 min at room temperature. Incubation time and dye to protein ratio were optimized by a SDS-Page labeling assay and observation of the protein labeling progression with a FluoroMax-3 spectrofluorometer (2.5.4.1). For proteins without C-terminal thioester modification the reaction was quenched after appropriate incubation time by addition of 2 mM β-mercaptoethanol. Finally, unreacted dye was removed by buffer exchange using a NAP-5 Column. Depending on the subsequent experimental setup, the labeled proteins were further concentrated using Vivaspin 500 Protein Concentrators (GE Healthcare).

2.4.2 Labeling of small GTPases with environment-sensitive iodoacetamide dyes

Thiol-reactive dyes carrying an iodoacetamide moiety used in this thesis include N-((2-(iodoacetoxy)ethyl)-N-Methyl)amino-7-Nitrobenz-2-Oxa-1,3-Diazole (IANBD), I-BA-s-IA (Mero61) and I-SO-s-IA (Mero87) from the group of Prof. Dr. Klaus Hahn (University of North Carolina at Chapel Hill, USA)[168]. IANBD was stored and used from a stock solution of 10 mM in DMSO. Mero dyes are instable in solution and were stored as crystalline powders. For labeling, a fresh stock solution was prepared by dissolving a small amount in 20 µl DMSO. To determine the dye concentration 1 µl of the stock solution was diluted 1:100-1:1000 in DMSO and the absorbance A_λ was determined at the wavelength λ corresponding to maximal absorption for the dyes (570 nm for Mero61, 592 nm for Mero87). With the respective extinction coefficient ε_λ the concentration was calculated using the Lambert–Beer law (Eq. 2-1).

$$A_\lambda = \varepsilon_\lambda \cdot c \cdot d \qquad \textbf{Eq. 2-1}$$

Protein labeling was carried out under similar conditions as described for the maleimide probes (2.4.1). To accommodate for the reduced labeling kinetics, the molar dye to protein ratio was increased (1:3-1:6) and incubation prolonged to 2-10 h. Exact incubation times and dye to protein ratio were optimized using a SDS-Page labeling assay and LC-ESI-MS analysis as described previously (2.4.1).

2.4.3 Reintroduction of C-terminal amino acids by native chemical ligation

For site-specific cysteine labeling, the Rab1b and KRas4b protein termini, -CC and -CVIM respectively, had to be removed. For native protein function however, these C-terminal amino acids are crucial, as they allow membrane attachment through C-terminal prenylation. Thus, the C-termini were reintroduced to restore full protein functionality by native chemical ligation (NCL) after completed protein labeling.

The protein was transferred into thiol-free labeling buffer (20 mM HEPES pH 7.5, 50 mM NaCl, 1 mM $MgCl_2$, 10 µM GDP) using a NAP-5 Column. Then it was concentrated to about 100 µl (6-10 mg/ml) and mixed with 50 µl thiol-free labeling buffer containing 150 mM MPAA and 60 mM TCEP. The final NCL buffer composition was 20 mM HEPES pH 7.5, 50 mM NaCl, 1 mM $MgCl_2$, 10 µM GDP, 50 mM MPAA and 20 mM TCEP. Accurate calibration of buffer pH after TCEP and MPAA addition is crucial for protein stability and ligation efficiency and was monitored using pH-test stripes (Merck Millipore).

The NCL mixture was incubated on ice overnight. MPAA was removed prior to microinjection experiments by repeated concentration in a Vivaspin 500 Protein Concentrator and dilution with MPAA free buffer (20 mM HEPES pH 7.5, 20 mM NaCl, 1 mM $MgCl_2$, 10 µM GDP). Successful ligation was confirmed by LC-ESI-MS (2.5.4).

2.4.4 Quantitative nucleotide exchange

After purification small GTPases are usually obtained in GDP-bound form. For quantitative nucleotide exchange to GTP or nucleotide analogs such as mantGDP and GppNHP (Jena Bioscience) the following protocol was used.

EDTA was added in a five times molar excess to the buffer Mg^{2+} concentration to reduce the GTPase's affinity to the bound nucleotide by Mg^{2+} chelation. The desired target nucleotide was added, to this mixture in a 5- (for mantGDP) or 20-times (for GTP and GppNHp) molar excess to the GDP buffer concentration and incubated at room temperature for at least 2 h. Finally, EDTA was removed by transferring the protein into buffer containing 20 mM HEPES pH 7.5, 50 mM NaCl, 1 mM $MgCl_2$, 2 mM DTE and the desired nucleotide at a concentration of 1 µM for mantGDP or 10 µM for GppNHp and GTP respectively, using a NAP-5 Column.

2.4.5 Immobilization of His-tagged sensor constructs on Ni-NTA beads

For *in vitro* fluorescence lifetime microscopy (2.7.1) small GTPase sensor constructs carrying a His-tag were immobilized in the surface of Ni-NTA superflow beads (Qiagen) and imaged on an object slide (Figure 2-1). For immobilization of the Rab1 sensor constructs, 50 µl of Ni-NTA beads were washed by suspending the beads in 500 µl GTPase buffer (20 mM HEPES pH 7.5, 20 mM NaCl, 2 mM DTE, 1 mM $MgCl_2$) and spinned down to remove the supernatant. The washing process was repeated three times with fresh buffer. 10-20 µl (1-3 mg/ml) of the protein solution was added to 10 µl of the suspended beads and incubated for 30-

60 min. After incubation the suspension was spun down, the supernatant was removed and the beads were washed twice with 200 µl fresh GTPase buffer.

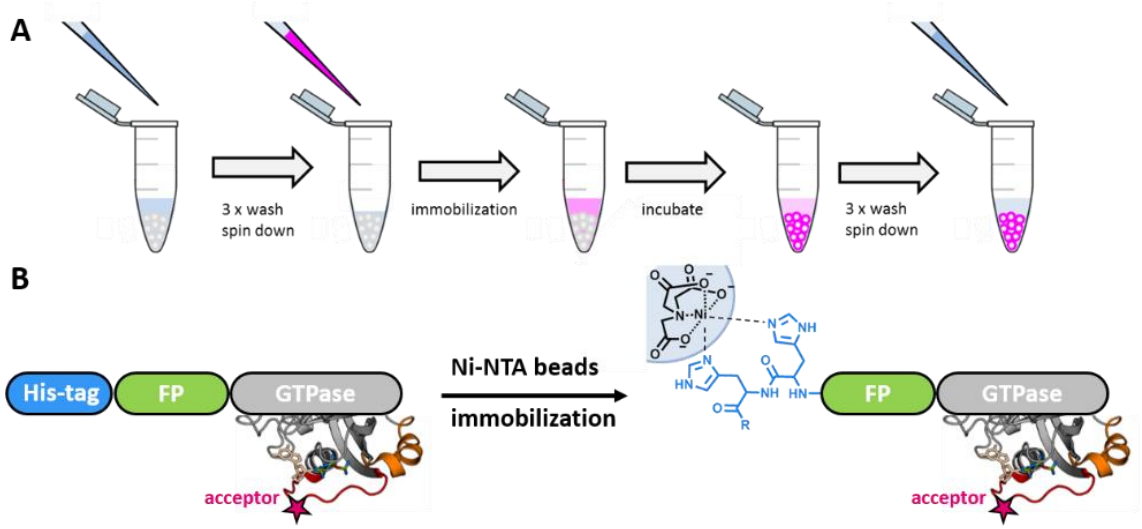

Figure 2-1: Immobilization of FRET-sensor on Ni-NTA beads.
(A) Scheme illustrating the procedure of immobilizing His-tagged Rab1 FRET-sensor on Ni-NTA beads. **(B)** Scheme depicting binding of the His-tagged protein sensor on the Ni-NTA surface.

To test the sensors response towards GEF-mediated nucleotide exchange the protein was incubated with $DrrA_{340-533}$ (1-2 µl, 14 mg/ml, 0.64 mM) in buffer containing 100 µM GTP prior to immobilization. For effector binding in addition to GEF and GTP, $OCRL1_{539–901}$ (50 µl, 11 mg/ml, 0.26 mM) and $LidA_{201-583}$ (10 µl, 12 mg/ml, 0.27 mM) were added. Finally, 20-50 µl of the bead suspension was transferred onto an object slide and imaged by FLIM through a 40x/1.35 UPlanSApo air objective (2.7.1).

2.5 Analytical and biophysical methods

2.5.1 Determination of protein concentration

To determine the concentration of a protein in solution the absorbance of the aromatic amino acid side chains at 280 nm was measured. For a protein of known sequence the mass and extinction coefficients at 280 nm were calculated by using the ProtParam tool of the ExPasy bioinformatics server.[169] The solution absorbance at 280 nm was measured using a Nanodrop Micro Volume Fluorospectrophotometer (PeqLab Biotechnology) according to the manufacturer's specification. The protein concentration was then obtained from the absorbance using the Lambert–Beer law (Eq. 2-1, section 2.4.2), here c is the protein concentration, A_λ is the absorbance at 280 nm, ε_λ is the corresponding extinction coefficient at 280 nm and d the light path length.

2.5.2 Determination of labeling efficiency by absorption spectroscopy

In addition to ESI-LC-MS and fluorescence spectroscopy the labeling efficiency of the fluorescent protein-tagged GTPases was determined by measuring the absorption of the labeled protein solution at different wavelengths. Using the spectral parameters listed in Table 2-17 and Eq. 2-1 the labeling efficiency can be obtained as the ratio of fluorescent protein to acceptor dye concentration.

Table 2-17: **Spectral properties of fluorophores.**

Fluorophore	ε_λ ($cm^{-1} \cdot M^{-1}$)	λ_{ex}(nm)	CF at 260 nm	CF at 280 nm
EGFP	56000	488		
mCitrine	77000	516		
Tide Fluor 3	85000	584	0.489	0.201
Tide Fluor 4	90000	618	0.331	0.436

The solution absorbance was measured using a Nanodrop Micro Volume Fluorospectrophotometer (PeqLab Biotechnology) according to the manufacturer's specification.

2.5.3 SDS-Polyacrylamide gel electrophoresis

SDS-Polyacrylamide gel electrophoresis is a preparative and analytical method used to separate and identify proteins by their size.

SDS-PAGE gels were obtained by polymerizing a layer of 5 % SDS stacking gel buffer on top of a previously polymerized 15 % SDS resolving gel buffer (2.1.3). The SDS samples were prepared by mixing 10-30 µl of the protein sample with the appropriate amount of 4x SDS loading buffer (2.1.3). The sample mixture was heated at 95 °C for 5 min to ensure homogenous denaturation. 10 µl of the denatured protein samples were loaded into the gel wells and the samples separated at a current of 60 mA immersed in SDS running buffer (2.1.3) until the leading bromophenol blue front reached the bottom of the gel. As a size reference low molecular weight (LMW) marker (GE Healthcare) was used. After completed separation the gels were

heated in Coomassie staining solution (2.1.3) and the background subsequently destained by repeated heating in 10 % (v/v) acetic acid.

2.5.4 Liquid chromatography-electrospray ionization mass spectrometry (LC-ESI-MS)

Electrospray ionization mass spectrometry is a highly sensitive detection technique that separates molecules after ionization based on their mass-to-charge ratio. For LC-ESI-MS, the mass spectrometer is combined with a liquid chromatography (LC) setup which separates molecules (e.g. proteins) based on differences in their affinity to a stationary phase (e.g. silica gel and alumina columns) and a mobile phase (e.g. eluents such as acetonitrile and water).

LC-ESI-MS measurements were performed on a LCQ Advantage Max mass spectrometer (Finnigan) coupled with an Agilent 1100 Series HPLC system (Agilent Technologies Inc.) equipped with a Grace Vydac 214TP C4-HPLC column (Thermo Fisher Scientific). Sample separation and desalting was achieved by elution from the HPLC column with a gradient of 20 % to 80 % acetonitrile with 0.08 % (v/v) TFA against aqueous buffer with 0.1 % (v/v) TFA. Data analysis and deconvolution was carried out by using the analysis software Xcalibur (Thermo Electron) and MagTran (Zhongqi Zhang, Amgen).

Fluorescence spectroscopy

2.5.4.1 Collection of fluorescence spectra

Fluorescence measurements were performed with a FluoroMax-3 (Horiba Jobin Yvon) spectrofluorometer in a 1 ml cuvette at 25 °C. Fluorescence spectra were obtained by setting the excitation monochromators at a suitable wavelength and detecting the fluorophore emission over a set wavelength range. Typical emission/excitation settings used for the fluorophores in this thesis are listed below in Table 2-18. All spectra were background corrected through subtraction of a blank buffer spectrum collected with identical settings.

Table 2-18: **Fluorescence spectra.**

Fluorophore	λ_{ex} (nm)	λ_{em} (nm)
EGFP	480	490-700
Mant	367	400-650
mCitrine	490	500-800
Mero61 (I-BA-s-IA)	560	570-750
Mero87 (I-SO-s-IA)	590	600-750
NBD	480	500-800
Tide Fluor 3	535	545-800
Tryptophan	298	310-500

2.5.4.2 Characterization of GEF-mediated nucleotide exchange and GAP induced GTP hydrolysis by fluorescence spectroscopy

The interaction of the small GTPases with their regulatory GEF and GAP proteins was assessed by fluorescence spectroscopy.

To monitor GEF-mediated nucleotide exchange three spectroscopic setups were employed: (1) using the fluorescently labeled GDP analog mantGDP, (2) measuring the FRET signal response for FRET sensor constructs and (3) by following the changes in fluorescence intensity of the environment sensitive dyes Mero61 and Mero87 attached at prominent positions in the small GTPases.

MantGDP-bound GTPase was obtained by quantitative nucleotide exchange as described in 2.4.4. GEF-mediated nucleotide exchange was then observed as a decrease of mant fluorescence intensity upon addition of GEF, 10 - 200 nM for DrrA or 0.125 - 2 μM for SOS respectively, to 100 or 200 nM mantGDP-bound GTPase in the presence of 100 μM GTP.

Similarly, the responses of FRET and ratiometric sensor constructs were characterized by monitoring the respective signal change after addition of varying amounts of GEF (10 - 200 nM for DrrA and 0.125 - 2 μM for SOS), to 100-200 nM mantGDP-bound GTPase in the presence of 100 μM GTP.

GAP induced GTP hydrolysis was observed for the FRET and ratiometric sensor constructs through addition of an excess of 1-2 μM TBC1D20 to preparatively GTP-loaded GTPase. Typical emission and excitation settings used for the described assays are summarized in Table 2-19.

Table 2-19: Fluorescence measurements settings for GEF and GAP assay.

Fluorophore	**λ_{ex} (nm)**	**λ_{em} (nm)**
EGFP	480	508
MantGDP	367	438
mCitrine	480	525
Mero61 (I-BA-s-IA)	565	590
Mero87 (I-SO-s-IA)	596	620
NBD	480	530
Sensitized emission	**λ_{ex} (nm)**	**λ_{em} (nm)**
EGFP → Tide Fluor 3	480	580
mCitrine → Tide Fluor 4	480	614

To determine the catalytic efficiency of the used GEFs and GAPs the following relations were used.

The Michaelis–Menten equation (Eq. 2-2), describing the rate of enzymatic reactions:

$$v = \frac{[S]}{K_M + [S]} \cdot v_{max} \qquad \textbf{Eq. 2-2}$$

v_{max} is the maximum reaction rate, $[S]$ is the substrate concentration and K_M is the Michaelis constant.

The relation for v_{max} and v can be described as:

$$v_{max} = k_{cat} \cdot [E]_0 \qquad \textbf{Eq. 2-3}$$

$$v = \frac{d[S]}{dt} = -k_1 \cdot [S] \cdot [E] + k_{-1} \cdot [ES] \qquad \textbf{Eq. 2-4}$$

In this context $[E]_0$ corresponds to the total enzyme concentration, $[ES]$ is the enzyme-substrate complex concentration and k_{cat} is the turnover rate. With $k_{-1} \cdot [ES] << -k_{-1} \cdot [ES]$ and $[E]_0 = [ES] + [E] \approx [E]$, Eq. 2-4 reduces to:

$$v = -k_1 \cdot [S] \cdot [E]_0 \text{, using } k_{obs} = [E]_0 \cdot [S]$$
$$v = -k_{obs} \cdot [S] \qquad \textbf{Eq. 2-5}$$

With $[S] << K_M$, Eq. 2-2 can be simplified to Eq. 2-6:

$$v = \frac{[S]}{K_M} \cdot v_{max} \qquad \textbf{Eq. 2-6}$$

Combining Eq. 2-5 and Eq. 2-6 yields the following relation:

$$\frac{k_{cat}}{K_M} = \frac{k_{obs}}{[E]_0} \qquad \textbf{Eq. 2-7}$$

Using this equation, the catalytic efficiency, k_{cat}/K_M, can be obtained as the slope of a linear fit of k_{obs} plotted against the total enzyme concentration. Under pseudo-first order conditions , k_{obs} can be obtained by fitting the fluorescence signal with the mono-exponential equation Eq. 2-8:

$$I = I_\infty + A \cdot e^{-k_{obs} \cdot t} \qquad \textbf{Eq. 2-8}$$

here I is the fluorescence intensity at time t, I_∞ is the intensity after signal saturation and k_{obs} the observed rate. For exponential and linear curve fitting the analysis software Origin 8.6 (OriginLab) was used.

2.5.4.3 Effector binding assay using fluorescence spectroscopy and fluorescence polarization

To assess the binding of effector proteins to the small GTPase sensor constructs fluorescence and fluorescence polarization spectroscopy were used.

Effector binding was analyzed by three different spectroscopic approaches: (1) by observing the changes in fluorescence polarization of a dye (e.g. EGFP) attached to the small GTPase upon effector binding, (2) by measuring the FRET signal response of the respective sensor constructs or (3) by monitoring the changes in fluorescence intensity of the environment sensitive dyes Mero61 and Mero87 attached to the small GTPases. Titration of increasing amounts of effector (e.g. OCRL1 or LidA) to a fixed concentration of GTPase (100-500 nM) resulted in an effector concentration dependent change in fluorescence polarization, FRET signal or fluorescence intensity. After correcting the signal for dilution effects, the observed signal change was plotted as a function of the effector concentration. This, allows the determination of K_D using the following expressions for a reversible second order reaction (Eq. 2-9),

$$\text{GTPase} + \text{E} \rightleftharpoons \text{GTPase:E} \qquad K_D = \frac{[\text{GTPase}]\cdot[\text{E}]}{[\text{GTPase:E}]} \qquad \textbf{Eq. 2-9}$$

Here [GTPase], [GTPase:E] and [E] are the concentrations at equilibrium and $[GTPase]_0$ and $[E]_0$ represent the initial concentration of GTPase and effector, respectively.

Using $[\text{GTPase}] = [\text{GTPase}]_0 - [\text{GTPase:E}]$ and $[\text{E}] = [\text{E}]_0 - [\text{GTPase:E}]$ one obtains:

$$K_D = \frac{([\text{GTPase}]_0 - [\text{GTPase:E}])\cdot([\text{E}]_0 - [\text{GTPase:E}])}{[\text{GTPase:E}]}$$

which can be rearranged and solved as a quadratic equation for the concentration of the GTPase-effector complex $[\text{GTPase:E}]$:

$$0 = [\text{GTPase:E}]^2 - [\text{GTPase:E}]\cdot(K_D \cdot [\text{GTPase}]_0 \cdot [\text{E}]_0) + [\text{GTPase}]_0 \cdot [\text{E}]$$

$$[\text{GTPase:E}] = \frac{1}{2}\left((K_D \cdot [\text{GTPase}]_0 \cdot [\text{E}]_0) \pm \sqrt{(K_D \cdot [\text{GTPase}]_0 \cdot [\text{E}]_0)^2 - 4\cdot[\text{GTPase}]_0 \cdot [\text{E}]_0}\right)$$

Using the above relation with the following equation (Eq. 2-10) describing the binding fraction in equilibrium as a change in fluorescence/polarization signal upon effector titration:

$$\frac{[\text{GTPase:E}]}{[\text{GTPase}]_0} = \left(\frac{I - I_0}{I_\infty - I_0}\right) \qquad \textbf{Eq. 2-10}$$

equation Eq. 2-11 can be derived:

$$I = I_0 + \frac{(I_\infty - I_0)}{2\cdot[\text{GTPase}]_0}\left((K_D \cdot [\text{GTPase}]_0 \cdot [\text{E}]_0) \pm \sqrt{(K_D \cdot [\text{GTPase}]_0 \cdot [\text{E}]_0)^2 - 4\cdot[\text{GTPase}]_0 \cdot [\text{E}]_0}\right) \qquad \textbf{Eq. 2-11}$$

Eq. 2-11 was then used to fit the measured titration curves with the program GraFit 5 (Erithacus Software) to obtain K_D values for the respective GTPase-effector complex.

2.5.4.4 Calculation of R_0 for FRET pairs

As discussed in section (1.2.1) factors determining the efficiency of energy transfer for a FRET pair (E_{FRET}) include the spectral overlap integral of donor emission and acceptor excitation (J (λ)), the refractive index of the surrounding medium (n), the dipole orientation factor (κ), the fluorescence quantum yield of the donor dye (Q_D) and the distances of the donor and acceptor fluorophore (r). This relation is described in Eq. 1-3 and Eq. 1-2.

$$E_{FRET} = \frac{1}{1 + \left(\frac{r}{R_0}\right)^6} \qquad \textbf{Eq. 1-2}$$

$$R_0^6 = 8.79 \cdot 10^{23} \cdot \frac{\kappa^2 \cdot Q_D \cdot J(\lambda)}{n^4} \qquad \textbf{Eq. 1-3}$$

To obtain R_0 (Förster radius, distance where E_{FRET}=0.5) for a specific fluorophore pair, the overlap integral of the donor emission and acceptor excitation integrated over the wavelengths λ has to be determined (Eq. 2-12).

$$J(\lambda) = \int_0^\infty \varepsilon_\lambda(\lambda)\lambda^4 \cdot F_D(\lambda)d\lambda \qquad \textbf{Eq. 2-12}$$

In Eq. 2-12 F_D represents the normalized donor emission spectrum and ε_λ the molar extinction coefficient of the acceptor fluorophore. For the FRET pairs used in this thesis the respective overlap integrals were calculated using a|e - UV-Vis-IR Spectral Software (FluorTools). Used constants and calculated J values are listed below in Table 2-20 and Table 2-21.

Table 2-20: **Overlap integrals.**

J ($nm^4 \cdot M^{-1} \cdot cm^{-1}$)	EGFP	mCitrine
Alexa Fluor 594	$3.11 \cdot 10^{15}$	$4.22 \cdot 10^{15}$
Tide Fluor 3	$2.85 \cdot 10^{15}$	$4.52 \cdot 10^{15}$
Tide Fluor 4	$2.54 \cdot 10^{15}$	$4.36 \cdot 10^{15}$

Table 2-21: **Quantum yields and extinction coefficients.**

Fluorophore	Q	ε_λ ($cm^{-1} \cdot M^{-1}$) at (λ (nm))
Alexa Fluor 594	0.66	105 000 (588)
Tide Fluor 3	0.80	85 000 (555)
Tide Fluor 4	0.91	90 000 (590)
EGFP	0.60	56 000 (484)
mCitrine	0.61	83 400 (514)

R_0 was calculated with a value of κ^2=0.66. Which is an approximation based on unrestricted, freely diffusing fluorophores. For the intramolecular FRET pair used in thesis this assumption might be inaccurate as the dyes are covalently attached to a protein and thereby restricted in their movement. However, it has been shown before, that assuming an orientation factor of 0.66 yields accurate R_0 values even for intramolecular FRET pairs.[170] The obtained R_0 for the FRET partners used in this thesis are summarized in Table 2-22.

Table 2-22: Förster radii.

R_0 (Å)	EGFP	mCitrine
Alexa Fluor 594	53.4	59.4
Tide Fluor 3	53.7	59.9
Tide Fluor 4	51.7	56.7

2.6 Cell biological methods

2.6.1 Cultivation of eukaryotic cell lines

All cell lines were cultured in 100 mm tissue culture dishes (Sarstedt) and 7-8 ml minimum essential medium (MEM) supplemented with 10 % (v/v) fetal bovine serum (FBS), 1 % (v/v) sodium pyruvate solution (100 mM), 1 % GlutaMAX and 1 % (v/v) non-essential amino acids (all Thermo Fisher Scientific) at 37 °C and 5 % CO_2. Cells were split every two to three days at a confluency of 70-80 %. After washing with 5 ml dulbecco's phosphate-buffered saline (DPBS) (Thermo Fisher Scientific) cells were detached by incubation with 1 ml 0,25 % (v/v) trypsin-EDTA (Thermo Fisher Scientific) at 37 °C and 5 % CO_2. Complete detachment was confirmed by microscopy and the cells were suspended in 4-9 ml supplemented MEM. Finally, 1 ml of the cell suspension were added to 7 ml supplemented MEM in a new 100 mm tissue culture dish.

2.6.2 Transient transfection of eukaryotic cells

Transient transfection was used to introduce exogenous transgenic DNA into cells to initiate expression of desired recombinant proteins. In this thesis the transfection reagent X-tremeGENE HP DNA (Roche diagnostics) was applied according to the manufacturer's recommendation. For transfection 0.5-1 ml cell suspension was added to a mixture of 1-3 μg plasmid DNA preincubated for 15-20 min in 200 μl Opti-MEM (Thermo Fisher Scientific) with 1-2 μl X-tremeGENE HP transfection reagent in a 35 mm glass bottom dish (MatTek). After transfection the cells were incubated overnight at 37 °C and 5 % CO_2 and subsequently used for microscopy (2.7) or microinjection (2.6.4).

2.6.3 Cell treatments

EGF induced KRas activation

To test the KRas sensor sensitivity *in vivo* MDCK cells were serum starved overnight through incubation with MEM containing 0.5 % FBS. The following day the respective GTPase sensor constructs were introduced through microinjection (2.6.4) and the injected cells incubated for 2-3 h at 37 °C and 5 % CO_2. KRas activation was then induced through addition of EGF to a final concentration of 100 ng/ml. The FRET sensor response was monitored by fluorescence lifetime image microscopy (2.7.3).

Microtubule disruption with nocodazole

To observe the effects of abolished microtubule dependent vesicular transport, cells were cooled on ice for 30 min and treated with 5 μg/ml nocodazole in imaging medium prior to FRAP and live cell imaging.

Treatment with EGFR kinase inhibitor Erlotinib

To test the KRas sensor's specificity towards EGF induced KRas activation, cells were treated with 5 μM of the tyrosine kinase inhibitor Erlotinib for at least 3 h before microinjection and EGF stimulation.

2.6.4 Microinjection

Microinjection is a technique for introducing non-cell permeable reagents into single cells. In this thesis microinjection was used to inject small amounts of GTPase sensors into wild type and transiently transfected HeLa, COS-7 and MDCK cells (2.1.6). After injection, the cells were examined by confocal (2.7.1) and fluorescence lifetime microscopy (2.7.1).

Microinjection needles were prepared using a PD-5 double-stage horizontal puller (Narishige). Microinjection was performed using a 40x oil immersion objective of a TCS SP2 Laser Scanning Confocal Microscope (Leica) equipped with an Transjector 5246 (Eppendorf). The cells were prepared for microinjection by plating 0.5-1 ml of wild type or transfected cells suspended in MEM in a 35 mm glass bottom dish (MatTek). The cells were incubated overnight at 37 °C and 5 % CO_2 and subjected to microinjection the next day.

The protein solution was concentrated to 6-10 mg/ml using Vivaspin protein concentrators (GE Healthcare) and then centrifuged at 13.000 rpm at 4 °C for 5 min to remove small particles and aggregates. 0.5 µl of the solution was loaded into the injection needle by pipetting into the blunt end of the capillary. The capillary was mounted onto the capillary holder and the needle tip positioned a few µm above the cell plane using the Eppendorf Micro manipulator 5171. The compensation pressure (Pc) was set to 50 hPa ensuring a slow continuous flow from protein solution out of the needle tip to prevent needle blockage. Proper needle function was confirmed by verifying the constant leakage of fluorescent protein in the appropriate fluorescence channel. The injection plane was set just below the top of the targeted cells. Automated injection of 50-150 cells was performed using the Eppendorf Transjector 5246 with the injection pressure (Pi) set at 100-180 hPa and an injection time (ti) of 0.2-0.4 s. After injection, the cells were incubated for 1-2 h at 37 °C and 5 % CO_2 to allow prenylation of the reconstituted C-termini through the endogenous cellular prenylation machinery.

2.7 Microscopy

2.7.1 Confocal laser scanning and fluorescence lifetime microscopy setup

Confocal laser scanning microscopy (CLSM) and fluorescence lifetime imaging microscopy (FLIM) were carried out using a FlouView FV1000 (Olympus) equipped with a time-correlated single-photon counting (TCSPC) LSM Upgrade Kit (PicoQuant). Cell images were collected through a 60x/1.35 UPlanSApo oil immersion objective (Olympus). Ni-NTA beads were imaged through a 40x/1.35 UPlanSApo air objective (Olympus). All measurements were carried out in an incubation chamber at 37 °C. Lasers used for excitation and settings for detection are listed below (Table 2-23). For live cell imaging the incubator was additionally supplemented with 5 % CO_2.

For FLIM measurements the samples were exited with a 470 nm pulsed diode laser (PicoQuant) at 36 % and a repetition rate of 40 MHz. Photons were collected by a single-photon counting avalanche photodiode

(PDM Series, MPD, PicoQuant) and timed using a time-correlated single-photon counting module (PicoHarp 300, PicoQuant) after being spectrally filtered using a narrow-band emission filter (HQ 525/15, Chroma) over a course of approximately 2 min with 1-2·10^5 photons. The FLIM data was subsequently analyzed as described in section 2.7.5.

Table 2-23: FlouView FV1000 settings for fluorescence confocal microscopy.

Fluorophore	Laser	λ_{ex} (nm)	Dichroic mirror (nm)	Barrier Filters settings (nm)
BFP	FV5-LD405	405	SDM510	425-475
EGFP	Argon Laser GLG 3135	488	SDM560	505-550
mCitrine	Argon Laser GLG 3135	488	SDM560	515-560
Tide Fluor 3	DPSS 85-YCA-020-230	561	Mirror	585-685
Tide Fluor 4	DPSS 85-YCA-020-230	561	Mirror	575-675
mKate2	DPSS 85-YCA-020-230	561	Mirror	585-685
Mero61	DPSS 85-YCA-020-230	561	Mirror	610-710
Mero87	DPSS 85-YCA-020-230	561	Mirror	610-710

2.7.2 Live cell imaging using fluorescence recovery after photobleaching (FRAP) and photoactivatable fluorescent proteins

Fluorescence recovery after photobleaching (FRAP) and photoactivatable fluorescent proteins (paFPs) are powerful tools to examine and quantify dynamic processes in cells with a high spatio-temporal resolution. In this thesis FRAP and paFPs were used to characterize the cycling of Rab1 between the Golgi compartment and its cytoplasmic fraction.

The FRAP and photoactivation experiments were carried out using a TCS SP5 microscope (Leica) equipped with a 63x/1.4 HCX PL APO (λ blue) oil immersion objective (Leica). Lasers and settings used for fluorophore excitation, bleaching, photoactivation and the respective detection filter settings are listed below (Table 2-24). All measurements were carried out in an incubation chamber at 37 °C and 5 % CO_2.

Table 2-24: TCS SP5 settings for bleaching and photoactivation settings.

Excitation of	Laser	λ_{ex} (nm)	Barrier Filters settings (nm)
BFP	Cube 1162002/AF	405	415-475
EGFP	Argon Laser LGK 7872 ML05	488	505-555
Tide Fluor 3	561 DPSS YLK 6120 T02	561	595-685
mKate2	561 DPSS YLK 6120 T02	561	595-685
Bleaching of EGFP	Argon Laser LGK 7872 ML05	488	-
Photoactivation of paGFP	Cube 1162002/AF	405	-

The general setup of a FRAP routine includes: (1) pre-bleaching imaging, (2) bleaching of the designated regions of interest (ROI) and (3) post-bleaching imaging to monitor the fluorescence recovery in the bleached area.

In this thesis FRAP measurements were performed to examine the role of Rab1 and its regulators on the transport processes that are directed towards the Golgi. To this end, the entire fluorescently tagged Rab1 population on the Golgi membrane was bleached. The following recovery of EGFP-Rab1 on the Golgi is then exclusively governed by vesicular and/or GDI-mediated transport from the cytoplasm to the Golgi. The appropriate ROI was identified by expression of the Golgi marker mKate2-giantin. At least three images were collected before bleaching, followed by extensive irradiation (10 repetitions over 12 s) with maximal laser power at 488 nm (100 %, Argon Laser LGK 7872 ML05). After bleaching, the fluorescence recovery was monitored over a period of at least 400 s with images collected every 2-10 s. The obtained fluorescence profiles were analyzed as described below (2.7.3).

The procedure for fluorescence loss after photoactivation experiments is similar to the previously described FRAP setup. Instead of a bleaching step, a fluorophore population is activated at a predefined ROI and the subsequent depletion from this area and/or the resulting increase in fluorescence at a different site is monitored. As for FRAP, a photoactivation procedure consists of three steps: (1) image acquisition before activation, (2) activation of the photoactivatable fluorophore at the predefined ROI and (3) imaging of the redistribution of the now fluorescent protein population.
In the pre-activation step for each experiment, three images were collected. Photoactivation of paGFP-Rab1 was performed through irradiation at 405 nm with 30-50 % of the maximal laser intensity (Cube 1162002/AF). Post activation images of paGFP-Rab1 and mKate2-giantin were collected every 2 seconds over a period of at least 300 s.
The activation of paGFP-Rab1 was used in two complementary experiments that visualize the depletion of Rab1 from the Golgi compartment and delivery of Rab1 from its cytoplasmic fraction to the Golgi respectively. To observe the transport originating from the Golgi, paGFP-Rab1 localized on the organelle was photoactivated and the subsequent depletion of Golgi fluorescence analyzed as described below (2.7.4), yielding the observed k_{G-C} rate. Conversely, transport from cytoplasm to Golgi was followed by photo activating the cytoplasmic fraction of paGFP-Rab1 and monitoring the subsequent increase in fluorescence on the Golgi compartment, yielding the observed k_{C-G} for cytoplasm to Golgi transport (2.7.4).

2.7.3 Fluorescence recovery after photobleaching (FRAP) analysis

For FRAP analysis the ROIs were identified through comparison of the pre-bleached image with the first image after the bleaching sequence. The mean fluorescence intensity on the Golgi was determined using the FRAP profiler plugin of the ImageJ Software, corrected for bleaching against the fluorescence intensity of the whole cell and normalized using Eq. 2-13:

$$I_{norm}(t) = \frac{I(t) - I_0}{I_{pre} - I_0} \qquad \textbf{Eq. 2-13}$$

Here I(t) is the fluorescence intensity at time t, I_0 the initial residual fluorescence after bleaching and I_{pre} is the mean intensity preceding photobleaching. The recovery of the mean fluorescence in the bleached region was fitted to the single exponential function Eq. 2-14.

$$I_{norm}(t) = I_{\infty}\left(1 - e^{-k_{obs} \cdot t}\right) \qquad \textbf{Eq. 2-14}$$

$$t_{1/2} = \frac{\ln(2)}{k_{obs}} \qquad \textbf{Eq. 2-15}$$

I_{norm} corresponds to the fluorescence intensity at time t, I_{∞} is the fluorescence intensity reached after completed recovery and k_{obs} is the observed rate constant for fluorescence recovery. From this and using Eq. 2-15 the half-time of the fluorescence recovery ($t_{1/2}$) and the rate constant for the trafficking of fluorophores to the bleached region $K_{G\text{-}C} = k_{obs}$ can be extracted.

2.7.4 Fluorescence loss/increase after photoactivation analysis

For photoactivation of paGFP-Rab1, the ROI was identified by using mKate2-giantin as a Golgi marker. For both experimental procedures (2.7.2), the mean fluorescence paGFP-Rab1 intensity on the Golgi was quantified as the ratio of paGFP to mKate2-giantin to account for changes in Golgi structure over the time course of the experiment (Eq. 2-16) and normalized as described previously (Eq. 2-13).

$$I(t) = \frac{I(t)_{paEGFP}}{I(t)_{mKate}} \qquad \textbf{Eq. 2-16}$$

To determine $k_{C\text{-}G}$ for the Rab1 flux from the cytoplasm to the Golgi site, the observed fluorescence increase at the Golgi following photoactivation at the cytoplasm was fitted by the single exponential function (Eq. 2-14).

For the reverse process of Rab1 trafficking from the Golgi membrane to the cytoplasm, the fluorescence depletion from the Golgi after activation was monitored. The resulting curve was fitted by the a single exponential function (Eq. 2-17) to yield $k_{G\text{-}C}$ as k_{obs}.

$$I_{norm}(t) = I_{\infty} + A \cdot e^{-k_{obs} \cdot t} \qquad \textbf{Eq. 2-17}$$

2.7.5 FLIM analysis and image processing

FLIM data was analyzed via a customized MATLAB script using global analysis.[171] For analysis of the observed lifetime for individual cells and at subcellular resolution, intensity and lifetime images generated by the global analysis script were further processed using ImageJ as described in the following.

To segment the cells from the background the intensity images where thresholded and a binary mask generated. The background was then removed through multiplying the mask with the lifetime map and the background set to “Not a Number”. The average lifetime of the cell or a specific are (e.g. the Golgi apparatus) was then determined using the ROI tool for the respective image section.

For figure display, the lifetime images were smoothed with a filter that replaces each pixel with the average of its 3×3 neighborhood, a LUT was applied and the displayed lifetime range set as indicated in the respective calibration bar.

3 Results and discussion

3.1 Development and characterization of small GTPase FRET sensors

Small GTPases regulate a great variety of highly dynamic biological processes such as signal transduction, cytoskeleton rearrangement, nuclear transport or membrane trafficking. Thus, sensors providing insight into the spatiotemporal aspects of GTPase activity have been a major interest in the field. A common methodology is based on effector domains that report on GTPase activation through specific binding to the GTP-bound protein (1.3). However, this approach is limited by the prerequisite of a suitable effector domain for each target GTPase and therefore not versatile. Furthermore, direct observation of the nucleotide governed conformational change upon GTPase activation would be advantageous as it preserves the proteins ability to bind to its effectors and interact with its regulatory partners.

To address this need, novel and universally applicable conformational sensors for GTPase activity (COSGAs) were developed and characterized in this thesis. The COSGA sensor principle was first established using Rab1b (referred to as Rab1) and later successfully expanded to the small GTPase KRas4b (referred to as KRas).

3.1.1 FRET sensor design

GTPases undergo significant changes in structural flexibility and conformation upon nucleotide exchange and effector binding (1.1.1). The sensor developed and characterized in this thesis is based on an intramolecular FRET that directly reports on conformational changes within the protein fold.

A basic scheme of the sensor design is depicted in Figure 3-1. The FRET pair is generated by decorating the GTPase with two fluorophores, using a combination of protein engineering and chemical labeling. The donor fluorophore of the intramolecular FRET pair is introduced by genetically fusing a fluorescent protein to the N-terminus of the GTPase. The FRET acceptor, a small organic dye, is attached in the protein fold by site-specific cysteine labeling (2.4.1).

The acceptor labeling sites were selected based on the following criteria: (1) Does the protein site undergo significant conformational changes upon nucleotide exchange? (2) Is the residue at this positon crucial for native protein functioning and its interaction with regulatory partners? (3) Is the labeling site solvent accessible to allow efficient labeling?

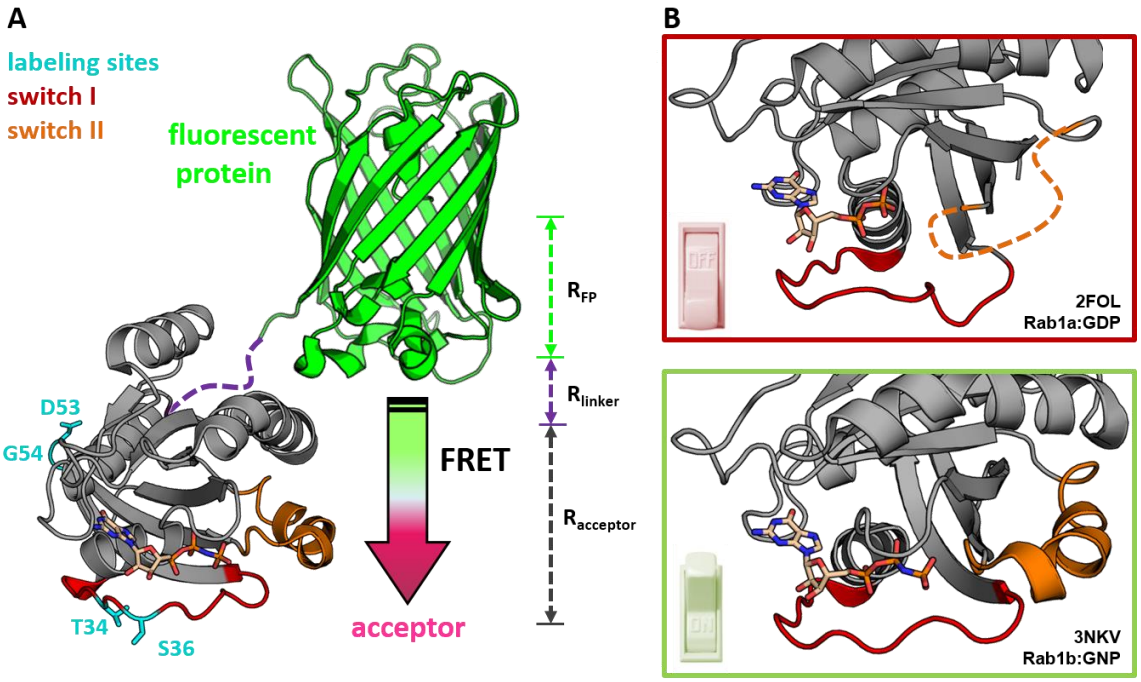

Figure 3-1: FRET sensor design.
(A) The sensor design combines an N-terminal fluorescent protein (green) with a small organic acceptor dye introduced in to the GTPase fold (gray). The organic dye is introduced by site-specific cysteine labeling at the positions indicated in turquoise. **(B)** Conformational changes in the switch regions of Rab1 in GTP- and GDP-bound states. Switch I and II are highlighted in red and orange respectively. The bound guanine nucleotide is depicted in beige with atoms highlighted in red (oxygen), blue (nitrogen) and orange (phosphorous).

Acceptor sites for Rab1 sensor

For the Rab1 sensor T34 was initially selected as an acceptor labeling site, because it is located in the switch I region and not directly involved in the interaction with Rab1 regulators or effectors. To identify additional labeling positions that undergo changes in flexibility and conformation upon GTP binding, molecular dynamics (MD) simulations were performed by Dennis Krüger. More specifically, the root mean square fluctuation (RMSF) of GTP- and GDP-bound Rab1 (based on PDB ID: 3NKV) were compared to identify hot spots of changes in flexibility. In addition to the expected maxima in ΔRMSF at the switch regions and the flexible C-terminus, the interswitch region showed a substantial change in RMSF between the two nucleotide bound protein forms (Figure 3-2). After excluding protein sites that are vital for protein function or unfavorably buried in the protein fold, S36 in the switch I and D53 and G54 in the interswitch region were chosen as labeling sites in addition to T34.

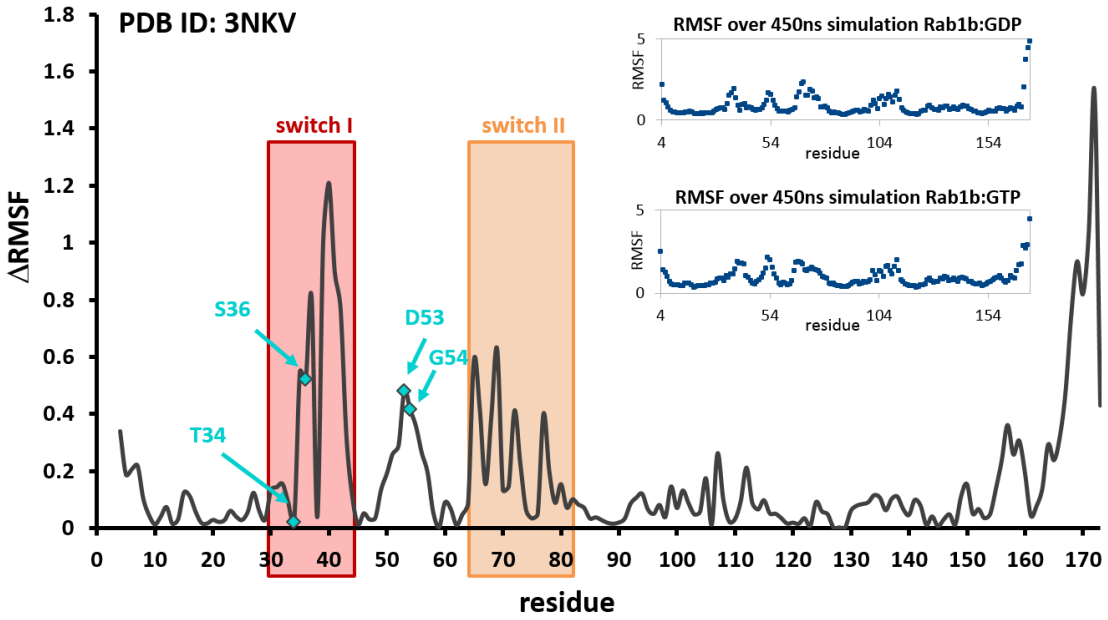

Figure 3-2: Molecular dynamics (MD) simulations of the root mean square fluctuation (RMSF) in GTP- and GDP- bound Rab1.
MD simulations of Rab1 were based on the X-ray structure of Rab1 bound to GppNHp (PDB ID: 3NKV). For the MD simulations AMP at Y77 was removed and GppNHp was substituted for either GDP or GTP. Here switch regions are highlighted in red (switch I) and orange (switch II) respectively. Acceptor labeling sites are marked in turquoise.

Crucial for efficient energy transfer is the distance and orientation of the two fluorophores in a FRET pair. For maximal sensitivity the distance between the two FRET partners should be as close as possible to R_0 (1.2.1). R_0 for FRET pairs utilized in this thesis was determined in section 2.5.4.4. An approximation of the distances between the fluorescent protein chromophore to the EGFP C-terminus (R_{FP}) and of the Rab1 N-terminus to the acceptor labeling site ($R_{acceptor}$) were estimated from available structural data of Rab1 (PDB ID: 3NKV) and EGFP (PDB ID: 2Y0G) using the software PyMOL. The last structurally resolved C_α of EGFP and the first resolved C_α of Rab1 were defined as the respective termini. Residues in between the termini were designated part of the linker, leading to a total linker length of 14 amino acids. The length of the proteinaceous linker region was approximated using a freely jointed chain of C_α atoms described by Eq. 3-1:

$$R_{linker} = \sqrt{C_n} \cdot b_0 \cdot \sqrt{n} \qquad \textbf{Eq. 3-1}$$

Here n is the number of amino acids, b_0=3.8 Å is the average distance between C_α atoms and C_n=2.3 is the characteristic ratio.[172] The estimated total donor to acceptor distances (R_{D-A}) for selected acceptor labeling positions in Rab1 are summarized below (Table 3-1). The obtained values are close to the calculated R_0 = 53-60 Å of the FRET pairs utilized for the sensor constructs (2.5.4.4). This indicates that the chosen intramolecular FRET pair assembly should display efficient FRET and be suitable to report conformational changes in the protein fold.

Table 3-1: Donor acceptor distances.

R (Å)	T34	S36	D53	G54
$R_{acceptor}$	31.8	32.1	12.8	10.8
R_{linker}		21.6		
R_{FP}		24.5		
R_{D-A}	**77.9**	**78.2**	**58.9**	**56.9**

Table 3-2: Truncated linker constructs.

R (Å)	T34	S36	D53	G54
$R_{acceptor}$	31.8	32.1	12.8	10.8
R_{linker}		8.2		
R_{FP_D11}		14.9		
R_{D-A}	**65.8**	**66.1**	**46.8**	**44.8**

For sensor optimization, constructs with a shortened linker region were prepared to shift the donor acceptor distance even closer to R_0 in order to increase the dynamic range. It has been shown previously that fluorescent proteins can be truncated at their termini without losing their favorable fluorescent properties.[173] This property was exploited by truncating the EGFP and mCitrine C-termini by eleven amino acids to minimize the flexible linker region between the fluorescent protein and the GTPase domain. The resulting donor to acceptor distances are summarized in Table 3-2.

Acceptor sites for KRas sensor

Based on the acceptor sites that proved sensitive towards the bound nucleotide in the Rab1 constructs, the FRET sensor design was expanded to KRas. Potential labeling sites in KRas were identified through structural alignment of the available crystal structures for Rab1 (PDB ID:3NKV) and KRas (PDB ID: 4LRW) (Figure 3-3).

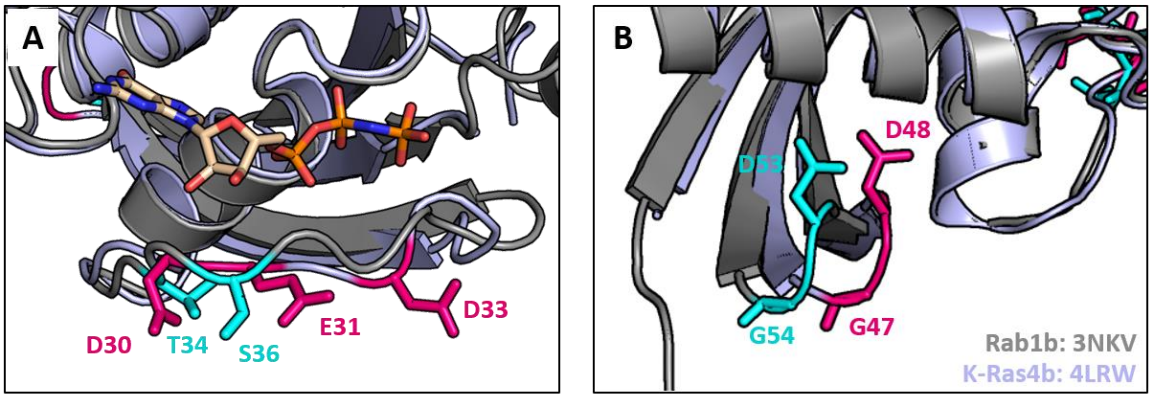

Figure 3-3: Structural alignment of Rab1 (PDB ID: 3NKV) and KRas (PDB ID: 4LRW).
(A) Detailed view of labeling sites in switch I and **(B)** interswitch region of Rab1 (gray, PDB ID: 3NKV) and KRas (light blue, PDB ID: 3LRW). Labeling sites are highlighted in turquoise (Rab1) and pink (KRas) respectively. The bound guanine nucleotide is depicted in beige with atoms highlighted in red (oxygen), blue (nitrogen) and orange (phosphorous).

Based on the structural alignment, three positions in the switch 1 (D30, E31 and D33) and two positions in the interswitch region (G47 and D48) were selected. Their sensitivity towards GEF-mediated nucleotide exchange was examined using the catalytic domain of SOS, a Ras GEF. (3.1.4). Similarly to Rab1, Dennis Krüger performed MD simulations for GDP and GTP-bound KRas based on the available crystal structure (PDB ID: 3GFT). The simulation indicated an additional potential site at position E107 for labeling.

3.1.2 Site-specific protein labeling with cysteine reactive dyes

A crucial feature of the described FRET sensors is the site-specific introduction of a small organic dye directly in the protein fold. For this purpose, cysteine labeling with thiol-reactive dyes proved to be a promising approach. Cysteine displays a unique combination of high nucleophilic reactivity and low natural occurance.[174] Additional advantages are the straight forward introduction of labeling sites through site-directed mutagenesis (2.2.1.3) and the abundance of commercially available thiol-reactive dyes.

However, when using a cysteine mediated labeling strategy, naturally occurring cysteines in the small GTPases and the fluorescent proteins have to be considered. It is crucial for site-specific labeling, that other potentially reactive sites, e.g. native cysteines, do not interfere with labeling. Natural occurring cysteines are rarely surface exposed and therefore exhibit only limited reactivity towards thiol-reactive probes.[175] To overcome these limitations the labeling reaction can be kinetically controlled[176,177] or the potentially interfering amino acids can be removed by site directed mutagenesis. Here these strategies were employed to achieve site-specific maleimide-mediated labeling.

Native cysteines - fluorescent proteins

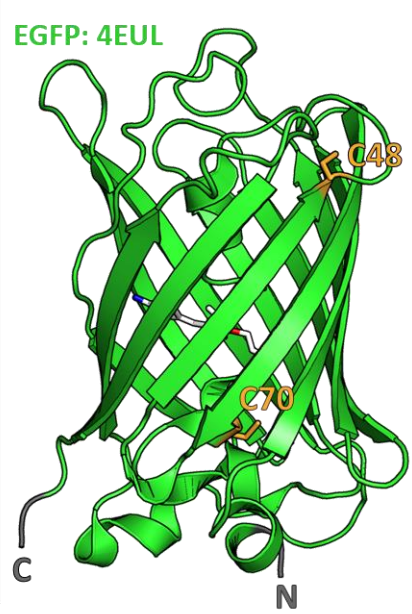

EGFP and mCitrine contain two natural cysteines, one at position 48 and one at position 70.[178,179] C70 is positioned on the inner helix, buried in the β-barrel. Thus, it is less likely to interfere with site-specific labeling. The second cysteine, C48, is located on the third β-strand and partially solvent accessible. It could potentially be modified by thiol-reactive probes. To assess the extent of unspecific labeling at this site, wild type GFP was incubated with a thiol reactive probe under the same conditions used for labeling and the extent of labeling was quantified by SDS-PAGE. Figure 3-4 depicts the position of the two natural occurring cysteines in the crystal structure of EGFP (PDB ID: 4EUL).

Figure 3-4: Cysteine positions in crystal structure of EGFP (PDB ID: 4EUL).
The cysteine residues are highlighted and labeled in yellow. C48 is partially solvent accessible and located on the third β-strand of the barrel structure. C70 is positioned on the inner helix. The chromophore is depicted in white, with oxygen and nitrogen atoms colored in red and blue, respectively.

Native cysteines - Rab1

Wild type Rab1 contains three cysteines, C23 is buried in the protein fold and two surface-exposed cysteines, C200 and C201 located at the very C-terminus (Figure 3-5). The two C-terminal cysteines would interfere with site-specific labeling and are crucial for proper GTPase functioning in the cellular context. These residues have to remain intact to be available for prenylation that facilitates membrane attachment. To preserve these crucial prenylation sites, the Rab1 C-terminus was truncated by two amino acids and genetically fused to an intein. After labeling with the acceptor dye the two cysteines were reintroduced through native chemical ligation (NCL) (2.4.3).

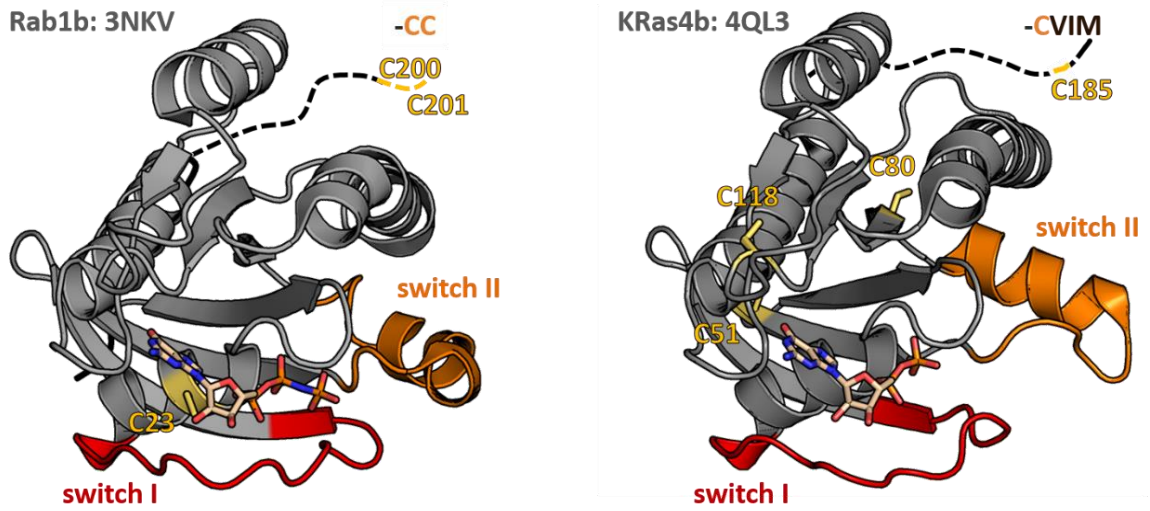

Figure 3-5: Cysteine positions in crystal structure of Rab1 (PDB ID: 3NKV) and KRas4b (PDB ID: 4QL3).
The cysteine residues are highlighted and labeled in yellow. The switch I and II regions are highlighted in red and orange, respectively. The bound guanine nucleotide is depicted in beige with atoms highlighted in red (oxygen), blue (nitrogen) and orange (phosphorous).

Native cysteines - KRas

KRas4b contains three cysteines in the GTPase-fold and a CAAX motif at its C-terminus (Figure 3-5). It has been previously reported that mutations of C51 and C118 to serine and C80 to leucine, respectively, do not alter the GTPase's structure or its ability to be activated through interaction with SOS.[124] Based on this study the natural cysteine residues were removed by site-directed mutagenesis to generate a cysteine free KRas construct. Analogous to Rab1, the C-terminal cysteine was removed by truncating the CAAX motif and later reconstituted through NCL after labeling.

Kinetic labeling of acceptor sites

In general, cysteines at the protein surface have a certain propensity to react with the maleimide probes used to introduce the acceptor dyes. This reactivity however, is not uniform and the differences in reaction velocity can be exploited to achieve site-specific labeling despite multiple reactive sites.

To assess the extent of undesired labeling of natural occurring cysteine residues in the fluorescent proteins, wild type GFP was incubated under the same conditions (2.4.1) as used for labeling the EGFP/mCitrine-tagged sensor constructs (Figure 3-6 A and B).

As indicated by the fluorescent bands in Figure 3-6 B, labeling of GFP was negligible for incubation times of up to 1 h (< 10 %). Even after incubation for 10 h, less than 17 % of the wild type GFP was labeled by the TF3 dye. In contrast, labeling of the cysteine sites identified for acceptor labeling (T34C, S36C, D53C and G54C) was typically completed (>90 %) within 30-60 min (Figure 3-6 C and D) under the same conditions. This is indicated by the saturation of the fluorescence intensity in the SDS-Page (Figure 3-6 C and D).

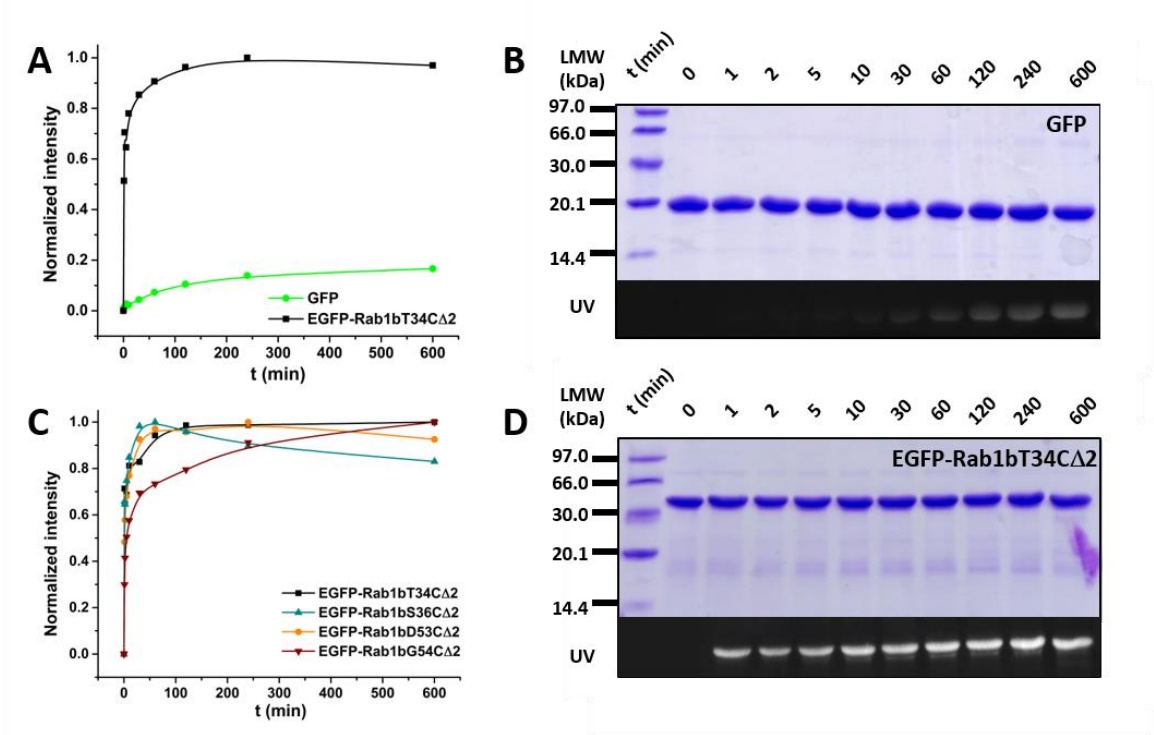

Figure 3-6: Site-specific labeling of EGFP-Rab1 constructs with thiol-reactive dyes.
(A) Quantification of labeling progression for GFP (green) and EGFP-Rab1T34CΔ2 (black) incubated with 1.5 eq Tide Fluor 3 maleimide. **(B)** SDS-PAGE of GFP labeling. The labeling mixture was quenched with β-mercaptoethanol after the indicated incubation times. Upper panel: Coomassie blue staining. Lower panel: excitation with UV light prior to Coomassie staining. **(C)** Quantification of labeling progression for EGFP-Rab1 mutants incubated with 1.5 eq Tide Fluor 3 maleimide. **(D)** SDS-PAGE of EGFP-Rab1T34CΔ2 labeling. Labeling mixture was quenched with β-mercaptoethanol after the indicated incubation times. Upper panel: Coomassie blue staining. Lower panel: excitation with UV light prior to Coomassie staining. For labeling quantification, the relative protein amount was determined from the Coomassie blue stained image using the software ImageJ.

Collectively, these results indicate that tentative acceptor labeling sites can be specifically addressed by maleimide-mediated labeling. Undesired labeling of the fluorescent protein that could interfere with the FRET signal read out or lead to loss of fluorescence from the fluorescent proteins is negligible under the used labeling conditions. Furthermore, the labeling reaction proceeds quickly and efficiently at neutral pH and room temperature, conditions that are beneficial to the overall stability of the protein constructs.

Sensor population is uniformly labeled

As stated previously, site-specific and homogenous labeling of the GTPase sensor is crucial for reliable FRET quantitation. Quantitative labeling in a 1:1 ratio was confirmed through LC-ESI-MS (2.5.4, 5.2) and absorption spectroscopy (Table 3-3, 2.5.2).

The deconvoluted ESI-MS spectra display single peaks for the protein constructs before incubation with the respective acceptor dye. After labeling the peaks shift to a higher mass indicating covalent binding of a single dye moiety (Figure 3-7).

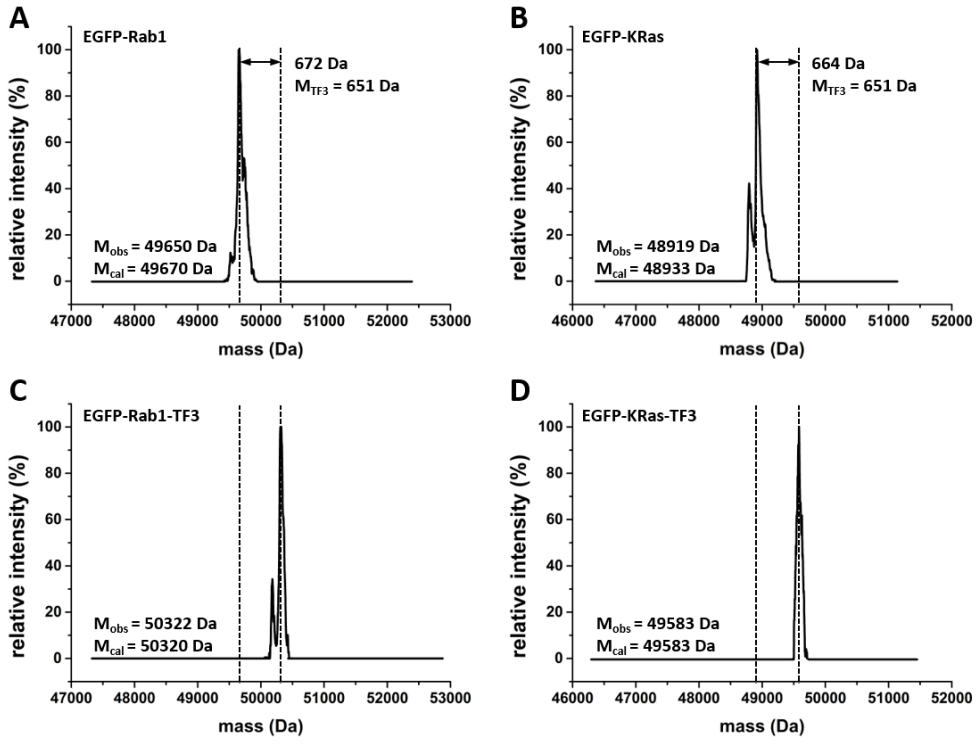

Figure 3-7: ESI-MS of site-specific labeling of GTPase constructs with thiol-reactive acceptor dye.
LC-ESI-MS of **(A)** EGFP-Rab1T34CΔ2-MESNA and **(B)** EGFP-KRasD30CΔ4-MESNA before and after **(C)-(D)** labeling with 1.2 eq Tide Fluor 3 maleimide. M_{obs}: observed weight, M_{cal}: theoretical weight.

Additionally, typical donor to acceptor ratios were determined by absorption spectroscopy (2.5.2). The ratios range around 0.90 to 1.10, indicating an approximately 1:1 ratio of donor to acceptor dye per molecule (Table 3-3). A ratio significantly above 1 would suggest undesired labeling of additional sites, e.g.

natural cysteines in the fluorescent protein or the GTPase. Ratios well below 1 would indicate incomplete labeling of the protein.

Table 3-3: Labeling ratio determined by absorption spectroscopy.

Sensor construct	Labeling site	[EGFP/mCitrine] (mM)	[TF3/TF4] (mM)	Donor/acceptor ratio
EGFP-Rab1-MESNA	T34C	0.0200	0.0183	1.09
	S36C	0.0285	0.0255	1.12
	D53C	0.0174	0.0176	0.99
	G54C	0.0101	0.0119	0.84
	T34C_Q67L	0.0178	0.0195	0.96
EGFP-KRas	D30C	0.0680	0.0650	1.05
	E31C	0.0294	0.0271	1.08
EGFPΔ11-KRas	D30C	0.0210	0.0200	1.05
	E31C	0.2093	0.2208	0.95
mCitrineΔ11-KRas	E31C	0.0540	0.0530	0.98

Collectively, the ESI-MS and absorption spectroscopic data indicate that the sensor population is uniformly and quantitatively labeled with a single acceptor dye.

Sensitized emission spectra of labeled sensor

Labeling progression and energy transfer from the donor to the acceptor fluorophore was confirmed by fluorescence spectra. Spectra collected at different time points during labeling show a time-dependent increase in acceptor emission with concomitant decrease in the donor emission, a characteristic feature of FRET (Figure 3-8 A).

As expected, energy transfer via FRET is more pronounced in constructs with a shorter linker region between the fluorescent protein and the GTPase (Figure 3-8 B). In comparison to the unlabeled donor only probes, the FRET constructs exhibit a significantly increased acceptor emission while donor emission is strongly reduced.

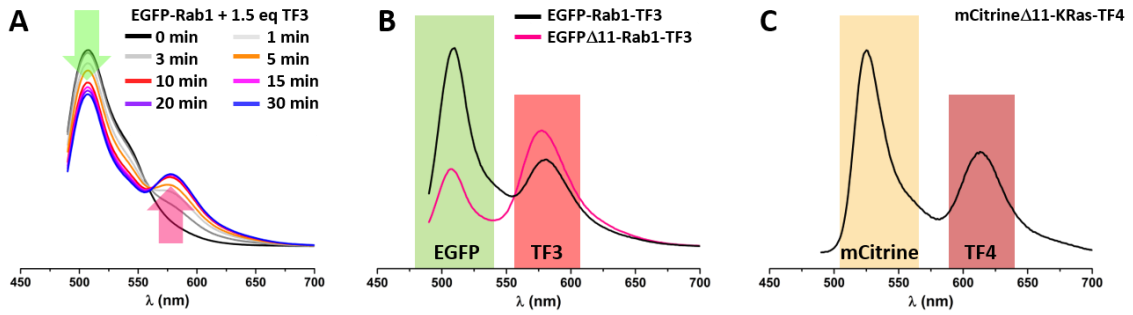

Figure 3-8: Fluorescence spectra of FRET sensor constructs.
(A) Fluorescence spectra of 200 nM EGFP-Rab1T34C incubated with 300 nM Tide Fluor 3 maleimide collected at indicated time points. **(B)** Overlay of spectra of 200 nM EGFP-Rab1T34C-TF3 (black) and 200 nM EGFPΔ11-Rab1T34C-TF3 (pink). **(C)** Spectrum of 200 nM mCitrineΔ11-KRasD30C-TF3. Fluorescence spectra were obtained with excitation set to 480 nm and emission collected at 490-700 nm.

3.1.3 Native chemical ligation for C-terminal reconstitution

Prenylation of C-terminal cysteine residues is a critical feature for proper GTPase functioning in cells. These lipid moieties are crucial for membrane attachment and the subcellular localization of the small GTPases. Furthermore, correct prenylation is essential for the interaction with regulators such as RabGDI.[180] After labeling, the truncated C-terminal amino acids were reintroduced by NCL[181] (2.4.3) to reconstitute full functionality.

To this end the truncated GTPase was genetically fused to an intein domain. After purification (2.3) the protein constructs were obtained with a C-terminal MESNA-thioester (2.3). The thioester-moiety is unreactive towards thiol-reactive dyes, e.g. maleimides, but can undergo efficient NCL with peptides that carry an N-terminal cysteine. For NCL the proteins were transferred into thiol-free labeling buffer, concentrated and mixed with thiol-free buffer containing MPAA, TCEP and the appropriate small peptide, -CC for Rab1 or -CVIM for KRas constructs respectively. Finally, the NCL mixture was incubated overnight on ice (Figure 3-9, for a detailed protocol see 2.4.3).

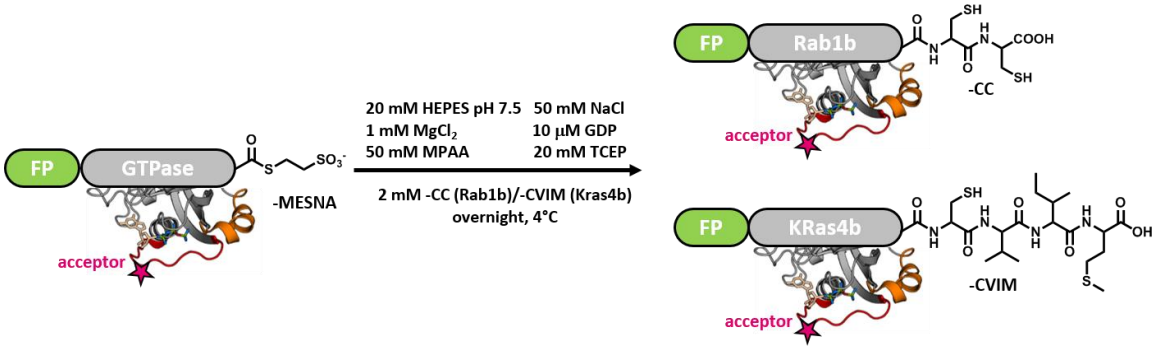

Figure 3-9: Scheme of native chemical ligation for reconstituting GTPases's C-terminus.
The C-terminal amino acids, -CC (Rab1) and -CVIM (KRas4b) were ligated with the GTPase thioester constructs through NCL as described in 2.4.3. Fluorescent protein (green), GTPase (gray): switch I (red), switch II (orange), acceptor labeling site (pink). Chemical structures are drawn for C-terminal thioester moiety (-MESNA) and amino acids (-CC, -CVIM) respectively.

Successful conversion to the full length GTPase was confirmed by LC-ESI-MS (Figure 3-10, 2.5.4 and 0). The observed shift to a higher mass in the deconvoluted ESI-MS spectra suggest ligation with the C-terminal cysteine motifs -CC or –CVIM, respectively.

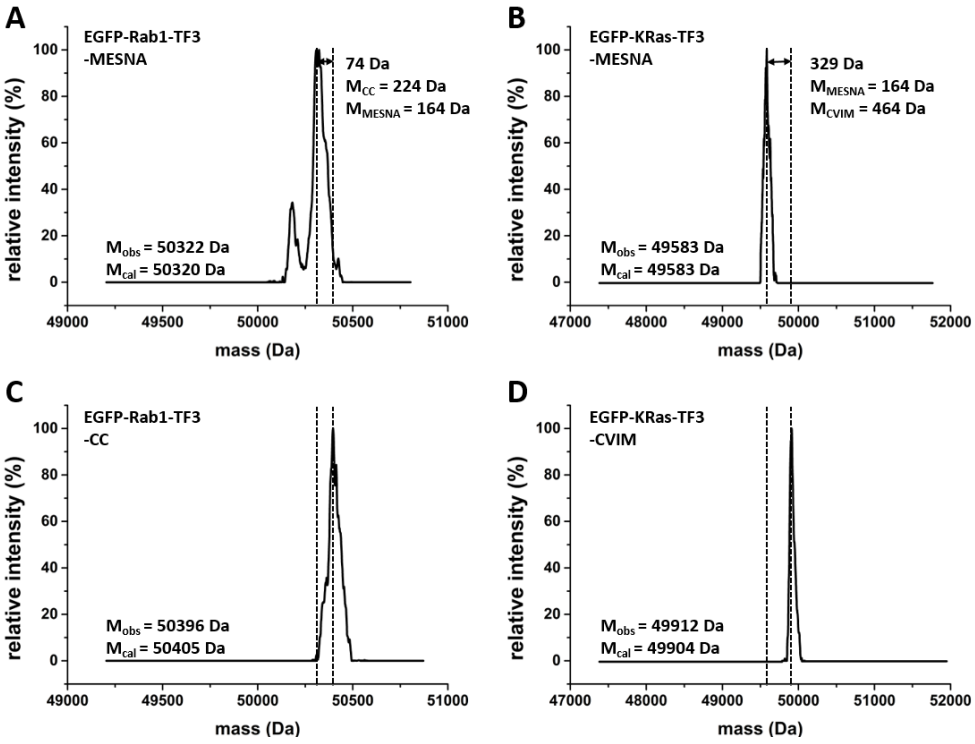

Figure 3-10: ESI-MS spectra of GTPase-thioesters and NCL products.
LC-ESI-MS of **(A)** EGFP-Rab1T34C-TF3-MESNA and **(B)** EGFP-KRasD30C-TF3-MESNA before and **(C)** EGFP-Rab1T34C-TF3-CC, **(D)** EGFP-KRasD30C-TF3-CVIM after NCL with reconstituted C-terminus. M_{obs}: observed weight, M_{cal}: theoretical weight.

3.1.4 Rab1 FRET sensor - GEF-mediated nucleotide exchange

The Rab1 sensor's sensitivity towards its nucleotide binding state was initially tested by GEF-mediated nucleotide exchange. Besides evaluating the response in regard to dynamic range and sensitivity, the interaction with the respective GEF was compared to the wild type protein to assess possible effects of the introduced modifications.

For Rab1, the GEF domain of the *Legionella pneumophila* GEF $DrrA_{340-533}$[71,78,182] (referred to as DrrA or $DrrA_{340-533}$) was used to characterize the sensors response to GDP to GTP exchange by fluorescence spectroscopy as described in 2.5.4.2. Nucleotide exchange was initiated through addition of varying amounts of $DrrA_{340-533}$ to 200 nM Rab1 sensor in the presence of 100 μM GTP. The change in FRET efficiency was monitored by sensitized emission. The donor EGFP was excited at 480 nm and the acceptor emission of Tide Fluor 3 was detected at 580 nm (2.5.4.2).

Previous studies utilizing mant-labeled nucleotides[71] or the intrinsic Rab1 tryptophan fluorescence[183], reported that the nucleotide exchange rate increased dramatically upon $DrrA_{340-533}$ addition (Figure 3-11 A, B and C). Here, this is indicated by the drop or increase in FRET signal. After the fluorescence signal is saturated, indicating completion of nucleotide exchange, further addition of $DrrA_{340-533}$ or GTP does not result in any further signal changes (Figure 3-11 A, B, C and Appendix).

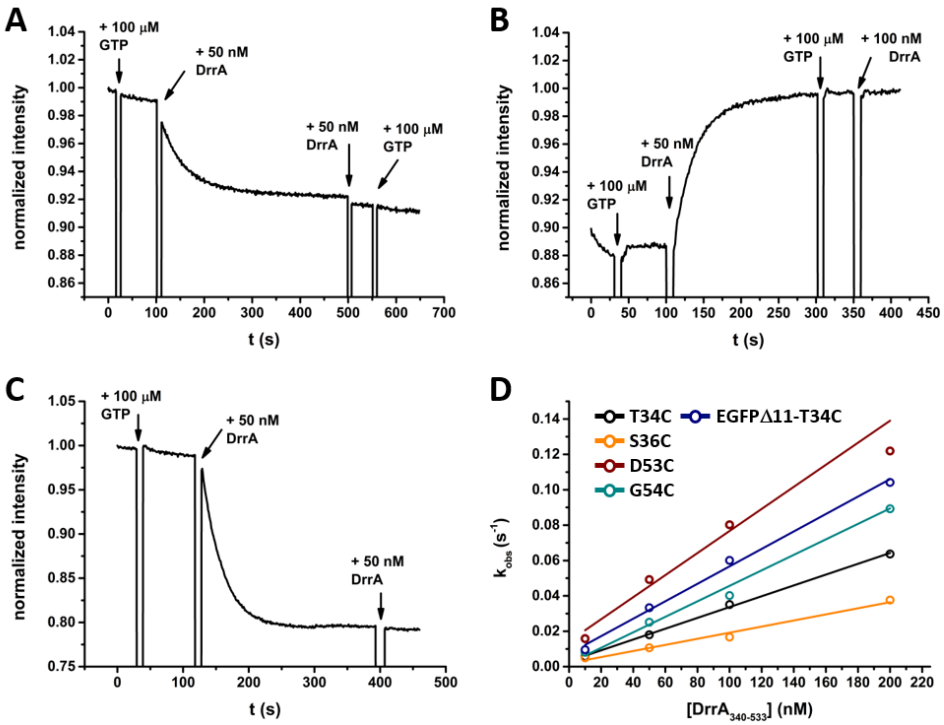

Figure 3-11: Rab1 FRET sensors are sensitive to DrrA-mediated nucleotide exchange.
Addition of 100 µM GTP and 50 nM $DrrA_{340-533}$ to **(A)** 200 nM GDP-bound EGFP-Rab1T34C-TF3 **(B)** 200 nM GDP-bound EGFP-Rab1G54C-TF3 and **(C)** EGFPΔ11-Rab1T34C-TF3 results in a steep decrease (T34C and Δ11-T34C) or increase (G54C) of the detected sensitized emission signal. Changes in FRET efficiency were observed by sensitized emission with donor excitation at 480 nm and acceptor emission collected at 580 nm. **(D)** By plotting k_{obs} against [$DrrA_{340-533}$] the catalytic efficiency can be extracted as the slope of a linear fit. Obtained k_{cat}/K_M values are summarized in Table 3-4.

The changes in FRET signal were fitted with a single exponential function (Eq. 2-8) to obtain the observed first order rate constants k_{obs}. As described in 2.5.4.2, the catalytic efficiency for the GEF mediated nucleotide exchange reaction can be extracted as the slope of a linear fit of k_{obs} plotted against the GEF concentration (Figure 3-11 D, Eq. 2-7). The obtained catalytic efficiencies and the observed relative changes of the fluorescence signal are summarized in Table 3-4.

Table 3-4: Catalytic efficiencies and dynamic range for DrrA-mediated nucleotide exchange.

Sensor construct	Labeling site	k_{cat}/K_M $(M \cdot s)^{-1}$	ΔI_{SE} (%)
EGFP-Rab1-MESNA	T34C	$(3.06 \pm 0.08) \times 10^5$	-9
	S36C	$(1.73 \pm 0.02) \times 10^5$	-10
	D53C	$(5.4 \pm 0.6) \times 10^5$	+9
	G54C	$(4.2 \pm 0.3) \times 10^5$	+11
EGFPΔ11-Rab1-MESNA	T34C	$(4.9 \pm 0.2) \times 10^5$	-21
Rab1wt[183,184]	-	2×10^5	-

The obtained catalytic efficiencies for the sensor constructs are in good agreement with the previously reported value wild type Rab1[71,183]. This indicates that the interaction between $DrrA_{340-533}$ and the modified Rab1 is not significantly impaired by the implemented modifications.

While the crystal structure of Rab1 in complex with $DrrA_{340-533}$ [185] shows that the P-loop, switch I and II and the interswitch regions of the GTPase are involved in crucial interactions with the GEF-domain (Figure 3-12), mutation and labeling at switch I did not have a marked effect on DrrA-mediated nucleotide exchange. For comparison, AMPylation at Y77[186] and phosphocholination at S76[183] in the switch II region of Rab1 lead to a drop in the catalytic efficiency for DrrA-mediated nucleotide exchange by 3- and 5-fold, respectively.

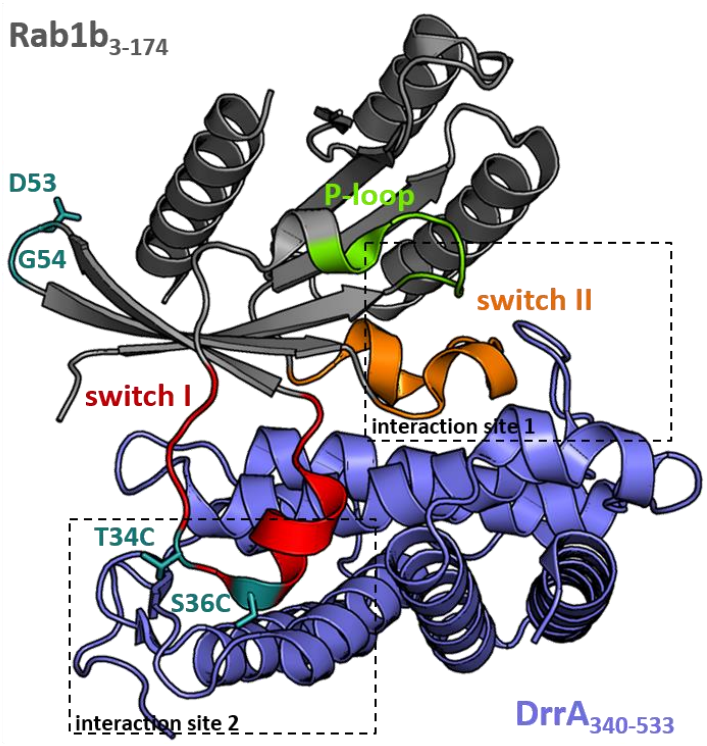

Figure 3-12: Crystal structure of nucleotide free $Rab1_{3-174}$ in complex with $DrrA_{340-533}$ (PDB ID: 3JZA).
The Rab1 structure is shown in gray and DrrA is colored in purple. The Rab1 labeling sites are highlighted and labeled in turquoise. The switch I and II regions are colored in red and orange respectively The P-loop is marked in green.
DrrA forms contacts with Rab1 at two primary interaction sites. These interactions open the GTPase's nucleotide binding pocket, thereby facilitating the release of the bound nucleotide.
At interaction site 1, DrrA contacts the P-loop and switch II region of Rab1. At the second interface DrrA binds to the switch I region and completely distorts the nucleotide binding pocket. Some switch I residues are displaced by ~30 Å. The acceptor labeling positions T34 and S36 lie directly in this interface. The complex structure reveals direct and water mediated polar interactions between the Rab1 residues T34 and S36 with DrrA.[71]

In contrast, the catalytic efficiencies for $DrrA_{340-533}$-mediated nucleotide exchange of the acceptor labeled Rab1 constructs are slightly higher than the values reported for nucleotide exchange of unmodified Rab1.[71,183] Possibly mutation and labeling reduce the GTPase's affinity towards the bound nucleotide, thereby accelerating the GEF-mediated nucleotide exchange.

All four tested Rab1 sensor constructs displayed an overall change in sensitized emission signal of about 9-10 %. It is of interest to note that the fluorescence signal upon nucleotide exchange decreased for the switch I acceptor constructs T34C and S36C but showed an increase for the interswitch mutants D53C and G54C (Table 3-4). A drop in the sensitized emission signal, as observed for the switch I mutants, indicates reduced FRET efficiency upon nucleotide exchange from GDP to GTP. A possible cause for the decrease in FRET could be the more rigid conformation of the switch I region in the GTP-bound state. The more defined structure might force the acceptor dye to adopt a position less favorable for efficient energy transfer.

The FRET sensor reports on both directions of nucleotide exchange. The initial fluorescence signal is partially restored after addition of excess GDP to GTP-bound Rab1 in the presence of DrrA (Figure 3-13 A and B). Two factors attribute to only a partial recovery of the initial fluorescence intensity: Firstly, GEFs act as general

catalyst for nucleotide exchange. As the initially added GTP is still present, the GEF accelerates the establishment of the Rab:GDP/GTP equilibrium. Secondly, the nucleotides exhibit an 'inner filter effect' (loss of fluorescence due to absorption of excitation light) resulting in reduced overall emission. This is especially relevant for measurements with high concentrations of nucleotides present.

When GDP instead of GTP is added to the GDP-bound Rab1 sensor in presence of the GEF, the FRET signal does not change (Figure 3-13 C). These findings further confirm that the observed signal changes upon addition of $DrrA_{340-533}$ and GTP are indeed directly linked to nucleotide-binding state of the GTPase and are not caused by the GTPase-GEF interaction.

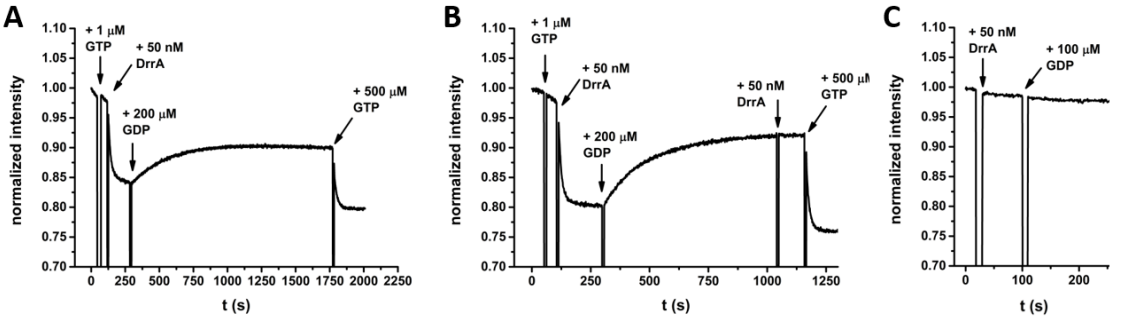

Figure 3-13: FRET sensor is specific and sensitive to GEF-mediated nucleotide exchange.
Addition of increasing amounts of GTP and GDP in turns to 50 nM $DrrA_{340-533}$ and **(A)** 200 nM GDP-bound EGFP-Rab1T34C-TF3 or **(B)** 200 nM GDP-bound EGFPΔ11-Rab1T34C-TF3 respectively. The observed initial signal change upon GDP to GTP exchange is reversed through addition of excess GDP. **(C)** Addition of 50 nM DrrA340-533 and 100 mM GDP to 200 nM EGFP-Rab1S36C-TF3 does not result in FRET signal change. Changes in FRET efficiency were observed by sensitized emission with excitation at 480 nm and emission collected at 580 nm.

Analogous experiments were performed using the sensor constructs featuring a shorter linker region variant (3.1.1). Compared to the initial construct the dynamic range increased from 9 % to 20 %, while maintaining similar values for the catalytic efficiency for the GEF-mediated nucleotide exchange (Table 3-4, Figure 3-11). The increased dynamic range can be attributed to the shortened distance between the donor and acceptor fluorophore. In this construct, the distance of the FRET pair is closer to R_0 where $E_{FRET} = 0.5$ and the response of FRET to distance is maximal (1.2.1).

However, DrrA is not the physiological GEF for Rab1 in mammalian cells and thus these experiments can only suggest preserved GTPases regulation *in vivo*. The native GEF in eukaryotes for Rab1 activation is the multisubunit Transport Protein Particle (TRAPP) complex. The catalytic efficiency of the bacterial protein DrrA is about 150-fold higher than for the TRAPP complex ($k_{cat}/K_M = 1 \cdot 10^3$ $(M \cdot s)^{-1}$)[75].

In the Rab1:Drra and the Rab1:TRAPP complex, the two labeling sites in the switch I region of the GTPase (T34 and S36) lie in close proximity to the GTPase-GEF interface as can be judged from the crystal structures (Figure 3-12 and Figure 3-14). More specifically, the YPT1 switch I residues 37–45 directly contact the C-terminus of Bet3-A. However, residues T34 and S36 are not resolved in the crystal structure, indicating conformational flexibility.[67]

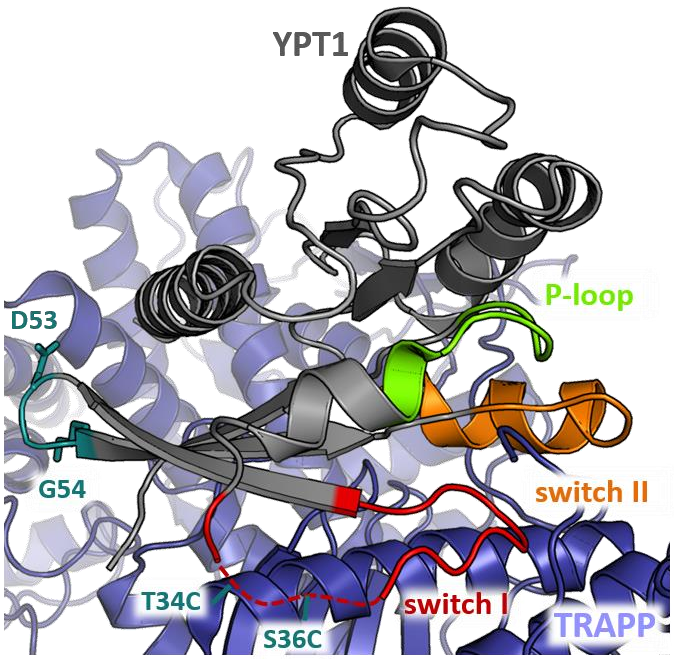

Figure 3-14: Crystal structure of nucleotide free YPT1 in complex with a TRAPP subassembly (PDB ID: 3CUE)[67].
The YPT1 structure is colored in gray and the TRAPP subunits directly interacting with the GTPase are shown in purple. The corresponding labeling sites are highlighted and labeled in turquoise. The switch I and II regions are colored in red and orange respectively The P-loop is marked in green.
The TRAPP complex forms its primary contacts with YPT1 at the central β-sheet as well as at the switch I and II, and the P-loop. Similar to DrrA, these interactions distort the nucleotide binding pocket thereby facilitating the release of the bound nucleotide.
The acceptor labeling positions T34 and S36 lie in the Bet3-A-switch I interface yet there exact positions are not resolved in the complex structure, indicating a certain degree of flexibility. D53 and G54 are facing away from the interacting surface.

Similar to the Rab1-DrrA complex, the interswitch labeling sites at D53 and G54 are facing away from the binding site and should therefore have no significant impact on the GTPase-GEF contact. Based on the aforementioned structural similarities, the endogenous GEF activity should be largely retained towards the Rab1 constructs.

3.1.5 Rab1 FRET sensor - GAP-induced GTP hydrolysis

GTPase-activating proteins (GAPs) are the regulatory counterpart of GEFs. GAPs attenuate GTPase signaling by accelerating the slow intrinsic GTPase activity. The bound GTP is hydrolyzed to GDP, thereby converting the "active" GTP-bound Rab1 to its "inactive" GDP-bound complement. To ensure full biological functionality of the Rab1 constructs, GTP-hydrolysis mediated by the GAP domain of TBC1D20 ($TBC1D20_{1-362}$, (Tre-2, Bub2, and Cdc16)) was examined by monitoring the FRET signal change through fluorescence spectroscopy (2.5.4.2).

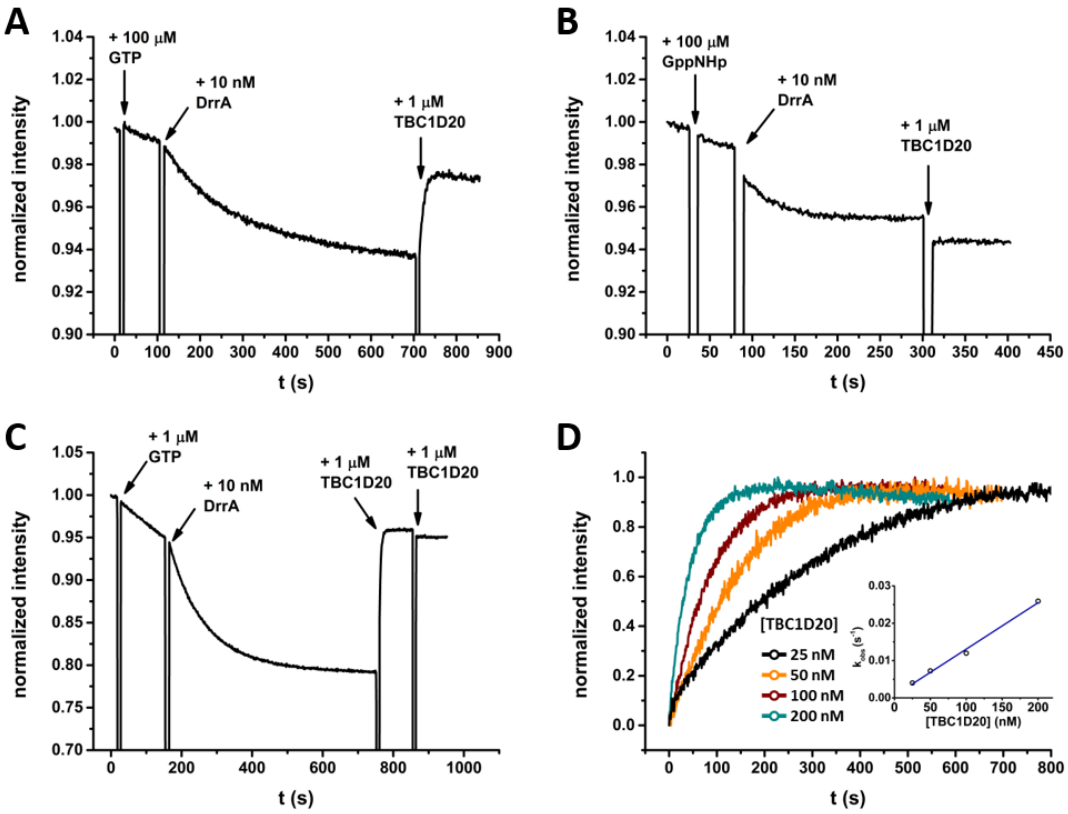

Figure 3-15: Rab1 FRET sensor reports on TBC1D20 induced GTP hydrolysis.
(A) Addition of 1 µM $TBC1D20_{1-362}$ to 200 nM GTP-bound EGFP-Rab1T34C-TF3 restores the initial FRET signal intensity. **(B)** Addition of 1 µM $TBC1D20_{1-362}$ to 200 nM GppNHp-bound EGFP-Rab1T34C-TF3 fails to reverse the initial FRET signal drop. **(C)** Addition of 1 µM $TBC1D20_{1-362}$ to 200 nM GTP-bound EGFPΔ11-Rab1T34C-TF3 restores the initial FRET signal intensity. Subsequent addition of TBC1D20 does not yield further changes in fluorescence signal. **(D**) The observed rate constant of GTP hydrolysis depends on $TBC1D20_{1-362}$ concentration. **(Inset)** By plotting k_{obs} against [$TBC1D20_{1-362}$] the catalytic efficiency can be extracted as the slope of the linear fit (solid blue line). Changes in FRET efficiency were observed by sensitized emission with excitation at 480 nm and emission collected at 580 nm.

To this end, 200 nM Rab1 sensor was incubated with 10 nM $DrrA_{340-533}$ in the presence of 100 µM GTP. The exchange of bound GDP for GTP to GTP was followed by sensitized emission until completion. GAP-mediated hydrolysis of the Rab1-bound GTP was then initiated through addition of excess $TBC1D20_{1-362}$. The initial FRET signal intensity is restored (Figure 3-15 A and C) through the GAP induced GTP hydrolysis. This converts

"active" GTP-bound Rab1 to "inactive" GDP-bound GTPase restoring the initial nucleotide state of the Rab1 sensor.

For the T34C sensor the changes in FRET signal for varying amounts of $TBC1D20_{1-362}$ were fitted with a single exponential function (Eq. 2-8) to obtain the respective observed first order rate constants k_{obs}. The catalytic efficiency for the GAP-induced GTP hydrolysis were then extracted as the slope of a linear fit of k_{obs} plotted against the $TBC1D20_{1-362}$ concentration (Figure 3-15 D).

To compare the measured catalytic efficiency with the properties of the unmodified GTPase, a similar experiment was performed using mantGTP loaded Rab1 (Figure 5-10 E and F). In comparison to wild type Rab1 (k_{cat}/K_M = (2.8 ± 0.4)·10^5 $(M{\cdot}s)^{-1}$), the catalytic efficiency observed for EGFP-Rab1T34C-TF3 (k_{cat}/K_M = (1.2 ± 0.07)·10^5 $(M{\cdot}s)^{-1}$) is reduced by a factor of 2.3. For comparison, AMPylation at Y77 and phosphocholination at S76 in the Rab1 switch II region lead to a reduction in k_{cat}/K_M for TBC1D20-induced GTP-hydrolysis by 20- and 4-fold, respectively.[183,186]

The available crystal structure of the Rab1-TBC1D20 complex indicates that S36 is directly involved in the GTPase-GAP interaction (Figure 3-16).[41] Furthermore, the structural data confirms that the residues modified for acceptor labeling are not directly involved in nucleotide hydrolysis.

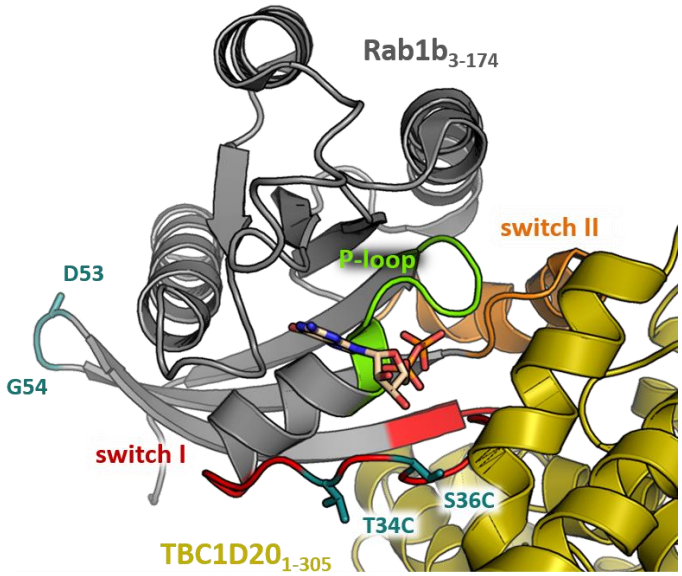

Figure 3-16: Crystal structure of $Rab1_{3-174}$:GDP in complex with $TBC1D20_{1-305}$ (PDB ID: 4HLQ).[41]
The Rab1 structure is shown in gray and TBC1D20 is colored in yellow. The Rab1 labeling sites are highlighted and labeled in turquoise. The switch I and II regions are colored in red and orange respectively The P-loop is marked in green. The bound guanine nucleotide is depicted in beige with atoms highlighted in red (oxygen), blue (nitrogen) and orange (phosphorous).
TBC1D20 forms direct contacts with the nucleotide and binds to the switch I and II and the P-loop of Rab1.
From the four acceptor labeling sites, only S36 lies directly in the GTPase-GAP interface. T34C, D53 and G54 are facing away from the interacting surface.

To further ascertain that the observed FRET responses are indeed caused by GAP induced GTP hydrolysis, the experiments were repeated using the non-hydrolysable GTP analog GppNHp (Figure 3-15 B). As expected, in this case $TBC1D20_{1-362}$ failed to reverse the FRET signal change in all Rab1 constructs (Figure 5-10). Collectively, these experiments demonstrate that the constructs serve as efficient FRET sensors for Rab1 activation and deactivation while largely preserving the proteins interaction with its regulatory partners, GEFs and GAPs.

3.1.6 Rab1 FRET sensor - effector binding

Interaction with effector proteins is another hallmark of GTPase function. Effector proteins discriminate between the two nucleotide states of the GTPases through interaction with the proteins switch regions. Most importantly, GTP locks the switch regions in a well-defined, ordered state.[12] This GTP-induced conformation preforms the GTPase's structure in the GTPase:effector complex, resulting in a higher affinity of the effector to the GTP-bound form.

To confirm that the introduced modifications on Rab1 do not interfere with native effector binding, the interactions of GTP-bound Rab1 constructs with the Rab-binding domains of OCRL1 ($OCRL1_{539–901}$)[187] and the *Legionella pneumophila* effector LidA ($LidA_{201-583}$)[184] were examined. To this end, the dissociation constants (K_D) were determined by equilibrium titration using sensitized emission and fluorescence polarization (2.5.4.3). Increasing amounts of the effector domain were titrated to a fixed concentration of Rab1 sensor (100-500 nM). The resulting changes in FRET signal (S36, D53 and G54) or fluorescence polarization (T34C) were plotted against the concentration of titrant and the K_D was extracted by fitting with the quadratic equation Eq. 2-11 as described in section 2.5.4.3.

It should be noted, that in contrast to the transient interaction with GEFs and GAPs in the experimental setups described here, GTP-bound Rab1 forms a stable complex the effector domains. Thus, binding of the effector proteins may also affect the FRET signal. Indeed, changes in the FRET signal were observed for all Rab1 constructs and upon binding of both effector proteins with the exception of the T34C construct binding to OCRL.

OCRL1

Initially, the effect of $OCRL1_{539–901}$ binding to the Rab1 constructs was examined through sensitized emission. The observed maximal changes in fluorescence signal and obtained K_D values are summarized in Table 3-5. Interestingly, a significant drop in FRET signal (10-12 %) is observed upon OCRL1 binding for S36C, D53C and G54C, but not for the T34C construct (Figure 3-17). Fluorescence spectra collected before and after effector binding showed an increase in donor emission with concomitant decrease in acceptor emission, a characteristic feature for changes in FRET efficiency (Figure 3-17 B inset and Figure 5-11). To exclude that the lack of signal change for T34C was caused by impeded effector binding, the titration experiment was repeated using fluorescence polarization (Table 3-5, Figure 5-11). In this case, OCRL1 binding was detected as an increase in polarization of the EGFP fluorescence signal.

Table 3-5: K_D valued determined for binding od Rab1 sensor with Rab-binding domains of OCRL1 and LidA.

Labeling site	$OCRL1_{539–901}$		$LidA_{201-583}$	
	ΔI (%)	K_D (μM)	ΔI (%)	K_D (nM)
T34C	-	4.9 ± 0.8*	-30	< 10
S36C	-12	1.5 ± 0.3	-20	< 10
D53C	-10	2.2 ± 0.4	-23	< 10
G54C	-11	2.9 ± 0.7	-24	< 10

*determined by fluorescence polarization

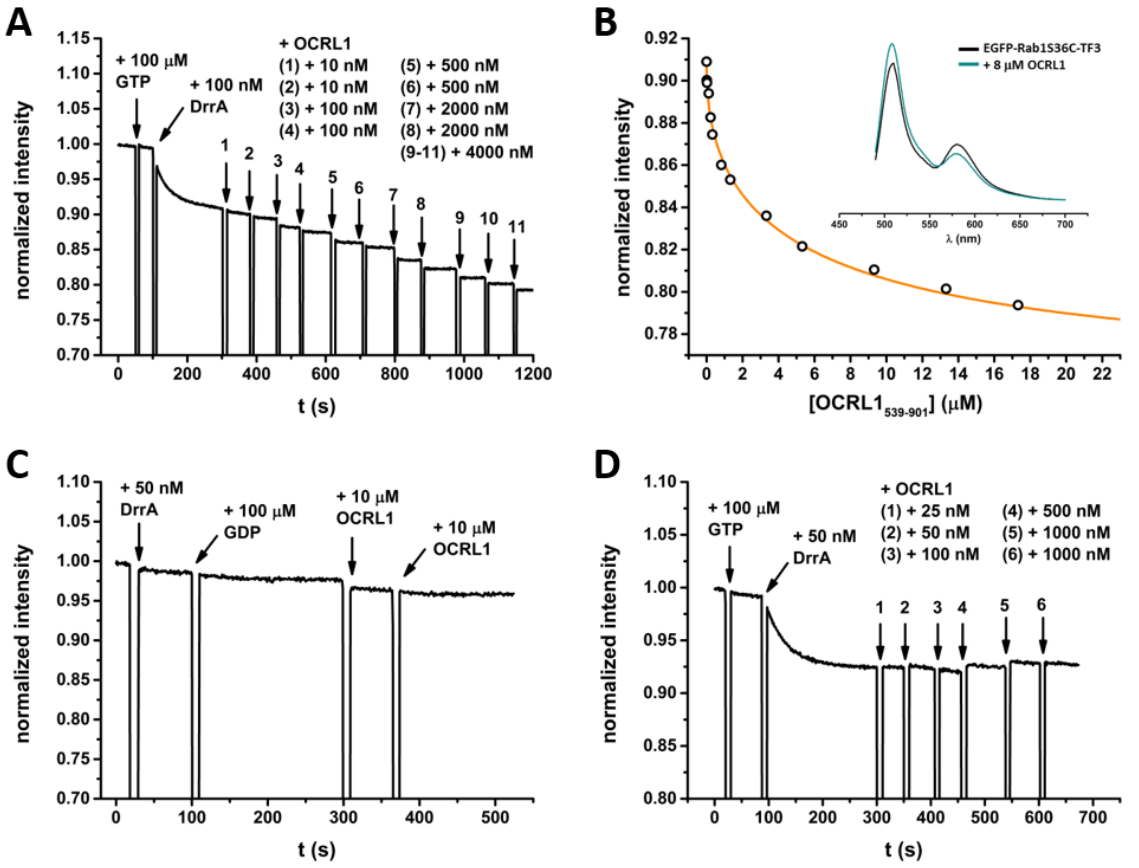

Figure 3-17: Titration of increasing amounts of OCRL1 to Rab1 FRET sensor constructs.
(A) After nucleotide exchange trough addition of 100 nM $DrrA_{340-533}$ and 100 μM GTP, increasing amounts of $OCRL1_{539–901}$ were added to 200 nM GTP-bound EGFP-Rab1S36C-TF3. **(B)** By plotting the change in fluorescence against the effector protein concentration, K_D can be obtained through fitting with a quadratic equation as described in in 2.5.4.3 (solid orange line). **(Inset)** Fluorescence spectra of EGFP-Rab1S36C-TF3 before (solid black line) and after (solid blue line) binding of $OCRL1_{539–901}$. **(C)** Addition of $OCRL1_{539–901}$ to 200 nM GDP-bound EGFP-Rab1S36C-TF3 does not lead to significant changes in the fluorescence signal. **(D)** Addition of increasing amounts of $OCRL1_{539–901}$ to 200 nM GTP-bound EGFP-Rab1T34C-TF3 does not lead to significant changes in the fluorescence signal. Changes in FRET efficiency were observed by sensitized emission with excitation at 480 nm and emission collected at 580 nm. Fluorescence spectra were obtained with excitation set to 480 nm and emission collected from 490-700 nm.

The obtained dissociation constants for $OCRL1_{539–901}$ binding are in good agreement with the previously reported value of 3.7 μM for wild type Rab1.[187] The S36C, D53C and G54C constructs display a slightly lower K_D (1.5-2.9 μM), while the K_D for T34C is slightly increased (4.9 μM, obtained through fluorescence

polarization). Furthermore, OCRL1 did not bind to a GDP-bound Rab1 sensor, confirming effector binding only to the active, GTP-bound sensor (Figure 3-17 B and C). This specificity towards the active state is an essential feature of the native Rab-effector interaction.

The crystal structure of Rab8 in complex with OCRL supports the observation that the chosen labeling sites in the switch I and the interswitch region do not compete with effector binding (Figure 3-18).[187] While OCRL forms contacts with the switch I, switch II and the interswitch region of Rab8, the residues corresponding to the acceptor labeling sites T34, S36, D53 and G54 in Rab1 are not directly involved in effector binding.

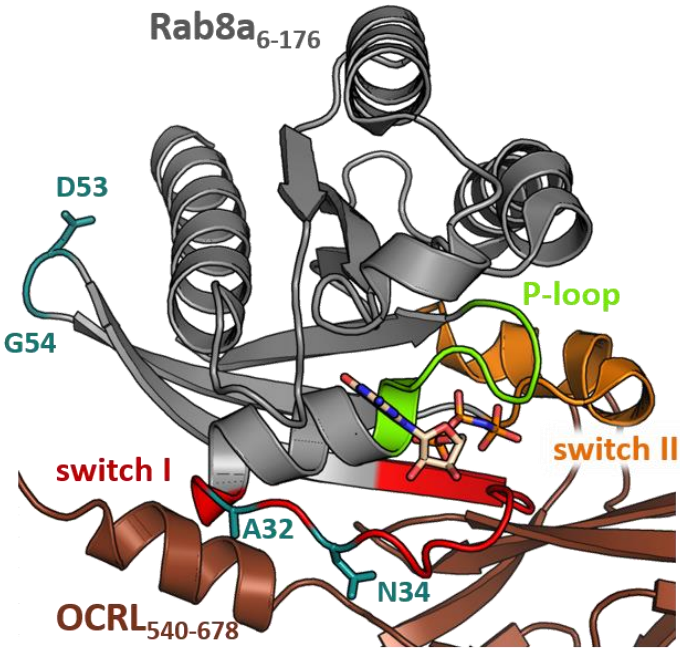

Figure 3-18: Crystal structure of Rab8a$_{6-176}$:GppNHp in complex with OCRL$_{540-678}$ (PDB ID: 3QBT).[187]
The Rab8 structure is shown in gray the OCRL structure is colored in brown. The labeling sites corresponding to T34, S36, D53 and G54 in Rab1 are highlighted and labeled in turquoise. The switch I and II regions are colored in red and orange respectively. The P-loop is marked in green. The bound guanine nucleotide is depicted in beige with atoms highlighted in red (oxygen), blue (nitrogen) and orange (phosphorous).
OCRL forms direct contacts with the switch I and II and the interswitch region of Rab8.
None of the four acceptor labeling sites lie in the GTPase-effector interface.

The primary interactions are mediated by E30, I41-I43 in the switch I and F45-T49 in the interswitch region, as well as R89, F70 and Y77 in the switch II region of the GTPase. The interswitch labeling positions at D53 and G54 are located on the opposite side of the Rab1-effector interface.

LidA

In addition to binding of the human effector protein OCRL, the interaction of the bacterial ”supereffector” LidA ($LidA_{201-583}$) with the Rab1 FRET sensor was characterized.[184]

Upon addition of LidA, all sensor constructs showed a 20 to 30 % decrease in FRET signal (Figure 3-19 and Table 3-5). In line with previous reports, the obtained dissociation constants are well below 10 nM. The exceptionally high affinity of LidA towards Rab1 prevents a more accurate assessment of the K_D by fluorescence titration.[184] In contrast to the typical nucleotide dependent binding of effector proteins, LidA binds to both GDP- and GTP-bound Rab1 with high affinity (Figure 3-19 and Figure 5-12). Due to this promiscuous binding behavior LidA was termed to be a Rab “supereffector”.[184]

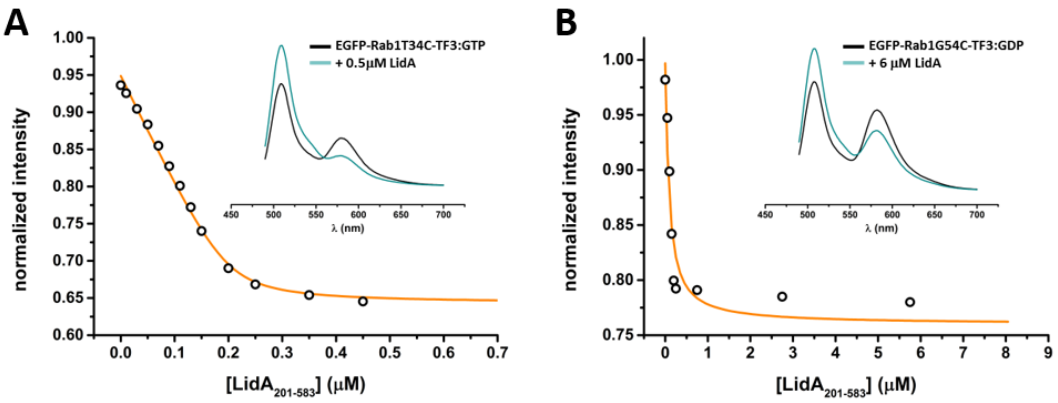

Figure 3-19 : Titration of increasing amounts of LidA to Rab1 FRET sensor constructs.
After nucleotide exchange trough addition of 100 nM $DrrA_{340-533}$ and 100 μM GTP, increasing amounts of $LidA_{201-583}$ were added to **(A)** 200 nM GTP-bound EGFP-Rab1T34C-TF3. By plotting the change in fluorescence against the effector protein concentration, K_D can be obtained through fitting with a quadratic equation as described in in 2.5.4.3 (solid orange line). **(Inset)** Fluorescence spectra of EGFP-Rab1T34C-TF3:GTP before (solid black line) and after (solid blue line) binding of $LidA_{201-583}$. After addition of 100 nM $DrrA_{340-533}$ and 100 μM GDP, increasing amounts of $LidA_{201-583}$ were added to **(B)** 200 nM GDP-bound EGFP-Rab1G54C-TF3. **(Inset)** Fluorescence spectra of EGFP-Rab1G54-TF3:GDP before (solid black line) and after (solid blue line) binding of $LidA_{201-583}$. Original titration data can be found in 0. Changes in FRET efficiency were observed by sensitized emission with excitation at 480 nm and emission collected at 580 nm. Fluorescence spectra were obtained with excitation set to 480 nm and emission collected from 490-700 nm.

Possible detrimental effects of the sensor modifications on LidA binding would probably be masked by the exceptionally high affinity of the effector towards Rab1. This is in keeping with the observation by Schoebel *et.al.* that AMPylation of the protein at residue Y77, located directly in the interaction interface, did not affect LidA binding to the extent that the binding affinity could be quantified accurately.[184]

Crystal structures of LidA in complex with Rab8[184] and Rab1[188] reveal an extraordinarily large GTPase-effector binding interface. The acceptor labeling sites in the switch I and the interswitch regions in Rab1 are not involved in LidA binding (Figure 3-20). Residues D53 and G54 are facing away from the Rab1-LidA contacting sites.

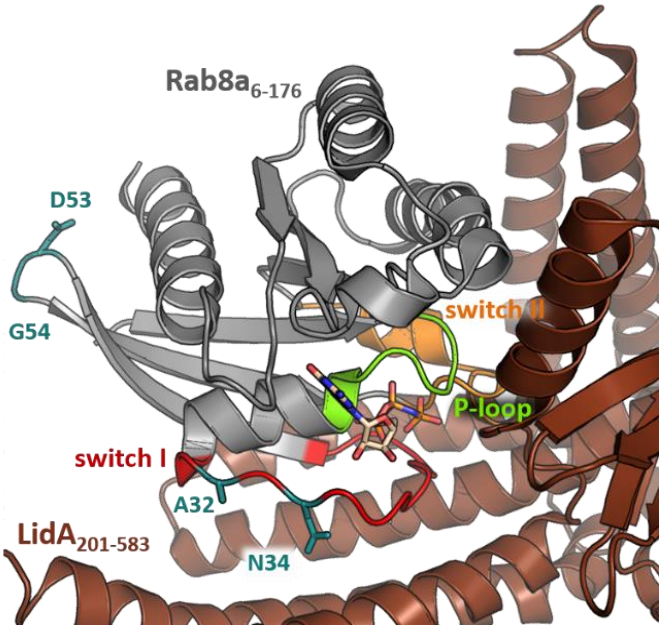

Figure 3-20: Crystal structure of Rab8a$_{6-176}$:GppNHp in complex with LidA$_{201-583}$ (PDB ID: 3TNF).[184]
The Rab8 structure is shown in gray, the LidA structure is colored in brown. The labeling sites corresponding to T34, S36, D53 and G54 in Rab1 are highlighted and labeled in turquoise. The switch I and II regions are colored in red and orange respectively. The P-loop is marked in green. The bound guanine nucleotide is depicted in beige with atoms highlighted in red (oxygen), blue (nitrogen) and orange (phosphorous).
LidA forms direct contacts with the switch I and II and the interswitch region of Rab8.
None of the four acceptor labeling sites clash with the bound effector.

In summary the tested Rab1 constructs are effective reporters of their nucleotide state and effector binding while largely maintaining their native interactions with GEFs, GAPs and effector proteins.

General considerations

The common binding mode of effector proteins with GTPases involves interactions with the switch I, switch II and the interswitch region.[8] The conformational state of these regions convey the protein's nucleotide binding state, e.g. if the GTPase is in the active, GTP-bound or in the inactive, GDP-bound configuration. The effector proteins tested in this thesis included the human effector OCRL1 which exhibits the quintessential effector behavior by discriminating between the GDP- and the GTP-bound GTPase and the *Legionella* effector LidA which displays exceptional Rab-binding properties by binding to both, the GDP and GTP-bound GTPase with high affinity (K_D < 10 nM). Binding of both effector proteins was not significantly affected by the modification associated with the Rab1 sensors. However, these two effector proteins can only reflect a small fraction of possible interactions Rab proteins encounter in the cellular environment. Binding of the human effector Mical-3 to activated Rab1, for instance, was completely abolished after AMPylation of the switch II residue Y77.[189] However, in this case the AMPylation site is directly located in the Rab-effector interface.[190] Conversely, the acceptor labeling sites of the FRET constructs do not lie in the interface of any reported Rab-effector complex structure (Figure 3-21).

Another aspect of the Rab1 sensor that should be considered, is the fluorescent protein at the N-terminus. The bulky fluorophore could severely impact effector binding of GTPase-effector pairs that involve the GTPase's N-terminal region, as recently reported for the Mical (molecules interacting with CasL) effector family.[190]

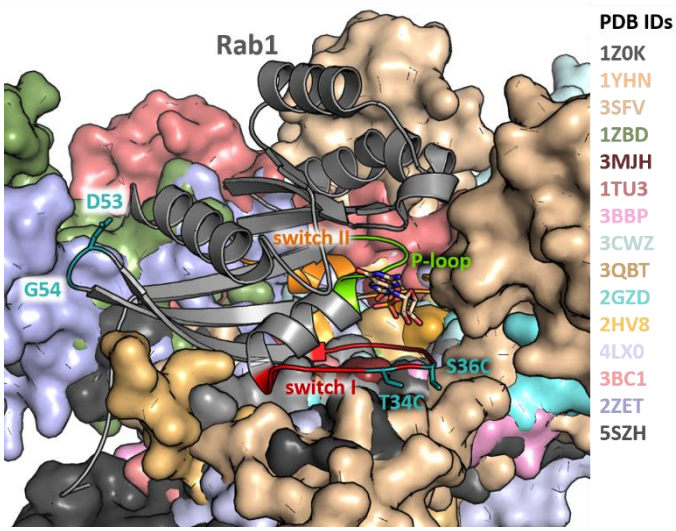

Figure 3-21: Overlay of available crystal structures of Rab:effector complexes.
The structure of Rab1 in the Rab1:LidA complex (PDB ID: 3SFV) is shown in gray. The effector structures in surface representation are highlighted according to the indicated color scheme.
The labeling sites T34, S36, D53 and G54 in Rab1 are highlighted and labeled in turquoise. The switch I and II regions are colored in red and orange respectively.
Switch I is involved in Rab-effector interaction, but the residues T34 and S36 do not form direct contacts in the complex structures with effector proteins. The interswitch labeling sites D53 and G54 are facing away from the main GTPase-effector interaction sites.

Another interesting finding of the experiments is the collective decrease in FRET efficiency upon effector binding for all Rab1 constructs independent of the labeling position within the protein (Table 3-5). This overarching tendency points towards a common mechanism for the influence of GTPase-effector interaction on the FRET signal. It could be speculated that the drop in FRET signal is caused by the effector limiting the available space for the N-terminally attached donor fluorophore. Effector binding might push the donor fluorophore away from the acceptor labeling site and thus leads to an increase in distance or an unfavorable orientation of the FRET dipoles (1.2.1). This notion is further supported by the observation that LidA with its exceptionally extensive GTPase-effector interface[184] leads to a much larger reduction in FRET efficiency than binding of the smaller effector domain of OCRL (Figure 3-22).

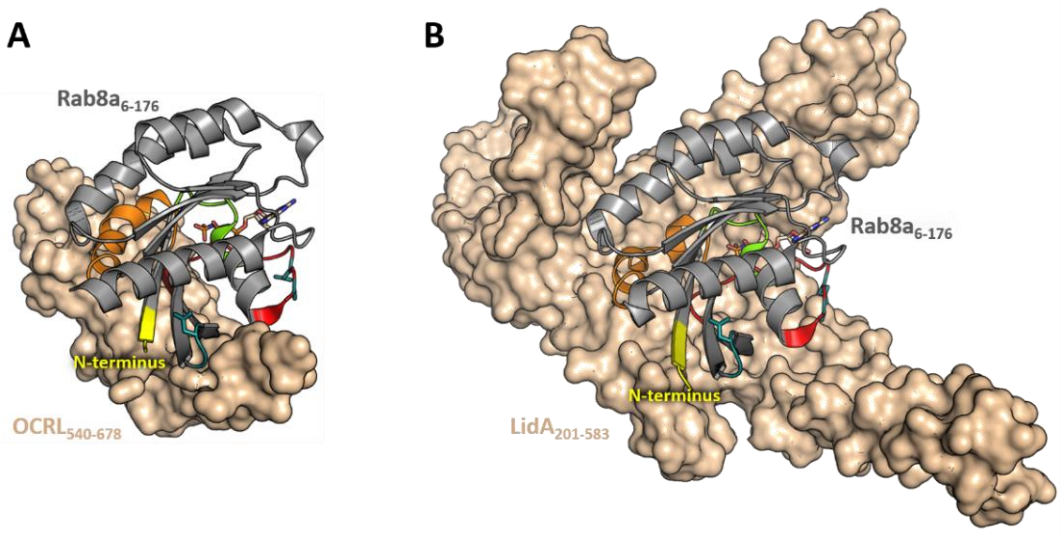

Figure 3-22: Surface representation of OCRL (PDB ID: 3QBT) and LidA (PDB ID: 3TNF) in complex with Rab8.
The Rab8 structures are shown in cartoon representation (gray), the effector structures **(A)** OCRL and **(B)** LidA are displayed as surface representations (g). The N-terminus of the Rab proteins is highlighted and labeled in yellow. The surface representation highlights the extensive interaction interface formed by LidA in complex with Rab8 and the steric hindrance of between of N-terminal modifications (e.g. N-terminal tagging with fluorescent proteins).

3.1.7 Characterization of Rab1 FRET sensor by FLIM-FRET on Ni-NTA beads

After evaluation by fluorescence spectroscopy, the constructs were immobilized on Ni-NTA beads and assessed by fluorescence lifetime imaging microcopy (FLIM). FLIM-FRET is an alternative method to traditional sensitized emission and ratiometric imaging of FRET. A significant advantage of FLIM in comparison to conventional FRET imaging is that it does not rely on changes in fluorescence intensity and thus does not need to be corrected for artifacts resulting from changes in local fluorophore concentration or donor fluorescence bleed through.[191] Changes in FRET efficiency can be directly extracted from the fluorescence lifetime of the donor fluorophore.

For *in vitro* FLIM imaging, the Rab1 constructs were immobilized on Ni-NTA beads through an N-terminal His-tag (2.4.5). Immobilization lead to a high signal to noise ratio. To examine the sensors response to GEF-mediated nucleotide exchange the Rab1 constructs were incubated with $DrrA_{340-533}$ in GTP-containing buffer prior to immobilization. For effector binding, $OCRL1_{539-901}$ or $LidA_{201-583}$ was added after activation by $DrrA_{340-533}$ and GTP (2.4.5). After washing, the protein loaded beads were suspended in GTPase buffer and transferred onto a glass object slide for subsequent FLIM measurements (2.7.1).

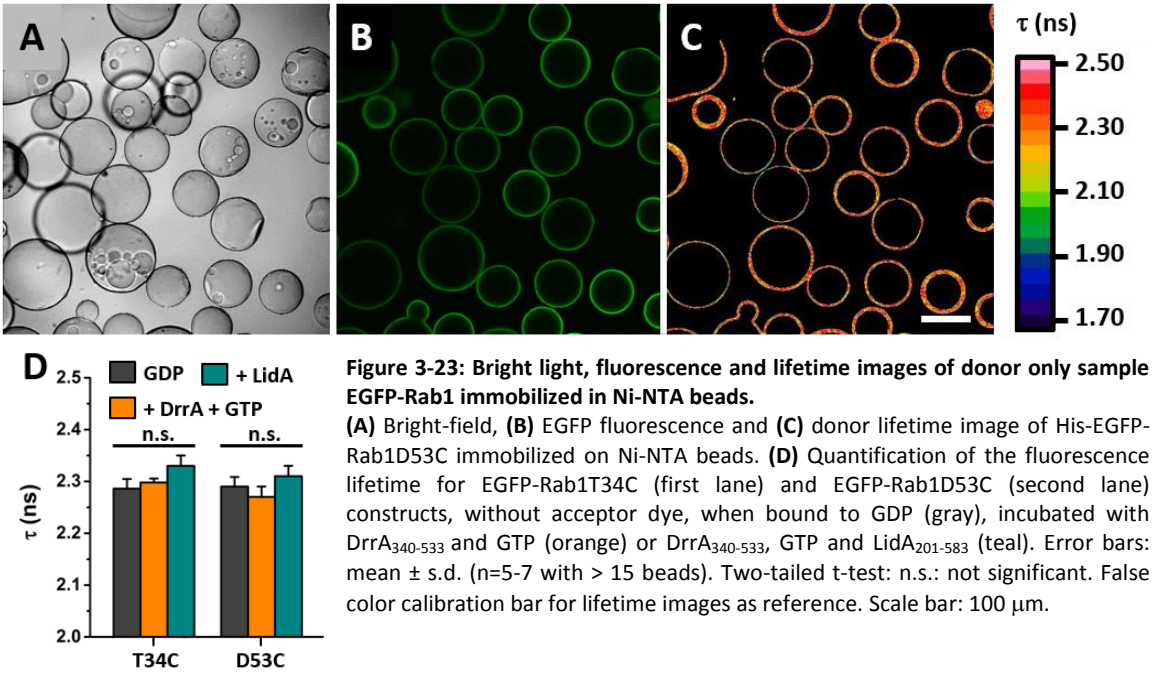

Figure 3-23: Bright light, fluorescence and lifetime images of donor only sample EGFP-Rab1 immobilized in Ni-NTA beads.
(A) Bright-field, **(B)** EGFP fluorescence and **(C)** donor lifetime image of His-EGFP-Rab1D53C immobilized on Ni-NTA beads. **(D)** Quantification of the fluorescence lifetime for EGFP-Rab1T34C (first lane) and EGFP-Rab1D53C (second lane) constructs, without acceptor dye, when bound to GDP (gray), incubated with $DrrA_{340-533}$ and GTP (orange) or $DrrA_{340-533}$, GTP and $LidA_{201-583}$ (teal). Error bars: mean ± s.d. (n=5-7 with > 15 beads). Two-tailed t-test: n.s.: not significant. False color calibration bar for lifetime images as reference. Scale bar: 100 µm.

Figure 3-23 displays typical bright-field, fluorescence and lifetime images of EGFP-Rab1D53C immobilized on Ni-NTA beads. The confocal fluorescence and lifetime images show circles of high fluorescence intensity representing the cross section of the protein immobilized on the beads surface. To analyze the collected FLIM data by global analysis[171], donor only samples lacking the acceptor dye were collected using EGFP-Rab1 constructs (Figure 3-23). Additionally, the two donor only samples (EGFP-Rab1T34C and EGFP-Rab1D53C) served as negative controls for GTPase activation and effector binding. As expected, no changes in donor lifetime were observed when these constructs were subjected to GEF-mediated nucleotide

exchange or effector binding (Figure 3-23 D). The observed average lifetime of about 2.3 ns is in keeping with previously reported lifetimes for EGFP *in vitro*.[192]

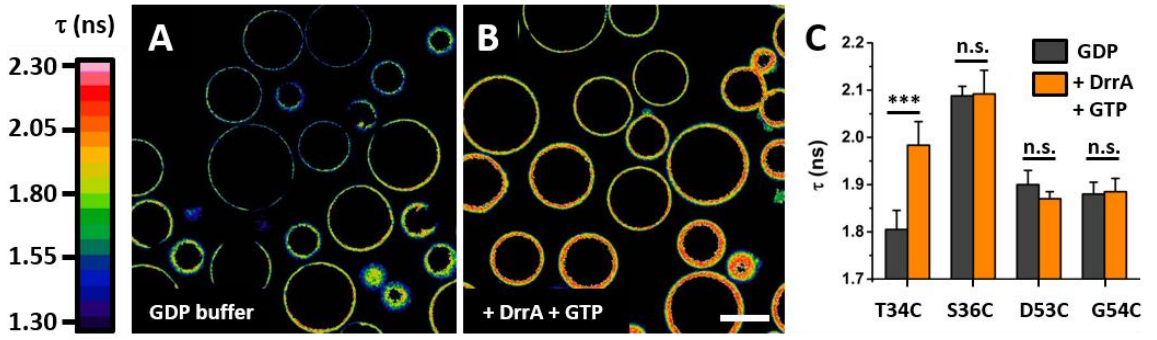

Figure 3-24: FLIM of GDP- and GTP-bound EGFP-Rab1-TF3 immobilized on Ni-NTA beads.
FLIM image of His-EGFP-Rab1T34C-TF3 immobilized on Ni-NTA beads in **(A)** GDP buffer and **(B)** after incubation with $DrrA_{340-533}$ and GTP. **(C)** Quantification of EGFP-Rab1-TF3 lifetime for the T34C, S36C, D53C and G54C constructs when bound to GDP (gray) or after incubation with $DrrA_{340-533}$ and GTP (orange). Error bars: mean ± s.d. (n = 5-7 with > 15 beads). Two-tailed t-test: n.s.: not significant, ***: $p < 0.001$. False color calibration bar for lifetime images as reference. Scale bar: 100 μm.

When testing the FRET constructs in the FLIM setup, only the T34C construct displayed a significant change (> 0.1 ns) in EGFP fluorescence lifetime upon GEF-mediated GDP to GTP exchange (Figure 3-24). The increase in donor lifetime correlates with the decrease of FRET efficiency observed sensitized emission (3.1.4). Similarly, binding of OCRL1 led to a substantial increase of the fluorescence lifetime in the D53C but not in the T34C construct (Figure 3-25). Due to their diametric sensitivity in the FLIM-FRET measurements, T34C and D53C can be used as complements for detecting GTPases activation and effector binding, respectively.

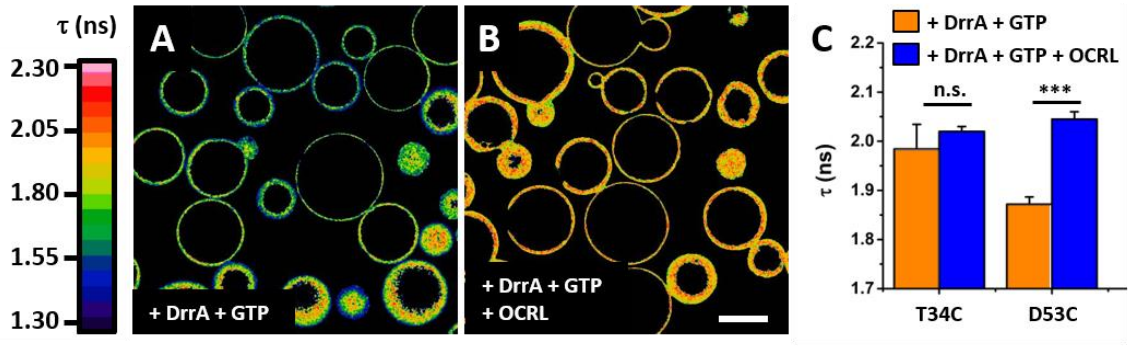

Figure 3-25: FLIM of effector free and OCRL-bound EGFP-Rab1-TF3 immobilized on Ni-NTA beads.
FLIM image of His-EGFP-Rab1D53C-TF3 immobilized on Ni-NTA beads after incubation with **(A)** $DrrA_{340-533}$ and GTP and **(B)** $DrrA_{340-533}$, GTP and $OCRL1_{539–901}$. **(C)** Quantification of EGFP-Rab1-TF3 lifetime for the T34C and D53C bound to GTP (gray) or after incubation with $DrrA_{340-533}$, GTP and $OCRL1_{539–901}$ (orange). Error bars: mean ± s.d. (n = 5-7 with > 15 beads). Two-tailed t-test: n.s.: not significant, ***: $p < 0.001$. False color calibration bar for lifetime images as reference. Scale bar: 100 μm.

In agreement with the results obtained by sensitized emission, all Rab1 constructs displayed a substantial increase in donor lifetime when incubated with the *Legionella* effector $LidA_{201-583}$. The D53C and the G54C constructs showed the largest increase in donor lifetime upon LidA binding (> 0.2 ns).

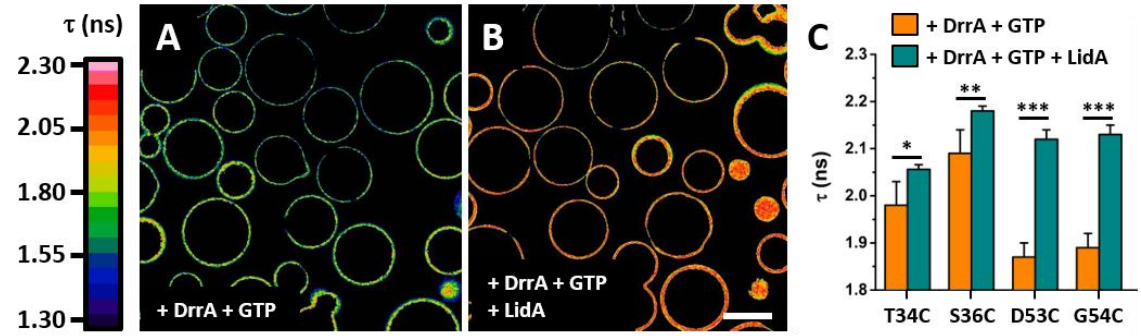

Figure 3-26: FLIM of effector free and LidA-bound EGFP-Rab1-TF3 immobilized on Ni-NTA beads.
FLIM image of His-EGFP-Rab1G54C-TF3 immobilized on Ni-NTA beads after incubation with **(A)** $DrrA_{340-533}$ and GTP and **(B)** $DrrA_{340-533}$, GTP and $LidA_{201-583}$. **(C)** Quantification of EGFP-Rab1-TF3 lifetime for the T34C and D53C bound to GTP (gray) or after incubation with $DrrA_{340-533}$, GTP and $LidA_{201-583}$ (orange). Error bars: mean ± s.d. (n=5-7 with > 15 beads). Two-tailed t-test: ***: $p < 0.001$, **: $p < 0.01$, *: $p < 0.05$. False color calibration bar for lifetime images as reference. Scale bar: 100 μm.

The results obtained *in vitro*, indicated that the Rab1 constructs might be suitable for visualizing Rab1 activity in living cells using FLIM-FRET. As the next step, the FRET sensor constructs were introduced to living cells.

3.1.8 Localization of Rab1 sensor *in vivo*

Correct subcellular localization is essential for proper GTPase functioning. In cells the C-terminal cysteines of Rab proteins are post-translationally modified with one or two geranylgeranyl moieties by Rab geranylgeranyltransferase (RabGGTase) with the support of the Rab escort protein (REP). The C-terminal prenyl anchors facilitate membrane attachment through hydrophobic interaction with the lipid bilayer.

To retain proper function of the Rab1 constructs in cells, the two C-terminal cysteines were reconstituted through NCL as described in 3.1.3. The full-length constructs were then introduced into HeLa cells by microinjection (2.6.4). Immediately after injection the Rab1 sensor fluorescence was distributed homogenously in the cell. After incubation for 30-60 min at 37 °C and 5 % CO_2, the EGFP and Tide Fluor 3 fluorescence enriched at a perinuclear structure, which largely colocalized with the Golgi marker BFP-Giantin. (Figure 3-28). Enrichment at the Golgi apparatus is consistent with the localization of wild type Rab1[193], suggesting that the reconstituted Rab1 constructs are successfully prenylated by the cellular machinery and function properly in living cells.

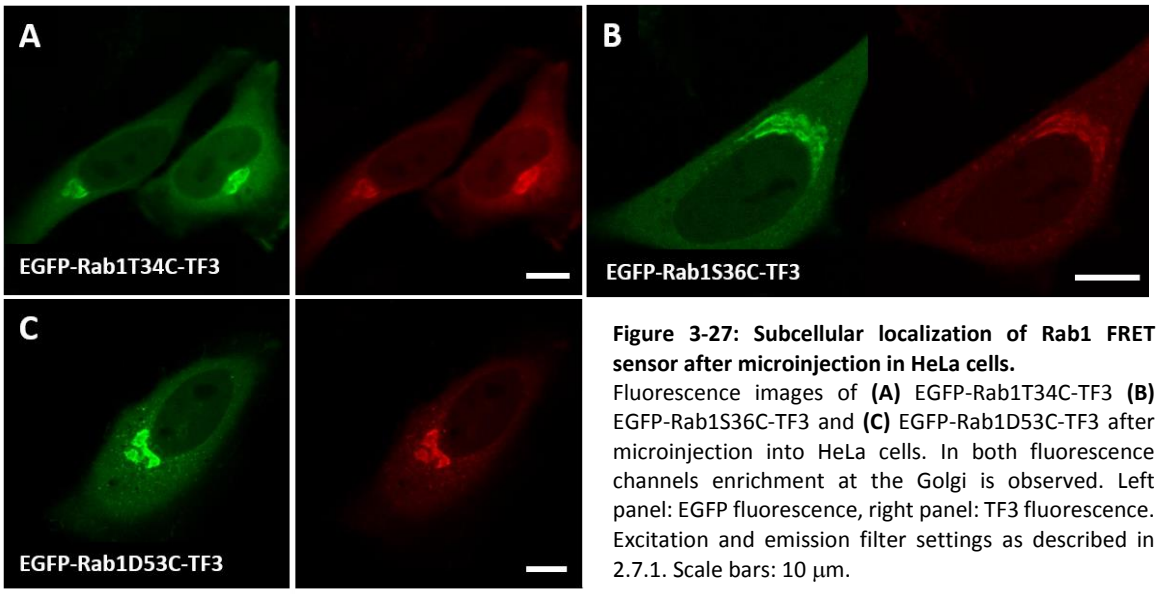

Figure 3-27: Subcellular localization of Rab1 FRET sensor after microinjection in HeLa cells.
Fluorescence images of **(A)** EGFP-Rab1T34C-TF3 **(B)** EGFP-Rab1S36C-TF3 and **(C)** EGFP-Rab1D53C-TF3 after microinjection into HeLa cells. In both fluorescence channels enrichment at the Golgi is observed. Left panel: EGFP fluorescence, right panel: TF3 fluorescence. Excitation and emission filter settings as described in 2.7.1. Scale bars: 10 μm.

As expected for a unimolecular FRET sensor, the donor and acceptor fluorescence colocalize well. It should be noted however, that prolonged incubation (> 2-3 h) after microinjection leads to formation of puncta that are observed exclusively in the TF3 channel, possibly due to degradation of the protein.

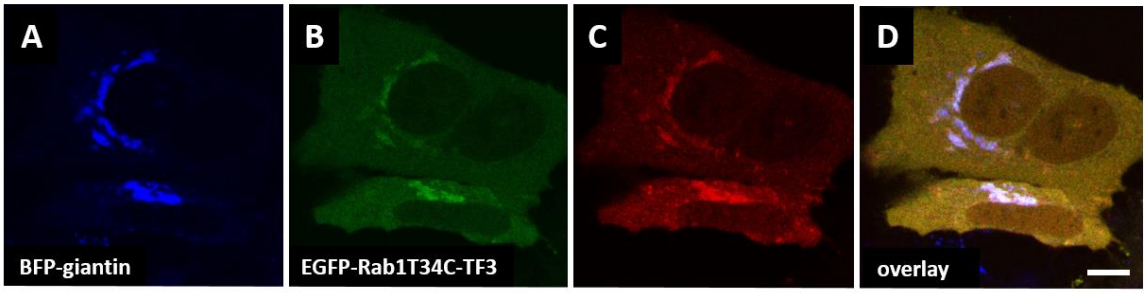

Figure 3-28: Subcellular localization of Rab1 FRET sensor in HeLa cells expressing BFP-giantin.
Fluorescence image of EGFP-Rab1T34C-TF3 after microinjection into HeLa cell expressing BFP-giantin. **(A)** BFP- **(B)** EGFP-, **(C)** TF3-channel and **(D)** overlay. Correlation of the Golgi marker BFP-Giantin with the sensor fluorescence confirms Golgi localization. Excitation and emission filter settings as described in 2.7.1. Scale bar: 10 μm.

As Rab proteins membrane localization depends on post translational modification of one or two C-terminal cysteine residues with isoprenyl moieties. Constructs lacking the C-terminal cysteines lose their Golgi localization and are homogenously distributed in the cell (Figure 3-29).

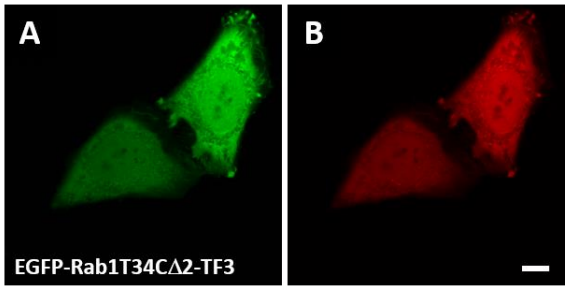

Figure 3-29: Subcellular localization of Rab1 FRET sensor with truncated C-terminus in HeLa cells.
Fluorescence image of EGFP-Rab1T34CΔ2-TF3 after microinjection into HeLa cell **(A)** EGFP- and **(B)** TF3-channel. Truncation of the two C-terminal cysteines leads to loss of Golgi localization of Rab1 FRET sensor constructs. Excitation and emission filter settings as described in 2.7.1. Scale bar: 10 μm.

In keeping with previous reports on the significance of GEF activity in Rab membrane targeting[54], the Rab1 sensor constructs also lose their predominant localization to the Golgi organelle when injected into cells expressing the GEF-domain of the *Legionella* protein DrrA$_{340\text{-}533}$ (Figure 3-30). The DrrA$_{340\text{-}533}$ construct is lacking its C-terminal P4M-domain that conveys plasma membrane localization in full length DrrA[78], thus BFP-DrrA$_{340\text{-}533}$ sequestered the Rab1 construct to the cytosol and the nucleus.

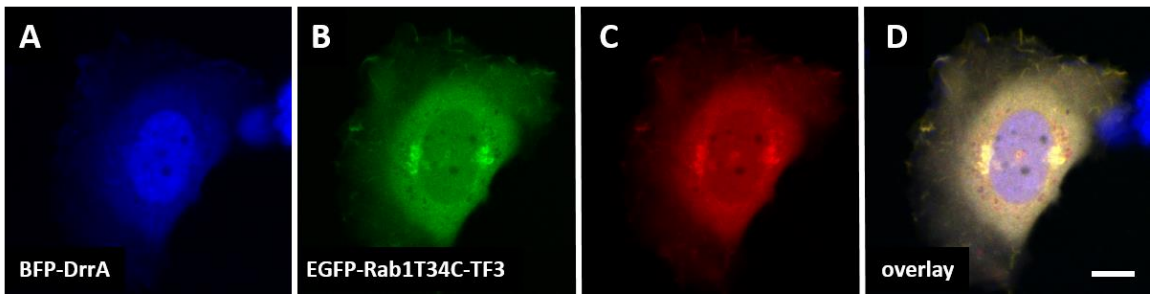

Figure 3-30: Subcellular localization of Rab1 FRET sensor in HeLa cells expressing BFP-DrrA$_{340\text{-}533}$.
Fluorescence image of EGFP-Rab1T34C-TF3 after microinjection into HeLa cell expressing BFP-DrrA$_{340\text{-}533}$ **(A)** BFP- **(B)** EGFP-, **(C)** TF3-channel and **(D)** overlay. Ectopic expression of BFP-DrrA$_{340\text{-}533}$ distorts sensor targeting from Golgi to the cytosol and nucleus. Excitation and emission filter settings as described in 2.7.1. Scale bar: 10 μm.

3.1.9 FRET sensor reveals nucleotide state of Rab1 in living cells

The Rab1 sensor was microinjected into living cells (2.6.4) to examine Rab1 activation *in vivo*. As described in the methods section, the cells were imaged using lifetime microscopy (2.7.2). The fluorescence lifetime was determined using global analysis.[171] The T34 construct was mainly used for imaging Rab1 activity in live cells.

FLIM-FRET of GDP- and GTP-bound Rab1 sensor in live cells

To correlate observed lifetimes to the appropriate nucleotide binding state, reference measurements of sensor variants that are predominantly active or inactive were used. A constitutively active Q67L mutant and cells expressing BFP-DrrA$_{340-533}$ served as references for the active, GTP-bound sensor. A C-terminal truncated sensor construct was employed as a references for predominantly inactive, GDP-bound sensor.

The Q67L mutation lacks a prominent glutamine that is involved in the intrinsic hydrolysis of GTP and stabilization of the GTPase-GAP interaction[41,43], leading to constitutively active, GTP-bound EGFP-Rab1T34C(Q67L)-TF3 (Figure 3-31 E-G). As a second reference for the GTP-bound state, the T34C sensor was injected into HeLa cells expressing BFP-DrrA$_{340-533}$. BFP-DrrA$_{340-533}$ expression results in ubiquitous activation of the Rab1 pool (Figure 3-31 A-D).[54] The donor lifetime obtained from these two experiments represents the lifetime for GTP-bound, active Rab1 sensor τ_{GTP} = 2.05 ± 0.03 ns (18 cells) (Figure 3-34 A).

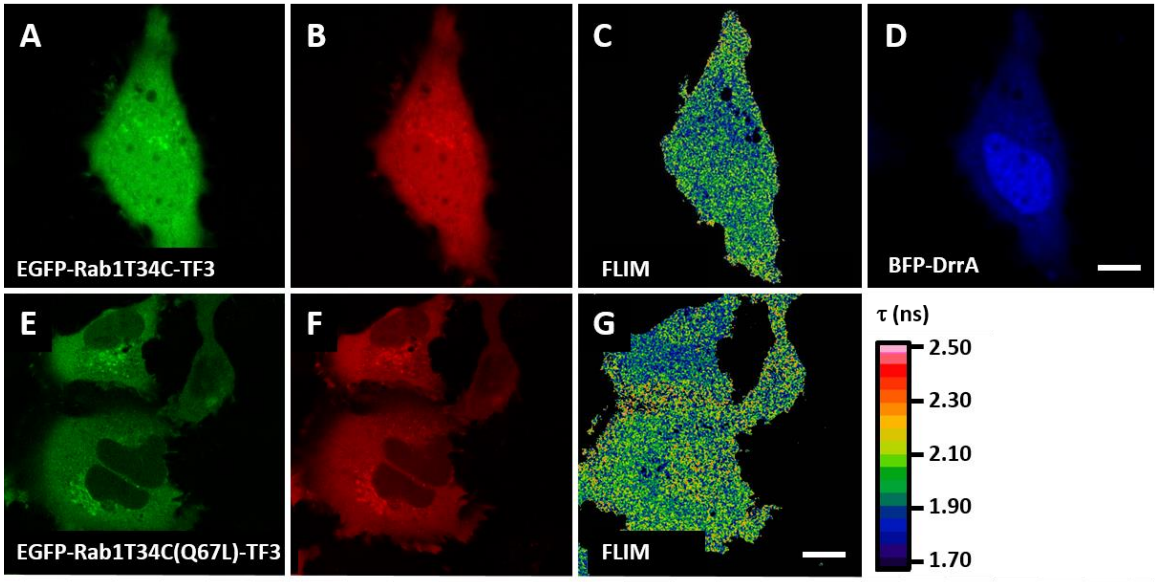

Figure 3-31: FLIM of EGFP-Rab1T34C-TF3 and EGFP-Rab1T34C(Q67L)-TF3 *in vivo*.
Fluorescence image of EGFP-Rab1T34C-TF3 after microinjection into HeLa cell expressing BFP-DrrA$_{340-533}$ **(A)** EGFP-, **(B)** TF3- and **(D)** BFP-channel. **(C)** Corresponding FLIM image. Fluorescence image of EGFP-Rab1T34C(Q67L)-TF3 after microinjection into wild type HeLa cell **(E)** EGFP- and **(F)** TF3-channel. **(G)** Corresponding FLIM image. False color calibration bar for lifetime images as reference. Scale bar: 10 μM.

As a control, a donor only construct (EGFP-Rab1) was injected into cells expressing BFP-DrrA$_{340-533}$. In this case no significant increase in donor lifetime was observed in BFP-DrrA$_{340-533}$ transfected cells (Figure 5-15 and Figure 5-16).

To determine the fluorescence lifetime of the GDP-bound sensor EGFP-Rab1T34CΔ2-TF3, a sensor construct lacking the two prenylatable C-terminal cysteines, was injected into wild type HeLa cells. Without the C-terminal cysteine residues the protein cannot attach to membranes, excluding it from regulation by GEFs and GAPs. This is evident from the cytoplasmic Rab1 localization (Figure 3-32). In agreement with previous *in vitro* results, the donor lifetime of the GDP-bound sensor is reduced in comparison to the activated, GTP-bound construct. The average lifetime was determined to be τ_{GDP} = 1.88 ± 0.08 ns (15 cells) (Figure 3-34).

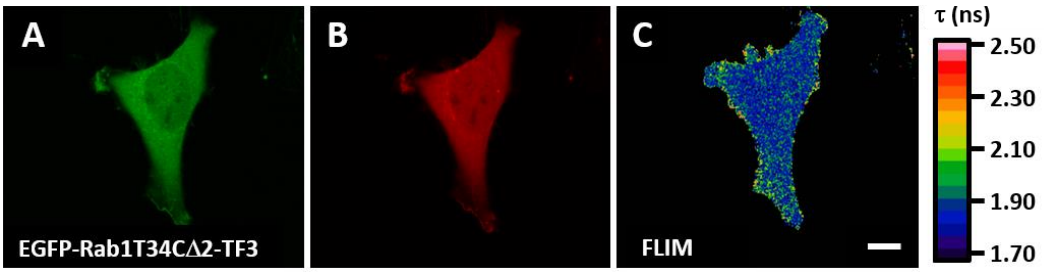

Figure 3-32: FLIM of EGFP-Rab1T34CΔ2-TF3 *in vivo*.
Fluorescence image of EGFP-Rab1T34CΔ2-TF3 after microinjection into wild type HeLa cell **(A)** EGFP- and **(B)** TF3-channel. **(C)** Corresponding FLIM image. False color calibration bar for lifetime images as reference. Scale bar: 10 μM.

Quantification of Rab1 activity in live cells

Using these τ_{GDP} and τ_{GTP} values as reference for the fluorescence lifetime of GDP and GTP-bound sensor respectively, the obtained fluorescence lifetime for the Rab1 sensor in cells can be correlated to the local Rab1 activity.

In the FLIM images each color coded pixel correlates to a fluorescence lifetime that is determined through the collected photons at this position. The average fluorescence lifetime at this position is composed of two fractions. One fraction represents the GDP-bound sensor and the other fraction correlates to the GTP-bound Rab1 FRET sensor. Assuming that the observed lifetime is a linear combination of these two sensor species the proportion of GDP to GTP-bound Rab1 can be calculated using the following relation:

$$\tau_{obs} = x \cdot \tau_{GDP} + y \cdot \tau_{GTP} \text{ with } 1 = x + y$$

$$x = \frac{\tau_{obs} - \tau_{GDP}}{\tau_{GTP} - \tau_{GDP}} \qquad \textbf{Eq. 3-2}$$

Here τ_{obs} is the lifetime of the FRET sensor at a specific location in the cell. The variable x correlates with the fraction of GTP-bound sensor and y with the fraction of GDP-bound sensor. τ_{GDP} and τ_{GTP} are the fluorescence lifetimes for sensor species bound exclusively to GDP or GTP, respectively.

As described earlier, the EGFP-Rab1T34C-TF3- CC construct enriches at the Golgi membrane in Hela cells (Figure 3-33). Interestingly Golgi-bound sensor displays a significantly lower lifetime than the cytoplasmic sensor fraction (Figure 3-33 C and F, Figure 3-34 A).

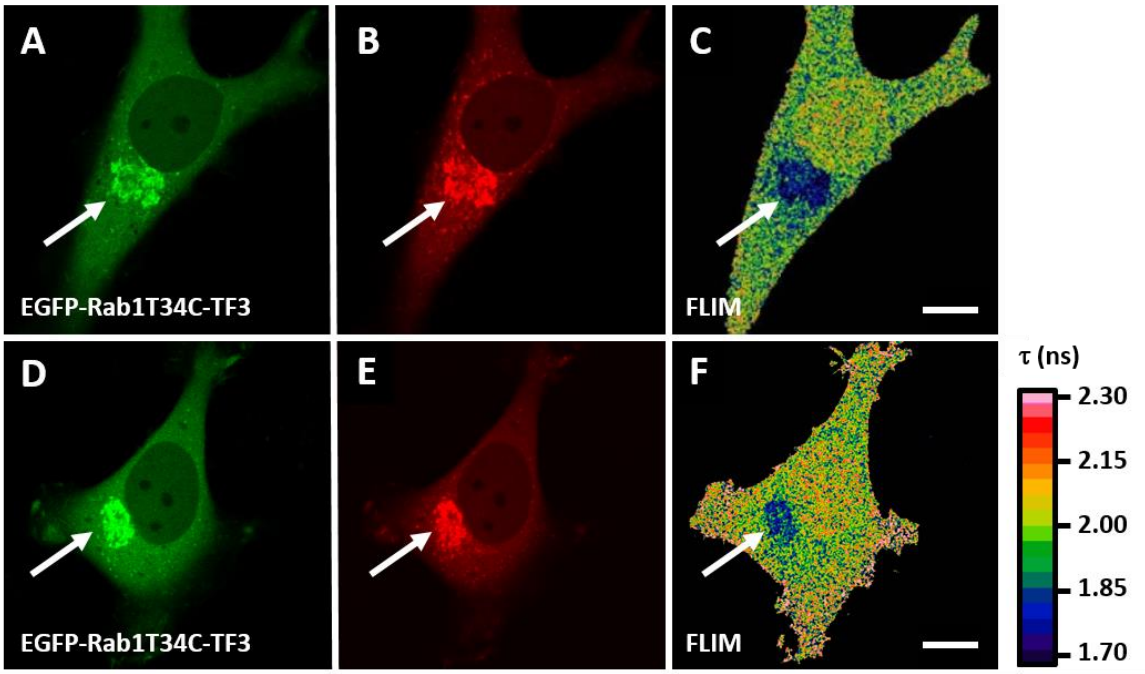

Figure 3-33: FLIM of EGFP-Rab1T34C-TF3 injected into wild type HeLa cells.
Fluorescence image of EGFP-Rab1T34C-TF3 after microinjection into wild type HeLa cell **(A)/(D)** EGFP- and **(B)/(E)** TF3-channel. **(C)/(F)** Corresponding FLIM image. False color calibration bar for lifetime images as reference. Scale bar: 10 μM.

The observed average lifetimes of τ_{cyto} = 2.02 ± 0.04 ns and τ_{Golgi} = 1.95 ± 0.07 ns (18 cells) indicate that Rab1 is predominately in the GDP-bound state when localized to the Golgi and largely in the GTP-bound state in the cytoplasm (Figure 3-34 B).

Using Eq. 3-2 the proportion of Rab1:GDP and Rab1:GTP can be estimated. Using this approximation, about 80 % of the Rab1 pool is GTP-bound in the cytoplasm, while only 40 % of the Golgi localized Rab1 molecules are GTP-bound (Figure 3-34 B). It should be noted that the obtained fluorescence lifetimes differ significantly from cell to cell, resulting in considerable variance of the determined GDP/GTP percentages. However, when directly comparing the lifetime of the cytoplasmic and the Golgi fraction in a cell, the sensor lifetime at the Golgi membrane is always substantially lower than in the cytoplasmic fraction. This difference from cytoplasmic to Golgi localized sensor fraction is not observed for the T34C(Q67L) construct (Figure 3-34 A). In another control experiment using EGFP-Rab1, a construct without the acceptor dye, the difference in fluorescence lifetime between Golgi and cytoplasm is not significant (Figure 5-16).

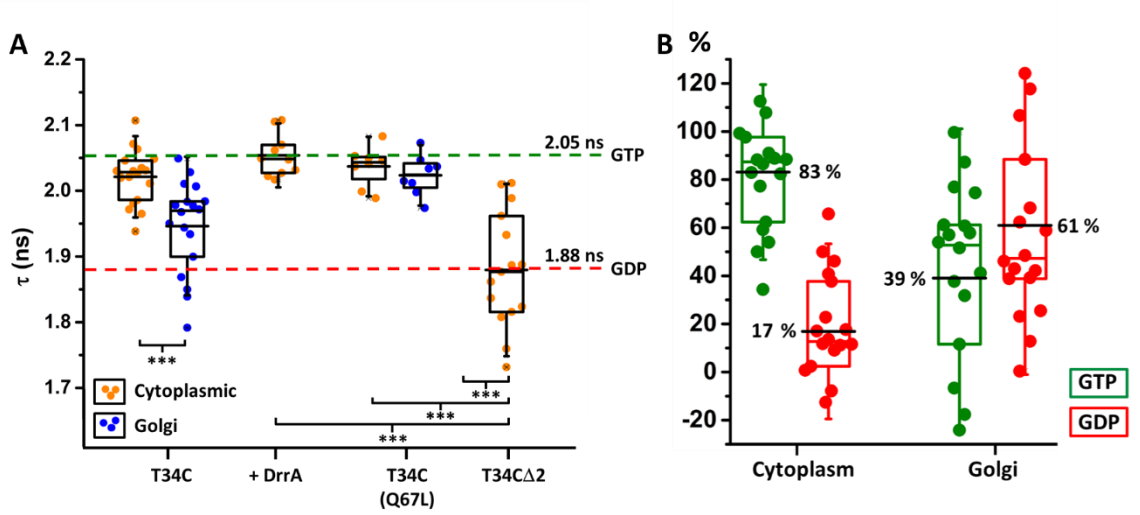

Figure 3-34: Quantification of Rab1 nucleotide binding state *in vivo*.
(A) Quantification of EGFP lifetime for T34C sensor constructs in cells. Orange and blue dots denote cytoplasmic and Golgi-localized protein fractions, respectively. (n = 7-25 cells, individual data points are plotted, box plots: - median, -- mean, upper hinge 75th percentile, lower hinge 25th Percentile, whiskers: s.d.. Two-tailed t-test, ***: $p < 0.001$) **(B)** Quantification of GTP- and GDP-bound fraction of cytoplasmic and Golgi-localized Rab1 sensor. Each dot represents one cellular FLIM measurement.

Here the aforementioned observation that the cytoplasmic Rab1 fraction is predominantly active/GTP-bound whereas Rab1 localized to the Golgi compartment is largely inactive/GDP-bound, is discussed in light of the current model for the spatial Rab cycle regulating vesicular transport (Figure 3-35).[4,46]

Rab1 regulates the ER to Golgi transport[94,97,194-198], thus the ER represents the donor compartment while the Golgi membrane correlates to the acceptor membrane. After microinjection the Rab1 construct binds to REP, is prenylated by RabGGTase and delivered to its donor membrane, the ER. At the ER the GTPase encounters GEFs and is subsequently activated. Following activation Rab1 binds/recruits effector proteins, such as p115[97], at the ER exit sites (ERES) and locates to budding vesicles.[199] The vesicular, activated Rab1 is then transported to the target membrane at the Golgi site, possibly undergoing an additional vesicular fusion/budding step at the ER-Golgi intermediate (ERGIC) compartment.[198] Vesicles originating at the ERES and the ERGIC require the action of the Rab1 specific GEF the TRAPP (transport protein particle) complexes.[74] After delivery to the Golgi, the vesicles fuse with the acceptor membrane through Rab1 mediated interactions with the tethering proteins p115[97] and GM130[94] and the Golgi resident giantin[200]. To close the spatial cycle Rab1 is deactivated by GAPs, thereby disrupting effector binding and enabling extraction by GDI. From the cytoplasm Rab1 is delivered to the ER membrane and can re-enter the ER to Golgi trafficking cycle.

In context of this model, the predominantly active Rab1 sensor in the cytoplasm (~ 80 % GTP-bound, Figure 3-34) can be attributed to the Rab1 population undergoing vesicular transport. Thus GDI-bound, inactive Rab1 represents about 20% of the Rab1 present in the cytoplasm. The Golgi compartment on the other hand serves as the acceptor compartment, where Rab1 is inactivated after vesicular fusion and thus features

a high GAP activity. This is in agreement with the observation that the Rab1 sensor is predominantly (~60 %) GDP-bound at the Golgi site. Together with the enrichment of Rab1 at the Golgi apparatus, this suggest that the Golgi compartment serves as the Rab1 reservoir in cells.

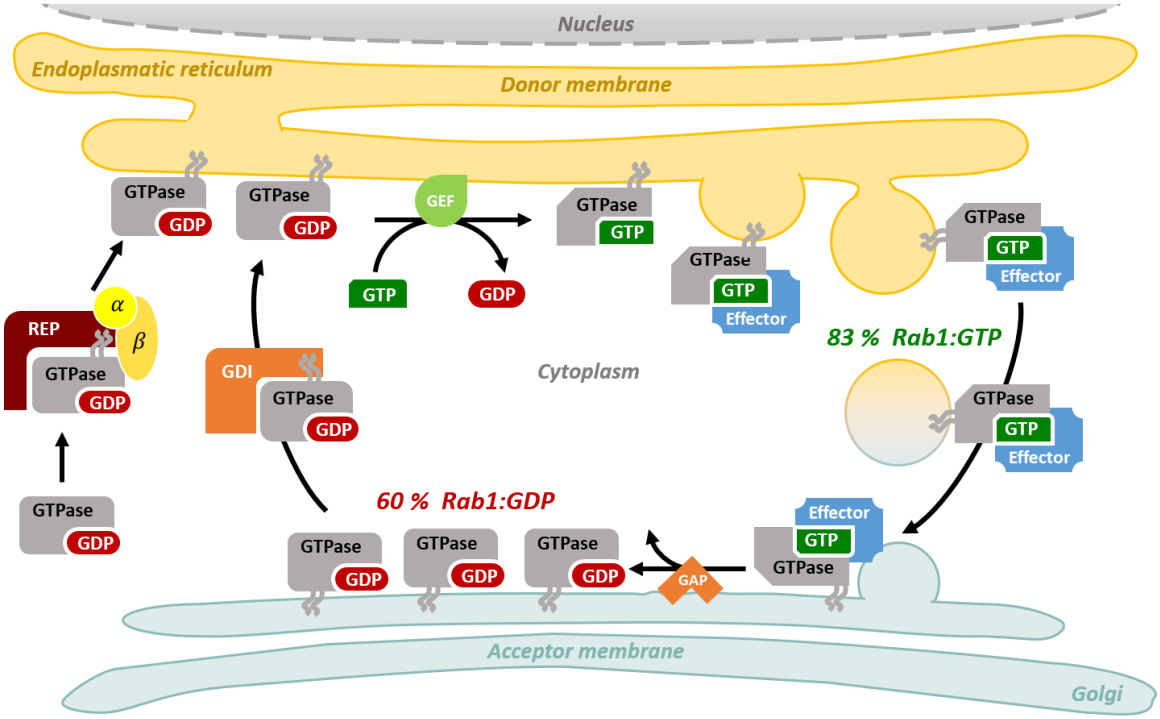

Figure 3-35: Rab1 cycling regulates vesicular transport between the ER and Golgi compartment.
Injected Rab sensor associates to REP and is prenylated through interaction with RabGGTase. The prenylated Rab1 sensor is then delivered to the ER, attaches to the membrane and is activated upon encountering a GEF, e.g. TRAPP. The GTP-bound Rab1 constructs then recruit/bind effector proteins to the ERES sites/budding vesicles. Guided by the recruited effector proteins, the Rab loaded vesicles enter the cytoplasm, resulting in the predominantly active Rab1 sensor population. Upon fusion with the Golgi membrane, the GTPase is inactivated through GAP-mediated GTP hydrolysis.

3.1.10 Rab1 FRET sensor reports on effector binding in living cells

When examining the different Rab1 FRET constructs *in vitro*, S36C, D53C and G54C proved to be effective reporters of OCRL1 binding while the T34C construct displayed no sensitivity towards OCRL1 (3.1.6 and 3.1.7). Thus in addition to probing the Rab1 nucleotide state in living cells using EGFP-Rab1T34C-TF3 (3.1.9), EGFP-Rab1S36C-TF3 and EGFP-Rab1D53C-TF3 were used to assess, whether the sensors are suitable reporters of effector binding in living cells.

To this end, the modified Rab1 constructs were introduced into Hela cells with or without expression of BFP-OCRL1$_{539–901}$. Consistent with the *in vitro* results, the donor lifetime increased significantly for the S36C and D53C constructs in cells expressing the OCRL1, but not for the T34 construct (Figure 3-37 and Figure 5-14).

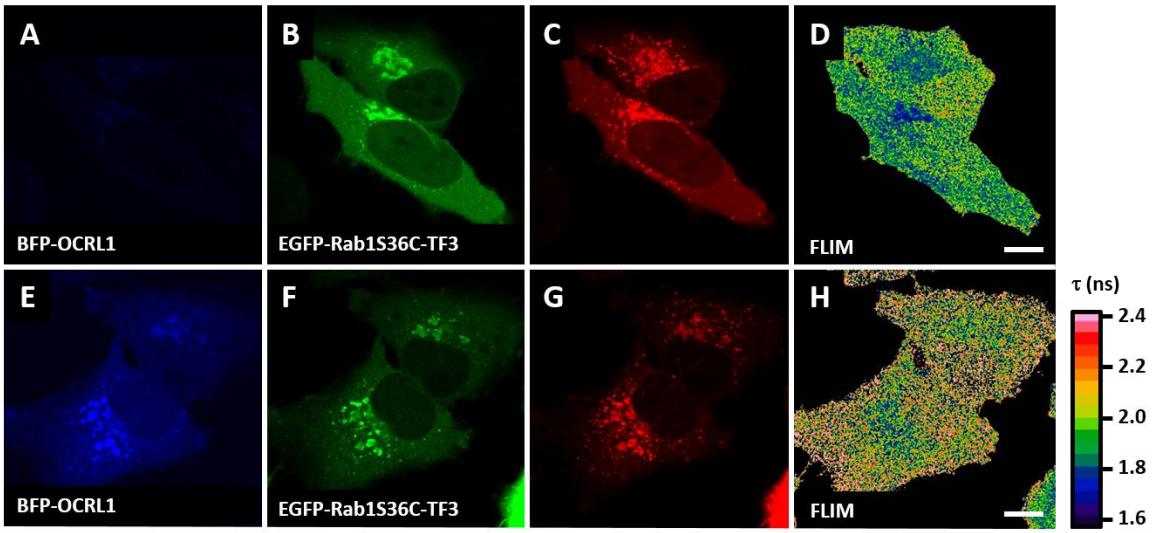

Figure 3-36: Rab1 FRET sensor reports on OCRL1 binding *in vivo*.
Fluorescence and FLIM images of EGFP-Rab1S36C-TF3 after microinjection into **(A)-(D)** wild type HeLa cell or **(E)-(H)** HeLa cell expressing BFP-OCRL1$_{539–901}$. **(A)/(E)** BFP- **(B)/(F)** EGFP-, **(C)/(G)** TF3-channel and **(D)/(H)** FLIM. Ectopic expression of BFP-OCRL1$_{539–901}$ results in higher donor lifetime of EGFP-Rab1S36C-TF3 sensor indicating effector binding. False color calibration bar for lifetime image as reference. Scale bars: 10 µm.

BFP-OCRL1 colocalized with the Rab1 sensors at the perinuclear region. Overexpression of the OCRL1 effector domain appeared to disrupt the Golgi organelle into smaller fragments that are distributed within the cytoplasm (Figure 3-36 E-G and Figure 5-13). This effect of OCRL overexpression on the Golgi structure has been reported previously.[201] To ensure that the observed increase in donor lifetime was indeed caused by OCRL1 - Rab1 sensor interaction and not through other factors such as expression of an additional fluorescent protein, the experiment was repeated with the donor only construct EGFP-Rab1 (Figure 3-37 C and Figure 5-13). As expected, the same fluorescence lifetimes were observed for the EGFP-Rab1 constructs in the presence and the absence of BFP-OCRL1 expression (Figure 3-37 C).

Collectively these findings clearly indicate that the described Rab1 sensor is an effective reporter of effector binding in living cells.

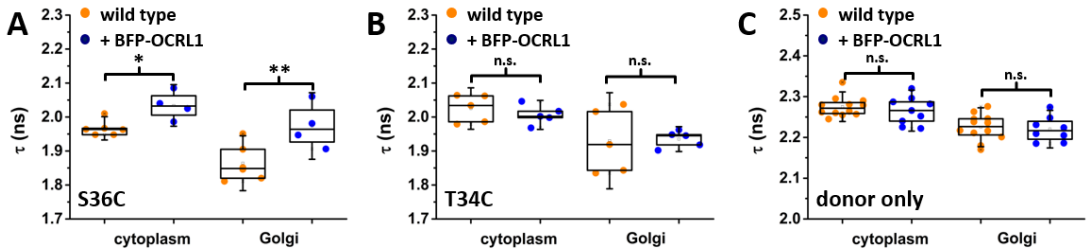

Figure 3-37: Quantification of FRET sensor donor lifetime in wild type and BFP-OCRL transfected HeLa cells.
Quantification of EGFP lifetime of **(A)** S36C, **(B)** T34C and **(C)** donor only sensor constructs. n = 5-12, individual data points are plotted, box plots: - median, □ mean, upper hinge 75th percentile, lower hinge 25th percentile, whiskers: s.d.. Two-tailed t-test: n.s.: not significant, **: $p < 0.01$, *: $p < 0.05$.

3.1.11 KRas FRET sensor - GEF-mediated nucleotide exchange

After establishing a FRET sensor for Rab1 activity, the sensor principle was expanded to the small GTPase KRas. Suitable acceptor labeling sites were identified as described in 3.1.1. To allow site-specific labeling with the acceptor dye, all naturally occurring cysteines were substituted appropriately. Analogous to the Rab1 sensor, the KRas sensors sensitivity towards its bound guanine nucleotide was initially tested by GEF-mediated GDP to GTP exchange *in vitro*. Besides evaluating the dynamic range and sensitivity, the interaction with the respective GEF was compared to the wild type protein.

For KRas the GEF domain of $SOS^{202-204}$ (referred to as $SOS_{564-1049}$ or SOS) was used to characterize the sensors' response to GDP/GTP exchange by fluorescence spectroscopy. An independent assay, using mantGDP (2.5.4.2), was utilized to examine the function of the KRas mutants. GEF-mediated nucleotide exchange was initiated through addition of varying amounts of $SOS_{564-1049}$ to 200 nM KRas sensor in the presence of 100 μM GTP. Constructs with a shortened linker region between the fluorescent protein and the GTPase domain (EGFPΔ11 and mCitrineΔ11, 5.1) were also tested. This shortens the donor-acceptor distance and fixes the fluorophores relative orientation for an improved dynamic range (2.5.4.4).

Assessment of GEF-mediated nucleotide exchange by mantGDP assay

As an initial test, the nucleotide exchange activity of $SOS_{564-1049}$ towards the KRas mutants (D30C, E31C, D33C, D47C, G48C and E107C) and unmodified KRas wild type was examined using mantGDP. By adding $SOS_{564-1049}$ in the presence of excess GTP, the bound mantGDP is released into the solution, causing a decrease in the mant fluorescence signal. The signal decrease can be fitted by a single exponential function to obtain the observed first order rate constant k_{obs} (Eq. 2-8). As described in 2.5.4.2 the catalytic efficiency can then be extracted as the slope of a linear fit of k_{obs} plotted against [$SOS_{564-1049}$] (Figure 5-17). The obtained catalytic efficiencies are summarized below (Table 3-6). The fluorescence profiles and linear regression for k_{cat}/K_M can be found in the appendix (5.6).

Table 3-6: Catalytic efficiencies for $SOS_{564-1049}$-mediated nucleotide exchange using mantGDP fluorescence.

KRas construct	Labeling site	k_{cat}/K_M $(M \cdot s)^{-1}$	$(k_{cat}/K_M (M \cdot s)^{-1})_{wt}$ / $k_{cat}/K_M (M \cdot s)^{-1}$
EGFP-KRas	D30C	$(1.58 \pm 0.25) \times 10^4$	3.3
	E31C	$(0.31 \pm 0.06) \times 10^4$	16.9
	D33C	$(0.17 \pm 0.04) \times 10^4$	30.8
	D47C	$(0.59 \pm 0.08) \times 10^4$	8.9
	G48C	$(8.38 \pm 0.07) \times 10^4$	0.6
	E107C	$(0.21 \pm 0.01) \times 10^4$	24.9
KRas wt	-	$(5.23 \pm 0.03) \times 10^4$	1

It is important to note that $SOS_{564-1049}$ features an allosteric Ras-binding site, which has a profound effect on its GEF activity.[203,204] The affinity of KRas to the catalytic site increases significantly when GDP:KRas, and to an even greater extent when GTP:KRas, is bound to the distal allosteric site of $SOS_{564-1049}$.[205,206] Due to the complex interplay of GDP/GTP-bound KRas concentration and the catalytic $SOS_{564-1049}$ domain one has to be

cautious when comparing the absolute values obtained using experimental setups. It is however, possible to compare the relative performance of $SOS_{564-1049}$ towards the tested KRas mutants and the wild type KRas. Except from G48C, all KRas mutants displayed a significantly reduced catalytic efficiency for $SOS_{564-1049}$-mediated nucleotide exchange. The smallest decrease, by a factor of three, was observed for D30C, while the largest drop in catalytic efficiency was observed for the D33C mutant with a reduction by a factor of around 30. For the EGFP-KRasG48C construct, $SOS_{564-1049}$ displayed a slightly higher k_{cat}/K_M. The rate of mantGDP release from KRas in the presence of 1 μM GEF, k_{obs} = 0.02-0.06 s^{-1}, is in the same order of magnitude (0.01-0.06 s^{-1}) as reported previously for mantGDP release (against unmodified GDP) with a total KRas concentration of 1 μM.[205]

KRas FRET sensor is sensitive towards GEF-mediated nucleotide exchange

The KRas constructs FRET signal response was assessed via sensitized emission, as described in 2.5.4.2. To this end, varying amounts of $SOS_{564-1049}$ were added to 200 nM KRas FRET sensor in the presence of excess GTP. The change in FRET efficiency was monitored by sensitized emission with the donor EGFP, EGFPΔ11 or mCitrineΔ11 excited at 480 nm and the acceptor emission detected at 580 nm for Tide Fluor 3 or 614 nm for Tide Fluor 4, respectively (2.5.4.2).

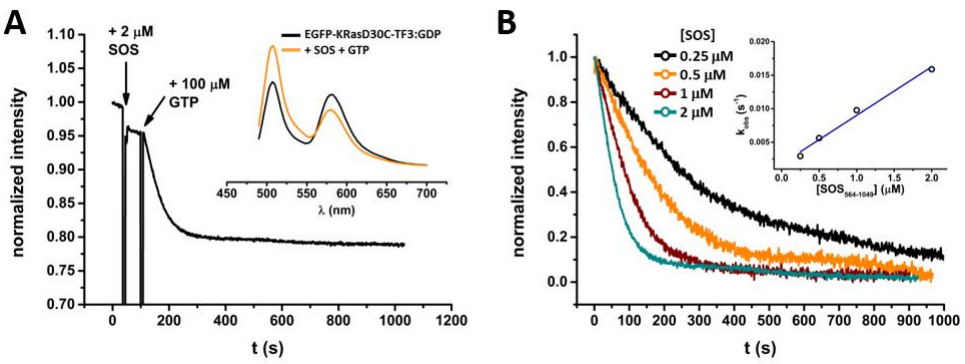

Figure 3-38: KRas FRET sensor reports on SOS-mediated nucleotide exchange.
(A) Addition of $SOS_{564-1049}$ to 200 nM EGFP-KRasD30C-TF3 induces rapid nucleotide exchange in the presence of excess GTP (100 μM). **(Inset)** Fluorescence spectra of EGFP-KRasD30C-TF3 before (solid black line) and after nucleotide exchange (solid orange line). **(B)** The observed rate constant for nucleotide exchange depends on $SOS_{564-1049}$ concentration. **(Inset)** By plotting k_{obs} against [$SOS_{564-1049}$] the catalytic efficiency can be extracted as the slope of the linear fit (solid blue line). FRET was monitored with excitation set to 480 nm and emission collected at 580 nm.

Similar to the Rab1 sensor, the FRET signal of the KRas sensor drops upon addition of the GEF, indicating accelerated nucleotide exchange. The obtained fluorescence curves can be fitted with a single exponential function to obtain a observed first order rate constant k_{obs} (2.5.4.2). The catalytic efficiency can then be extracted as the slope of the linear fit of k_{obs} plotted against [$SOS_{564-1049}$] (Figure 3-38 B and Table 3-7).

Table 3-7: Catalytic efficiencies for $SOS_{564-1049}$-mediated nucleotide exchange using sensitized emission.

Sensor construct	Labeling site	k_{cat}/K_M $(M \cdot s)^{-1}$	$(k_{cat}/K_M (M \cdot s)^{-1})_{wt}$ / $k_{cat}/K_M (M \cdot s)^{-1}$
EGFP-KRas-TF3	D30C	$(0.73 \pm 0.06) \times 10^4$	7.2
EGFPΔ11-KRas-TF3	D30C	$(0.8 \pm 0.2) \times 10^4$	6.5
mCitrineΔ11-KRas-TF4	D30C	$(0.8 \pm 0.1) \times 10^4$	6.5
	E31C	$(0.26 \pm 0.06) \times 10^4$	20.1
KRas wt	-	$(5.23 \pm 0.03) \times 10^4$	1

Of all tested KRas constructs only the D30C and E31C constructs displayed substantial change in FRET efficiency upon SOS-mediated nucleotide exchange. For both mutants the sensitized emission signal drops following GDP to GTP exchange. Fluorescence spectra collected before and after nucleotide exchange show an increase in donor emission and concomitant decrease in acceptor fluorescence (Figure 3-38 A inset and Figure 5-18 insets). The obtained catalytic efficiencies are consistent for all three D30C constructs suggesting that shortening of the linker does not impair the KRas-SOS interaction. In contrast to the Rab1 sensor, the dynamic range did not improve significantly for the constructs with shortened linker regions between the fluorescent protein and the GTPase domain. It should be noted that the relative change in fluorescence signal increased with higher $SOS_{564-1049}$ concentrations (Figure 5-18 insets). Presumably, this concentration dependent behavior can be attributed to binding of the KRas constructs to the allosteric or the catalytic SOS sites. For the E31C mutant, only the mCitrineΔ11 construct displayed a sizeable change in FRET efficiency. However, the observed signal drop was only minor when observed by sensitized emission, yet up to 25 % (Figure 5-18 M inset) when monitored through donor emission. A similar pattern was observed for EGFPΔ11- KRasD30C-TF3 and to a lesser extent for mCitineΔ11-KRasD30C-TF4 (Figure 5-18 A, D and G). In comparison to wild type KRas, the observed nucleotide exchange rate was reduced by a factor of 7 for the D30C constructs and a factor of 20 for the E31C construct (Table 3-7).

As expected, SOS mediates nucleotide exchange in both directions. After completed GDP to GTP exchange, addition of excess GDP partially restores the initial fluorescence signal intensity, indicating that GTP is exchanged for the more abundant GDP (Figure 3-39). This further confirms that the observed FRET signal change is indeed governed by the bound nucleotide and not caused by the GTPase-GEF interaction.

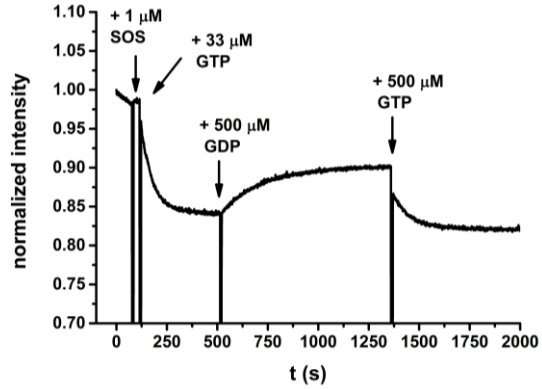

Figure 3-39: KRas FRET sensor is reversible.
Increasing amounts of GTP and GDP are added in turns to 200 nM GDP-bound EGFP-KRasD30C-TF3 and 1 μM $SOS_{564-1049}$. The observed initial signal change upon GDP to GTP exchange is partially reversed through addition of excess GDP. FRET was monitored by excitation set at 480 nm and emission collected at 580 nm.

$SOS_{564-1049}$ features a catalytic and a distal allosteric Ras-binding site, the affinity towards either of these sites depends on the nucleotide-binding state of the GTPase.[203,204] Furthermore, binding of Ras:GTP at the allosteric site accelerates the nucleotide exchange activity at the catalytic site.[204,206] The physiologically most relevant scenario constitutes binding of GTP-bound Ras to the allosteric site, leading to increased affinity of the catalytic site towards inactive, GDP-bound Ras, thereby generating a positive feedback for rapid GTPase activation.[203,204,206] A comprehensive review of this intricate interplay is not the focus of this thesis. However, the implications of binding to either sites for the FRET signal and the effect of modified switch I residues on the interaction with the catalytic SOS site are of importance and are discussed here. The following conclusions are inferred from the complex structure of $SOS_{566-1046}$ bound to nucleotide-free HRas at the catalytic site and activated HRas:GNP at the distal allosteric site (Figure 3-40).[205]

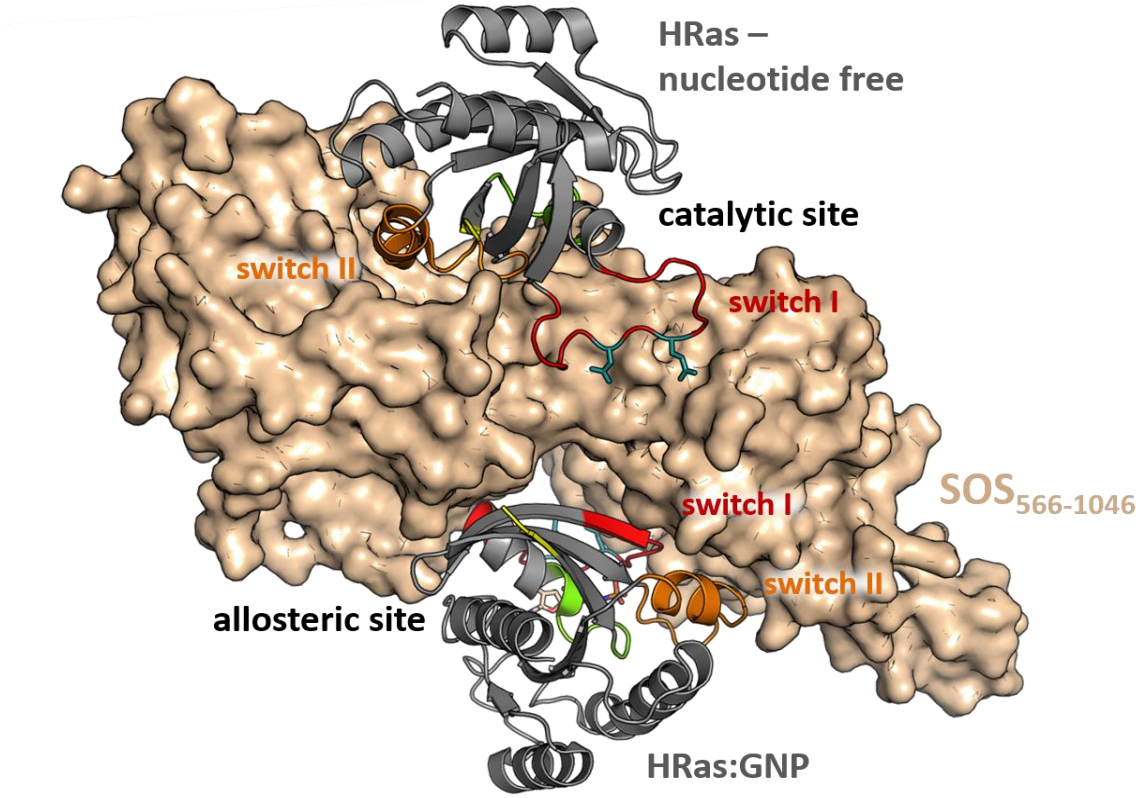

Figure 3-40: Crystal structure of $SOS_{566-1046}$ in complex with nucleotide free HRas bound at the catalytic site and HRas:GNP bound to the allosteric site (PDB ID: 1NVW).[203]
The HRas structures are shown in cartoon representation (gray), the SOS structure is displayed in surface representation (beige). The switch I and II regions are colored in red and orange respectively. The P-loop is marked in green. The N-terminal regions of the HRas proteins are highlighted in yellow. The acceptor labeling sites are colored in turquoise.

The binding affinity of Ras:GDP to either SOS site is relatively low (K_D > 50 μM)[205,206]. Thus, binding of the GDP-bound species should therefore be negligible in the present experimental setup. However, upon nucleotide exchange the affinity increases ($K_D \sim$ 10 μM)[205,206] and could potentially lead to binding of a significant amount of then GTP-bound KRas molecules to the allosteric site of SOS. Due to the interaction between the allosteric SOS site with the switch I region and the position of the N-terminus in close proximity to the GEF surface, this could have an impact on the observed FRET signal. However, an effect on the FRET signal was not observed in the conditions used in this work. Furthermore, excess GDP (Figure 3-39) and GAP-induced GTP hydrolysis (Figure 3-41) restore the initial fluorescence signal, clearly indicating that the observed FRET signal change is indeed reporting on the nucleotide binding state of the KRas sensor.

Besides a possible corruption of the FRET signal through binding at the allosteric site, the resulting stimulation of the nucleotide exchange activity at the catalytic SOS site could complicate the kinetic analysis of the nucleotide exchange activity.

3.1.12 KRas FRET sensor - GAP-induced GTP hydrolysis

In an effort to test if the KRas sensors are susceptible to GAP-mediated deactivation, activated KRas was incubated with an excess of the p120 GAP domain (referred to as $RasGAP_{714-1047}$ or RasGAP) and the FRET signal change was monitored through sensitized emission (2.5.4.2).

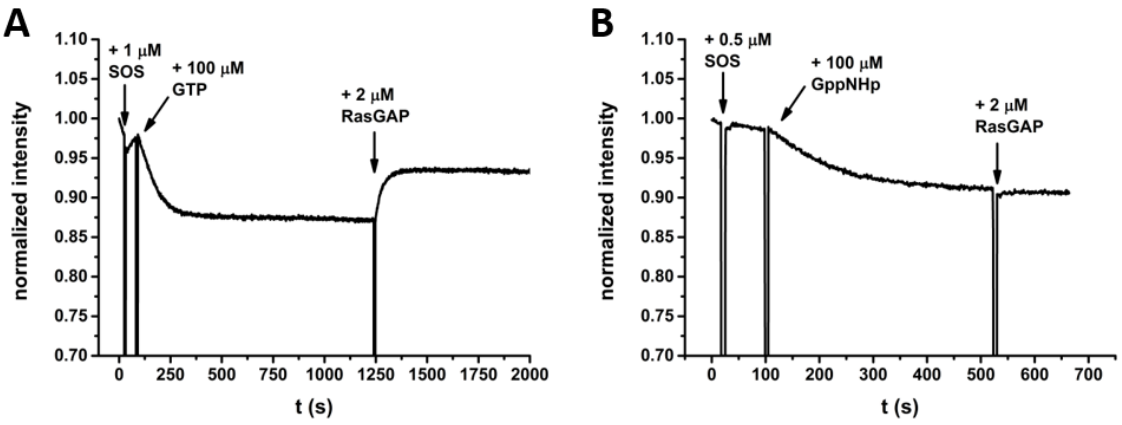

Figure 3-41: KRas FRET sensor reports on RasGAP-induced GTP hydrolysis.
(A) Addition of 2 μM $RasGAP_{714-1047}$ to 200 nM GTP-bound EGFP-KRasD30C-TF3 reverses the initial drop in FRET signal intensity upon nucleotide exchange. **(B)** Addition of 2 μM $RasGAP_{714-1047}$ to 200 nM GppNHp-bound EGFP-KRasD30C-TF3 fails to reverse the change in fluorescence signal. Changes in FRET efficiency were observed by sensitized emission with excitation at 480 nm and emission collected at 580 nm.

200 nM KRas sensor were activated through addition of 1 μM $SOS_{564-1049}$ in the presence of 100 μM GTP. After completion of the nucleotide exchange, 2 μM of $RasGAP_{714-1047}$ were added (Figure 3-41 and Figure 5-19). As expected, the change in FRET signal after GDP to GTP exchange, was reversed through addition of RasGAP, restoring the initial signal intensity. The experiments were repeated using the non-hydrolysable GTP analog GppNHp instead of GTP (Figure 3-41 B), to ascertain that the observed FRET response was indeed caused by GTP hydrolysis,. In this case, $RasGAP_{714-1047}$ failed to reverse the FRET signal change.

To assess the influence of the introduced modifications on the GAP kinetics, the catalytic efficiencies of EGFP-KRasD30C-TF3, mCitrineΔ11-KRasE31C-TF4 and wild type KRas were determined as described previously (3.1.5). In comparison to $KRas_{wt}$ ($k_{cat}/K_M = (1.4 \pm 0.3) \cdot 10^5\ (M \cdot s)^{-1}$), the catalytic efficiency observed for EGFP-KRasD30C-TF3 ($k_{cat}/K_M = (8 \pm 1) \cdot 10^5\ (M \cdot s)^{-1}$) is reduced by a factor of 1.7 (Figure 5-20 A, B and E,F). For mCitrineΔ11-KRasE31C-TF4 ($k_{cat}/K_M = (4.3 \pm 0.4) \cdot 10^4\ (M \cdot s)^{-1}$) the catalytic efficiency drops by a factor of 31 (Figure 5-20 C and D). Note that a similar decrease was observed in the GEF assay for these mutants (3.1.11), the GEF-mediated nucleotide exchange of the D30C mutant was slightly impaired (by a factor of 6-7 in the GEF essay) while the E31C mutation reduced the catalytic performance of SOS by a factor of >20. Simultaneous decrease in both GEF and GAP activities towards the KRas constructs may lead to a balanced effect in the KRAs function in cells.

The crystal structure of the HRas-RasGAP complex reveals that the residues E31 and D30 are located in the GTPase-GAP interface but their side chains are not directly involved in interactions with the RasGAP protein

(Figure 3-16).[39] However, the main chain carbonyl group of E31 is involved in binding the catalytic arginine finger via a water molecule. This involvement in the HRas-RasGAP contact site could explain the marked reduction in GAP-mediated GTP hydrolysis for the E31 construct.

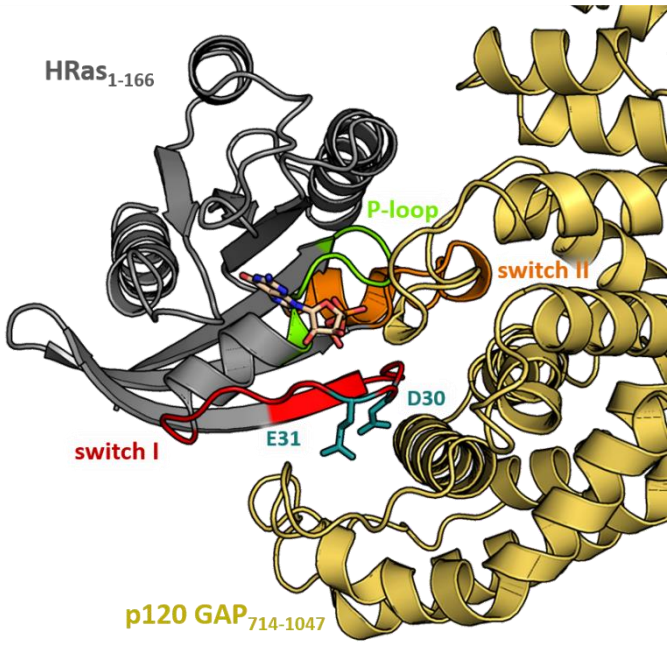

Figure 3-42: Crystal structure of $HRas_{1-166}$:GDP in complex with p120 $GAP_{714-1047}$ (PDB ID: 1WQ1).[39]
The HRas structure is shown in gray and RasGAP is colored in yellow. The HRas labeling sites are highlighted and labeled in turquoise. The switch I and II regions are colored in red and orange respectively. The P-loop is marked in green. The bound guanine nucleotide is depicted in beige with atoms highlighted in red (oxygen), blue (nitrogen) and orange (phosphorous).
Residues from switch I and II region and the P-loop of HRas are involved in the in GTPase-GAP interaction.
The two acceptor labeled residues lie directly in the HRas:RasGAP interface but do not form direct contacts with the GAP molecule in this structure. The main chain carbonyl group of E31 contacts a water molecule in the interaction interface.

Collectively, these experiments demonstrate that the KRas sensors serve as efficient reporters for KRas activation and deactivation. While the interaction with its regulatory partners is preserved, the kinetics are significantly reduced for the E31C construct.

3.1.13 KRas sensor reports on EGF-induced activation *in vivo*

In wild type cells KRas4b enriches on the plasma membrane where it can be activated by SOS in response to upstream signals such as growth factor stimulation. KRas4bs localization at the plasma membrane is governed by electrostatic interaction between a polybasic stretch at the proteins C-terminal region with negatively charged phospholipids in the inner plasma membrane leaflet[207] and by hydrophobic interactions via a farnesylated C-terminal CAAX box.

After labeling, the KRas construct's C-terminus was reconstituted by NCL (3.1.3) with the respective tetrapeptide (-CVIM) to allow protein prenylation in cells. Following microinjection, the cells were incubated for 30-60 min to facilitate prenylation of the reconstituted C-terminus by the endogenous prenylation machinery. After incubation the sensor constructs accumulated at the plasma membrane, suggesting proper prenylation in cells (Figure 3-43 A-C and Figure 3-44). In contrast, injection of a KRas construct, lacking the –CAAX motif, led to cytosolic localization (Figure 3-43 D).

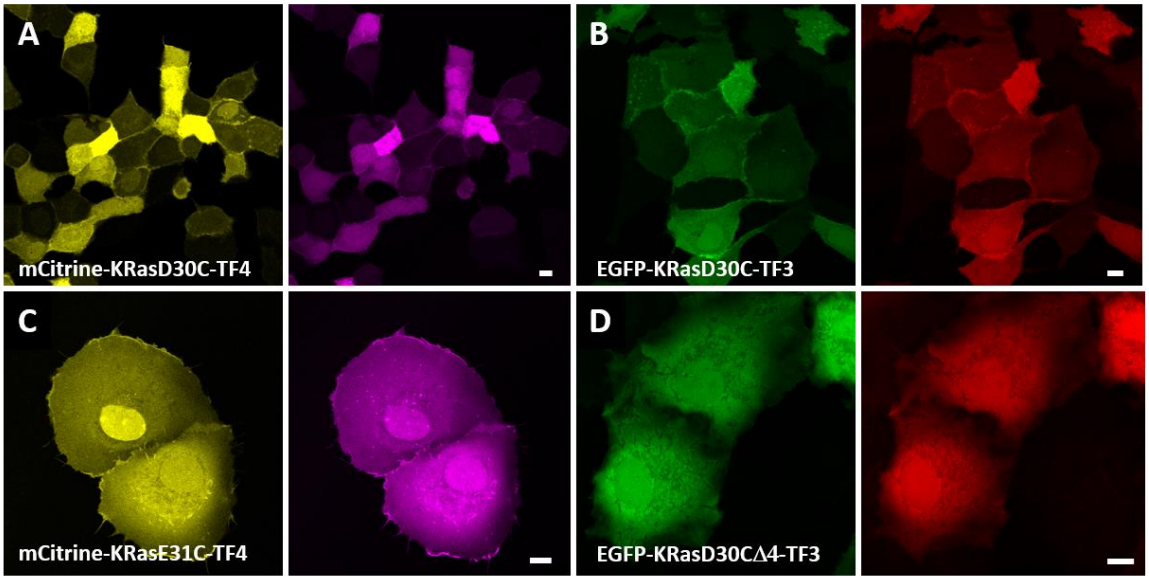

Figure 3-43: KRas FRET sensor injected into MDCK and COS-7 cells.
Fluorescence images of **(A)** mCitrine-KRasD30C-TF4-CVIM and **(B)** EGFP-KRasD30C-TF3-CVIM after injection into MDCK cells. In both channels sensor enrichment at the plasma membrane is observed. **(C)** mCitrine-KRasE31C-TF4-CVIM after microinjection into COS-7 and **(D)** EGFP-KRasD30CΔ4-TF3 CVIM after microinjection into MDCK cells. mCitrine-KRasE31C-TF4 -CVIM enriches at the COS-7 plasma membrane. EGFP-KrasD30CΔ4-TF4 in homogenously distributed in cytoplasm. Left panels: mCitrine (yellow)/EGFP (green), right panels: TF4 (purple)/TF3 (red) fluorescence. Excitation and emission filter settings as described in 2.7.1. Scale bars: 10 μm.

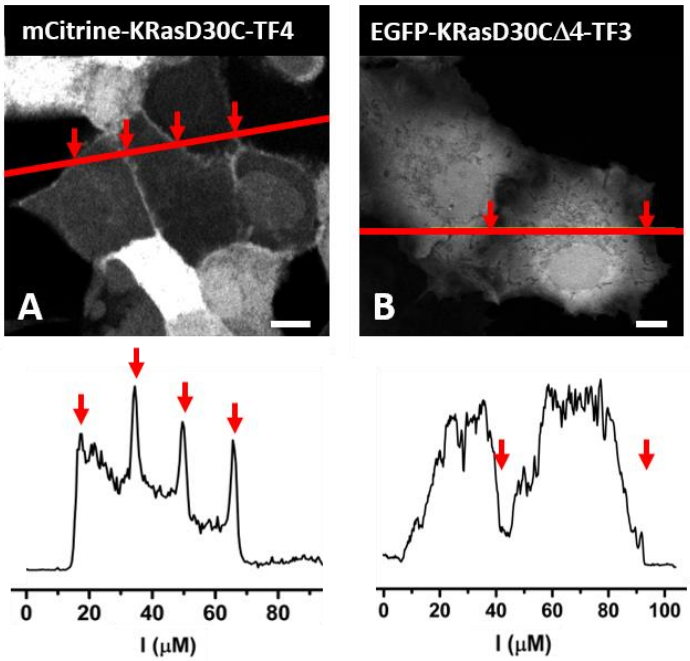

Figure 3-44: C-terminal –CAAX motif is essential for KRas plasma membrane localization.
Upper panel: Fluorescence images and lower panel: corresponding intensity profile plots of **(A)** mCitrine-KRasD30C-TF4-CVIM and **(B)** EGFP-KRasD30CΔ4-TF3 after injection into MDCK cells. mCitrine-KRasD30C-TF4 displays high intensity at the plasma membrane as indicated by red arrows in the fluorescence image and the fluorescence intensity profile plot along the indicated cross section (red line). For EGFP-KrasD30CΔ4-TF4 the sensor fluorescence is homogenously distributed in the cell cytoplasm. Due to reduced cell thickness, lower intensity is observed at the cell edges (indicated by the red arrows along the indicated cross section (red line)). Excitation and emission filter settings as described in 2.7.1. Scale bars: 10 μm.

Addition of epidermal growth factor (EGF) to cell medium triggers cell proliferation. This process is mediated by the transmembrane EGF receptor (EGFR). Upon EGF binding the receptor dimerizes and undergoes autophosphorylation, inducing the formation of signaling complexes (Figure 1-7 C). Here, EGF stimulation was used to observe activation of the KRas sensor in cells.

In vitro KRas activation through SOS-mediated nucleotide exchange resulted in a decrease in FRET efficiency, evident as a drop in sensitized emission signal (3.1.11). Thus, an increase in donor fluorescence lifetime in FLIM measurements upon KRas activation would be expected.

To increase the cells' sensitivity towards EGF stimulation, they were serum starved overnight (0.5 % serum) prior to microinjection and imaging. Stimulation of microinjected cells with EGF (100 ng/ml) led to a rapid increase of the donor fluorescence lifetime in both MDCK and COS-7 cells, indicating EGF induced KRas activation (Figure 3-45 and Figure 3-46). KRas activation in MDCK cells occurred predominantly at the plasma membrane as indicated by the higher fluorescence lifetime observed in these areas (Figure 3-45 C).

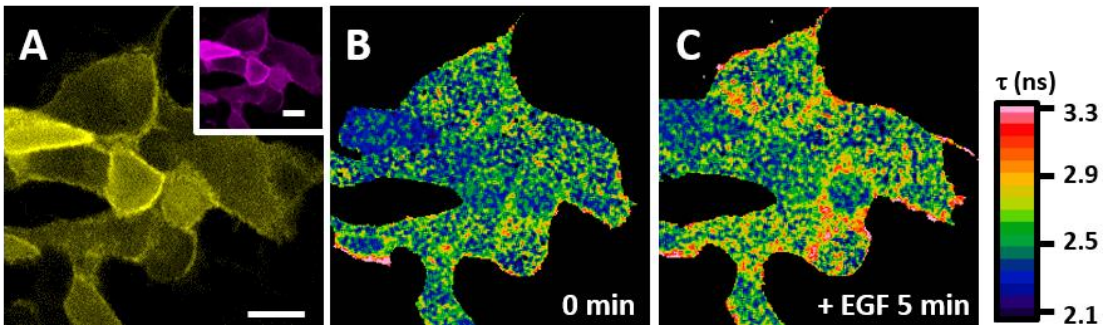

Figure 3-45: Imaging of EGF induced KRas activation in cells by FLIM.
(A) Confocal images of mCitrine-KRasE31C-TF4-CVIM injected into serum starved MDCK cells. FLIM images of mCitrine lifetime **(B)** before and **(C)** 5 min after EGF stimulation. False color calibration bar for lifetime images as reference. Scale bar: 20 μm.

Activation at the plasma membrane is consistent witch EGFR-Grb2 mediated SOS recruitment.

The sensor response upon EGF stimulation was monitored in batch experiments for multiple cells over a time course of >20 min with FLIM images collected every 1-2 min. For analysis the injected cells were separated from the background using a binary mask generated by intensity thresholding. Lifetime profiles were generated by selecting single cells as ROIs and using the ImageJ software to determine the average lifetime at each time point. For control experiments, EGF stimulation was repeated with cells injected with donor only constructs (Figure 5-21 A and B), constructs lacking the C-terminal prenylation motif (Figure 5-21 C and D) and cells treated with the EGFR kinase inhibitor Erlotinib (Figure 5-21 E and F).[208,209] In contrast to the intact sensor constructs, no significant change in donor lifetime was observed in these control experiments (Figure 3-46).

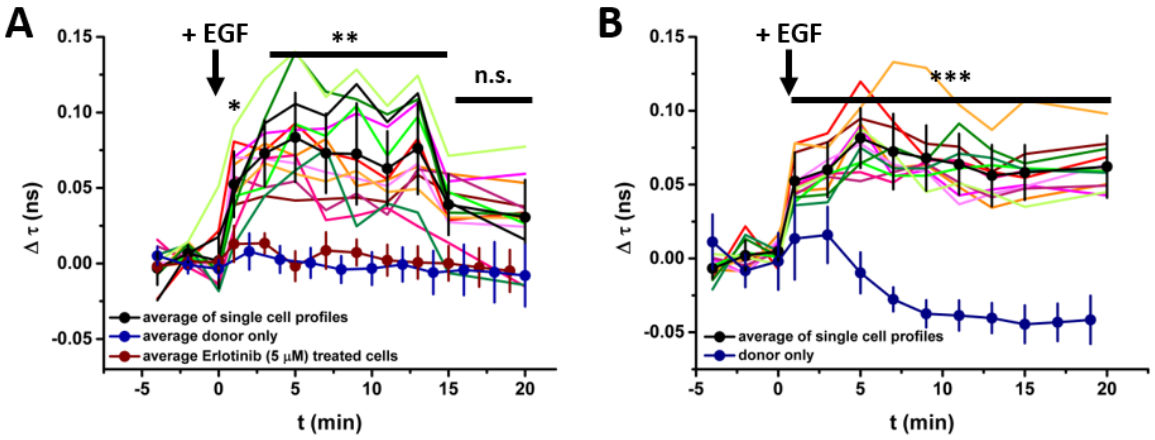

Figure 3-46: Quantification of fluorescence lifetime change after EGF stimulation
Colored lines represent individual cell lifetime changes of MDCK cells injected with **(A)** mCitrine-KRasE31C-TF4-CVIM or **(B)** EGFP-KRasD30C-TF3-CVIM respectively. The black arrow at t=0 s indicates addition of 100 ng/ml EGF to cell medium. Black lines with error bars represent mean ± s.d. (n=12-13 cells). Blue line and red line with error bars represent control measurements of donor only constructs (mean ± s.d. (n =13 cells)) or cells treated with Erlotinib (mean ± s.d. (n=14 cells)), respectively. Two-tailed t-test: *: $p < 0.05$, **: $p < 0.01$, ***: $p < 0.001$.

KRas activity peaks at 5 min after EGF stimulation. In most cases the initial increase in KRas activation was sustained over the time course of 20 min (Figure 3-46 B). Rapid and persisting increase in Ras activity upon continuous EGF stimulation is consistent with previous reports using HRas sensors.[210] Western blot analysis of KRas activation in PANC-1 cells using the Ras binding domain of c-Raf revealed maximal KRas activation 5 min after EGF treatment and gradual decline of the GTP bound KRas fraction after about 15 min.[211]

EGF-induced membrane ruffles displayed increased fluorescence intensity at the edge of the cell, indicating KRas enrichment. However, in contrast to HRas that is activated at the free cell edge[149], KRas activity is lower at this area (Figure 3-47 A-D). The opposing gradients of H- and KRas activity imply different mechanisms for regulating each Ras isoform. Furthermore, unstimulated COS-7 cells displayed an activity gradient with lower lifetime at the cell edges (Figure 3-47 F and H). The difference in lifetime between cell edge and center persisted throughout EGF stimulation while the overall KRas activity increased as indicated by higher donor lifetime (Figure 3-47 H). This activity gradient may be caused by a negative feedback on KRas activation from the signaling of actin rearrangement.

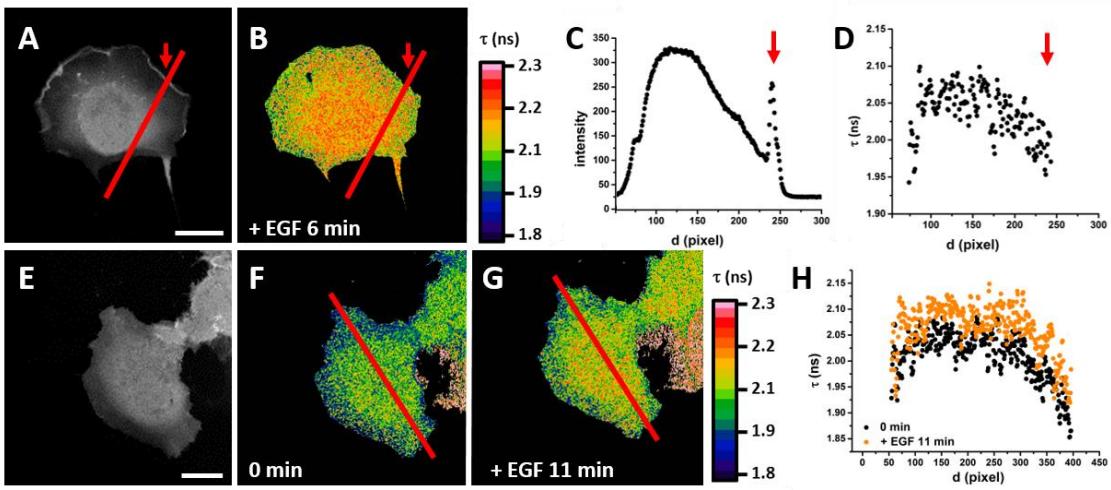

Figure 3-47: KRas sensor enriches at membrane ruffles, but does not display increased KRas activity. KRas activity exhibits a gradient in COS-7 cells.
(A) Intensity and **(B)** FLIM image of EGFP-KRasD30C-TF3 after EGF stimulation in a serum starved COS-7 cell. Arrow indicates membrane ruffling. Profiles of fluorescence intensity **(C)** and fluorescence lifetime **(D)** along the indicated line in **(A)** and **(B)**. **(E)** Intensity and **(F-G)** FLIM image of EGFP-KRasD30C-TF3-CVIM in serum starved COS-7 cells **(F)** before and **(G)** 11 min after EGF stimulation. **(H)** Quantification of the fluorescence lifetime along the indicated cross section (red line) in **(E)** and **(F)**. Lifetime plot before (black) and after (orange) EGF stimulation. False color calibration bar for lifetime images as reference. Scale bar: 20 μm.

3.2 Rab1 trafficking

While fulfilling their regulatory roles in vesicular trafficking most Rab proteins travel from one subcellular compartment to another. To re-enter their functional cycle, they have to return to their initial membrane. This highly dynamic process is linked to the GTPase's activation/deactivation cycle and is tightly regulated by GEFs and GAPs. This spatial cycling further depends on binding of solubilization factors such as GDI and REP (Figure 1-6).

Here, the dynamics of Rab1 trafficking between the cytoplasmic pool and the Golgi organelle were examined using fluorescence recovery after photobleaching (FRAP) and photoactivation experiments. The kinetics of Rab1 delivery to the Golgi membrane were studied by two complementary approaches: (1) by FRAP of the Golgi localized Rab1 fraction and (2) by photoactivation of the cytoplasmic Rab1. The opposite direction of Rab1 trafficking, originating at the Golgi membrane, was investigated by localized activation of paGFP-Rab1 at the Golgi membrane (3.2.2).

3.2.1 Characterization of Rab1 trafficking from cytoplasm to Golgi

k_{C-G} determined by Golgi bleaching

To obtain the apparent rate constant of Rab1 trafficking from the cytoplasm to the Golgi, Golgi-localized EGFP-Rab1 was bleached by extensive irradiation with maximal laser power. The course of a typical Golgi bleaching experiment of EGFP-Rab1 is depicted below (Figure 3-48).

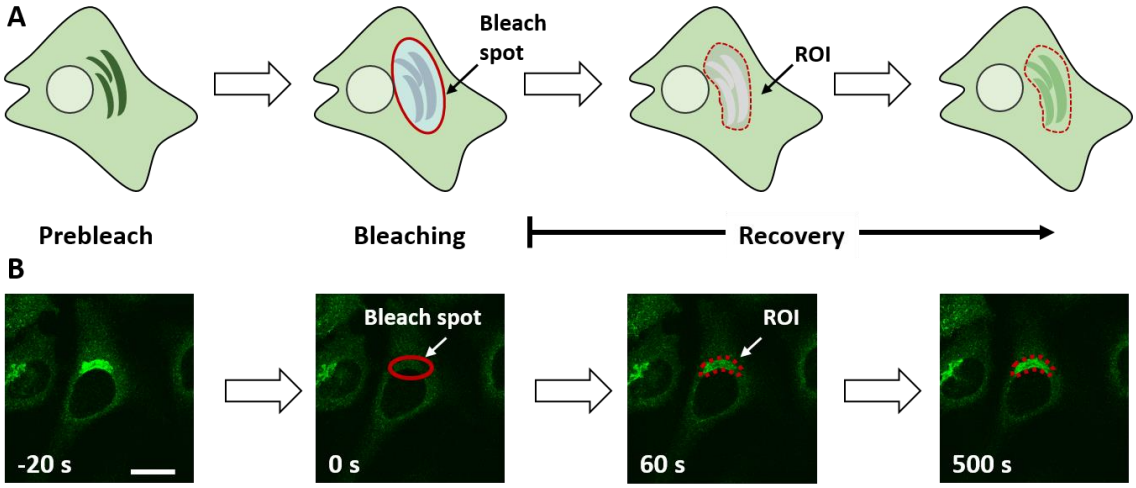

Figure 3-48: Bleaching of EGFP-Rab1$_{wt}$ at the Golgi body.
(A) Scheme depicting a typical bleaching experiment to determine k_{C-G} for Rab1 trafficking from cytoplasm to Golgi. **(B)** Exemplary EGFP fluorescence images of a cell expressing EGFP-Rab1$_{wt}$. The bleached area is circled in red. After bleaching the fluorescence intensity increases at the region of interest (ROI, dashed red line) on the Golgi was followed by time-lapse imaging. Scale bar: 20 µm.

For image analysis, the mean fluorescence intensity at the Golgi was determined using the FRAP profiler plugin of ImageJ and normalized to the prebleach intensity as described in the method section (2.7.3). A typical FRAP profile is displayed in Figure 3-49.

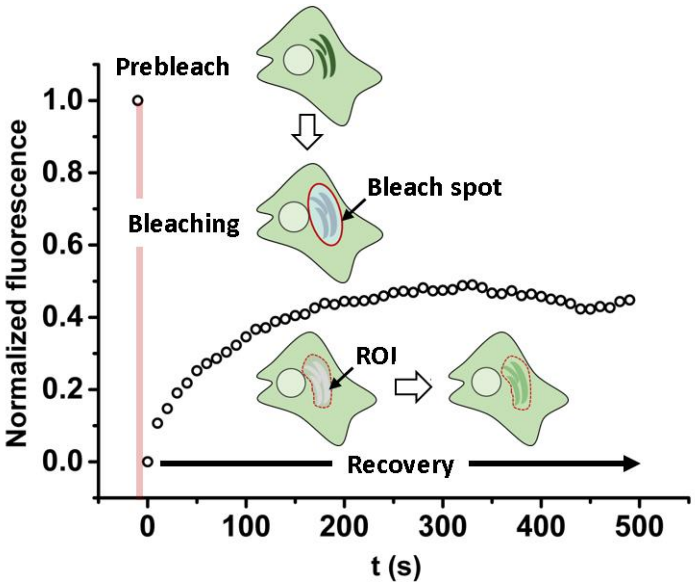

Figure 3-49: Exemplary intensity profile of EGFP-Rab1 during Golgi FRAP experiment.
The graph depicts the course of the average EGFP-Rab1$_{wt}$ intensity at the marked ROI (dashed red line) during a typical bleaching experiment. The fluorescence intensity at the ROI was normalized to the prebleach intensity.

After photobleaching the fluorescence intensity partially recovers and reaches a plateau. The recovery curve can be fitted with the single exponential function Eq. 2-14 to obtain the apparent rate constant k_{obs} for Rab1 flux from the cytoplasm to the Golgi organelle.

$$I_{norm}(t) = I_{\infty}\left(1 - e^{-k_{obs} \cdot t}\right) \qquad \textbf{Eq. 2-14}$$

$$t_{1/2} = \frac{\ln(2)}{k_{obs}} \qquad \textbf{Eq. 3-3}$$

Here, I_{norm} is the fluorescence intensity at time t, I_{∞} is the fluorescence intensity reached after completed equilibration and k_{obs} is the observed rate constant for fluorescence recovery. Using Eq. 2-15, the half-time of the fluorescence recovery ($t_{1/2}$) can be calculated from k_{obs}. The apparent rate constant $k_{C\text{-}G}$ for Rab1 delivery from the cytoplasm to the Golgi was obtained as the average of 3-6 recovery curves fitted individually. Due to the fluidity of Golgi-bound proteins it is crucial that bleaching of the Golgi localized material is complete to exclude attenuation of the observed recovery through lateral diffusion of unbleached Golgi localized EGFP-Rab1.

k_{C-G} for $Rab1_{wt}$ trafficking from cytoplasm to Golgi by FRAP

After bleaching of EGFP-Rab1 on the Golgi the recovery of fluorescence intensity reached a plateau after approximately 200 s at about 50 % of the initial prebleach intensity (Figure 3-50 A). The average apparent rate constant for EGFP-Rab1 delivery from the cytoplasm to the Golgi was determined as $k_{C-G} = (1.6 \pm 0.4) \cdot 10^{-2}$ 1/s. The corresponding recovery half-time is $t_{1/2} = 43$ s.

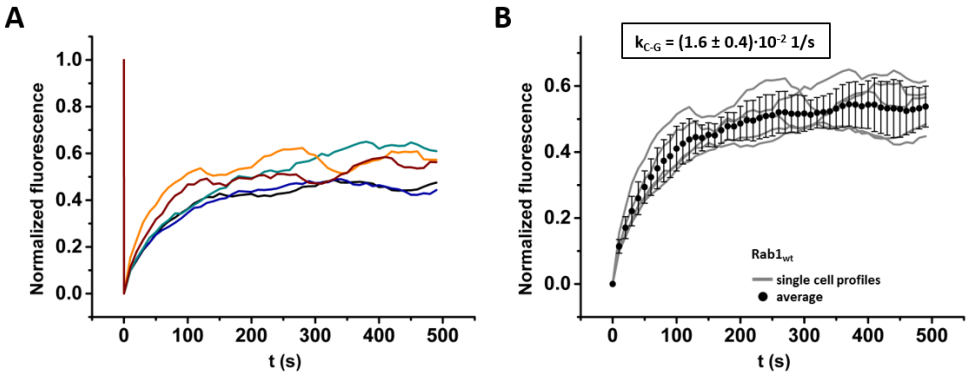

Figure 3-50: Recovery curves for EGFP-$Rab1_{wt}$ photobleaching at the Golgi and average k_{C-G}.
(A) Plot of normalized average EGFP intensity at Golgi ROI during FRAP experiment. Each line represents one bleaching experiment. **(B)** Plot of individual (gray lines) and average (black circles, mean ± s.d.) recovery curves. k_{C-G} was obtained as the average of individual k_{obs} values. k_{obs} was determined for each recovery curve by fitting with the monoexponential function (Eq. 2-14).

When performing FRAP experiments, the contribution of newly synthesized protein and photobleaching through continuous time-lapse imaging have to be considered. The observed recovery of fluorescence after photobleaching could result from protein redistribution of fluorescent protein localized outside the bleaching ROI and/or newly protein synthesized in the ROI. By comparing the kinetics of EGFP-$Rab1_{wt}$ recovery in untreated and in cells treated with the protein synthesis inhibitor cycloheximide, the effect of protein synthesis on the course of fluorescence recovery can be assessed. As can be discerned from the obtained recovery curves (Figure 5-22) and the corresponding apparent rate constants ($k_{C-G} = (1.8 \pm 0.4) \cdot 10^{-2}$ 1/s), the newly synthesized EGFP-$Rab1_{wt}$ did not affect the fluorescence recovery of EGFP-Rab1 after Golgi photobleaching.

To evaluate the effect of photobleaching during imaging, the FRAP experiment was repeated omitting the bleaching step. Over the time course of time-lapse imaging the fluorescence intensity decreased by less than 5 % of the initial value (Figure 5-23). Thus, photobleaching during imaging can be neglected.

k_{C-G} determined by fluorescence localization after photoactivation (FLAP)

In a complementary approach k_{C-G} for Rab1 trafficking from the cytoplasm to the Golgi was determined by fluorescence localization after photoactivation (FLAP). specific photoactivation of the cytoplasmic Rab1 fraction,

The cytoplasmic area of cells expressing paGFP-Rab1 was irradiated at 405 nm. The subsequent increase of paGFP-Rab1 fluorescence at the Golgi was then monitored by time-lapse imaging (2.7.3). The course of a typical experiment with paGFP-Rab1 photoactivation in the cytoplasm is depicted in Figure 3-51.

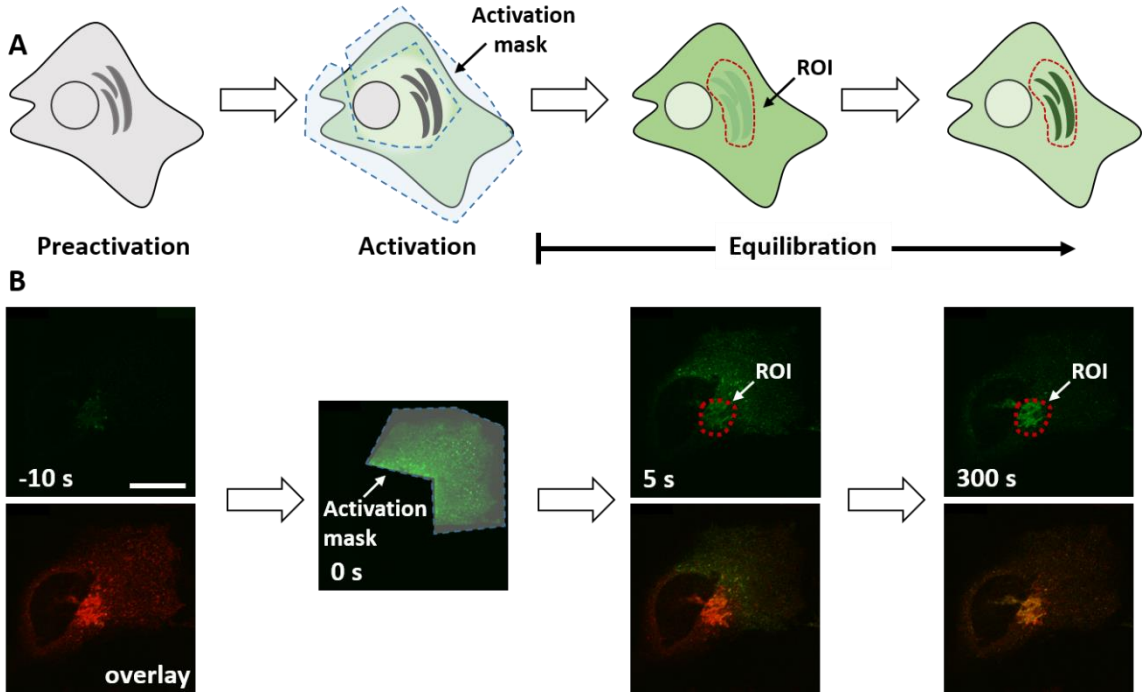

Figure 3-51: Photoactivation of paGFP-Rab1$_{wt}$ in the cytoplasm.
(A) Scheme depicting a typical photoactivation experiment for determining k_{C-G} for cytoplasm to Golgi trafficking. **(B)** Exemplary fluorescence images of a cell expressing paGFP-Rab1$_{wt}$. Upper panel paGFP-Rab1 fluorescence, lower panel overlay with Cherry-Rab1$_{wt}$. The area selected for irradiation is highlighted (dashed blue). After photoactivation, the fluorescence intensity increase at the region of interest (ROI, dashed red line) on the Golgi was followed by time-lapse imaging. Scale bar: 10 µm.

After photoactivation the fluorescence intensity on the Golgi membrane increases and reaches a plateau upon completed equilibration. After normalization, the course of the intensity increase can be fitted with the single exponential equation Eq. 2-14 (2.7.4) yielding the apparent rate constant k_{obs} for Rab1 flux from the cytoplasm to the Golgi.

$$I_{norm}(t) = I_{\infty}\left(1 - e^{-k_{obs} \cdot t}\right) \qquad \textbf{Eq. 2-14}$$

The apparent rate constant k_{C-G} was obtained as the average of individual fits of at least three measurements. An exemplary fluorescence intensity profile for the described photoactivation experiment is displayed in Figure 3-52.

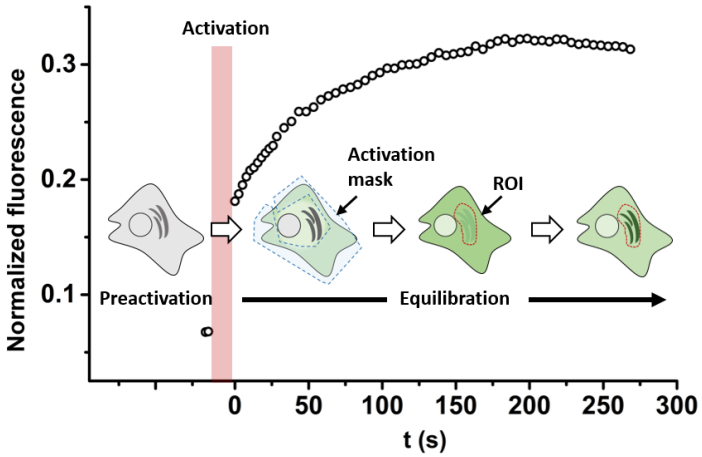

Figure 3-52: Exemplary intensity profile of paGFP-Rab1 at the Golgi following photoactivation in the cytoplasm. The graph depicts the course of the average paGFP-Rab1$_{wt}$ intensity at the marked ROI (dashed red line) during a typical photoactivation experiment. The fluorescence intensity at the ROI was normalized to the intensity prior to irradiation.

In contrast to the FRAP experiments, the observed fluorescence increase on the Golgi cannot be distorted through lateral diffusion of Golgi residing Rab1 or newly synthesized paGFP-Rab1 as these molecules remain "invisible" throughout the experiment.

$k_{C\text{-}G}$ for Rab1$_{wt}$ trafficking from cytoplasm to Golgi by photoactivation

Photoactivation of paGFP-Rab1$_{wt}$ in the cytoplasm leads to increasing fluorescence on the Golgi organelle (Figure 3-53). In agreement with the previous FRAP experiments the intensity reached saturation after about 170-180 s following activation.

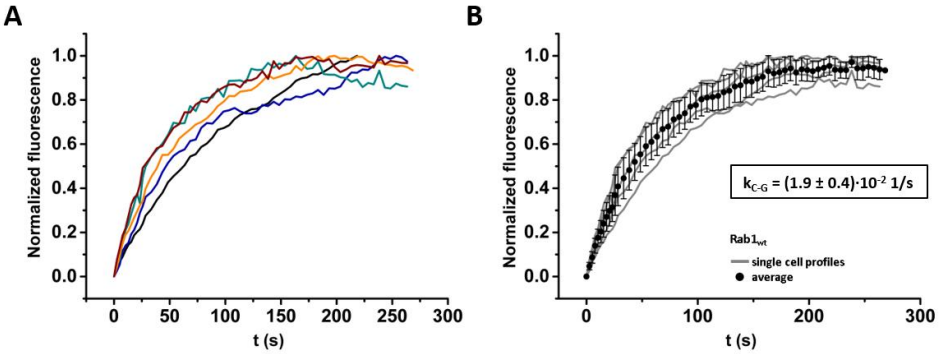

Figure 3-53: Fluorescence intensity increase at Golgi following photoactivation of paGFP-Rab1$_{wt}$ in the cytoplasm. **(A)** Plot of normalized average paGFP intensity at Golgi ROI following photoactivation in the cytoplasm. Each line represents a single photoactivation experiment. **(B)** Plot of individual (gray lines) and average (black circles, mean ± s.d.) intensity curves. $k_{C\text{-}G}$ was obtained as the average of individual k_{obs} values. k_{obs} was determined for each curve by fitting with the monoexponential function (Eq. 2-14).

The average rate of paGFP-Rab1 delivery from the cytoplasm was determined with $k_{C\text{-}G}$ = (1.9 ± 0.4)·10^{-2} 1/s and a corresponding half-time of $t_{1/2}$ = 36 s. These values are in good keeping with the rate constant obtained via the corresponding FRAP experiment ($k_{C\text{-}G,\ FRAP}$ = (1.6 ±0.4)·10^{-2} 1/s, $t_{1/2}$ = 43 s).

Effect of impaired Rab1 functioning on cytoplasm to Golgi transport kinetics

Rab1 delivery to the Golgi organelle is mediated by two pathways: a non-vesicular pathway facilitated by GDI[62,197,212,213] and a vesicular pathway derived from the ER-Golgi transport[194,195,214] (Figure 3-54). Both pathways contribute to the observed rate constant for Rab1 delivery from the cytoplasm to the Golgi (k_{C-G}).

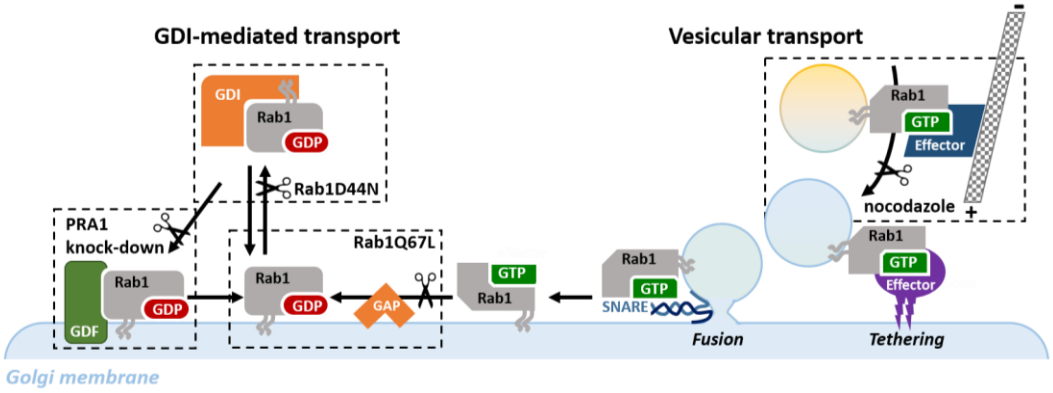

Figure 3-54: Rab1 trafficking from cytoplasm to Golgi.
Delivery of Rab1 to the Golgi membrane is mediated by GDI-based transport and vesicular transport. Here, the effect of impaired Rab1 deactivation (Rab1Q67L), abolished GDI-binding (Rab1D44N), disrupted vesicular transport (nocodazole treatment) and PRA1 knock-down on the kinetics of Rab1 delivery to the Golgi membrane were examined.

To assess the effect of impaired GTPase functioning on Rab1 trafficking from cytoplasm to Golgi, the FRAP and photoactivation experiments were repeated with: (1) the constitutively active Rab1Q67L mutant[41,43], (2) the GDI-binding deficient mutant Rab1D44N[212], (3) after treatment with nocodazole[139,140] and (4) in PRA1 knock-down cells[215]. The obtained rate constants for cytoplasm to Golgi delivery (k_{C-G}) are summarized in Figure 3-55. Furthermore, the relative fluorescence intensity of Rab1 localized to the cytoplasm compared to the Golgi was quantified.

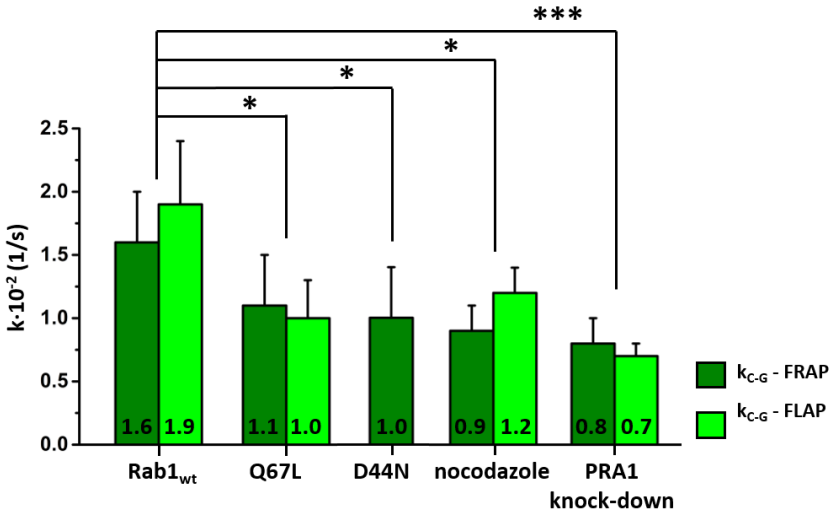

Figure 3-55: Summary of obtained rate constants k_{C-G}.
Summary of the apparent rate constants for cytoplasm to Golgi trafficking for Rab1 wild type, Rab1Q67L, Rab1D44N, Rab1 wild type in cells treated with nocodazole and in PRA1 knock-down cells.

Inhibition of GTPase cycle suppresses Rab1 delivery to Golgi and leads to accumulation of enlarged vesicles

Rab1 activity is critical for biogenesis and maintenance of a functional Golgi.[216] When the ability of Rab1 to interact with effector proteins is inhibited, e.g. through TBC1D20 overexpression, dominant-negative mutants or Rab1 depletion, the ER to Golgi transport is blocked and the Golgi organelle disintegrates.[193,216] The effects of expressing the predominantly active mutant Rab1Q67L are not as severe. The Golgi organelle remains largely intact and ER to Golgi transport is preserved.[216] However, the cells display a different phenotype than cells expressing wild type Rab1 (Figure 3-56 and Figure 3-57) and the kinetics of Rab1 delivery from the cytoplasm to the Golgi membrane are significantly slowed (Figure 3-55).

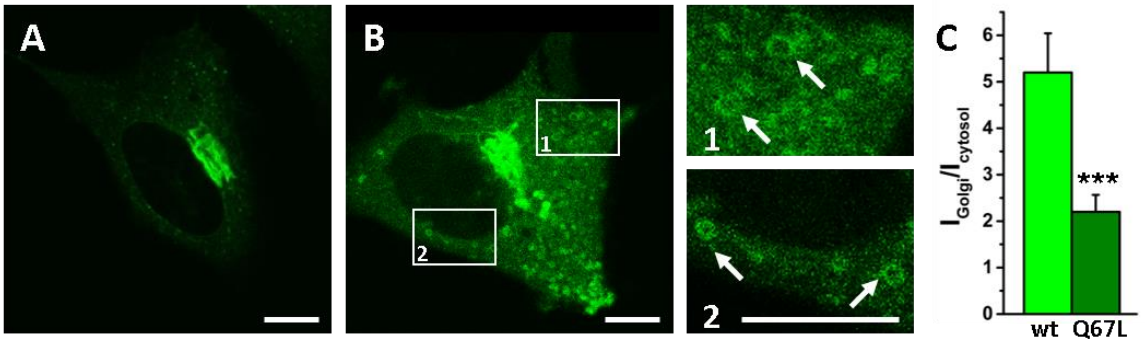

Figure 3-56: Rab1Q67L expression led to increased cytosolic localization and the formation of enlarged vesicles. Fluorescence images of HeLa cells expressing **(A)** EGFP-$Rab1_{wt}$ and **(B)** EGFP-Rab1Q67L. For **(B)** two parts of the image were enlarged (Box 1 and 2) Vesicular structures are highlighted by white arrows. **(C)** Ratio of the average EGFP fluorescence at Golgi to cytoplasm. Error bars: mean ± s.d. (n=3-7). Two-tailed t-test: ***: $p < 0.001$. Excitation and emission filter settings as described in 2.7.1. Scale bars: 10 μm.

Expression of Rab1Q67L led to the formation of enlarged vesicles in the cytoplasm. Furthermore, the relative fluorescence intensity of the cytoplasm compared to the Golgi was significantly increased in comparison to cells expressing wild type Rab1 (Figure 3-56). The same observation was made after photoactivation of paGFP-Rab1Q67L in the cytoplasm (Figure 3-57).

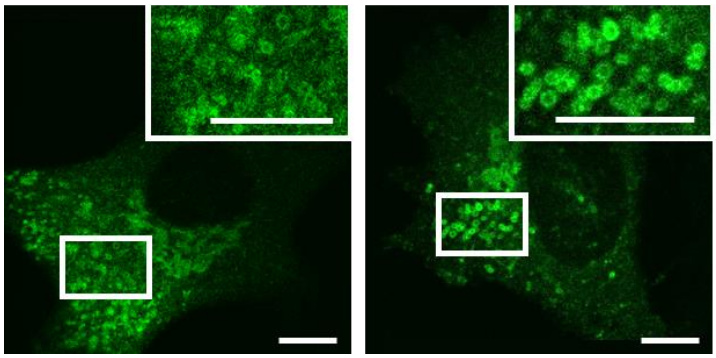

Figure 3-57: Following photoactivation of paGFP-Rab1Q67L enlarged vesicles in the cytoplasm become visible. Fluorescence images of HeLa cells expressing paGFP-Rab1Q67L after photoactivation. Boxed images are enlarged in the inset. Insets show vesicular structures in the cytoplasm. Excitation and emission filter settings as described in 2.7.1. Scale bars: 10 μm.

Rab1Q67L showed a significantly reduced $k_{C\text{-}G}$ rate of $(1.0 \pm 0.4)\cdot10^{-2}$ 1/s when compared to wild type Rab1 ($k_{G\text{-}C,wt} = (1.9 \pm 0.4)\cdot10^{-2}$ 1/s). In the analogous FRAP experiments, $k_{C\text{-}G}$ was also reduced with $k_{C\text{-}G,wt} = (1.6 \pm 0.4)\cdot10^{-2}$ 1/s and $k_{C\text{-}G,Q67L} = (1.1 \pm 0.4)\cdot10^{-2}$ 1/s, respectively.

In contrast to its dominant-negative mutant, RabQ67L maintains the ability to interact with its effector proteins and thus can drive ER-mediated vesicular transport. Rab1Q67L overexpressing does not interfere with Golgi biogenesis, however the reduced kinetics in Rab1 delivery to the Golgi membrane suggest that compromised Rab1 deactivation prevents efficient spatial cycling of Rab1.

The enrichment of enlarged vesicular structures further suggests, that constitutively active Rab1 leads to (partially) defective vesicular transport. Rab1 activity at ER exit sites is regulated by its GAP TBC1D20. It is plausible to assume that TBC1D20 activity is targeted towards maintaining the local Rab1 activity at a level that allows for sufficient assembly of transport vesicles by continuous Rab1 deactivation. Thus, persistent Rab1Q67L activity could bypass the regulatory role of TBC1D20 at the ER, leading to the formation of vesicles that cannot proceed properly in vesicular transport (Figure 3-58).

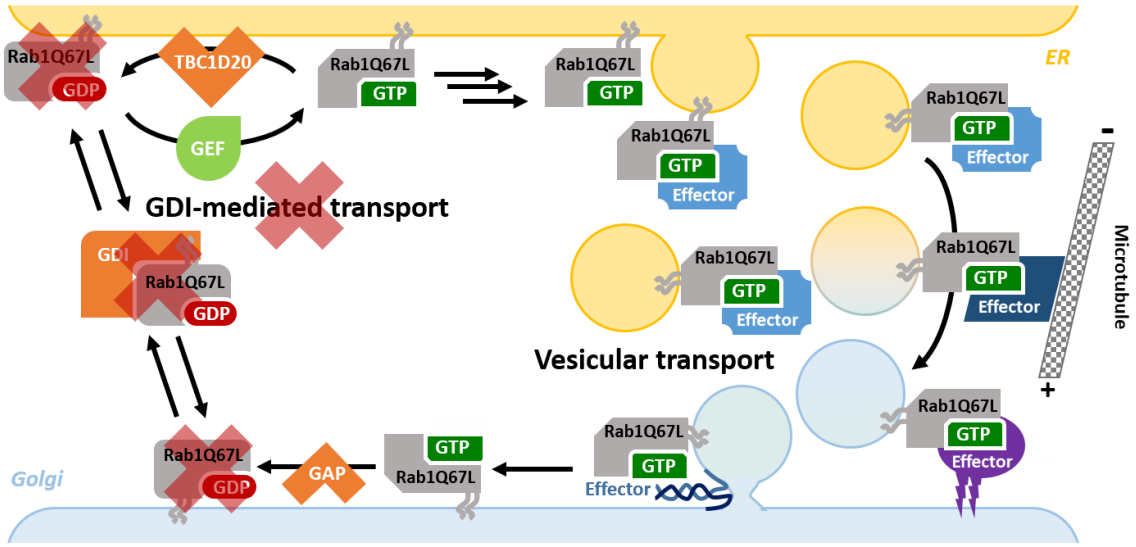

Figure 3-58: Model for effect of constitutively active Rab1Q67L on ER to Golgi trafficking.
Rab1Q67L cannot be effectively deactivated by the ER localized GAP TBC1D20, possibly leading to increased vesicle formation at ER exit sites. Due to low affinity of GDI towards GTP-bound Rab1, GDI-mediated transport is abrogated.

An alternative explanation is that high Rab1 activity leads to continuous recruitment of effector proteins and thus initiates vesicle budding at sites that are usually not involved in the formation of transport vesicles. Another critical interaction that depends on the nucleotide binding state of the GTPase, is its extraction of membrane bound Rab1 through GDI. The affinity of GDI towards Rab proteins is reduced by three orders of magnitude between the inactive GDP-bound and active GTP-bound GTPase.[63] Thus, constitutively active Rab1Q67L cannot be efficiently extracted by GDI and remains attached to membranes. According to these findings, delivery of Rab1Q67L to the Golgi should be exclusively mediated by the vesicular transport pathway.

GDI-binding deficiency leads to slower kinetics of Rab1 delivery to Golgi

The switch I mutant Rab1D44N is unable to associate with GDI but retains its initial membrane targeting through prenylation and interaction with REP (although reduced to about 50 % in comparison to wild type Rab1).[212,217] Based on the current model of Rab cycling, this inability to be recycled through GDI-mediated membrane extraction should result in a "dead end" for Rab1 at the Golgi membrane.

Here, Rab1D44N delivery to the Golgi membrane was observed after photobleaching at the Golgi membrane (Figure 5-27). However, the kinetics were significantly reduced from $k_{C\text{-}G} = (1.6 \pm 0.4)\cdot 10^{-2}$ 1/s for the wild type protein to $k_{C\text{-}G} = (1.0 \pm 0.4)\cdot 10^{-2}$ 1/s for Rab1D44N. It can be speculated that the maintained ER to Golgi transport can be attributed to endogenous Rab1. It has been suggested in a previous report that continuous delivery of newly prenylated Rab1D44N to the ER donor compartment would allow for at least one "round" of vesicular delivery.[212] The observed rate constant for Rab1D44N delivery is in keeping with that of another GDI-binding deficient mutant, Rab1Q67L ($k_{C\text{-}G,\,Q67L} \approx 1\cdot 10^{-2}$ 1/s , Figure 3-55).

When comparing the Golgi to cytoplasmic localization, EGFP-Rab1D44N is significantly more abundant in the cytoplasm than $Rab1_{wt}$ (Figure 3-59). As the cytosol should be completely devoid of any GDI-bound Rab1D44N[212], the accumulation of EGFP-Rab1D44N in the cytoplasm most likely arises from unprenylated species. It should be noted, that D44 is located directly in the Rab-effector interface and it cannot be excluded that Rab1D44N interferes with downstream effector binding. However, retained ability to facilitate ER to Golgi transport suggests that interaction with effectors crucial for vesicular transport is partially maintained.

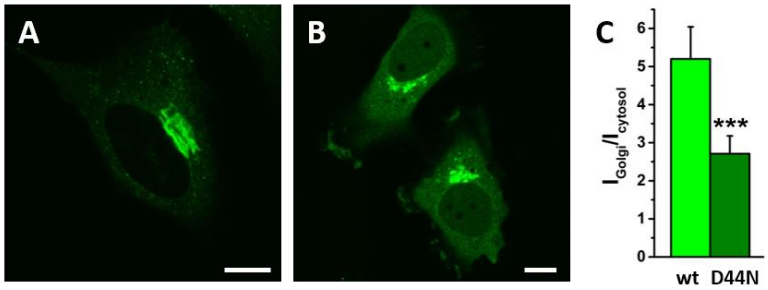

Figure 3-59: Rab1D44N displays increased cytosolic protein localization.
Fluorescence images of HeLa cells expressing **(A)** EGFP-$Rab1_{wt}$ and **(B)** EGFP-Rab1D44N. **(C)** Ratio of the average EGFP fluorescence at Golgi to cytoplasm. Error bars: mean ± s.d. (n=6-7). Two-tailed t-test: ***: $p < 0.001$. Excitation and emission filter settings as described in 2.7.1. Scale bars: 10 μm.

In paGFP-Rab1D44N transfected cells, activation of the cytoplasm did not lead to a significant increase in GFP fluorescence at the Golgi. The fluorescence intensity generated through photoactivation was not sufficient to result in a significant increase at the Golgi ROI. This deficiency can be attributed to the abolished binding of prenylated Rab1D44N to GDI. Thus, only unprenylated Rab1 that cannot attach to the Golgi membrane and a small amount of newly synthesized REP-bound Rab1 are present in the cytoplasm.[212]

Disrupted vesicular transport leads to Golgi fragmentation and slows Rab1 delivery to the Golgi

To assess the effect of abolished vesicular transport on Rab1 trafficking, Rab1 transfected cells were treated, with nocodazole, which prevents microtubule polymerization. Due to interrupted ER to Golgi transport the Golgi apparatus disintegrates and ministacks form at the ER exit sites (Figure 3-60).[139] These stacks continuously exchange Golgi resident enzymes through ER transport. The observed fluorescence recovery kinetics after photobleaching were slowed down from $k_{C\text{-}G}$ = (1.6-1.9)·10^{-2} 1/s for untreated cells to $k_{C\text{-}G,\,FRAP}$ = (0.9 ± 0.3)·10^{-2} 1/s and $k_{C\text{-}G,\,paGFP}$ = (1.2 ± 0.3)·10^{-2} 1/s respectively after nocodazole treatment. This indicates that vesicular transport via microtubules plays an important role in Rab1 trafficking towards the Golgi organelle. However, it is evident that nocodazole treatment did not completely eliminate incoming Golgi traffic. The exchange rate of Golgi resident proteins between peripheral Golgi stacks is to slow (~2 h till equilibration)[139] to account for the comparably fast fluorescence recovery observed for Rab1 ($t_{1/2}$ = 70 s). The fluorescence recovery can presumably be attributed to GDI-mediated transport.

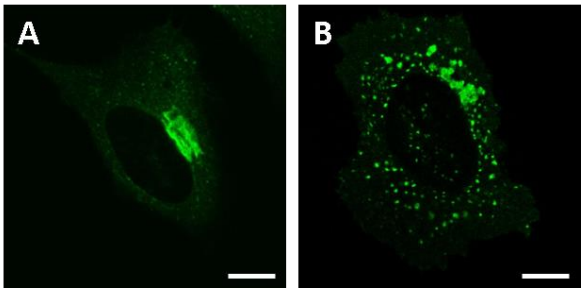

Figure 3-60: Nocodazole treatment interferes with microtubule polymerization resulting in Golgi fragmentation.
Fluorescence images of HeLa cells expressing EGFP-$Rab1_{wt}$ **(A)** before and **(B)** after nocodazole treatment Following nocodazole treatment EGFP-$Rab1_{wt}$ localizes to small fragments that are scattered over the cell. Excitation and emission filter settings as described in 2.7.1. Scale bars: 10 μm.

PRA1 is important for Rab1 delivery to the Golgi

PRA1 is the human homologue of yeast Yip3, which was the first protein shown to exhibit GDF activity.[66] It has been hypothesized that PRA1 fulfills a similar role for Rab:GDI complexes. In PRA1 knock-down cells Rab1 maintained its Golgi localization (Figure 3-61) and the Golgi to cytoplasm intensity ratio remained unchanged. However, the rate of Rab1 delivery to the Golgi was significantly reduced ($k_{C\text{-}G,\,FRAP}$ = (0.8 ± 0.2)·10^{-2} 1/s and $k_{C\text{-}G,\,paGFP}$ = (0.7 ± 0.1)·10^{-2} 1/s) in the PRA1 knock-down cells (Figure 5-28 and Figure 3-55). These findings suggest that PRA1 plays an essential role in Rab1 membrane delivery, potentially by acting as a GDF towards the GDI:Rab1 complex.

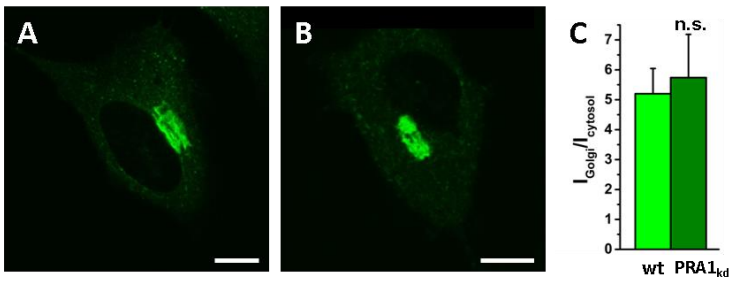

Figure 3-61: $Rab1_{wt}$ retains Golgi localization in PRA1 knock-down cells.
Fluorescence images of EGFP-$Rab1_{wt}$ expressed in **(A)** wild type and **(B)** PRA1 knock-down HeLa cells. **(C)** Ratio of the average EGFP fluorescence at Golgi to cytoplasm. Error bars: mean ± s.d. (n=6-7). Two-tailed t-test: n.s.: not significant. Excitation and emission filter settings as described in 2.7.1. Scale bars: 10 μm.

3.2.2 Rab1 trafficking from Golgi to Cytoplasm

The kinetics of Rab1 trafficking originating from the Golgi were examined through specific activation of paGFP-tagged Rab1 localized at the Golgi. After activation through UV irradiation, the depletion of GFP fluorescence was monitored by time-lapse imaging. The course of a typical photoactivation experiment is depicted below (Figure 3-62).

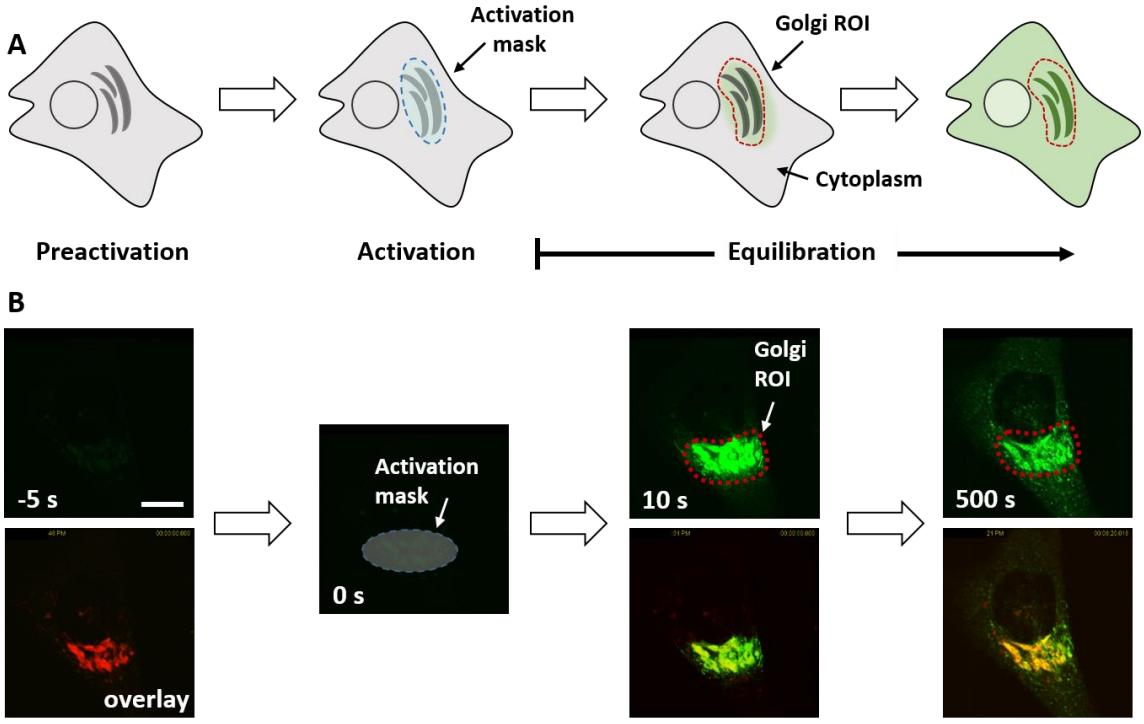

Figure 3-62: Photoactivation of paGFP-Rab1$_{wt}$ at the Golgi.
(A) Scheme depicting a typical photoactivation experiment for determining $k_{G\text{-}C}$. **(B)** Exemplary fluorescence images of a cell expressing paGFP-Rab1$_{wt}$ and the Golgi marker mKate2-giantin. Upper panel paGFP-Rab1 fluorescence, lower panel overlay with mKate2-giantin. The area selected for irradiation is highlighted (dashed blue). After photoactivation the fluorescence intensity decrease at the Golgi membrane was followed by time-lapse imaging. Scale bar: 10 µm.

After photoactivation the initial fluorescence intensity in the Golgi decreases over time while the fluorescence in the cytoplasm increases. The gradual fluorescence depletion can be fitted with the single exponential function Eq. 2-17 to obtain the apparent rate constant k_{obs} for Rab1 departing from the Golgi.

$$I_{norm}(t) = I_{\infty} + A \cdot e^{-k_{obs} \cdot t} \qquad \text{Eq. 2-17}$$

Here I_{norm} is the fluorescence intensity at time t, I_{∞} is the fluorescence intensity reached after completed equilibration and k_{obs} is the observed rate constant. $k_{G\text{-}C}$ for Golgi derived Rab1 trafficking was obtained as the average of individual fits of data from at least three recovery experiments. A representative fluorescence intensity profile obtained for the described photoactivation experiment is depicted in Figure 3-63.

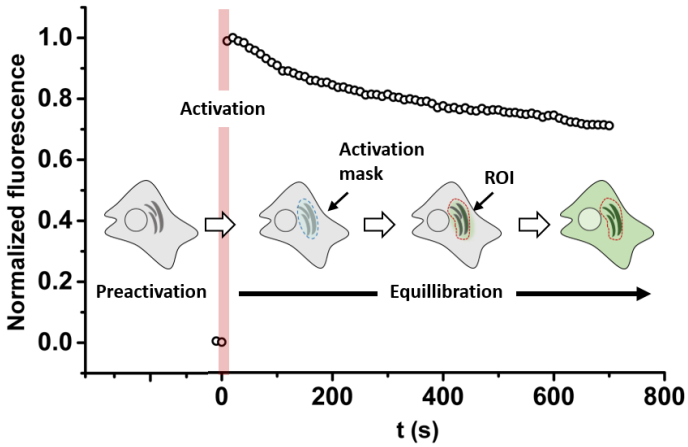

Figure 3-63: Exemplary intensity profile of paGFP-Rab1 at the Golgi after photoactivation.
The graph depicts the course of the average pGFP-Rab1$_{wt}$ intensity at the marked ROI (dashed red line) after a typical photoactivation experiment. The fluorescence intensity at the ROI was normalized to the intensity prior to irradiation.

Rab1$_{wt}$

For wild type EGFP-Rab1 the following fluorescence profiles (Figure 3-64) with an average rate constant $k_{G\text{-}C}$= (0.3 ± 0.1)·10^{-2} 1/s were obtained. As anticipated, the depletion rate of Rab1 is significantly lower than the rate of Rab1 delivery to the Golgi ($k_{G\text{-}C}$ ≈ 1.5-2.0·10^{-2} 1/s). This surplus of Rab1 influx leads to the seemingly stationary localization of Rab1 at the Golgi membrane in the steady state. However, the previously described findings indicating rapid Rab1 influx and the continuous depletion of Rab1 from the Golgi underscore the highly dynamic nature of Rab1 trafficking.

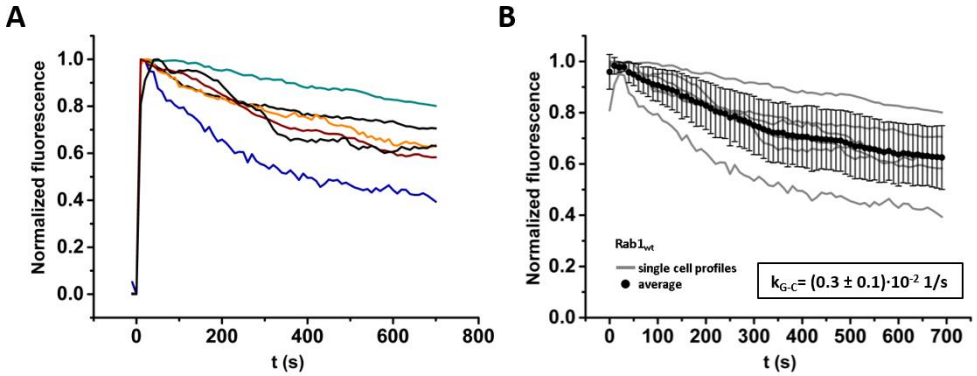

Figure 3-64: Fluorescence intensity decrease at Golgi following photoactivation of paGFP-Rab1$_{wt}$.
(A) Plot of normalized average paGFP intensity at Golgi ROI following photoactivation. Each line represents a single photoactivation experiment. **(B)** Plot of individual (gray lines) and average (black circles, mean ± s.d.) intensity curves. $k_{C\text{-}G}$ was obtained as the average of individual k_{obs} values. k_{obs} was determined for each curve by fitting with the monoexponential function (Eq. 2-14).

No increase in paGFP fluorescence could be observed in the control experiment lacking the activation step, thereby ruling out unintended activation of paGFP through light exposure during imaging (Figure 5-24).

Effect of impaired Rab1 functioning on transport exiting the Golgi

The effect of impaired GTPase functioning on Rab1 trafficking originating from the Golgi was assessed by FLAP experiments utilizing: (1) the constitutively active Rab1Q67L mutant[41,43], (2) the GDI-binding deficient mutant Rab1D44N[212], (3) after treatment with nocodazole[139,140] and (4) in PRA1 knock-down cells[215]. The obtained rate constants for Rab1 traffic exiting the Golgi, $k_{G\text{-}C}$ are summarized in Figure 3-65.

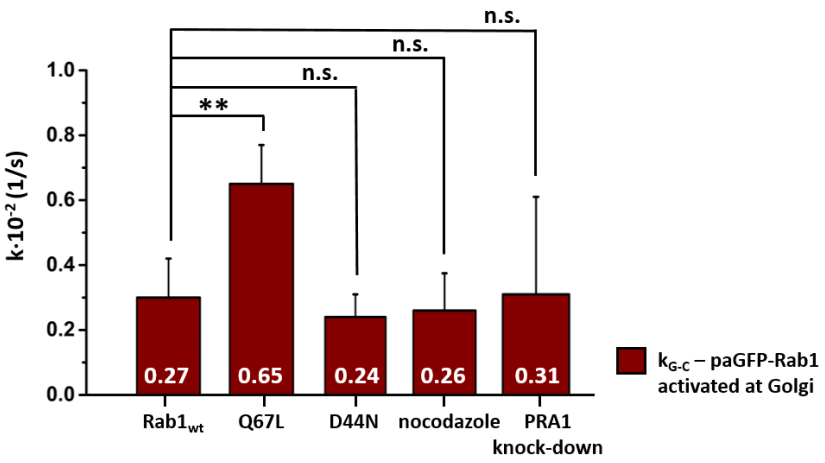

Figure 3-65: Summary of obtained $k_{G\text{-}C}$.
Summary of the apparent rate constants for Golgi to cytoplasm trafficking for Rab1 wild type, Rab1Q67L, Rab1D44N, Rab1 wild type in cells treated with nocodazole and in PRA1 knock-down cells.

Trafficking from the Golgi is significantly accelerated for Rab1Q67L

For the dominant-active Q67L mutant the $k_{G\text{-}C}$ was significantly increased $(0.6 \pm 0.1)\cdot10^{-2}$ 1/s in comparison to $Rab1_{wt}$ ($k_{G\text{-}C} = (0.27 \pm 0.1)\cdot10^{-2}$ 1/s) (Figure 5-32) and large vesicular structures enrich in the cytoplasm (Figure 3-56 and Figure 3-57). Rab1 recycling from the Golgi is believed to be largely governed by GDI-mediated transport. GDI-mediated membrane extraction/transport is expected to be impeded due to Rab1Q67L being constitutively active. Possibly, the rate increase in trafficking exiting the Golgi can be attributed to a shift from (slower) GDI-governed Rab1 recycling to a higher percentage of membrane derived-vesicular transport from the Golgi. As speculated earlier, high Rab1 activity could lead to the formation of transport vesicles at sites that are usually not destined for Rab1 mediated vesicular budding. Thus, the observed increase might be attributed to a rise in Golgi-derived vesicular trafficking.

Disrupted vesicular transport does not change kinetics of Rab1 trafficking out of the Golgi

The observed rate constant for paGFP-Rab1 depletion from the Golgi after nocodazole treatment $k_{C\text{-}G} = (0.26 \pm 0.1)\cdot10^{-2}$ 1/s is nearly identical to untreated cells (Figure 3-65). Presumably, the retained outgoing Rab1 trafficking can be attributed to GDI-mediated transport.

GDI-binding deficiency - Rab1D44N

The GDI-binding deficient Rab1 mutant D44N, displays similar kinetics for Rab1 trafficking departing from the Golgi (k_{G-C} = (0.24 ± 0.07)·10^{-2} 1/s) as wild type Rab1 k_{G-C} = (0.27 ± 0.1)·10^{-2} 1/s (Figure 5-34). To date, Rab1 recycling after completed transport has been generally attributed to GDI-mediated transport. As GDI-binding is abolished through the D44N mutation, Rab1 exiting then Golgi membrane should only be possible through membrane dependent trafficking.

Indeed, vesicular and tubular structures originating from the Golgi membrane are observed exiting the Golgi after photoactivation. Similar observations were made for wild type Rab1, indicating that Golgi derived membrane-associated Rab1 transport is not limited to the GDI-binding deficient mutant. In combination with the increased k_{G-C} for the Q67L mutant these findings suggest that membrane derived transport has to be considered as a crucial contributor for Rab1 traffic departing from the Golgi organelle.

Possibly, these polymorphic tubular structures represent ER-Golgi intermediate compartments (ERGIC), also referred to as vesicular tubular clusters (VTCs). Generally, VTCs are believed to form through fusion of newly budded COPII vesicles. They are involved in the anterograde ER to the Golgi transport and the retrograde recycling transport pathways.[218,219] VTCs mature through recycling and recruitment of specific proteins and the exchange of COPII for the COPI coat complex.[138,220] This implicates Rab1 involvement in the retrograde transport and could explain depletion from the Golgi organelle independent of GDI-mediated transport.

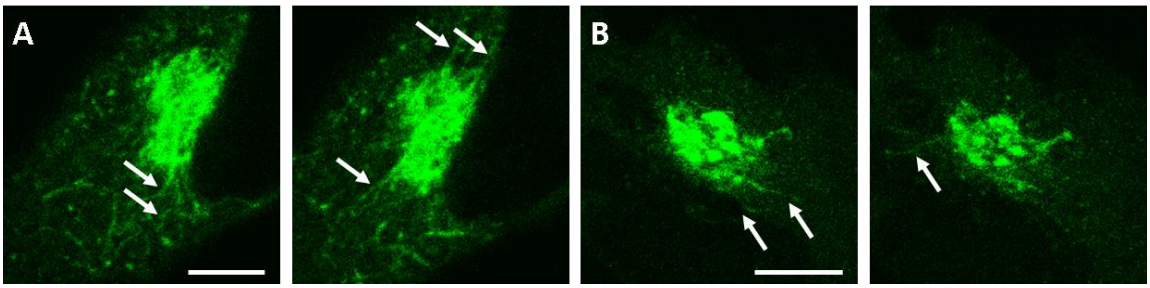

Figure 3-66: Tubular and vesicular structures exiting the Golgi after photoactivation.
Fluorescence images of HeLa cells expressing **(A)** EGFP-$Rab1_{wt}$ and **(B)** EGFP-Rab1D44N. White arrows indicate tubular structures exiting the Golgi during time-lapse imaging. Excitation and emission filter settings as described in 2.7.1. Scale bars: 5 μm.

PRA1 is not essential for Rab1 trafficking from the Golgi

The kinetics of Rab1 trafficking from the Golgi are not significantly altered in PRA1 knock-down cells with k_{C-G} = (0.31 ± 0.03)·10^{-2} 1/s (Figure 5-35). This suggests that, the proposed GDF activity of PRA1 regulates the delivery of Rab1 to the Golgi membrane. e.g. by assisting in the release of Rab1 from the GTPase:GDI complex, but not the retrieval of Rab1 from the Golgi.

3.2.3 GTPase cycle drives Rab1 spatial cycle

Based on the current model of Rab-regulated vesicular transport, Rab1 trafficking should occur via two distinct pathways: vesicular trafficking between the ER and the Golgi, driven by membrane-associated Rab1[194,216] and membrane-independent transport mediated by GDI[196,213]. GDI-mediated trafficking is believed to enable recycling of Rab1 from membranes to the cytosol. Recycling to the ER is necessary to facilitate multiple rounds of Rab1 regulated ER to Golgi transport.[212] Both trafficking pathways are governed by the nucleotide state of the GTPase. GDI only binds to the inactive, GDP-bound GTPase with high affinity[63], while vesicular ER to Golgi transport strongly depends on activated, GTP-bound Rab1. Rab1 activation is required to recruit and interact with effector proteins that are critically involved in the successive transport steps.[214,216] Thus, the GTPase's ability to switch between its two nucleotide states is crucial to proceed through all steps of its spatial cycle. Furthermore, the importance of the inherent switching ability of GTPases for initial membrane targeting has been demonstrated in experiments using Rab5 covalently locked in its active or inactive state.[55]

Overall, the performed FRAP and FLAP experiments underscore the highly dynamic nature of Rab1 trafficking between the Golgi and the cytoplasm. The rate for Rab1 delivery onto the Golgi is about 5-6-fold higher than for Rab1 traffic departing the Golgi and leads to the observed enrichment of Rab1 at the Golgi organelle (Figure 3-67). The high turnover of Rab1 molecules localized at the Golgi, suggests that Rab1 molecules undergo multiple rounds of ER to Golgi transport. This is further supported by the unchanged cycling kinetics and maintained Golgi structure in cells treated with the protein synthesis inhibitor cycloheximide (Figure 5-22).

Overexpression of GTPase cycling deficient mutants of Rab1, e.g. the constitutively active Rab1Q67L or dominant-negative Rab1N121I, severely impacts ER to Golgi transport and Rab1' spatial cycling. Overexpression of Rab1N121I leads to abrogated Golgi biogenesis[216,221], while Rab1Q67L expression results in the formation of enlarged vesicular structures in the cytoplasm (Figure 3-57). More specifically, Rab1N121I expression has been shown to arrest VSV G transport at ER exit sites and leads to Golgi "fragmentation".[216] The scattered Golgi arises from abolished vesicular transport between ER and Golgi, resulting in the formation of Golgi ministacks at ER exit sites. In accordance with the hypothesis that defective Rab1 activation leads to arrested ER- to Golgi-transport, the same phenotype is observed when Rab1 is depleted by siRNA or the negative Rab1 regulator TBC1D20, a ER-associated GAP, is overexpressed.[216] Fragmentation of the Golgi organelle is also observed when cells are treated with nocodazole, an inhibitor of microtubule polymerization (Figure 3-60).[139]

The effect of the Rab1Q67L mutant is less severe, as the overall Golgi structure remains intact and ER to Golgi transport is sustained.[216] Presumably, this can be attributed to RabQ67L's maintained ability to bind effector proteins that drive ER-mediated vesicular transport. However, the rate for Rab1 delivery to the Golgi is significantly slowed (Figure 3-55) and large vesicular structures enrich in the cytoplasm (Figure 3-57).

This suggest that compromised Rab1 deactivation inhibits efficient spatial cycling of Rab1, e.g. by preventing recycling to the ER through GDI-mediated transport.

It can be argued, that the Rab1Q67L mutant primarily undergoes transport via the vesicular pathway, as GTP-bound Rab1 has a substantially lower affinity towards GDI than GDP-bound Rab1.[63] Similarly, Rab1 trafficking observed in the FRAP and FLAP experiments in the presence of nocodazole, should be largely derived from GDI-mediated transport, as microtubule-dependent vesicular transport is abrogated under these conditions (Figure 3-67).

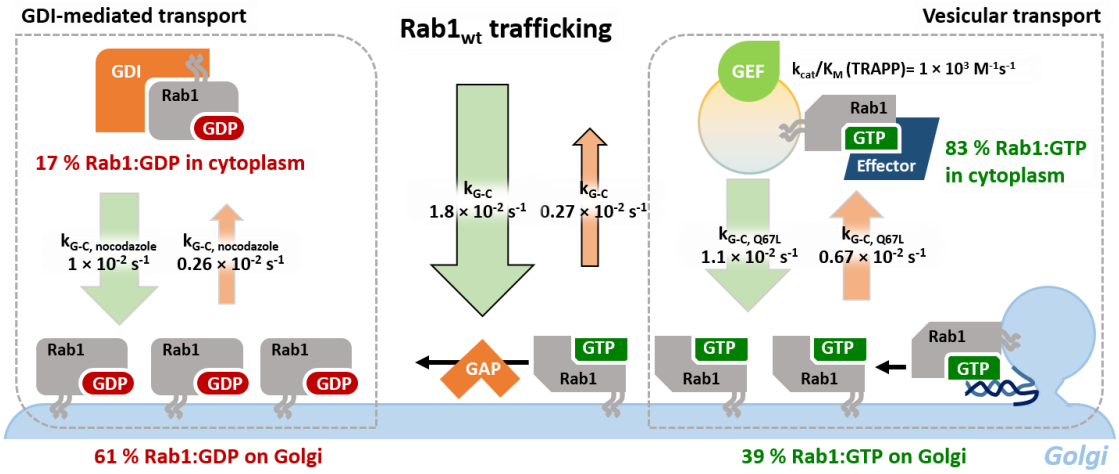

Figure 3-67: Summary of Rab1 trafficking rates between Cytoplasm and Golgi.
Summary of the obtained rate constants for Rab1 delivery from the cytoplasm to the Golgi ($k_{C\text{-}G}$), as determined by FRAP and FLAP experiments. The opposed direction trafficking from Golgi to cytoplasm ($k_{G\text{-}C}$), was assessed by photoactivation of paGFP-Rab1 at the Golgi, followed by time-lapse imaging to monitor the subsequent fluorescence decrease. Rab1 trafficking is believed to occur via two key pathways, GDI-mediated transport and vesicular transport. Rates obtained in cells previously treated with nocodazole, should be devoid of microtubule dependent transport, limiting Rab1 trafficking to transport via the GDI association. The constitutively active Rab1Q67L mutant should be restricted to membrane derived trafficking, as the GTP-bound GTPase possesses a relatively low affinity towards GDI binding.

The crucial role of the GDI-bound Rab1 pool has been demonstrated in a previous report.[196] Addition of Rab1:GDI to cells whose cytosol has been depleted of Rab1, restores the cell's ability for ER to Golgi transport. Interestingly, addition of excess GDI has been shown to disrupt Rab1-mediated ER to Golgi transport by extracting Rab1 from membranes, trapping the protein in the cytosol.[196] This suggests that the amount of available GDI in the cytosol is limited, preventing exuberant retrieval of Rab1 from membranes. Here, the comparable rate for Rab1 trafficking out of the Golgi for untreated cells and cells treated with nocodazole, is in keeping with the assumption that Rab1 recycling from the Golgi membrane is primarily mediated by GDI (Figure 3-67). In contrast, the rate for Rab1Q67L trafficking from the Golgi to the cytoplasm is about 2-fold higher than observed for wild type Rab1.

For the Q67L mutant, the rate for Rab1 delivery towards the Golgi is significantly lower than for wild type Rab1. This decrease can potentially be attributed to the impeded ability of the constitutively active Rab1 to be recycled by GDI. Moreover, Rab1Q67L is not subject to regulation by GEFs and GAPs, disrupting its GTPase cycle, which is essential for efficient spatial cycling between cellular compartments.

4 Final discussion and perspectives

For each scientific question the suitable tools and the right experimental setup have to be chosen. In this regard, each method features a unique combination of advantages and limitations that have to match the demands of the particular problem that needs solving. As the relevant questions become more complex and challenging, the arsenal of tools scientists have to their disposal has to be expanded and fitted accordingly.

4.1 Advantages and limitations of the new sensor design

When examining processes that require spatiotemporal resolution, the combination of fluorescence microscopy with FRET- or ratiometric based biosensors has proven to be especially valuable. Due to their key role in highly dynamic processes, GTPases have been a popular target for the development of biosensors. This led to the evolution of a wide range of different sensor approaches. Depending on their specific design, each sensor exhibits certain strengths and weaknesses as discussed in the introduction (1.3). The sensor design described in this thesis was developed to address some of the weaknesses of established sensor to allow further insight into the principles underlying GTPase functioning. Its benefits and drawbacks are discussed below in comparison to other established approaches.

The distinct feature of the novel FRET probe reported in this thesis is the combination of a fluorescent protein with a small organic dye that is introduced directly in the GTPase fold. This unique setup allows a direct read out of the intrinsic conformational change upon nucleotide exchange. A detailed description of the architecture of the sensor design can be found in section 3.1.1.

4.1.1 Effector-free sensing

Most GTPase sensors reported to date rely on an indirect signal read out generated through binding of an engineered effector domain to the activated, GTP-bound GTPase. This is an elegant approach as it employs the effectors ability to differentiate between the two nucleotide states. However, this methodology is severely limited, as it can only be used for small GTPases where suitable effector domains are available. This is a rather substantial constraint as for some GTPases there are only few, if any, effectors known.[84] Once identified, these domains have to be optimized for suitable affinity[151,222,223] and dynamic range[157] to work as efficient reporters. In contrast, the new sensor design reported here does not require the identification and optimization of a suitable effector affinity tag. It utilizes the conformational change within the protein-fold as a direct indicator for GTPase activation.

The most minimalistic GTPase sensor approaches, rely on engineered effector domains that are fused to fluorescent proteins and specifically translocate to regions of increased GTPase activity.[224,225] A drawback of this bimolecular sensor methodology can arise from promiscuous binding of effector domains to multiple GTPases.[144,226,227] While this specificity problem can be addressed by more sophisticated bi- and unimolecular FRET sensors, other weaknesses are inherent to the use of effector-based affinity tags.

One crucial drawback is that upon activation the affinity tag binds to the GTPase-effector interface, essentially blocking it from interaction with other binding partners. This can potentially affect downstream and upstream GTPase functioning and result in aberrant *in vivo* signaling. Especially interference with binding of upstream regulatory proteins such as GEFs, GAPs and solubilization factors is potentially problematic for proper GTPases functioning. Preservation of upstream regulation is crucial as it directly affects the GTPase activity that is being monitored. For instance, tightly bound effector domains compete with GDI binding and the deactivation through GAP proteins, leading to a high overall activation, thereby reducing the sensors dynamic range or slowing the signal decay after stimulated activation[222].

The risk of obstructing the GTPases interaction interface is greatly reduced by the sensor developed in course of this thesis. The perturbation of upstream regulation and downstream signaling is minimal. This claim is fully supported by the *in vitro* assays, demonstrating preserved regulation of multiple Rab1 and KRas sensor constructs by their GEFs and GAPs, as well as retained binding of the Rab1 sensors to two effector proteins (3.1.4-3.1.13).

4.1.2 *In vitro* characterization

A majority of FRET-based GTPase biosensors utilize a pair of fluorescent proteins in a single chain construct. While this allows direct genetic encoding and reliable FRET analysis, it also leads to rather large proteins (>90 kDa) that cannot be readily purified easily for *in vitro* characterization. In these cases, the sensor performance is evaluated primarily based on cellular assays through co expression with regulatory partners (e.g. GEFs and GAPs) or by using mutants that are constitutively active or nucleotide binding deficient.[157,160] Using these assays, the sensors performance can be evaluated regarding its dynamic range and these assays can give an indication on the GTPase sensor's ability to be regulated by its native interaction partners. However, it is not possible to assess the kinetics of these interactions. Yet, kinetic parameters are decisive for tight spatiotemporal control as it is observed for GTPase functioning. A more thorough and quantitative assessment of how the implemented modifications affect the interaction between GTPases and their various regulatory partners is possible through *in vitro* fluorescence measurement.

Here lies one of the major advantages of the sensor described in this thesis. The use of a small organic dye as one of the FRET partners minimizes sensor size while preserving the advantages of an unimolecular sensor construct. This allows for simple *in vitro* purification and subsequent quantitative assessment of the protein-protein interactions that are crucial for GTPase functioning. Still, it should be kept in mind, that *in vitro* characterization of isolated proteins and their interactions suffers from its own drawbacks. In particular, membrane attachment and compartmentalization can result in profound changes of protein behavior, which is the case for membrane associated protein such as small GTPases.[228] Moreover, protein purification can be a tedious process in comparison to direct expression of genetically encoded sensor constructs in cells. *In vitro* characterization might not be practical for all protein targets, especially if post-

translational modifications are essential for the protein-protein interactions. However, if feasible, direct and specific assessment in a well-defined setup is particularly useful when modifications can lead to functional defects. The cause of these deficiencies can then be identified more easily by systematically dissected the numerous interactions that are involved in GTPases signaling.

Regulation by GEFs and GAPs

Since the described FRET sensor design requires a modification within the protein fold, it is especially important to ensure that the GTPases retain their native fold and ability to be governed by upstream regulators and to bind to downstream effectors. Consequently, the sensors for Rab1 and KRas were examined regarding their sensitivity towards GEF-mediated nucleotide exchange and GAP-induced GTP hydrolysis (3.1.4/3.1.5 and 3.1.11/3.1.12). In addition, binding of two effector domains to the Rab1 sensor was quantified (3.1.6). In the case, of Rab1 the observed catalytic efficiencies are in keeping with the values observed for the wild type protein, suggesting that the modifications do not affect the function of the switch I or interswitch region, respectively. In contrast, the KRas mutants (E31C and D33C) (Table 3-6) and to an even greater extent the acceptor dye labeled constructs (Table 3-7), displayed a significant reduction in the catalytic efficiency for SOS-mediated nucleotide exchange. A similar decrease was detected for GAP-induced GTP hydrolysis by RasGAP (Figure 5-20). Activation and deactivation were not completely abolished but severely slowed. These subtle deficiencies would likely go unnoticed in cell based assays, where elevated expression of the respective GEFs and GAPs can overcompensate the described effect, leading to uniformly activated/deactivated sensor population.

Interestingly, the KRas sensor did not exhibit delayed KRas activation in response to EGF stimulation in microinjected cells (3.1.13). In agreement with previous reports, the increase in lifetime, correlating to KRas activation, is observed immediately after EGF addition (Figure 3-45) and reaches its maximum at around 5 min.[211] This indicates that the reduction in efficiency for GEF and GAP regulation observed *in vitro*, does not result in perceivable changes in sensor response *in vivo*. It can be speculated that this lack of response delay can be attributed to the mechanism of EGF-induced KRas activation. It is conceivable, that the reduction in GEF-mediated nucleotide exchange is minor in comparison to the increase in GTPase-GEF interaction following the EGF induced SOS-translocation to the plasma membrane. Another explanation could be that along with the GEF mediated-activation, RasGAP-governed deactivation is impaired. As these effects would neutralize each other, no net change in EGF-induced Ras activation kinetics would be observed. For other small GTPases the detected reduction in activation and deactivation kinetics might constitute a severe obstacle for proper GTPase functioning.

Effector binding

A major benefit of this new effector domain-free sensor is the retained ability to bind to endogenous effector proteins. While competition with endogenous effector binding in itself does not constitute a detriment, native interaction with downstream effector is preferable to observe native GTPase functioning.[160] The obtained dissociation constants are in excellent agreement with previous reports and suggest that the Rab1 sensor is accessible for effector binding *in vivo*.[184,187] Available structural data of Rab-effector and KRas-effector complexes (Figure 3-21), further support this notion. As described in 3.1.6, the Rab1 FRET sensor constructs display remarkable changes in FRET efficiency upon effector binding. While this is an interesting finding, that allows for a convenient read out for the binding of effector domains through fluorescence titration, it also complicates the interpretation of the FRET signal if the GTPase can interact with multiple partners.

This unexpected sensitivity towards effector binding can pose a problem for the interpretation of the FRET signal especially in complex environments such as *in vivo* measurements. In cells, the GTPase is likely present in different states of activation and bound to diverse effector proteins, if these interactions result in conflicting FRET responses it can be hard to distinguish the exact cause for an observed signal. Taking this caveat into consideration, the following conclusions can be made from the *in vitro* results.

The rapid transitional interaction between the GTPases and their GEFs and GAPs did not result in changes in the FRET signal when monitored by sensitized emission (Figure 3-11, Figure 3-15, Figure 3-38 and Figure 3-41). These interactions should therefore not interfere with the signal interpretation in a system with more than one possible interaction partner. In contrast, effector domain binding resulted in a robust decrease in FRET efficiency in all cases, regardless of the labeling position or which effector domain was used. With a notable exception of the T34C construct binding to the OCRL effector domain (Table 3-5). Probably, binding of effectors, regardless of the exact binding mode, exerts the same effect on FRET efficiency by pushing the N-terminal fluorescent protein away from the acceptor side, leading to an increased relative distance or an unfavorable orientation of the fluorophore dipoles (1.2.1). This assumption is supported by the more pronounced drop in FRET efficiency upon binding of the LidA effector domain (20-30 %) in comparison to OCRL binding (~10 %). LidA features an exceptionally large GTPase-effector interface[184] and it is plausible to assume that this extensive interaction leads to a marked distortion of the N-terminal fluorescent protein. Intriguingly, this consistent drop in FRET signal upon effector binding can be used to enhance the dynamic range of the FRET sensor signal upon GTPase activation. When choosing a sensor construct that displays a drop in FRET efficiency upon GTP binding, subsequent effector binding will enhance the observed FRET signal decrease further.

Binding to solubilization factors and membrane attachment

Two key aspects of GTPase regulation that have not been addressed in the *in vitro* experiments, are the binding to solubilization factors such as GDI[196] and PDEδ[229] and the effect of membrane attachment. As both these interactions are mediated by posttranslational modifications, two geranylgeranyl moieties in case of Rab1 and a farnesyl moiety in case of KRas, *in vitro* reconstitution of this feature is challenging. While different approaches for the generation of Rab and Ras proteins with their corresponding C-terminal prenylanchors have been reported, ranging from semisynthetic[230,231] and *in vitro* prenylation[232] strategies to baculovirus-based insect cell expression systems[233-235], they cannot easily be applied to the FRET sensor construct described here, as the prenylation would have to follow the initial acceptor dye labeling and the introduction of the C-terminal amino acids through NCL. Furthermore, these highly lipophilic modifications would lead to increasingly insoluble constructs that require the use of detergents, blocking the GTPase from direct interaction with solubilization factors and lipid membranes.

A promising strategy to overcome these issues could be to use the Rab-REP interaction as a surrogate for GDI binding. GDI and REP are structurally alike and their interaction mode with Rab proteins is very similar (Figure 4-1). In contrast to GDI that requires the C-terminal prenyl-modification for tight binding, REP binds prenylated and unprenylated Rab proteins with high affinity.[62,236] This approach could give a good indication if the Rab1-GDI interaction remains intact and what effect binding to the solubilization factors has on the FRET signal.

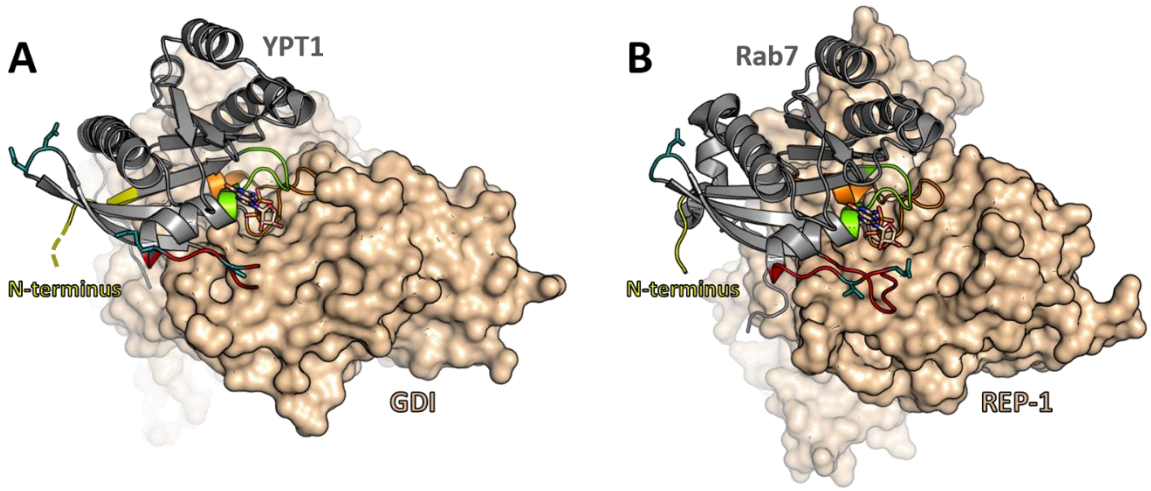

Figure 4-1: Interaction of YPT1 with GDI (PDB ID:2BCG) and Rab7 with REP-1 (PDB ID:1VG0).
YPT1 and Rab7 structures are shown in cartoon representation (gray), the structures of **(A)** GDI and **(B)** REP-1 are displayed as surface representations (beige). The N-terminus of the Rab proteins is highlighted and labeled in yellow. The switch I and II regions are colored in red and orange respectively. The P-loop is marked in green. The corresponding acceptor labeling sites in switch I and II are highlighted in turquoise.

It can be speculated that binding to REP and GDI could exert a similar effect on the FRET signal as effector binding as this interaction should persist over a similar timescale and is not transient as it is for GEFs and GAPs. Yet, the available complex structures of YPT1:GDI and Rab7:REP-1 indicate that in this case the N-

terminus of the GTPase is located distal to the interaction interface (Figure 4-1). This suggests that the N-terminally attached fluorescent protein position should not be distorted through binding of the solubilization factors. Furthermore, the interactions with the switch I region of the GTPases are limited to residues downstream from the acceptor labeling sites. Thus, binding to GDI or REP should not result in major changes of the acceptor dye environment and orientation. This notion is further supported by the *in vivo* measurement conducted in this thesis (3.1.9). As a general observation, the *in vivo* lifetimes, that include the interaction with aforementioned REP and GDI, of GDP and GTP-bound FRET sensor (τ_{GDP} = 1.88 ± 0.08 ns and τ_{GTP} = 2.05 ± 0.03 ns, 3.1.9) are consistent with the lifetimes observed for immobilized sensor on Ni-NTA beads (τ_{GDP} = 1.81 ± 0.04 and τ_{GTP} = 1.98 ± 0.05, Figure 3-24).

Immobilization on Ni-NTA beads

Another benefit of *in vitro* purified sensor constructs is the possibility of immobilizing the FRET sensor on beads by their affinity tag. Immobilization generates probes with a high local concentration, that allow for a robust signal with minimal expense of protein. The high signal intensity facilitates convenient FRET read out by lifetime microscopy. In contrast to cell based formats, this bead-based setup generates a uniform sensor population in a highly controlled setting. Possible interacting partners can be applied simultaneously or subsequently and at predetermined concentrations. Thus, the sensor loaded beads provide a practical basis for screening approaches to identifying GTPase interaction partners[237] or inhibitors of GTPase activation[238].

Another interesting application lies in the systematic mapping of signaling networks as recently described for HRas.[239] In this report by Coyle et. al., the read out is generated through the recruitment of a fluorescently labeled effector domain to immobilized HRas on Ni-NTA beads upon GEF-mediated activation. While this is a serviceable approach to quantify the output of (competing) GEF and GAP regulation, it is limited when analyzing effector binding, as the reporter domain competes with the downstream effector binding. As effector-domain free sensing constitutes one of the major advances of the FRET design reported here it should be a valuable tool to address this particular aspect of GTPase signaling.

4.1.3 *In vivo* application

Sensor delivery into cells

A major challenge of the FRET sensor design in this work, that limits widespread *in vivo* application is the necessity to introduce the sensor into cells after *in vitro* purification and acceptor dye labeling. Here microinjection was used, a laborious method that requires specialized equipment and can only produce a limited number of cells for live cell imaging. Furthermore, the final sensor concentration cannot be effectively controlled using microinjection. It has been shown for an RhoA activation sensors, that overexpression can saturate the pool of available endogenous RhoGDI.[153] This led to a high overall activation in cellular assays, due to accumulation of the sensor at the plasma membrane where it was then activated through interaction with GEFs. In this case, the problem was solved by reducing the biosensor concentration through an optimized expression system for live cell imaging.

An indication for retained wild type like behavior is the subcellular localization observed for the GTPases probes in cells. As expected, Rab1 localized predominantly to the Golgi[193] and KRas to the plasma membrane[207] (3.1.8 and 3.1.13).

Recently, new methods for efficient delivery of proteins into living cells have been reported that could alleviate these methodical limitations. Especially electroporation[240] and cell squeezing[241,242] emerge as powerful methods for high-throughput delivery of proteins into cells at defined concentrations.

An alternative, more elaborate, methodology could be based on incorporation of unnatural amino acids through amber codon suppression[243] in combination with biorthogonal *in vivo* labeling. This would allow for a purely genetically encoded sensor. After sensor expression under supplement of the unnatural amino acid, acceptor labeling could be accomplished *in vivo* by biorthogonal labeling techniques[244] such as strain promoted azide-alkyne cycloaddition using p-azido-phenylalanine[245] or Diels-Alder cycloaddition between Bicyclononyne lysine and tetrazine-tagged dyes[246].

Sensor localization in cells

In order to observe natural protein behavior, a biosensor should co-localize with the endogenous protein. This holds particularly true for small GTPases where localization to specific membranes constitutes a crucial part of their functioning.[1,4]

One of the first GTPase sensor designs, termed Ras and interacting protein chimaeric unit (Raichu) sensors, was established by Matsuda *et.al.* for HRas and Rap1.[149] Later this approach was applied to numerous other small GTPases such as Rab5[156] and multiple members of the Rho family[151,152]. The Raichu scaffold sandwiches the GTPase and the corresponding affinity tag between the donor and acceptor fluorophore to achieve maximal conformation change upon GTPase activation. As a consequence, both GTPase termini are blocked by the flanking domains. Obstruction of the protein termini is problematic as for most GTPases they are crucial for interaction with regulatory partners (such as GDIs) or mediate (reversible) membrane

attachment. Initially, this problem was addressed by fusing the KRas localization signal to the C-terminal fluorescent protein.[247] The CAAX motif anchors the sensor to the plasma membrane but does not allow for native interaction with regulatory partners such as GDI. These artificial localization signals can target sensors to only a few of the various small GTPase dominions and often do not account for reversible membrane association. Another approach is to remove the localization signal altogether leading to cytosolic sensor constructs.[161] It should be noted that it is not exclusively the C-terminus that mediates membrane association. In case of Arf6, intracellular membrane localization is mediated by a myristoylation at the N-terminal protein end.[22] Thus, the sensor approaches had to be adjusted to allow for an unmodified N-terminus to preserve native protein localization.[248,249] These examples, illustrate the restrictions that tight regulation by multiple interaction partners and defined subcellular localization pose on the design of small GTPase sensors. It also further underscores the demand for diverse and flexible sensor strategies that have minimal effect on native protein functioning.

In comparison, the sensor described in course of this thesis requires only one fluorescent protein to be appended to the GTPase and not multiple domains (e.g. affinity tags and/or a second fluorescent protein). As described before, Rab1 and KRas membrane localization is in part mediated through prenylation of cysteine residues at their C-termini.[60,207] For KRas an additional polybasic sequence located near the prenylated carboxyl-terminal end is required for its native localization at the plasma membrane. Thus, conservation of the GTPases C-terminal end was a primary objective throughout the development of the FRET sensor. Consequently, the fluorescent protein acting as the FRET donor, was attached at the proteins N-terminus. Using this strategy, the C-terminus remains unmodified and accessible for posttranslational modification and regulation through GDI[196] and PDEδ[229] respectively. However, to facilitate site-specific and uniform labeling through thiol reactive maleimide-based chemistry, all reactive surface exposed cysteines had to be removed. This includes the prenylatable C-terminal double cysteine motive of Rab1 and the CAAX motif required for KRas localization. Cysteine labeling was selected, due to its easy implementation, a plethora of commercially available probes and the ease of introducing new modification sites. To enable thiol reactive labeling while retaining native protein localization in the cellular context, the GTPases where C-terminally truncated and purified as a C-terminal thioester. Native chemical ligation allowed reconstitution of the C-terminus after *in vitro* acceptor labeling (2.4.3). One has to bear in mind that, NCL requires an additional ligation step and multiple buffer changes, that significantly reduced sensor yield. While, thioesters are susceptible to degradation to the non-reactive carboxylic acid, substantial degradation was excluded through ESI-MS analysis of the ligation product (3.1.3 and 0). Yet, even small amounts of unprenylatable sensor would diminish the sensors sensitivity *in vivo.* A C-terminal deficient sensor construct would be excluded from the GTPase activation cycle leading to an overall inactive sensor fraction (Figure 3-29). This could potentially lead to a smaller overall change in FRET signal.

FLIM-FRET for *in vivo* imaging

Another advantage of the new sensor design is that it allows for easy *in vivo* FRET quantification by lifetime microscopy.

Because of its compatibility with conventional microscopy setups, sensitized emission remains one of the most popular approaches for imaging small GTPase FRET sensors in cells.[157,159,250,251] When using sensitized emission, the FRET efficiency is determined from the ratio of acceptor to donor emission while specifically exciting the donor fluorophore population. A drawback of this approach is the potential signal contamination by spectral bleed through and cross-talk that require image corrections and the collection of several reference images.[130] In case of bimolecular sensors, the relative concentration of the two fluorescently-tagged components has to be considered as well. This is especially important when bearing in mind the distinct subcellular localization of many small GTPases in comparison to the often cytosolic, unspecific localization of the engineered effector domains.

Fluorescence lifetime imaging in contrast, allows for a more reliable FRET analysis as it only depends on the donor fluorophore signal. When using FLIM-FRET, the energy transfer efficiency is determined from the decay curve of the excited donor fluorophore population and therefore independent from acceptor crosstalk and probe concentration. One caveat of this method is the relatively high signal intensity required for reliable lifetime analysis, which can require increased sensor concentrations or prolonged exposure during imaging.[130] However, due to its superior properties for accurate and reliable FRET quantification and improved accessibility through commercially available microscopy setups, FLIM-FRET is becoming increasingly popular for monitoring GTPase activity in live cells.[210,222,252]

It should be noted that not every FRET pair is suitable for lifetime imaging. The donor fluorophore should be largely insensitive to its microenvironment to exclude signal artifacts through differences in local pH or salt concentration. This criterion strongly favors fluorescent proteins in comparison to organic dyes as their chromophore is shielded from its surrounding through the ß-barrel structure.[253] Furthermore, the donor fluorophore should undergo single-exponential decay to allow for a reliable quantification of the FRET efficiency.[171,192]

4.1.4 Sensor optimization and consideration

Optimization is a central aspect of biosensor development. For unimolecular GTPase sensors that utilize an intramolecular fluorescent protein FRET pair, the starting point for optimization is shuffling of the relative positions of the different sensor domains to identify the most reliable and sensitive combination.[254] The original Raichu-scaffold[149] for instance has been altered multiple times to accommodate for an unmodified C-terminus or to identify the optimal positioning for a specific GTPase-effector domain pair[251]. Other possibilities to improve the dynamic range and sensitivity of a FRET sensor, include varied linker length and

flexibility[159,160], modification of the spectral properties of the employed fluorescent proteins[255,256] or their relative dipole orientation through circular permutation[257,258].

In light of these strategies, the rationales behind certain aspects of the reported sensor design and potential avenues for further improvement are discussed below.

Fluorescent proteins as donor fluorophores

The main reasons for choosing EGFP and mCitrine as the donor fluorophores of the FRET pair in this sensor, are the simple introduction of genetically encoded fluorescent proteins to the GTPases and their compatibility with fluorescence lifetime microscopy (4.1.3).

Another benefit of genetically appending fluorophores in comparison to *in vitro* labeling strategies is that the whole protein population is essentially homogeneously labeled after purification, in contrast to chemical labeling that requires two dyes to be introduced in succession. If quantitative conversion of either labeling step is not efficiently controlled, labeling would result in a mixture of nonuniformly labeled sensor species. This would be particularly problematic for intensity-based FRET quantification where the observed relative intensity of both FRET partners greatly influence the local FRET signal read out.

EGFP and mCitrine were chosen in particular, because of their favorable spectral properties and the abundance of suitable FRET acceptor fluorophores. They can be efficiently excited by the well-established Argon laser source and both fluorophores exhibit good photostability, brightness and a low propensity for oligomerization.[259,260] Something that has to be kept in mind when using green and yellow fluorescent proteins however, is their pH sensitivity.[261] This can be problematic for applications that require localization to acidic subcellular compartments such as lysosomes or under conditions that lead to significant changes in the intracellular pH.[261]

As apparent in section 2.7.5 another critical property when choosing a fluorescent protein as a FRET donor for lifetime microcopy is its decay kinetics. FLIM monitors the average fluorescence lifetime of the donor fluorophore. When non-radiative energy transfer (FRET) occurs from the donor to the acceptor fluorophore the average lifetime of the excited donor fluorophore decreases. The extent of the lifetime shift depends on the respective FRET efficiency observed for the specific sensor molecule. Thus, different population of high and low FRET are reflected in the overall decay kinetics of the excited donor fluorophores. To accurately assess the different sensor populations, single exponential decay kinetics of the donor is desirable.[171,192] The decay of mCitrine and EGFP can reliably be described by a single exponential function and they are therefore widely used as donors in FLIM-FRET.[192,262,263] An alternative fluorescent protein with very favorable decay kinetics and spectral properties is mTurquoise[264,265]. mTurquoise exhibits a comparatively high fluorescent lifetime ($\tau_{mTurquoise} \approx 3.5$ ns, $\tau_{EGFP} \approx 2.4$ ns, $\tau_{mCitrine} \approx 3.0$ ns, in cells)[192], which should allow for an increased dynamic range. For the same reason the GFP variant NowGFP ($\tau_{NowGFP} \approx$ 4-4.5 ns, in cells) qualifies as an alternative donor.[255]

A major disadvantage of fluorescent proteins in comparison to organic dyes is their comparably large size (≈25 kDa). This limits their application to the N- or C-terminus of a proteins, especially when used for labeling smaller proteins such as small GTPases (21-30 kDa). For larger proteins however, e.g. G-protein-coupled receptors[266] or EPH Receptor A2[262], the fluorescent proteins can be inserted into noncritical loop regions.
An additional interesting approach for improving the dynamic range of the FRET sensor would be the use of circular permutated fluorescent protein variants. Through rearrangement of the N- and C-terminus the chromophore orientation can be altered while preserving the proteins favorable fluorescence properties.[100]
As described in the introduction (1.2.1) the efficiency of the energy transfer between the two FRET partners depends on the relative dipole orientation of the chromophores. As changes in the relative orientation most likely contribute significantly to the observed FRET signal changes, optimization of the relative chromophore orientation in the active and inactive state of the GTPase could greatly increase the dynamic range of the sensor.[254,258,267]

Acceptor labeling and organic dyes

Smaller organic dyes were chosen as FRET acceptors since they have to be introduced directly in the protein fold to report on the conformational change upon GTPase activation. Furthermore, organic fluorophores feature superior spectral properties such as a wider spectral range, high photostability and increased brightness.[268]
One problematic aspect of the used acceptor dye that needs to be addressed is the cysteine-mediated labeling. Due to the exposed C-terminal cysteine residues that are critical for proper GTPase functioning, the maleimide derived labeling strategy requires a strategic detour to allow for site-specific labeling and a functional C-terminus (3.1.1-3.1.3). To circumvent the rather tedious C-terminal reconstitution process and the need for in *vitro* sensor purification, *in vivo* labeling techniques such as FLAsH and ReAsH[269] could be considered. A potential problem with these approaches pose the comparably large sequence modifications they require. Because the acceptor dye is directly introduced into the GTPase sequence, it is vital to minimize the effect of acceptor labeling on the protein fold and function. Furthermore, undesired side reactions of the Rab proteins C-terminal cysteine motifs with the thiophilic arsenic probes should be kept in mind when considering this labeling strategy. The criterion of site-specific labeling in the interior of the protein precludes the usage of other popular *in vivo* labeling techniques such as Halo[270], SNAP[271]- and CLIP-tag[272] for acceptor incorporation. However, these self-labeling enzymatic domains could be used to expand the range of possible fluorophores at the GTPase's N-terminus from fluorescent proteins to chemical dyes.
As mentioned previously, an alternative, more elaborate, methodology could be based on incorporation of unnatural amino acids through amber codon suppression[243] in combination with biorthogonal *in vivo* labeling[244].

A great advantage of the cysteines-mediated labeling methodology is the variety of commercially available probes and the ease of introducing new modification sites by site-directed mutagenesis. Here, maleimide conjugated Tide Fluor 3 and Tide Fluor 4 were used as partners for EGFP and mCitrine, respectively. They possess overlapping donor emission and acceptor excitation and the reactive maleimide group allows for efficient labeling. Other suitable candidates for acceptor dyes are the Alexa Fluor family, especially probes with varied linker length between the conjugation site and the fluorophore would be of interest to probe the effect of different linker on the FRET signal.

Another intriguing approach would be the use of conformationally restricted dyes[273] or multivalent probes that are locked in a defined orientation. The relative dipol-dipol orientation is a decisive factor for the efficiency of fluorescence energy transfer[274,275] (1.2.1) and restriction of the rotational freedom could be a useful tool to increase the sensors dynamic range.

Linker

Another approach for improving a FRET sensors performance is to utilize linkers with specific characteristics. Linkers can be varied in length and flexibility, thereby directly affect the relative distance and orientation of the two FRET fluorophores.[159,160] As described in and 3.1.1 the donor-acceptor distance should be as close as possible to the Förster distance R_0 for optimal sensor sensitivity and dynamic range. Furthermore, the change in relative fluorophore distance between the two sensor states, here GDP and GTP-bound GTPase, should be as large as possible. Specialized proteinaceous linker can be used to address this aspect of the sensor topology.

More specifically, the amino acids linking the fluorescent protein to the GTPases N-terminus can be probed for a varied chain length and flexibility. In a first attempt, the C-terminal part of the fluorescent protein was truncated by eleven amino acids, to shorten the flexible region, moving the two fluorophores closer together. This resulted in a substantial increase from ≈10 % to ≈20 % change in the sensitized emission signal upon nucleotide exchange (3.1.4) for the T34C construct. This indicates that probing different linker lengths for the distance between the N-terminal fluorescent protein and the GTPase can significantly improve the signal read out.

Besides reducing the FRET pair distance by removing flexible protein segments, rigid linker can be used to fix fluorophores in a specific distance and orientation. This can lead to a high change in FRET signal if the two states of the sensor correspond to two positions that feature significantly different FRET efficiencies. By fixing the fluorescent protein in a defined position in relation to the GTPase-fold the relative change in distance and orientation of the acceptor dye upon nucleotide exchange should be increased, which could then lead to an improved overall FRET signal read out.

A less conventional approach would be needed to allow for the variation of the linkage of the acceptor dye as it is located within the protein fold. However, as discussed for the fluorescent proteins, introduction of

proteinaceous linkers into noncritical sections of a protein is feasible and could be considered for this sensor design as well.[262,266] However, this approach would be most likely be limited to only a selected few sites that are not directly involved in the protein functioning. Furthermore, it is likely that these sites do not undergo significant structural changes upon nucleotide exchange.

5 Appendices

5.1 Protein and sensor construct sequences

Rab1b

```
        10          20          30          40          50          60
MNPEYDYLFK LLLIGDSGVG KSCLLLRFAD DTYTESYIST IGVDFKIRTI ELDGKTIKLQ

        70          80          90         100         110         120
IWDTAGQERF RTITSSYYRG AHGIIVVYDV TDQESYANVK QWLQEIDRYA SENVNKLLVG

       130         140         150         160         170         180
NKSDLTTKKV VDNTTAKEFA DSLGIPFLET SAKNATNVEQ AFMTMAAEIK KRMGPGAASG

       190         200
GERPNLKIDS TPVKPAGGGC C
```

KRas4b

```
        10          20          30          40          50          60
MTEYKLVVVG AGGVGKSALT IQLIQNHFVD EYDPTIEDSY RKQVVIDGET CLLDILDTAG

        70          80          90         100         110         120
QEEYSAMRDQ YMRTGEGFLC VFAINNTKSF EDIHHYREQI KRVKDSEDVP MVLVGNKCDL

       130         140         150         160         170         180
PSRTVDTKQA QDLARSYGIP FIETSAKTRQ GVDDAFYTLV REIRKHKEKM SKDGKKKKKK


SKTKCVIM
```

EGFP

```
        10          20          30          40          50          60
MVSKGEELFT GVVPILVELD GDVNGHKFSV SGEGEGDATY GKLTLKFICT TGKLPVPWPT

        70          80          90         100         110         120
LVTTLTYGVQ CFSRYPDHMK QHDFFKSAMP EGYVQERTIF FKDDGNYKTR AEVKFEGDTL

       130         140         150         160         170         180
VNRIELKGID FKEDGNILGH KLEYNYNSHN VYIMADKQKN GIKVNFKIRH NIEDGSVQLA

       190         200         210         220         230
DHYQQNTPIG DGPVLLPDNH YLSTQSALSK DPNEKRDHMV LLEFVTAAGI TLGMDELYK
```

mCitrine

```
        10          20          30          40          50          60
MVSKGEELFT GVVPILVELD GDVNGHKFSV SGEGEGDATY GKLTLKFICT TGKLPVPWPT

        70          80          90         100         110         120
LVTTFGYGLM CFARYPDHMK QHDFFKSAMP EGYVQERTIF FKDDGNYKTR AEVKFEGDTL

       130         140         150         160         170         180
VNRIELKGID FKEDGNILGH KLEYNYNSHN VYIMADKQKN GIKVNFKIRH NIEDGSVQLA

       190         200         210         220         230
DHYQQNTPIG DGPVLLPDNH YLSYQSLLSK DPNEKRDHMV LLEFVTAAGI TLGMDELYK
```

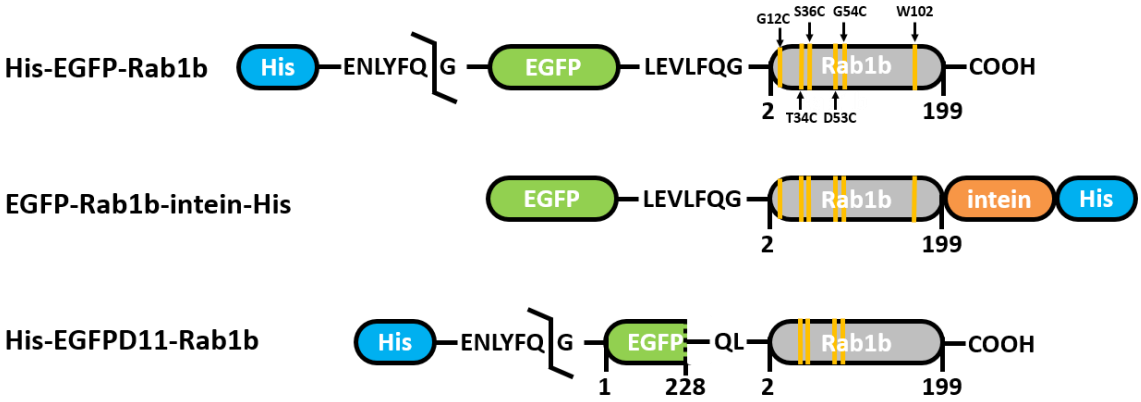

Figure 5-1: Rab1b sensor constructs used in the course of this thesis.
are indicated in different colors: blue: Hexahistidine-tag, green: EGFP, gray: Rab1b, intein: orange. Linking sections are displayed as single amino acid code. Acceptor labeling sites/cysteine mutations are marked with arrows and highlighted in yellow.

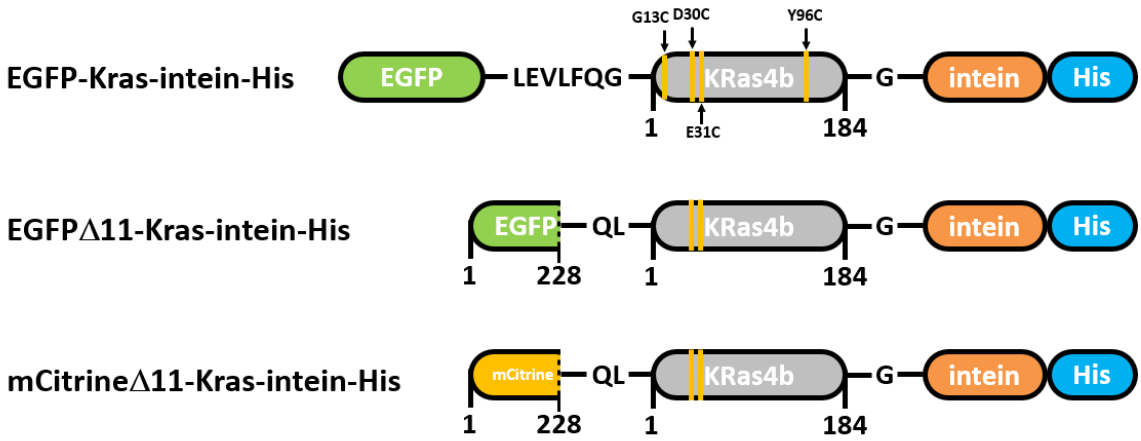

Figure 5-2: KRas sensor constructs used in the course of this thesis.
are indicated in different colors: blue: Hexahistidine-tag, green: EGFP, gray: Rab1b, intein: orange. Linking sections are displayed as single amino acid code. Acceptor labeling sites/cysteine mutations are marked with arrows and highlighted in yellow.

5.2 SDS-Gels acceptor labeling

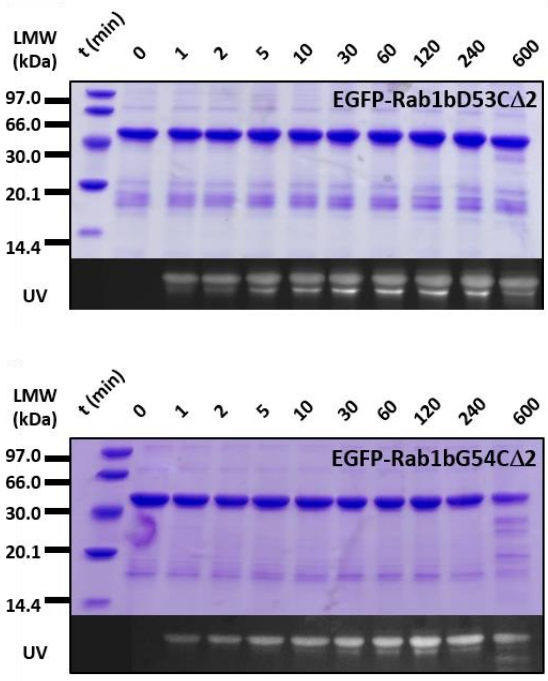

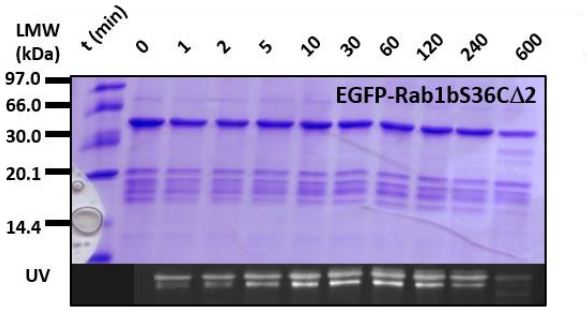

Figure 5-3: Site-specific labeling of His-GTPase constructs with thiol-reactive acceptor dye.
SDS-PAGE of EGFP-Rab1Δ2 constructs labeling. Labeling mixture was quenched with β-mercaptoethanol after the indicated incubation time. Upper panels: Coomassie blue staining. Lower panel: excitation with UV light before staining.

5.3 LC-ESI-MS

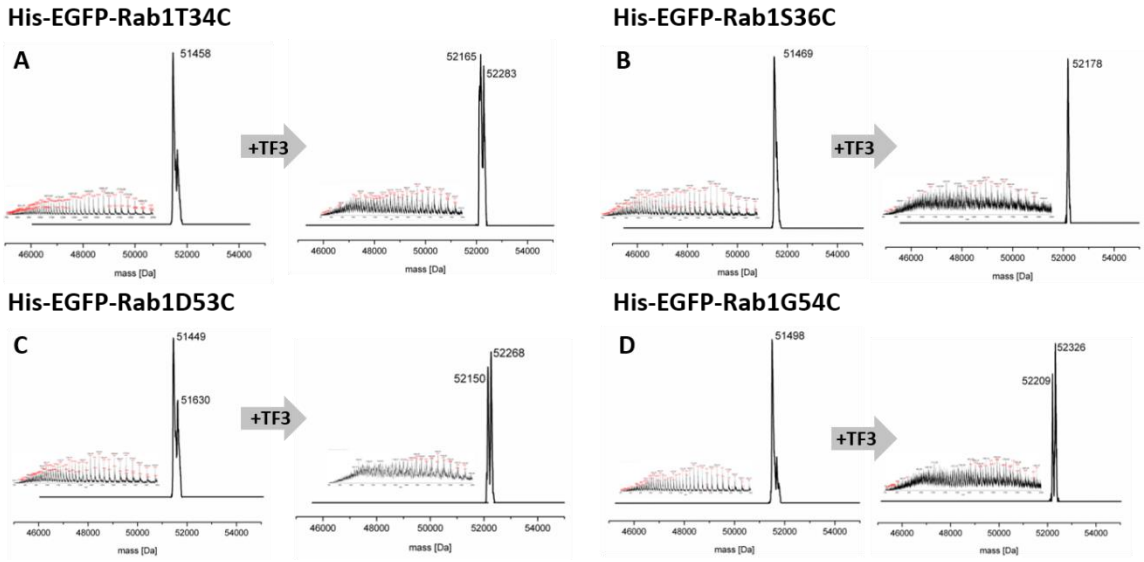

Figure 5-4: ESI-MS of site-specific labeling of Rab1 constructs with thiol-reactive acceptor dye Tide Fluor 3.
ESI-MS of **(A)** His-EGFP-Rab1T34C, **(B)** His-EGFP-Rab1S36C, **(C)** His-EGFP-Rab1D53C and **(D)** His-EGFP-Rab1G54C before and after labeling with 1.2 eq Tide Fluor 3 maleimide (2.4.1).

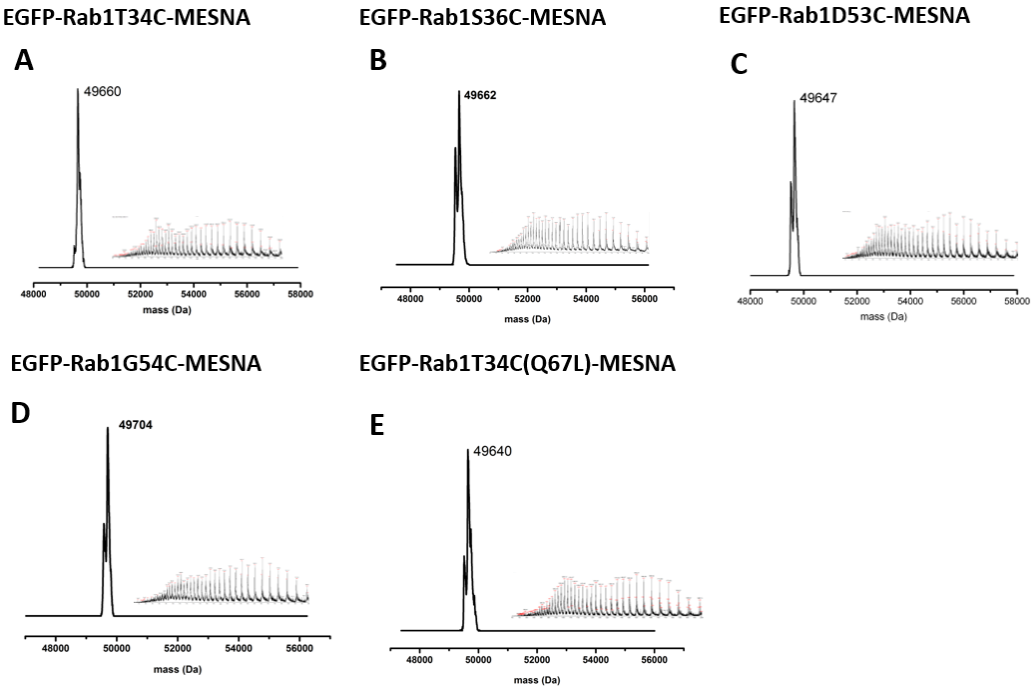

Figure 5-5: ESI-MS of Rab1-thioester constructs after thiolysis with MESNA.
ESI-MS of **(A)** EGFP-Rab1T34C-MESNA, **(B)** EGFP-Rab1S36C-MESNA, **(C)** EGFP-Rab1D53C-MESNA, **(D)** EGFP-Rab1D53C-MESNA and **(E)** EGFP-Rab1T34C(Q67L)-MESNA after purification (2.3.3).

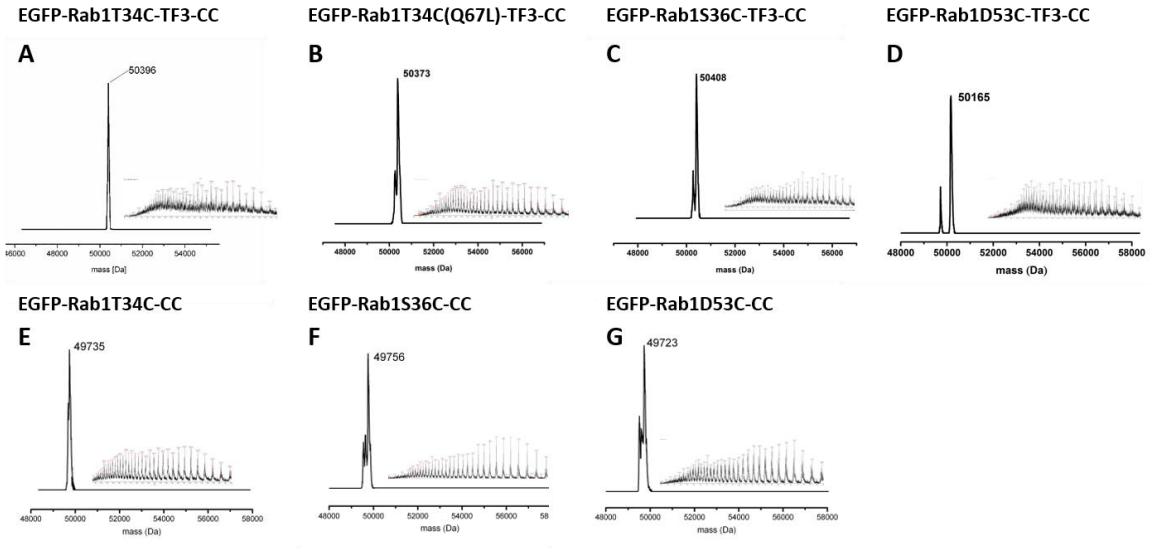

Figure 5-6: ESI-MS of Rab1 constructs after labeling with thiol-reactive acceptor dye Tide Fluor 3 and N-terminal NCL with Cys-Cys.
ESI-MS of **(A)** EGFP-Rab1T34C-TF3-CC, **(B)** EGFP-Rab1T34C(Q67L)-TF3-CC, **(C)** EGFP-Rab1S36C-TF3-CC and **(D)** EGFP-Rab1D53C-TF3-CC after labeling of the Rab1-MESNA constructs with thiol-reactive acceptor dye Tide Fluor 3 (2.4.1) and N-terminal NCL with Cys-Cys (2.4.3). ESI-MS of **(E)** EGFP-Rab1T34C-CC, **(F)** EGFP-Rab1S36C-CC and **(G)** EGFP-Rab1D53C-CC after NCL of the EGFP-Rab1-MESNA constructs with Cys-Cys (2.4.3).

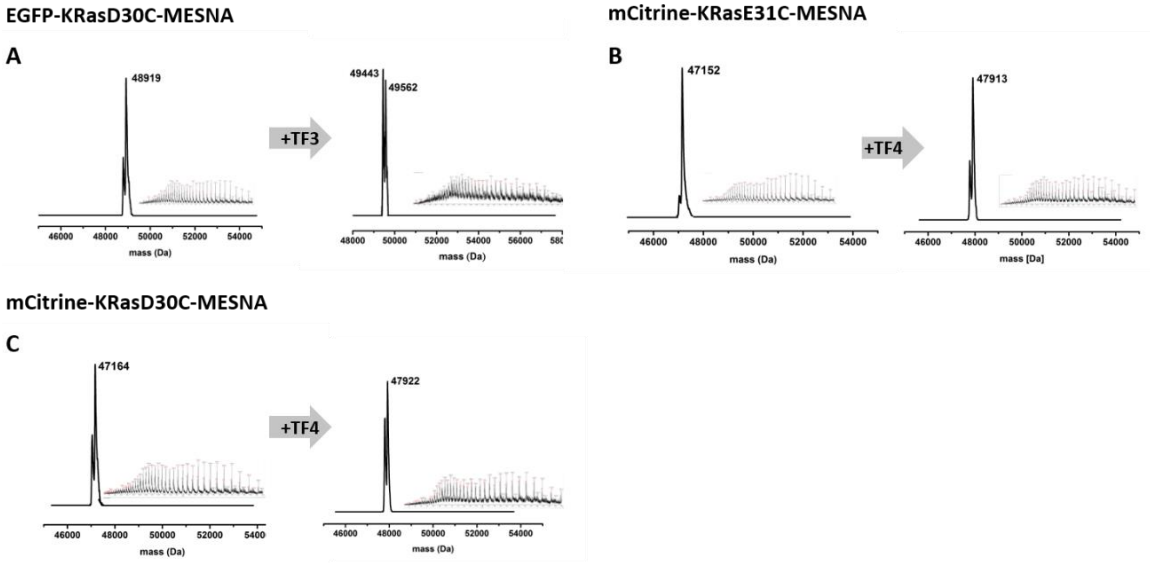

Figure 5-7: ESI-MS of site-specific labeling of KRas constructs with thiol-reactive acceptor dye Tide Fluor 3 or Tide Fluor 4.
ESI-MS of **(A)** EGFP-KRasD30C-MESNA, **(B)** mCitrine-KRasE31C-MESNA and **(C)** mCitrine-KRasD30C-MESNA before and after labeling with 1.2 eq Tide Fluor 3/4 maleimide (2.4.1).

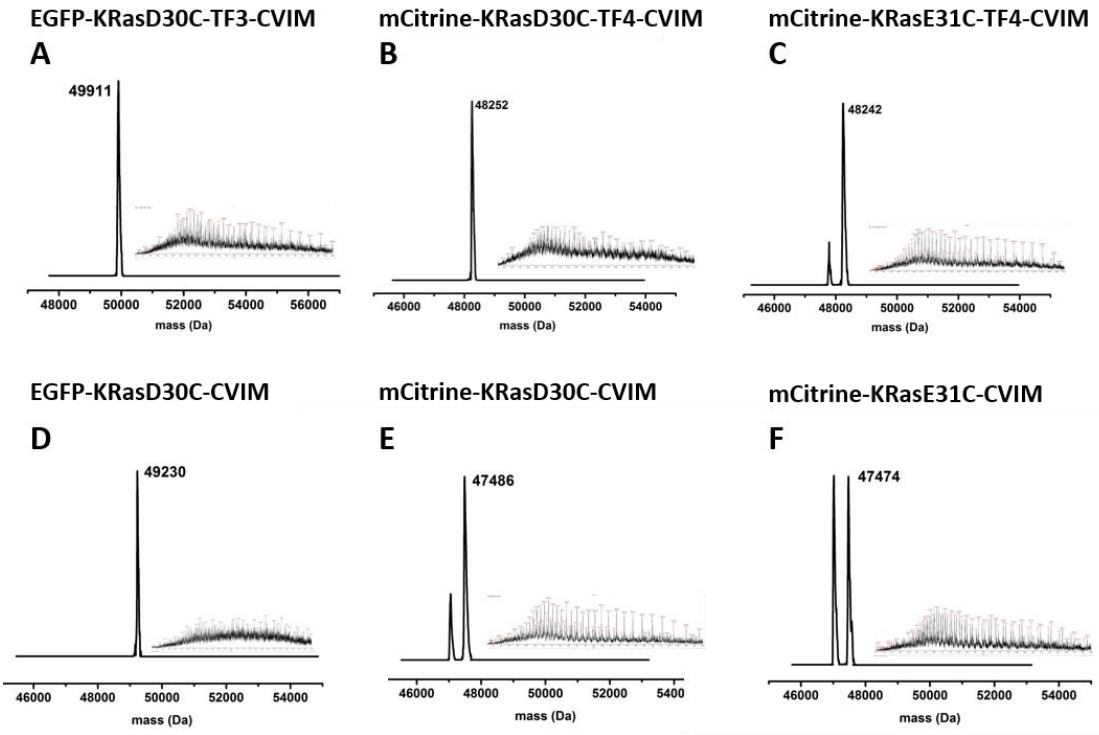

Figure 5-8: ESI-MS of KRas constructs after labeling with thiol-reactive acceptor dye Tide Fluor 3/4 and N-terminal NCL with the tetrapeptide -CVIM.

ESI-MS of **(A)** EGFP-KRasD30C-TF3-CVIM, **(B)** mCitrine-KRasD30C-TF4-CVIM, **(C)** mCitrine-KRasE31C-TF4-CVIM after labeling of the KRas-MESNA constructs with thiol-reactive acceptor dye Tide Fluor 3/4 (2.4.1) and N-terminal NCL with the tetrapeptide -CVIM (2.4.3). ESI-MS of **(D)** EGFP-KRasD30C-CVIM, **(E)** mCitrine-KRasD30C-CVIM and **(F)** mCitrine-KRasE31C-CVIM after NCL of the KRas-MESNA constructs with the tetrapeptide -CVIM (2.4.3)

5.4 Rab1 sensor *in vitro* - GEF, GAP and effector interaction

DrrA

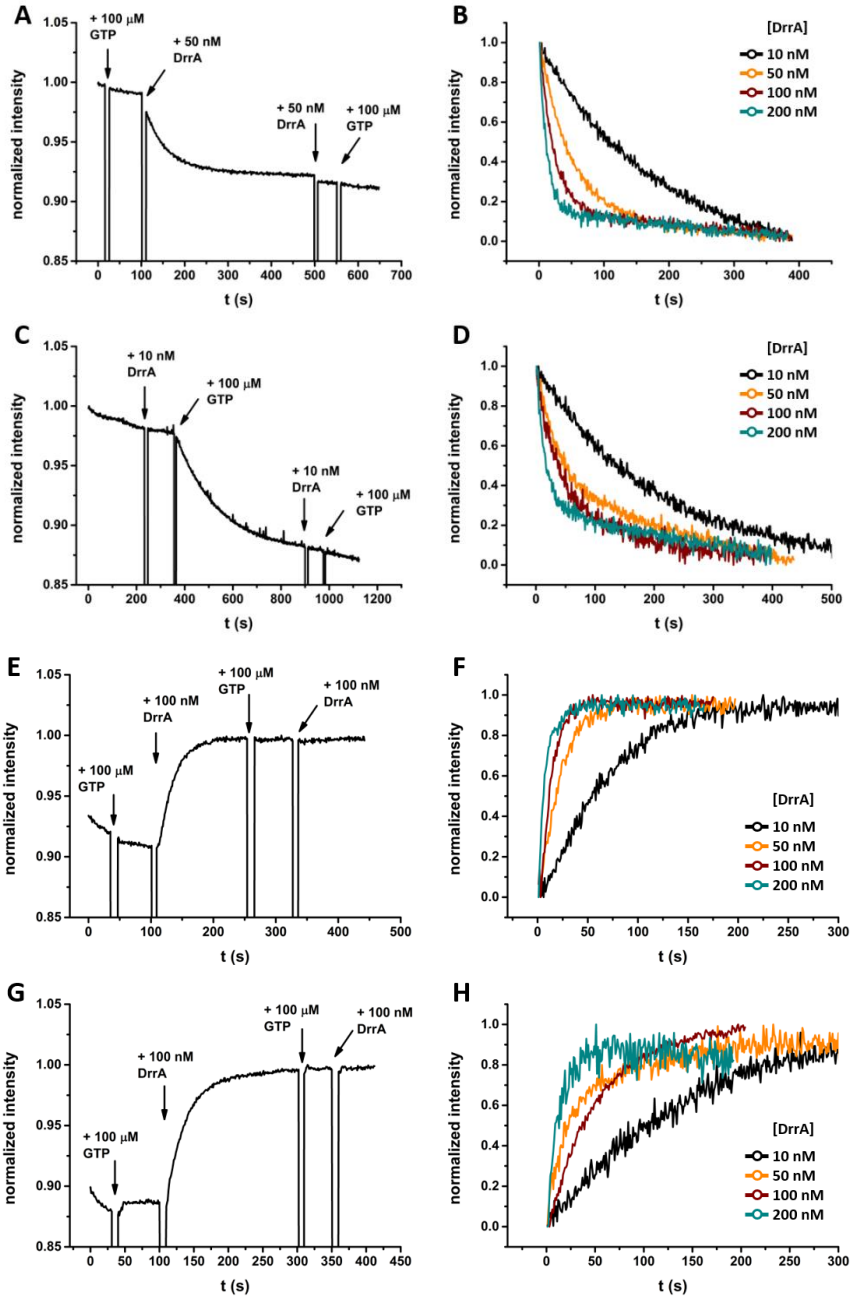

Figure 5-9: DrrA mediated nucleotide exchange of Rab1 FRET sensors.
Addition of 100 µM GTP and 10-100 nM $DrrA_{340-533}$ to 200 nM GDP-bound **(A)** EGFP-Rab1T34C-TF3, **(C)** EGFP-Rab1S36C-TF3, **(E)** EGFP-Rab1D53C-TF3 and **(G)** EGFP-Rab1G54C-TF3 result in a steep decrease (T34C and S36C) or increase (D53C and G54C) of the detected sensitized emission signal. Rate constants of nucleotide exchange depend on [$DrrA_{340-533}$]. **(B)** EGFP-Rab1T34C-TF3, **(D)** EGFP-Rab1S36C-TF3, **(F)** EGFP-Rab1D53C-TF3 and **(H)** EGFP-Rab1G54C-TF3. Changes in FRET efficiency were observed by sensitized emission with excitation at 480 nm and emission collected at 580 nm.

TBC1D20

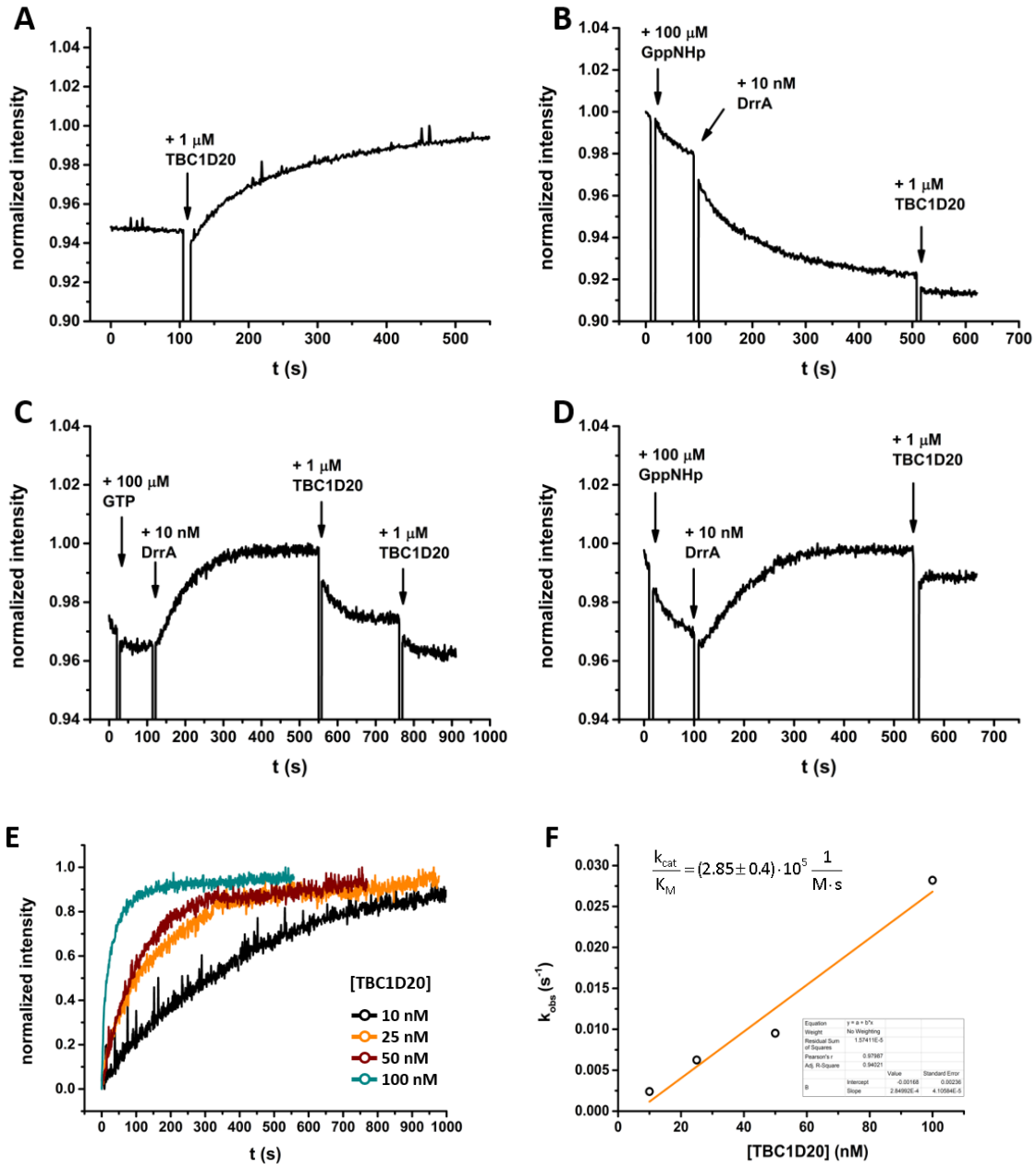

Figure 5-10: Fluorescence measurement of TBC1D20 induced GTP hydrolysis.
GAP-induced GTP hydrolysis was observed through addition of 1-2 µM TBC1D20$_{1-362}$ to **(A)** 200 nM EGFP-Rab1S36C-TF3 and **(C)** 200 nM EGFP-Rab1D53C-TF3 constructs after DrrA$_{340-533}$-mediated GDP to GTP exchange. When GDP is exchanged to GppNHp, TBC1D20$_{1-362}$ failed to reverse the FRET signal change for **(B)** 200 nM EGFP-Rab1S36C-TF3 and **(D)** 200 nM EGFP-Rab1D53C-TF3. Changes in FRET efficiency were observed by sensitized emission with excitation at 480 nm and emission collected at 580 nm **(E)** The observed rate constant of GTP hydrolysis depends on TBC1D20$_{1-362}$ concentration. To determine the catalytic efficiency 10 nM - 1 µM of TBC1D20$_{1-362}$ were added to 1 µM mantGTP:Rab$_{wt}$. **(F)** By plotting k_{obs} against [TBC1D20$_{1-362}$] the catalytic efficiency can be extracted as the slope of the linear fit (solid blue line). The change in mantGTP upon GTP hydrolysis was monitored with excitation set at 360 nm and emission at 438 nm.

OCRL

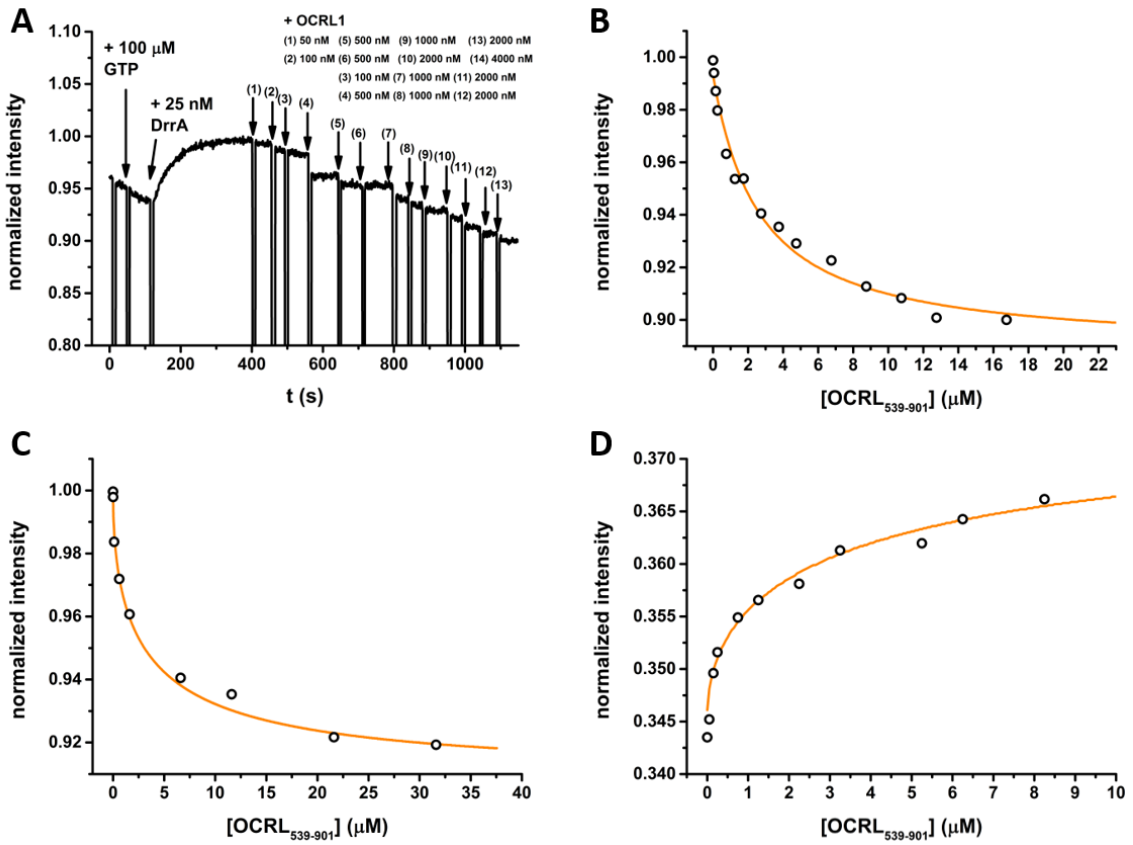

Figure 5-11: OCRL1 binding to Rab1 FRET-sensor constructs.
(A) After nucleotide exchange trough addition of 100 µM GTP and 25 nM $DrrA_{340-533}$, increasing amounts of $OCRL1_{539-901}$ were added to 200 nM GTP-bound EGFP-Rab1D53C-TF3. By plotting the change in fluorescence against the effector protein concentration, K_D was obtained through fitting with a quadratic equation as described in in 2.5.4.3 (solid orange line) for **(B)** 200 nM GTP-bound EGFP-Rab1D53C-TF3 and **(C)** 200 nM GTP-bound EGFP-Rab1G54C-TF3. **(D)** For 200 nM GTP-bound EGFP-Rab1T34C-TF3 the K_D for OCRL binding was measured by fluorescence polarization with excitation at 480 nm, emission collected at 510 nm and an interval time of 13 s. Changes in FRET efficiency **(A)**-**(C)** were observed by sensitized emission with excitation at 480 nm and emission collected at 580 nm.

LidA

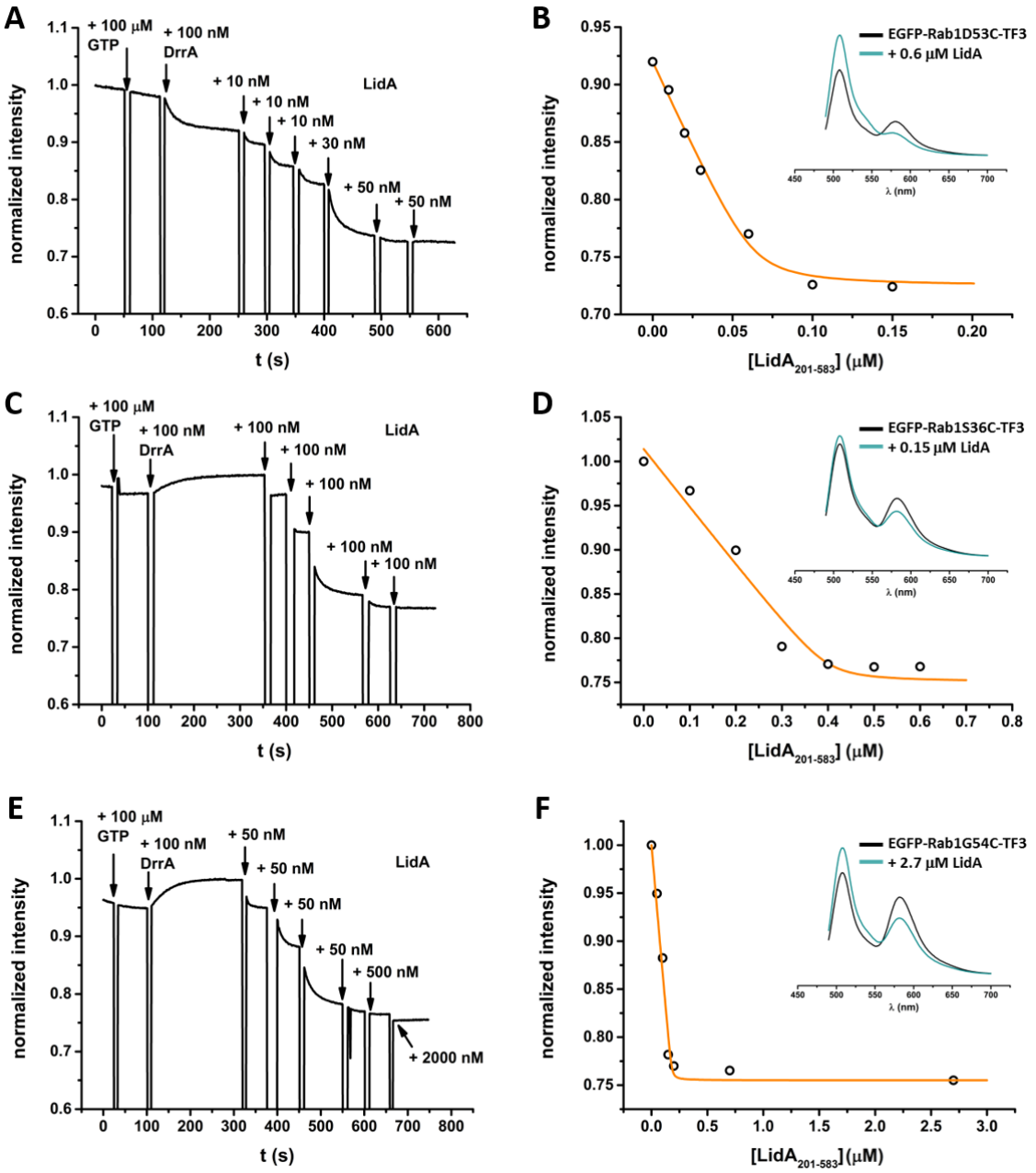

Figure 5-12: LidA binding to Rab1 FRET-sensor constructs.
Addition of increasing amounts of $OCRL1_{539-901}$ to **(A)** 100 nM GTP-bound EGFP-Rab1S36C-TF3, **(C)** 500 nM GTP-bound EGFP-Rab1S36C-TF3 or **(E)** 300 nM GTP-bound EGFP-Rab1G54C-TF3 after nucleotide exchange trough addition of 100 µM GTP and 100 nM $DrrA_{340-533}$. By plotting the change in fluorescence intensity against the effector protein concentration the K_D for $LidA_{201-583}$ binding was obtained through fitting with a quadratic equation as described in 2.5.4.3 (solid orange line) for **(B)** 100 nM EGFP-Rab1S36C-TF3, **(D)** 500 nM EGFP-Rab1S36C-TF3 and **(F)** 300 nM EGFP-Rab1G54C-TF3. **(Insets)** Fluorescence spectra of **(B)** EGFP-Rab1S36C-TF3, **(D)** 500 nM EGFP-Rab1S36C-TF3 and **(F)** 300 nM EGFP-Rab1G54C-TF3 before (solid black line) and after (solid teal) binding of $LidA_{201-583}$. Changes in FRET efficiency were observed by sensitized emission with excitation at 480 nm and emission collected at 580 nm. Fluorescence spectra were obtained with excitation set to 480 nm and emission collected from 490-700 nm.

5.5 Rab1 FRET sensor *in vivo*

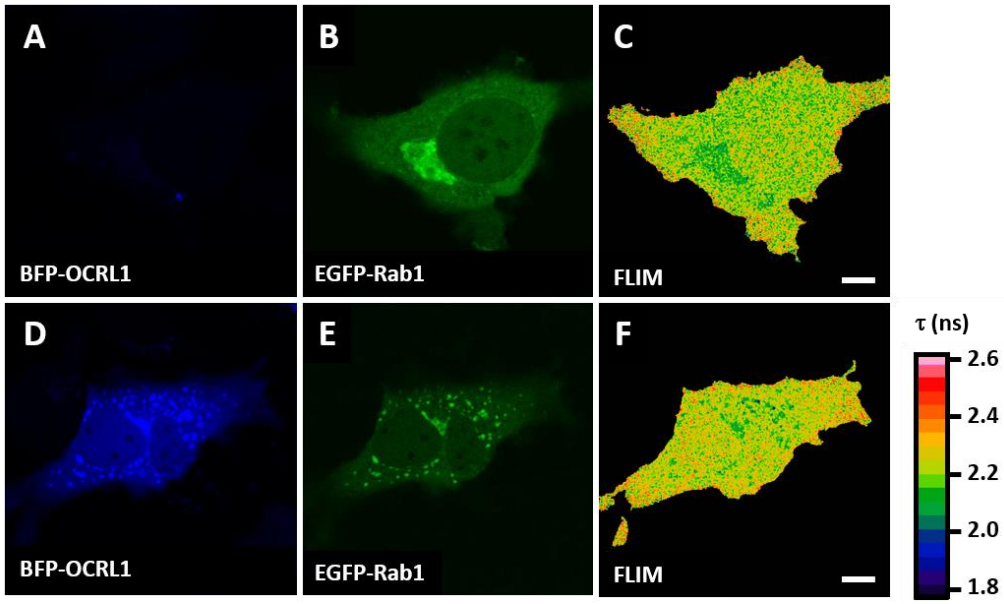

Figure 5-13: Donor only Rab1 constructs in HeLa cells expressing BFP-OCRL1.
Fluorescence and FLIM images of EGFP-Rab1 after microinjection into **(A)-(C)** wild type HeLa cell and **(D)-(F)** cells expressing BFP-OCRL1$_{539–901}$. **(A)/(D)** BFP- **(B)** EGFP-fluorescence and **(C)/(F)** FLIM images. Ectopic expression of BFP-OCRL1$_{539–901}$ does not results in higher donor lifetime of EGFP-Rab1. False color calibration bar for lifetime image as reference. Scale bars: 10 µm.

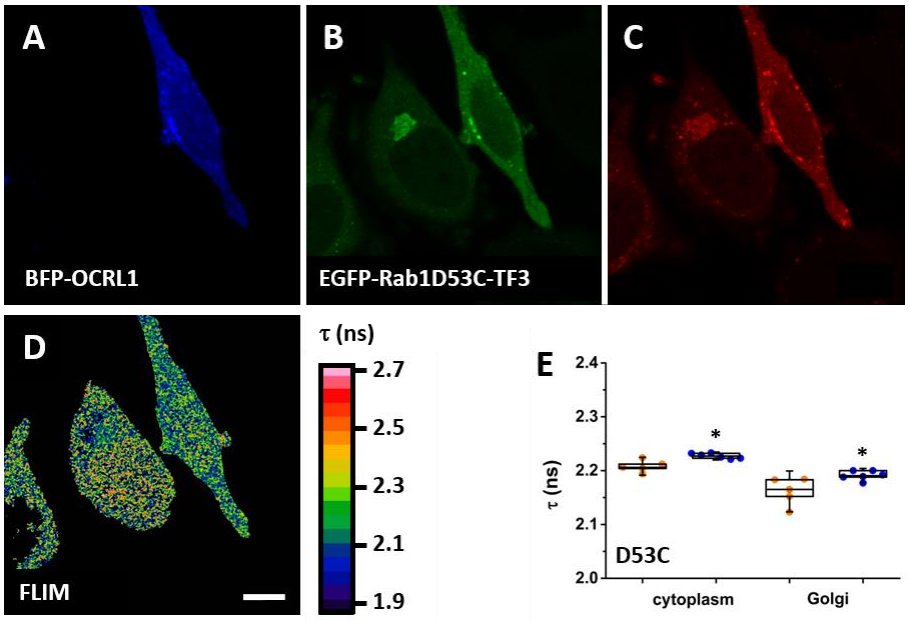

Figure 5-14: EGFP-Rab1D53C-TF3 sensor reports on OCRL1 binding *in vivo*.
Fluorescence and FLIM images of EGFP-Rab1D53C-TF3 after microinjection into a wild type and as HeLa cells expressing BFP-OCRL1$_{539–901}$. **(A)**BFP- **(B)** EGFP-, **(C)** –TF3 fluorescence and **(D)** FLIM images. **(E)** Quantification of EGFP donor lifetime at: first two panels cytoplasmic fraction, third and fourth represent Golgi localized sensor fraction. n = 5-7, individual data points are plotted, box plots: - median, □ mean, upper hinge 75th percentile, lower hinge 25th percentile, whiskers: s.d., *: $p < 0.05$. False color calibration bar for lifetime image as reference. Scale bar: 10 µm.

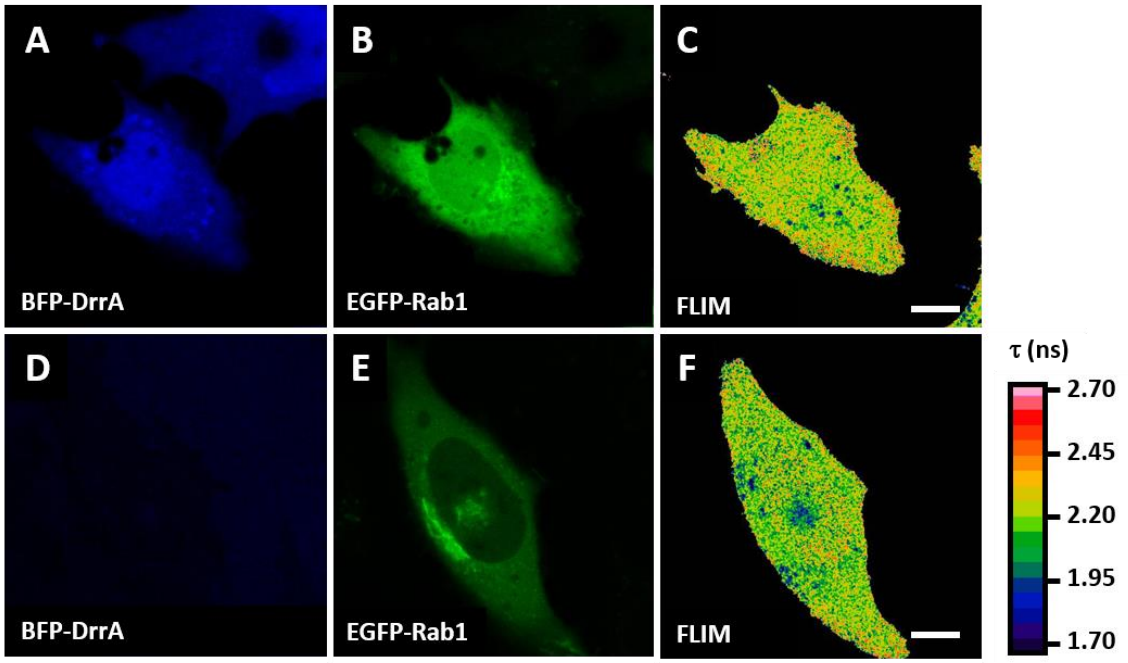

Figure 5-15: Donor only Rab1 construct in HeLa cells expressing BFP-DrrA.
Fluorescence and FLIM images of EGFP-Rab1 after microinjection into **(A)-(C)** cells expressing BFP-DrrA$_{340-533}$ and **(D)-(F)** wild type HeLa cells. **(A)/(D)** BFP- **(B)** EGFP-fluorescence and **(C)/(F)** FLIM images. Ectopic expression of BFP-DrrA$_{340-533}$ does not results in higher donor lifetime of EGFP-Rab1. False color calibration bar for lifetime image as reference. Scale bars: 10 µm.

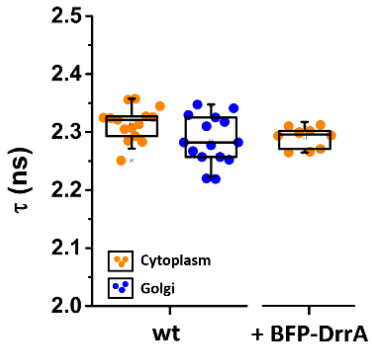

Figure 5-16: Quantification of donor lifetime of donor only probe injected in wild type and BFP-DrrA transfected cells.
Quantification of EGFP lifetime for T34C donor only construct in cells. Orange and blue dots denote cytoplasmic and Golgi-localized protein fractions. (n = 10-21 cells, individual data points are plotted, box plots: - median, upper hinge 75th percentile, lower hinge 25th Percentile, whiskers: s.d.).Left panel: Lifetime in wild type cells, right panel: lifetime in BFP-DrrA$_{340-533}$ transfected cells.

5.6 KRas sensor *in vitro* - GEF and GAP interaction

SOS - mantGDP

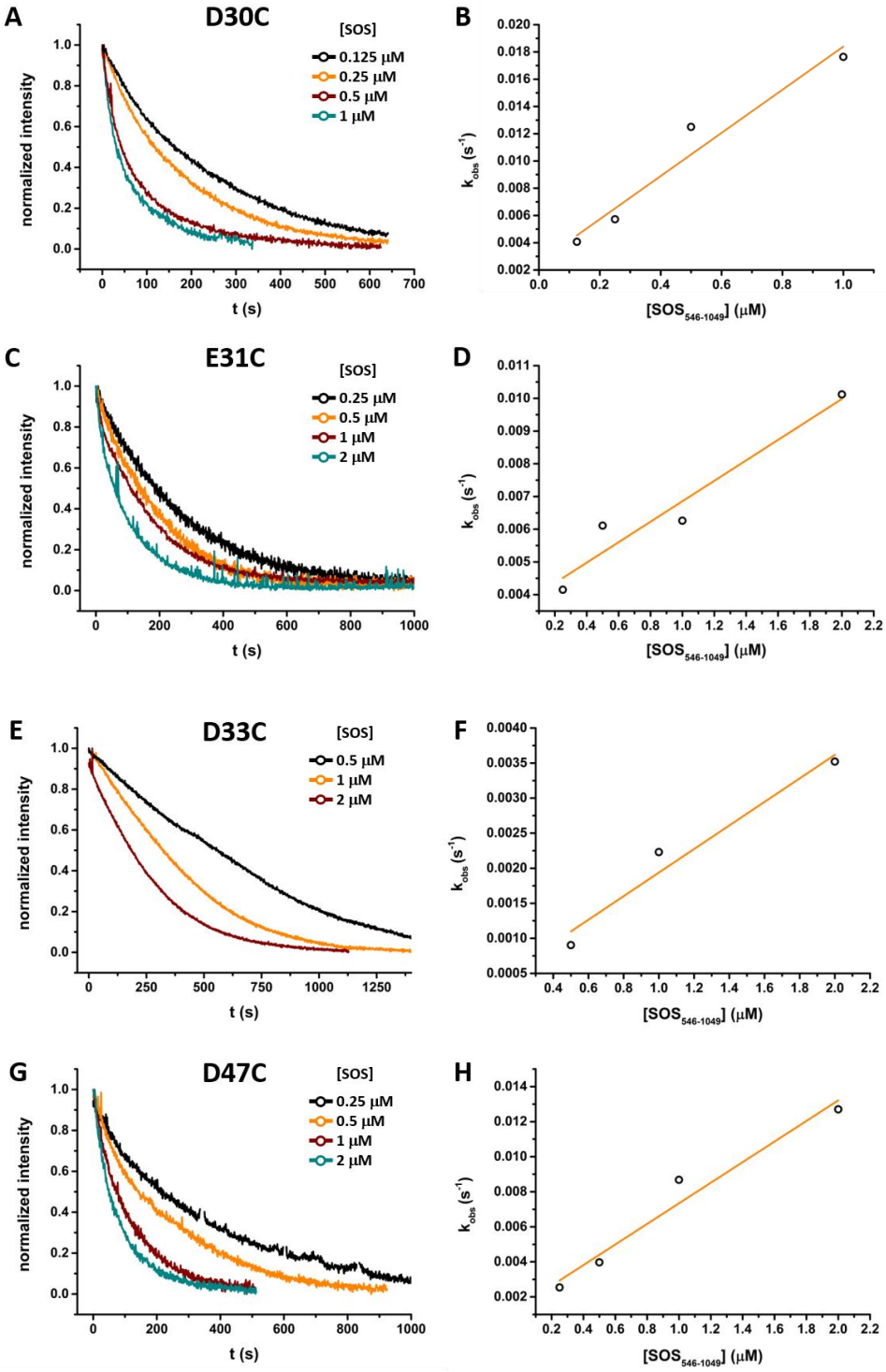

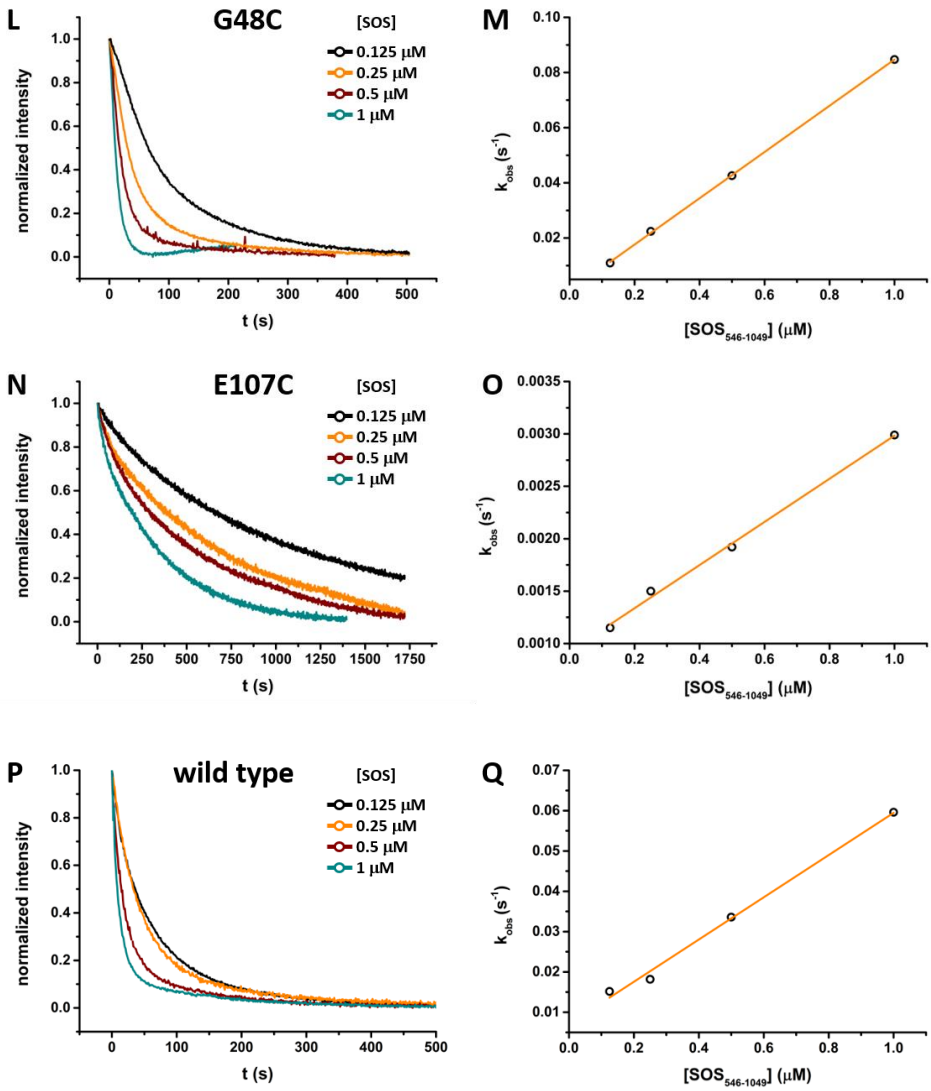

Figure 5-17: SOS-mediated nucleotide exchange of mantGDP:KRas mutants.
Addition of 100 µM GTP and varying amounts of $SOS_{564-1049}$ to 200 nM mantGDP-bound **(A)** EGFP-KRasD30C, **(C)** EGFP-KRasE31C, **(E)** EGFP-KRasD33C, **(G)** EGFP-KRasD47C, **(L)** EGFP-KRasG48C, **(N)** EGFP-KRasE107C and **(P)**$KRas_{wt}$ result in a steep decrease of the detected mant signal. The rate constants of nucleotide exchange depend on [$SOS_{564-1049}$]. The change in mant fluorescence upon nucleotide exchange was monitored with excitation set at 360 nm and emission at 438 nm. The catalytic efficiency was obtained as the slope of the linear fit (solid orange line) of k_{obs} plotting against [$SOS_{564-1049}$]. Linear fit for obtained k_{obs} values for **(B)** EGFP-KRasD30C, **(D)** EGFP-KRasE31C, **(F)** EGFP-KRasD33C **(H)** EGFP-KRasD47C, **(M)** EGFP-KRasG48C, **(O)** EGFP-KRasE107C and **(Q)** $KRas_{wt}$.

SOS - sensitized emission

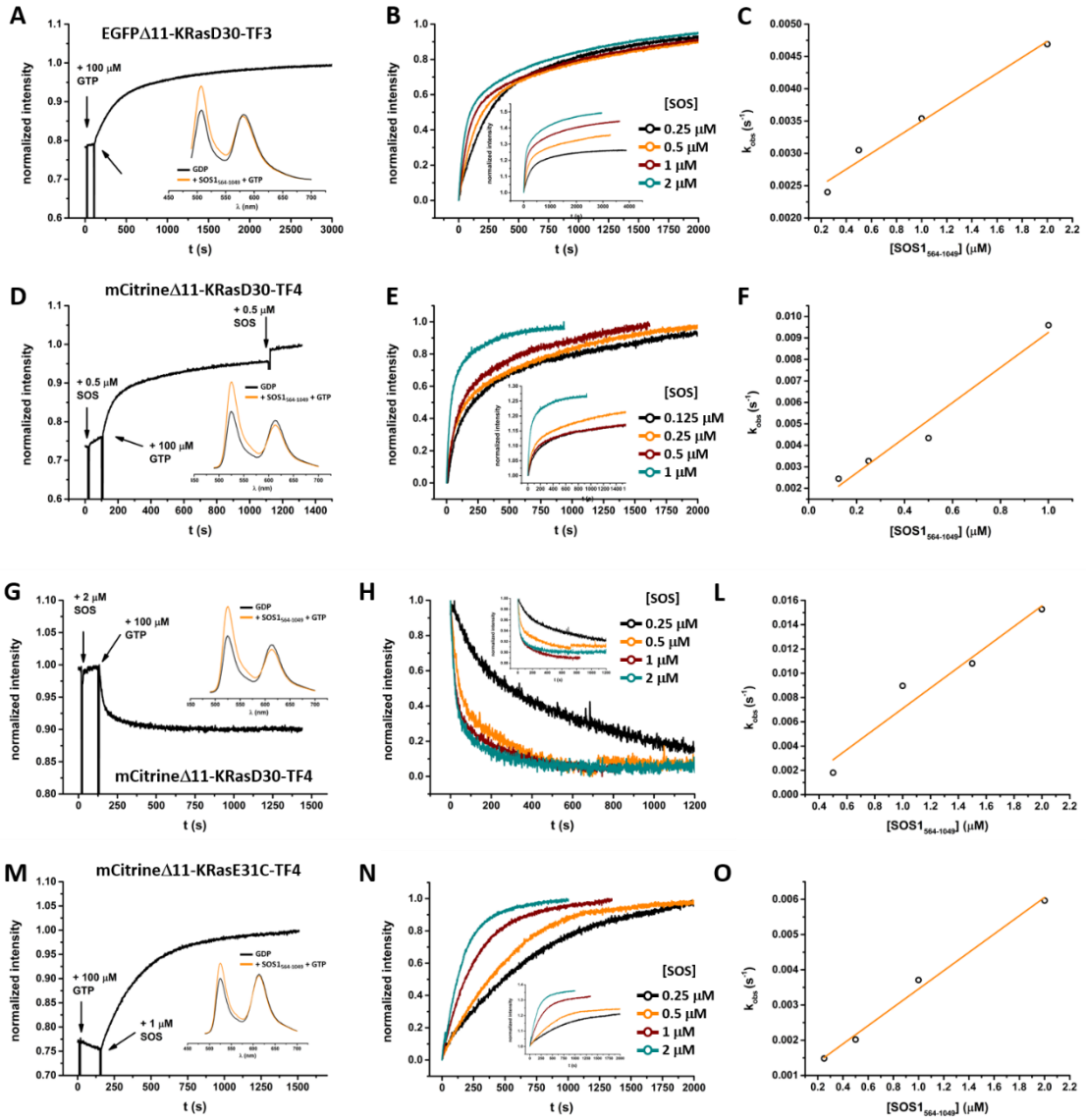

Figure 5-18: SOS-mediated nucleotide exchange of KRas FRET sensors.
Addition of $SOS_{564-1049}$ to 200 nM KRas FRET sensor constructs induces rapid nucleotide exchange in the presence of excess GTP (100 µM). Typical fluorescence curves for **(A)** EGFPΔ11-KRasD30C-TF3, **(D)** and **(G)** mCitrineΔ11-KRasD30C-TF4 (mCitrine fluorescence) and **(M)** mCitrineΔ11-KRasE31C-TF4 (mCitrine fluorescence) **(Insets)** Fluorescence spectra of KRas FRET sensors before (solid black line) and after nucleotide exchange (solid orange line). **(B)-(N)** Rate constants of nucleotide exchange depend on $SOS_{564-1049}$ concentration. **(C)-(O)** By plotting k_{obs} against [$SOS_{564-1049}$] the catalytic efficiency can be extracted as the slope of the linear fit (solid orange line). FRET efficiency change was monitored by sensitized emission (excitation set at 480 nm and emission at 580 nm (TF3)/ 614 nm (TF4) or directly from the donor fluorescence (mCitrine: excitation set at 480 nm and emission at 525 nm).

RasGAP

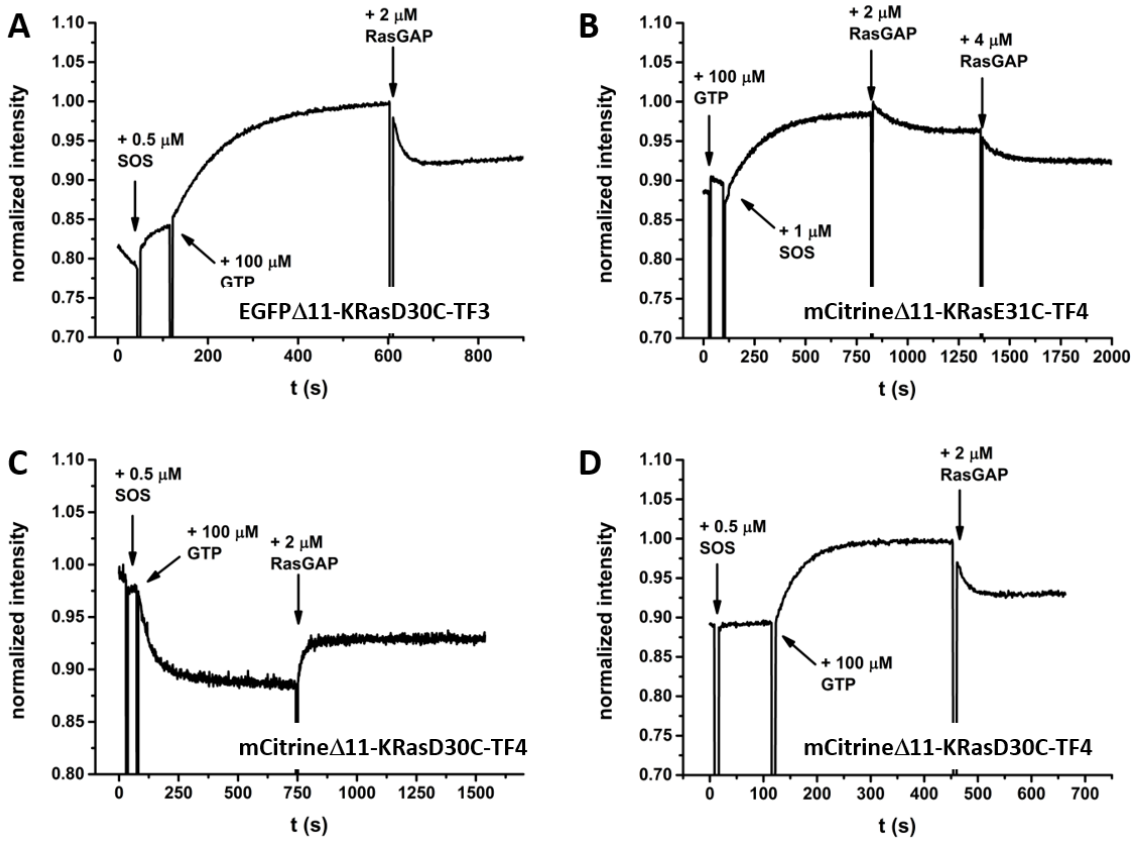

Figure 5-19: Fluorescence measurement of RasGAP induced GTP hydrolysis.
Addition of $RasGAP_{714-1047}$ to 200 nM GTP-bound KRas Fret sensor reverses the initial drop in FRET signal intensity upon nucleotide exchange through $SOS_{564-1049}$. Fluorescence profile for **(A)** EGFPΔ11-KRasD30C-TF3, **(B)** mCitrineΔ11-KRasE31C-TF4 and **(D)** mCitrineΔ11-KRaD30C-TF4 activation with subsequent deactivation through addition of $RasGAP_{714-1047}$ monitored by donor fluorescence signal with excitation at 480 nm and emission collected at 510 nm (EGFP) or 525 nm (mCitrine). Fluorescence measurement of **(C)** mCitrineΔ11-KRaD30C-TF4 activation with subsequent deactivation through addition of $RasGAP_{714-1047}$ monitored by sensitized emission with excitation at 480 nm and emission collected at 614 nm.

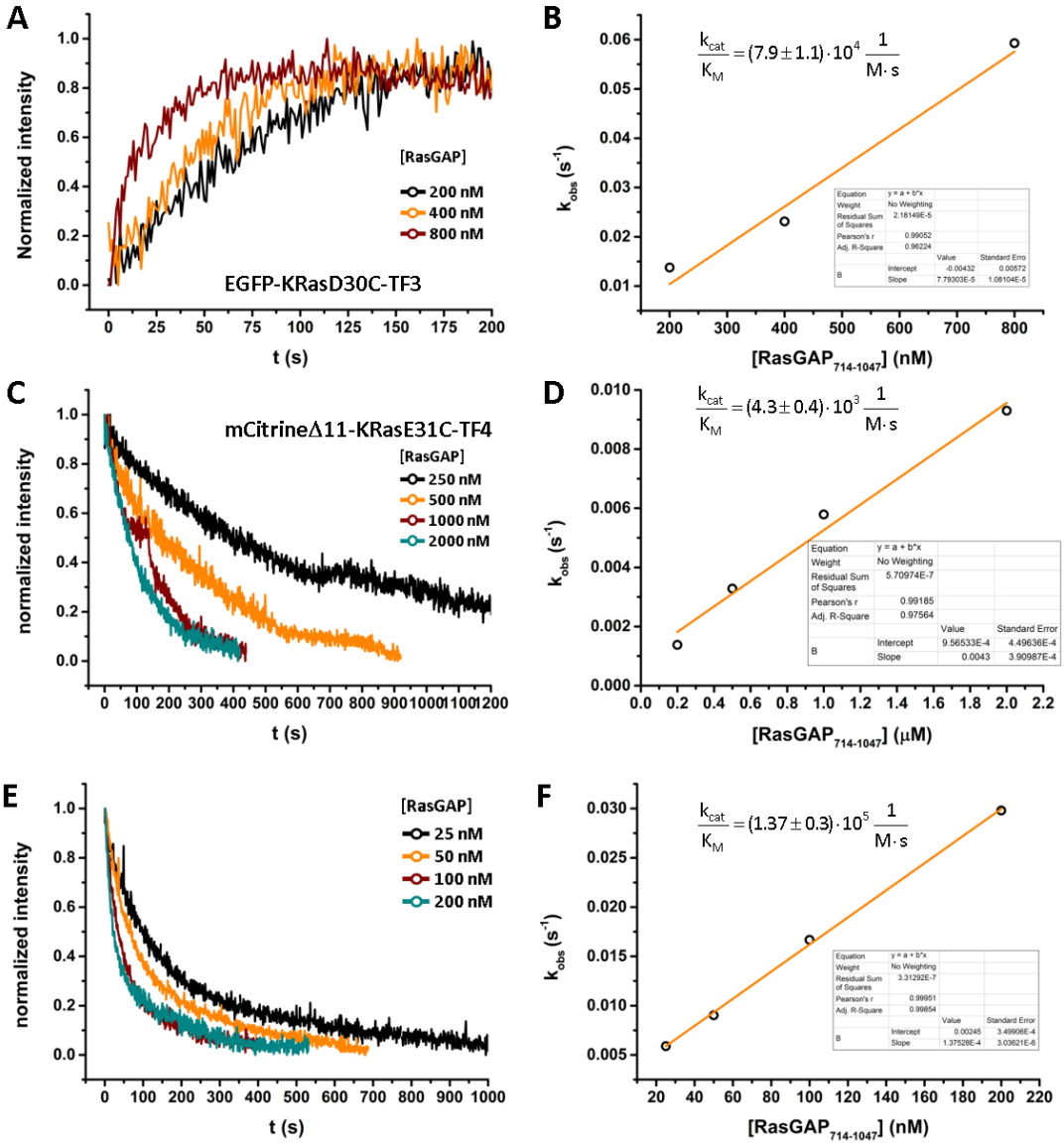

Figure 5-20: Catalytic efficiency of RasGAP towards KRas FRET sensors.
The observed rate constants of GTP hydrolysis depend on RasGAP$_{714-1047}$ concentration. To determine the catalytic efficiency varying amounts of RasGAP$_{714-1047}$ were added to 200 nM GTP-bound **(A)** EGFP-KRasD30C-TF3, **(C)** mCitrineΔ11-KRasE31C-TF4 and **(E)** mantGTP-bound KRas$_{wt}$. By plotting k_{obs} against [RasGAP$_{714-1047}$] the catalytic efficiency can be extracted as the slope of the linear fit (solid orange line). Linear fit for obtained k_{obs} values for **(B)** EGFP-KRasD30C-TF3, **(D)** mCitrineΔ11-KRasE31C-TF4 and **(F)** KRas$_{wt}$. **(A)** EGFP-KRasD30C-TF3 deactivation monitored by sensitized emission with excitation at 480 nm and emission collected at 580 nm. **(C)** mCitrineΔ11-KRasE31C-TF4 deactivation monitored by donor fluorescence with excitation at 480 nm and emission collected at 525 nm. **(E)** The change in mantGTP upon GTP hydrolysis was monitored with excitation set at 360 nm and emission at 438 nm.

5.7 KRas sensor *in vivo*

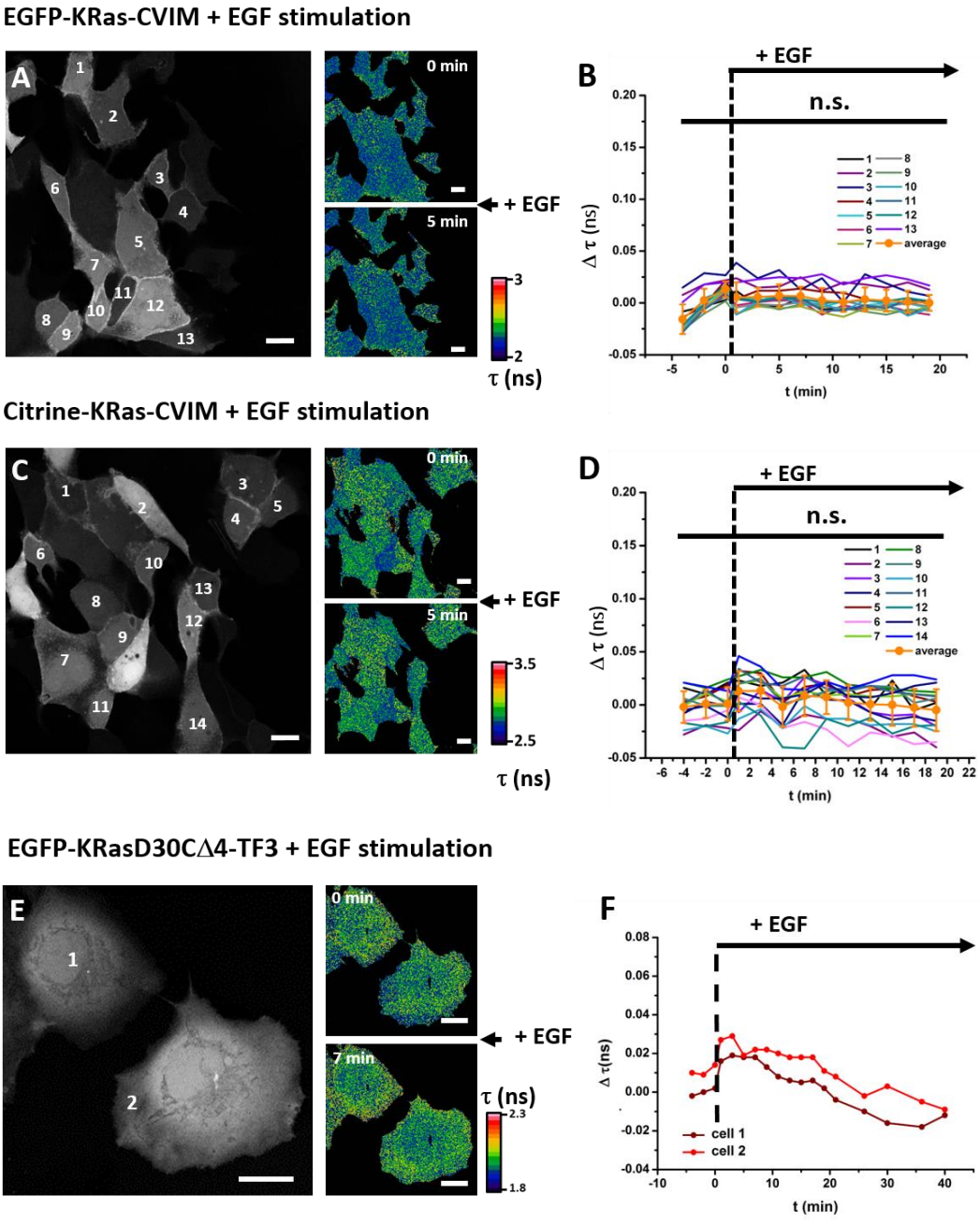

Figure 5-21: Control experiments for EGF induced KRas activation *in vivo*.
Confocal and FLIM images of donor only **(A)** EGFP-KRas and **(C)** mCitrine-KRas-CVIM in serum starved MDCK cells. FLIM images are shown before (upper panel, 0 min) and 5 min after EGF stimulation (lower panel). mCitrine lifetime before **(B)** and 5 min after **(C)** EGF stimulation. False color calibration bar for lifetime images as reference. Scale bars: 20 μM.

5.8 Rab1 cycling

Control measurements - cycloheximide treatment

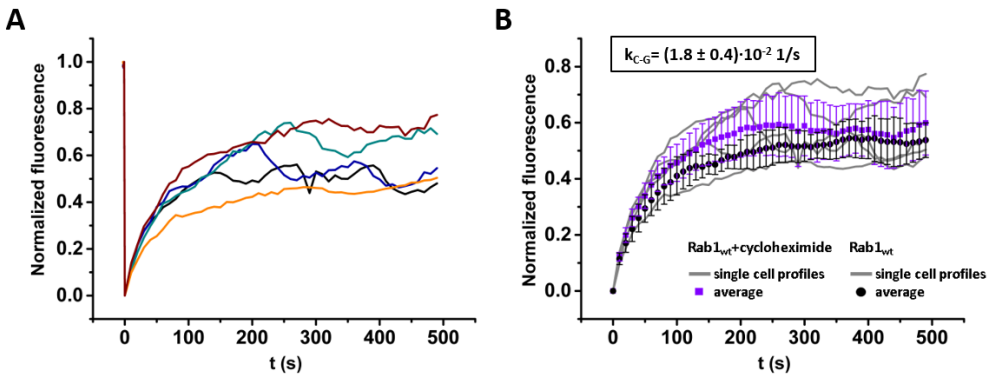

Figure 5-22: Recovery curves for EGFP-Rab1$_{wt}$ bleaching at the Golgi and average k_{C-G} after cycloheximide treatment. **(A)** Plot of normalized average EGFP intensity at Golgi ROI during FRAP experiment. Each line represents one bleaching experiment. **(B)** Plot of individual (gray lines) and average (purple squares, mean ± s.d.) recovery curves in comparison to average EGFP-Rab1$_{wt}$ recovery in untreated cells (black circles, mean ± s.d.). k_{C-G} was obtained as the average of individual k_{obs} values. k_{obs} was determined for each recovery curve by fitting with the monoexponential function (Eq. 2-14).

Bleaching

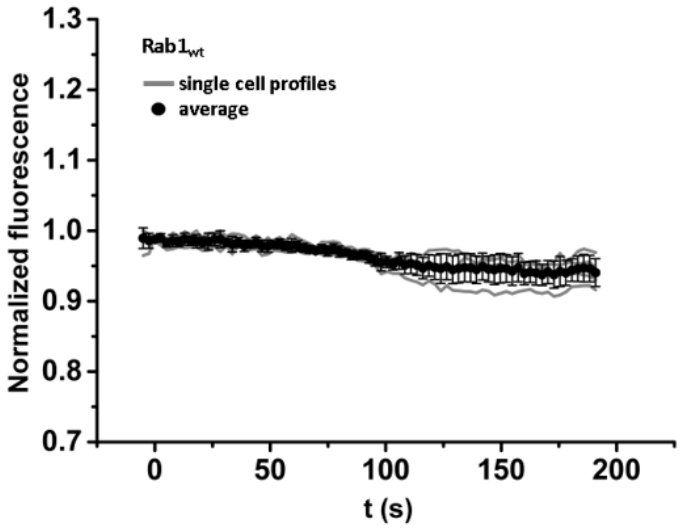

Figure 5-23: Bleaching control of EGFP-Rab1$_{wt}$ on Golgi during FRAP experiment.
Plot of normalized average EGFP intensity at Golgi ROI during FRAP experiment without bleaching step. Plot of individual (gray lines) and average (black circles, mean ± s.d.) fluorescence intensity in Golgi ROI.

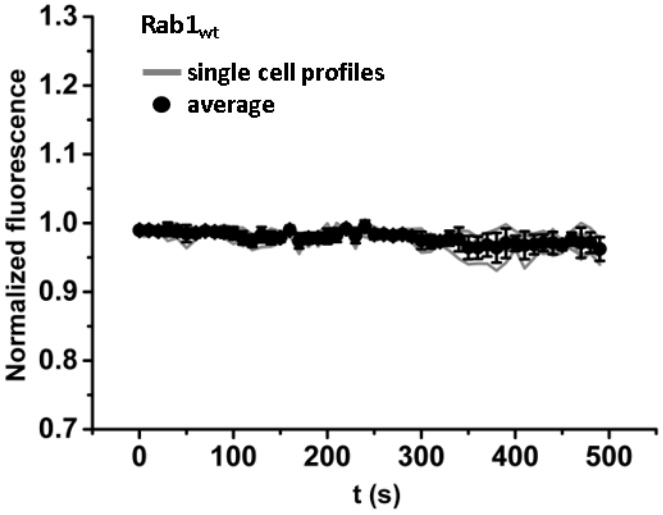

Figure 5-24: Photoactivation by imaging control of paGFP-Rab1$_{wt}$.
Plot of normalized average paGFP intensity during time-lapse imaging without photo activation step. Plot of individual (gray lines) and average (black circles, mean ± s.d.) fluorescence intensity in cells.

FRAP - k_{C-G}

Rab1 wt + nocodazole

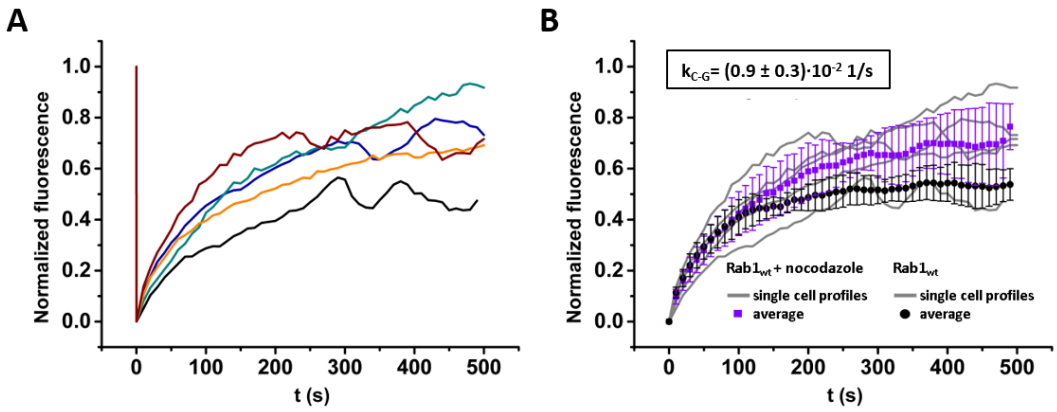

Figure 5-25: Recovery curves for EGFP-Rab1$_{wt}$ bleaching at the Golgi and average k_{C-G} after nocodazole treatment.
(A) Plot of normalized average EGFP intensity at Golgi ROI during FRAP experiment. Each line represents one bleaching experiment. **(B)** Plot of individual (gray lines) and average (purple squares, mean ± s.d.) recovery curves in comparison to average EGFP-Rab1$_{wt}$ recovery in untreated cells (black circles, mean ± s.d.). k_{C-G} was obtained as the average of individual k_{obs} values. k_{obs} was determined for each recovery curve by fitting with the monoexponential function (Eq. 2-14).

Rab1Q67L

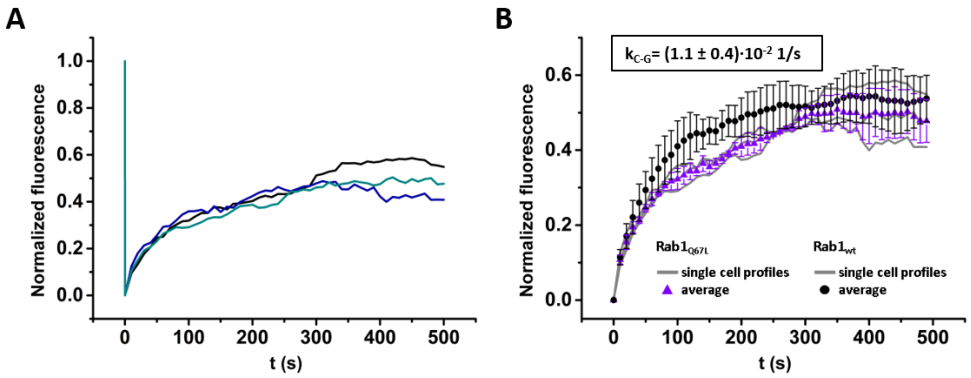

Figure 5-26: Recovery curves for EGFP-Rab1Q67L bleaching at the Golgi and average k_{C-G}.
(A) Plot of normalized average EGFP intensity at Golgi ROI during FRAP experiment. Each line represents one bleaching experiment. **(B)** Plot of individual (gray lines) and average (purple triangles, mean ± s.d.) recovery curves in comparison to average of EGFP-$Rab1_{wt}$ recovery in untreated cells (black circles, mean ± s.d.). k_{C-G} was obtained as the average of individual k_{obs} values. k_{obs} was determined for each recovery curve by fitting with the monoexponential function (Eq. 2-14).

Rab1D44N

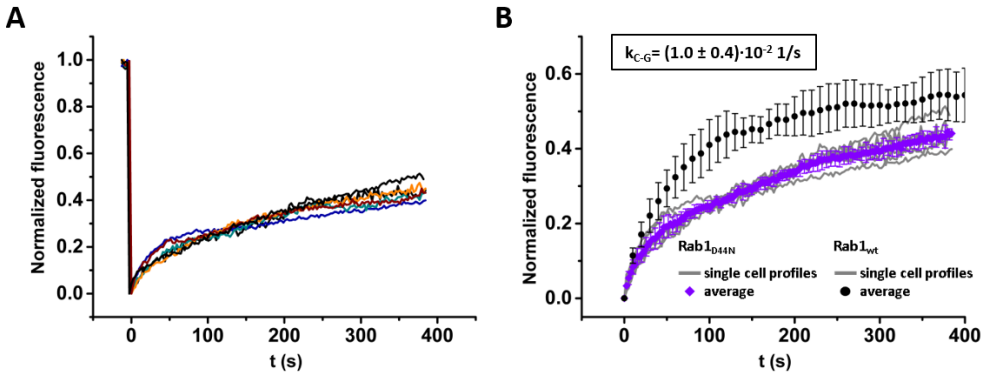

Figure 5-27: Recovery curves for EGFP-Rab1D44N bleaching at the Golgi and average k_{C-G}.
(A) Plot of normalized average EGFP intensity at Golgi ROI during FRAP experiment. Each line represents one bleaching experiment. **(B)** Plot of individual (gray lines) and average (purple diamonds, mean ± s.d.) recovery curves in comparison to average of EGFP-$Rab1_{wt}$ recovery in untreated cells (black circles, mean ± s.d.). k_{C-G} was obtained as the average of individual k_{obs} values. k_{obs} was determined for each recovery curve by fitting with the monoexponential function (Eq. 2-14).

PRA1 knock-down

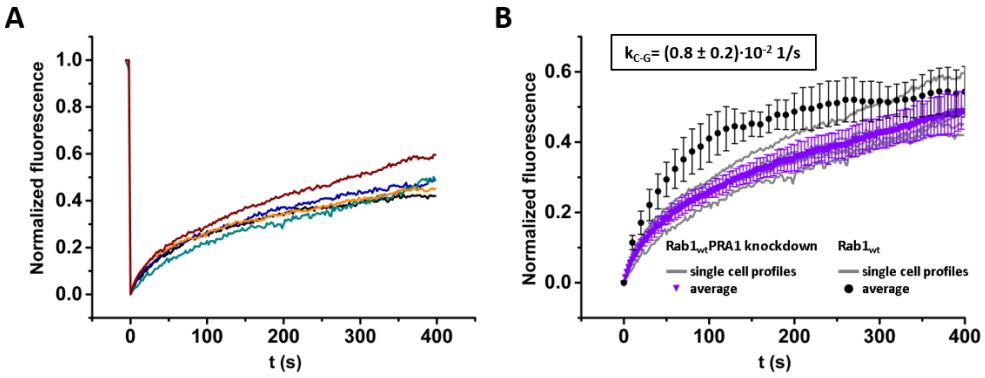

Figure 5-28: Recovery curves for EGFP-Rab1$_{wt}$ bleaching at the Golgi in PRA1 knock-down cells and average k_{C-G}.
(A) Plot of normalized average EGFP intensity at Golgi ROI during FRAP experiment. Each line represents one bleaching experiment. **(B)** Plot of individual (gray lines) and average (purple triangles, mean ± s.d.) recovery curves in comparison to average of EGFP-Rab1$_{wt}$ recovery in wild type cells (black circles, mean ± s.d.). k_{C-G} was obtained as the average of individual k_{obs} values. k_{obs} was determined for each recovery curve by fitting with the monoexponential function (Eq. 2-14).

Photoactivation - k_{C-G}

Rab1$_{wt}$ + nocodazole

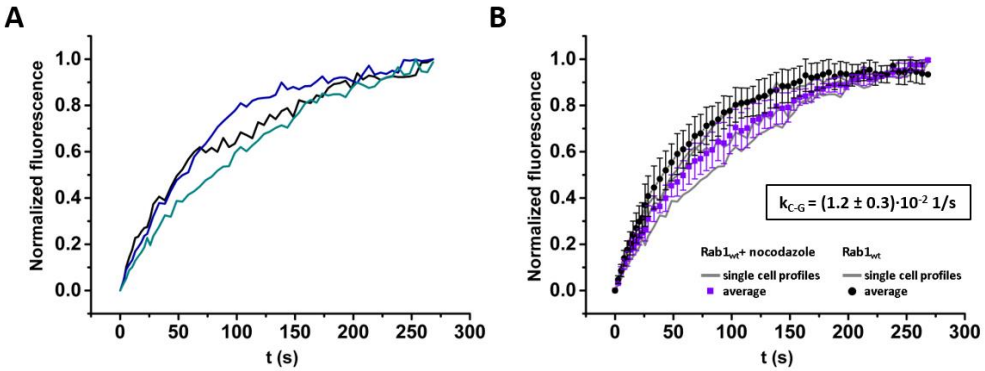

Figure 5-29: Fluorescence intensity increase at Golgi following photoactivation of paGFP-Rab1$_{wt}$ in the cytoplasm after nocodazole treatment.
(A) Plot of normalized average paGFP intensity at Golgi ROI following photoactivation in the cytoplasm. Each line represents a single photoactivation experiment. **(B)** Plot of individual (gray lines) and average (purple squares, mean ± s.d.) intensity curves in comparison to average paGFP-Rab1$_{wt}$ activation in untreated cells (black circles, mean ± s.d.). k_{C-G} was obtained as the average of individual k_{obs} values. k_{obs} was determined for each curve by fitting with the monoexponential function (Eq. 2-14).

Rab1Q67L

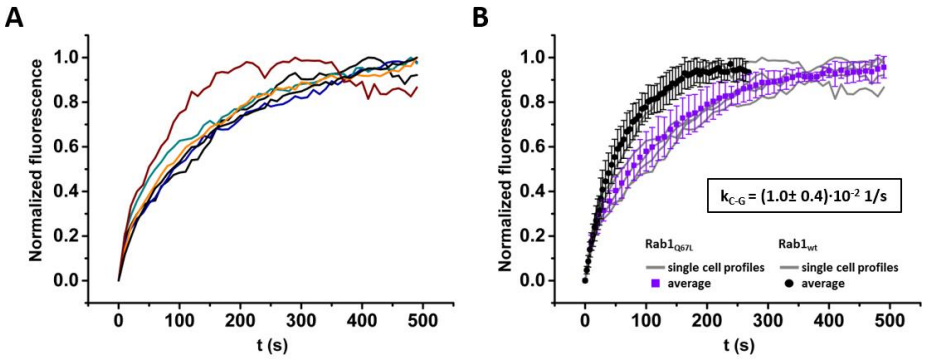

Figure 5-30: Fluorescence increase at the Golgi following photoactivation of paGFP-Rab1Q67L in the cytoplasm.
(A) Plot of normalized average paGFP intensity at Golgi ROI following photoactivation in the cytoplasm. Each line represents a single photoactivation experiment. **(B)** Plot of individual (gray lines) and average (purple squares, mean ± s.d.) intensity curves in comparison to average paGFP-Rab1$_{wt}$ activation (black circles, mean ± s.d.). k_{C-G} was obtained as the average of individual k_{obs} values. k_{obs} was determined for each curve by fitting with the monoexponential function (Eq. 2-14).

PRA1 knock-down

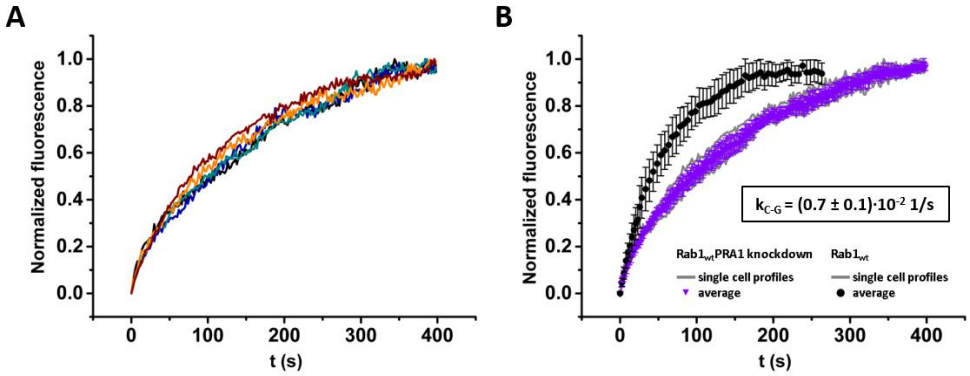

Figure 5-31: Fluorescence intensity increase at Golgi following photoactivation of paGFP-Rab1$_{wt}$ in the cytoplasm of PRA1 knock-down cells.
(A) Plot of normalized average paGFP intensity at Golgi ROI following photoactivation in the cytoplasm. Each line represents a single photoactivation experiment. **(B)** Plot of individual (gray lines) and average (purple triangles, mean ± s.d.) intensity curves in comparison to average paGFP-Rab1$_{wt}$ activation in wild type cells (black circles, mean ± s.d.). k_{C-G} was obtained as the average of individual k_{obs} values. k_{obs} was determined for each curve by fitting with the monoexponential function (Eq. 2-14).

Photoactivation – k_{G-C}

Rab1Q67L

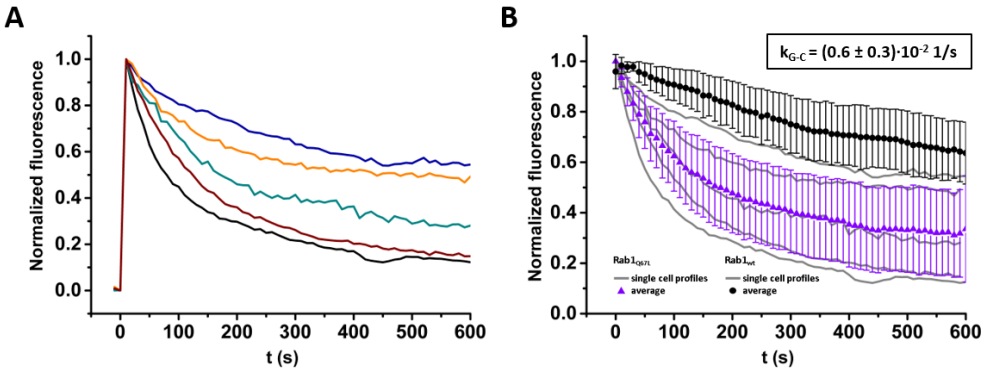

Figure 5-32: Fluorescence intensity decrease at Golgi following photoactivation of paGFP-Rab1Q67L.
(A) Plot of normalized average paGFP intensity at Golgi ROI following photoactivation. Each line represents a single photoactivation experiment. **(B)** Plot of individual (gray lines) and average (purple triangles, mean ± s.d.) intensity curves in comparison to average paGFP-Rab1$_{wt}$ activation (black circles, mean ± s.d.). k_{G-C} was obtained as the average of individual k_{obs} values. k_{obs} was determined for each curve by fitting with the monoexponential function (Eq. 2-14).

Rab1D44N

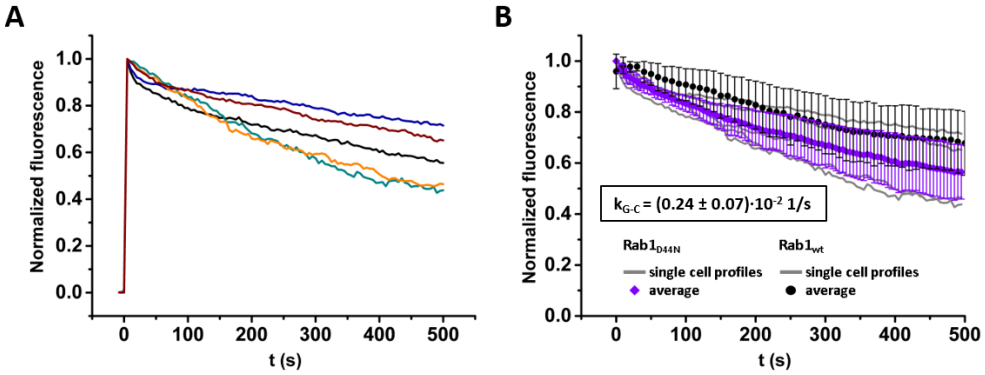

Figure 5-33: Fluorescence intensity decrease at Golgi following photoactivation of paGFP-Rab1D44N.
(A) Plot of normalized average paGFP intensity at Golgi ROI following photoactivation. Each line represents a single photoactivation experiment. **(B)** Plot of individual (gray lines) and average (purple diamonds, mean ± s.d.) intensity curves in comparison to average paGFP-Rab1$_{wt}$ activation (black circles, mean ± s.d.). k_{G-C} was obtained as the average of individual k_{obs} values. k_{obs} was determined for each curve by fitting with the monoexponential function (Eq. 2-14).

Rab1$_{wt}$ + nocodazole

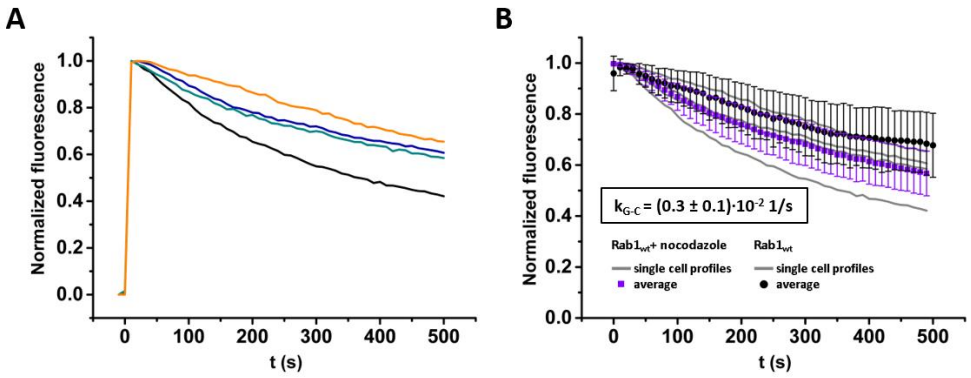

Figure 5-34: Fluorescence intensity decrease at Golgi following photoactivation of paGFP-Rab1$_{wt}$ after nocodazole treatment.
(A) Plot of normalized average paGFP intensity at Golgi ROI following photoactivation. Each line represents a single photoactivation experiment. **(B)** Plot of individual (gray lines) and average (purple squares, mean ± s.d.) intensity curves in comparison to average paGFP-Rab1$_{wt}$ activation in untreated cells (black circles, mean ± s.d.). k_{G-C} was obtained as the average of individual k_{obs} values. k_{obs} was determined for each curve by fitting with the monoexponential function (Eq. 2-14).

PRA1 knock-down

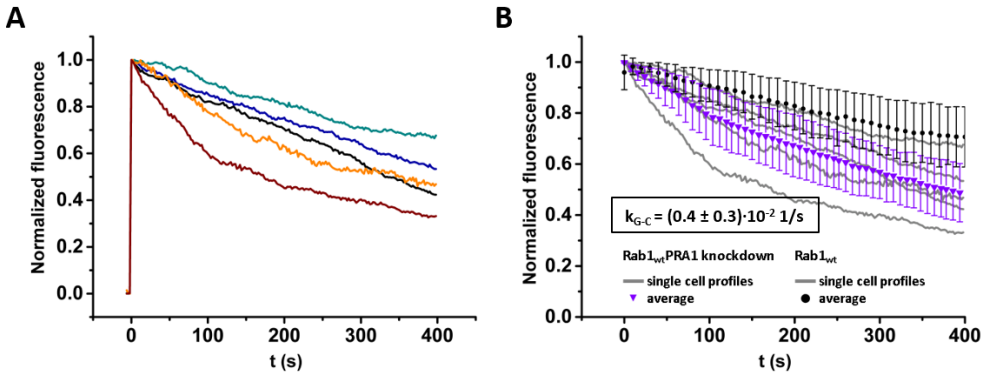

Figure 5-35: Fluorescence intensity decrease at Golgi following photoactivation of paGFP-Rab1$_{wt}$ in PRA1 knock-down cells.
(A) Plot of normalized average paGFP intensity at Golgi ROI following photoactivation. Each line represents a single photoactivation experiment. **(B)** Plot of individual (gray lines) and average (purple triangles, mean ± s.d.) intensity curves in comparison to average paGFP-Rab1$_{wt}$ activation in wild type cells (black circles, mean ± s.d.). k_{G-C} was obtained as the average of individual k_{obs} values. k_{obs} was determined for each curve by fitting with the monoexponential function (Eq. 2-14).

6 References

1. Takai, Y., Sasaki, T. & Matozaki, T. Small GTP-binding proteins. *Physiol Rev* **81**, 153-208 (2001).

2. Prior, I.A., Lewis, P.D. & Mattos, C. A comprehensive survey of Ras mutations in cancer. *Cancer Res* **72**, 2457-67 (2012).

3. Ridley, A.J. Rho family proteins: coordinating cell responses. *Trends Cell Biol* **11**, 471-7 (2001).

4. Stenmark, H. Rab GTPases as coordinators of vesicle traffic. *Nat Rev Mol Cell Biol* **10**, 513-25 (2009).

5. Zerial, M. & McBride, H. Rab proteins as membrane organizers. *Nat Rev Mol Cell Biol* **2**, 107-17 (2001).

6. Weis, K. Regulating access to the genome: nucleocytoplasmic transport throughout the cell cycle. *Cell* **112**, 441-51 (2003).

7. Li, H.Y., Cao, K. & Zheng, Y. Ran in the spindle checkpoint: a new function for a versatile GTPase. *Trends Cell Biol* **13**, 553-7 (2003).

8. Itzen, A. & Goody, R.S. GTPases involved in vesicular trafficking: structures and mechanisms. *Semin Cell Dev Biol* **22**, 48-56 (2011).

9. Wittinghofer, A. & Vetter, I.R. Structure-function relationships of the G domain, a canonical switch motif. *Annu Rev Biochem* **80**, 943-71 (2011).

10. Cherfils, J. & Zeghouf, M. Regulation of small GTPases by GEFs, GAPs, and GDIs. *Physiol Rev* **93**, 269-309 (2013).

11. Bos, J.L., Rehmann, H. & Wittinghofer, A. GEFs and GAPs: critical elements in the control of small G proteins. *Cell* **129**, 865-77 (2007).

12. Vetter, I.R. & Wittinghofer, A. The guanine nucleotide-binding switch in three dimensions. *Science* **294**, 1299-304 (2001).

13. Klebe, C., Prinz, H., Wittinghofer, A. & Goody, R.S. The kinetic mechanism of Ran--nucleotide exchange catalyzed by RCC1. *Biochemistry* **34**, 12543-52 (1995).

14. Traut, T.W. Physiological concentrations of purines and pyrimidines. *Mol Cell Biochem* **140**, 1-22 (1994).

15. Simon, I., Zerial, M. & Goody, R.S. Kinetics of interaction of Rab5 and Rab7 with nucleotides and magnesium ions. *J Biol Chem* **271**, 20470-8 (1996).

16. Pai, E.F. et al. Structure of the guanine-nucleotide-binding domain of the Ha-ras oncogene product p21 in the triphosphate conformation. *Nature* **341**, 209-14 (1989).

17. Pai, E.F. et al. Refined crystal structure of the triphosphate conformation of H-ras p21 at 1.35 A resolution: implications for the mechanism of GTP hydrolysis. *EMBO J* **9**, 2351-9 (1990).

18. Walker, J.E., Saraste, M., Runswick, M.J. & Gay, N.J. Distantly related sequences in the alpha- and beta-subunits of ATP synthase, myosin, kinases and other ATP-requiring enzymes and a common nucleotide binding fold. *EMBO J* **1**, 945-51 (1982).

19. Vetter, I. The Structure of the G Domain of the Ras Superfamily. in *Ras Superfamily Small G Proteins: Biology and Mechanisms 1* (ed. Wittinghofer, A.) 25-50 (Springer Vienna, 2014).

20. Rensland, H. et al. Substrate and product structural requirements for binding of nucleotides to H-ras p21: the mechanism of discrimination between guanosine and adenosine nucleotides. *Biochemistry* **34**, 593-9 (1995).

21. Donaldson, J.G. & Jackson, C.L. ARF family G proteins and their regulators: roles in membrane transport, development and disease. *Nat Rev Mol Cell Biol* **12**, 362-75 (2011).

22. D'Souza-Schorey, C. & Stahl, P.D. Myristoylation is required for the intracellular localization and endocytic function of ARF6. *Exp Cell Res* **221**, 153-9 (1995).

23. Schlichting, I. et al. Time-resolved X-ray crystallographic study of the conformational change in Ha-Ras p21 protein on GTP hydrolysis. *Nature* **345**, 309-15 (1990).

24. Feltham, J.L. et al. Definition of the switch surface in the solution structure of Cdc42Hs. *Biochemistry* **36**, 8755-66 (1997).

25. Kraulis, P.J., Domaille, P.J., Campbell-Burk, S.L., Van Aken, T. & Laue, E.D. Solution structure and dynamics of ras p21.GDP determined by heteronuclear three- and four-dimensional NMR spectroscopy. *Biochemistry* **33**, 3515-31 (1994).

26. Ito, Y. et al. Regional polysterism in the GTP-bound form of the human c-Ha-Ras protein. *Biochemistry* **36**, 9109-19 (1997).

27. Loh, A.P., Guo, W., Nicholson, L.K. & Oswald, R.E. Backbone dynamics of inactive, active, and effector-bound Cdc42Hs from measurements of (15)N relaxation parameters at multiple field strengths. *Biochemistry* **38**, 12547-57 (1999).

28. Spoerner, M., Herrmann, C., Vetter, I.R., Kalbitzer, H.R. & Wittinghofer, A. Dynamic properties of the Ras switch I region and its importance for binding to effectors. *Proc Natl Acad Sci U S A* **98**, 4944-9 (2001).

29. Spoerner, M. et al. Conformational states of Ras complexed with the GTP analogue GppNHp or GppCH2p: implications for the interaction with effector proteins. *Biochemistry* **44**, 2225-36 (2005).

30. Farrar, C.T., Ma, J., Singel, D.J. & Halkides, C.J. Structural changes induced in p21Ras upon GAP-334 complexation as probed by ESEEM spectroscopy and molecular-dynamics simulation. *Structure* **8**, 1279-87 (2000).

31. Spoerner, M. et al. Conformational states of human H-Ras detected by high-field EPR, ENDOR, and 31P NMR spectroscopy. *Magn Reson Chem* **43 Spec no.**, S74-83 (2005).

32. Gavriljuk, K. et al. Reaction mechanism of adenylyltransferase DrrA from Legionella pneumophila elucidated by time-resolved fourier transform infrared spectroscopy. *J Am Chem Soc* **136**, 9338-45 (2014).

33. Pasqualato, S., Renault, L. & Cherfils, J. The GDP/GTP Cycle of Arf Proteins. in *ARF Family GTPases* 23-48 (Springer Netherlands, Dordrecht, 2003).

34. Scheffzek, K., Klebe, C., Fritz-Wolf, K., Kabsch, W. & Wittinghofer, A. Crystal structure of the nuclear Ras-related protein Ran in its GDP-bound form. *Nature* **374**, 378-81 (1995).

35. John, J. et al. Kinetics of interaction of nucleotides with nucleotide-free H-ras p21. *Biochemistry* **29**, 6058-65 (1990).

36. Hutchinson, J.P. & Eccleston, J.F. Mechanism of nucleotide release from Rho by the GDP dissociation stimulator protein. *Biochemistry* **39**, 11348-59 (2000).

37. Lenzen, C., Cool, R.H., Prinz, H., Kuhlmann, J. & Wittinghofer, A. Kinetic analysis by fluorescence of the interaction between Ras and the catalytic domain of the guanine nucleotide exchange factor Cdc25Mm. *Biochemistry* **37**, 7420-30 (1998).

38. Goody, R.S. & Hofmann-Goody, W. Exchange factors, effectors, GAPs and motor proteins: common thermodynamic and kinetic principles for different functions. *Eur Biophys J* **31**, 268-74 (2002).

39. Scheffzek, K. et al. The Ras-RasGAP complex: structural basis for GTPase activation and its loss in oncogenic Ras mutants. *Science* **277**, 333-8 (1997).

40. Rittinger, K., Walker, P.A., Eccleston, J.F., Smerdon, S.J. & Gamblin, S.J. Structure at 1.65 A of RhoA and its GTPase-activating protein in complex with a transition-state analogue. *Nature* **389**, 758-62 (1997).

41. Gavriljuk, K. et al. Catalytic mechanism of a mammalian Rab.RabGAP complex in atomic detail. *Proc Natl Acad Sci U S A* **109**, 21348-53 (2012).

42. Nottingham, R.M., Ganley, I.G., Barr, F.A., Lambright, D.G. & Pfeffer, S.R. RUTBC1 protein, a Rab9A effector that activates GTP hydrolysis by Rab32 and Rab33B proteins. *J Biol Chem* **286**, 33213-22 (2011).

43. Langemeyer, L. et al. Diversity and plasticity in Rab GTPase nucleotide release mechanism has consequences for Rab activation and inactivation. *Elife* **3**, e01623 (2014).

44. Scrima, A., Thomas, C., Deaconescu, D. & Wittinghofer, A. The Rap-RapGAP complex: GTP hydrolysis without catalytic glutamine and arginine residues. *EMBO J* **27**, 1145-53 (2008).

45. Seewald, M.J., Korner, C., Wittinghofer, A. & Vetter, I.R. RanGAP mediates GTP hydrolysis without an arginine finger. *Nature* **415**, 662-6 (2002).

46. Hutagalung, A.H. & Novick, P.J. Role of Rab GTPases in Membrane Traffic and Cell Physiology. *Physiological Reviews* **91**, 119-149 (2011).

47. Touchot, N., Chardin, P. & Tavitian, A. Four additional members of the ras gene superfamily isolated by an oligonucleotide strategy: molecular cloning of YPT-related cDNAs from a rat brain library. *Proc Natl Acad Sci U S A* **84**, 8210-4 (1987).

48. Pereira-Leal, J.B. & Seabra, M.C. The mammalian Rab family of small GTPases: definition of family and subfamily sequence motifs suggests a mechanism for functional specificity in the Ras superfamily. *J Mol Biol* **301**, 1077-87 (2000).

49. Lee, M.T., Mishra, A. & Lambright, D.G. Structural mechanisms for regulation of membrane traffic by rab GTPases. *Traffic* **10**, 1377-89 (2009).

50. Pfeffer, S.R. Structural clues to Rab GTPase functional diversity. *J Biol Chem* **280**, 15485-8 (2005).

51. Chavrier, P. et al. Hypervariable C-terminal domain of rab proteins acts as a targeting signal. *Nature* **353**, 769-72 (1991).

52. Brennwald, P. & Novick, P. Interactions of three domains distinguishing the Ras-related GTP-binding proteins Ypt1 and Sec4. *Nature* **362**, 560-3 (1993).

53. Ali, B.R., Wasmeier, C., Lamoreux, L., Strom, M. & Seabra, M.C. Multiple regions contribute to membrane targeting of Rab GTPases. *J Cell Sci* **117**, 6401-12 (2004).

54. Blumer, J. et al. RabGEFs are a major determinant for specific Rab membrane targeting. *J Cell Biol* **200**, 287-300 (2013).

55. Wiegandt, D. et al. Locking GTPases covalently in their functional states. *Nat Commun* **6**, 7773 (2015).

56. Ali, B.R. & Seabra, M.C. Targeting of Rab GTPases to cellular membranes. *Biochem Soc Trans* **33**, 652-6 (2005).

57. Pfeffer, S. & Aivazian, D. Targeting Rab GTPases to distinct membrane compartments. *Nat Rev Mol Cell Biol* **5**, 886-96 (2004).

58. Li, F. et al. The role of the hypervariable C-terminal domain in Rab GTPases membrane targeting. *Proc Natl Acad Sci U S A* **111**, 2572-7 (2014).

59. Alexandrov, K. et al. Characterization of the ternary complex between Rab7, REP-1 and Rab geranylgeranyl transferase. *Eur J Biochem* **265**, 160-70 (1999).

60. Farnsworth, C.C., Seabra, M.C., Ericsson, L.H., Gelb, M.H. & Glomset, J.A. Rab geranylgeranyl transferase catalyzes the geranylgeranylation of adjacent cysteines in the small GTPases Rab1A, Rab3A, and Rab5A. *Proc Natl Acad Sci U S A* **91**, 11963-7 (1994).

61. Alexandrov, K., Horiuchi, H., Steele-Mortimer, O., Seabra, M.C. & Zerial, M. Rab escort protein-1 is a multifunctional protein that accompanies newly prenylated rab proteins to their target membranes. *EMBO J* **13**, 5262-73 (1994).

62. Wu, Y.W., Tan, K.T., Waldmann, H., Goody, R.S. & Alexandrov, K. Interaction analysis of prenylated Rab GTPase with Rab escort protein and GDP dissociation inhibitor explains the need for both regulators. *Proc Natl Acad Sci U S A* **104**, 12294-9 (2007).

63. Wu, Y.W. et al. Membrane targeting mechanism of Rab GTPases elucidated by semisynthetic protein probes. *Nat Chem Biol* **6**, 534-40 (2010).

64. Shapiro, A.D. & Pfeffer, S.R. Quantitative analysis of the interactions between prenyl Rab9, GDP dissociation inhibitor-alpha, and guanine nucleotides. *J Biol Chem* **270**, 11085-90 (1995).

65. Dirac-Svejstrup, A.B., Sumizawa, T. & Pfeffer, S.R. Identification of a GDI displacement factor that releases endosomal Rab GTPases from Rab-GDI. *EMBO J* **16**, 465-72 (1997).

66. Sivars, U., Aivazian, D. & Pfeffer, S.R. Yip3 catalyses the dissociation of endosomal Rab-GDI complexes. *Nature* **425**, 856-9 (2003).

67. Cai, Y. et al. The structural basis for activation of the Rab Ypt1p by the TRAPP membrane-tethering complexes. *Cell* **133**, 1202-13 (2008).

68. Sato, Y., Fukai, S., Ishitani, R. & Nureki, O. Crystal structure of the Sec4p.Sec2p complex in the nucleotide exchanging intermediate state. *Proc Natl Acad Sci U S A* **104**, 8305-10 (2007).

69. Delprato, A. & Lambright, D.G. Structural basis for Rab GTPase activation by VPS9 domain exchange factors. *Nat Struct Mol Biol* **14**, 406-12 (2007).

70. Wu, X. et al. Insights regarding guanine nucleotide exchange from the structure of a DENN-domain protein complexed with its Rab GTPase substrate. *Proc Natl Acad Sci U S A* **108**, 18672-7 (2011).

71. Schoebel, S., Oesterlin, L.K., Blankenfeldt, W., Goody, R.S. & Itzen, A. RabGDI displacement by DrrA from Legionella is a consequence of its guanine nucleotide exchange activity. *Mol Cell* **36**, 1060-72 (2009).

72. Carney, D.S., Davies, B.A. & Horazdovsky, B.F. Vps9 domain-containing proteins: activators of Rab5 GTPases from yeast to neurons. *Trends Cell Biol* **16**, 27-35 (2006).

73. Marat, A.L., Dokainish, H. & McPherson, P.S. DENN domain proteins: regulators of Rab GTPases. *J Biol Chem* **286**, 13791-800 (2011).

74. Barrowman, J., Bhandari, D., Reinisch, K. & Ferro-Novick, S. TRAPP complexes in membrane traffic: convergence through a common Rab. *Nat Rev Mol Cell Biol* **11**, 759-63 (2010).

75. Chin, H.F. et al. Kinetic analysis of the guanine nucleotide exchange activity of TRAPP, a multimeric Ypt1p exchange factor. *J Mol Biol* **389**, 275-88 (2009).

76. Sacher, M. et al. TRAPP, a highly conserved novel complex on the cis-Golgi that mediates vesicle docking and fusion. *EMBO J* **17**, 2494-503 (1998).

77. Geisberg, J.V., Moqtaderi, Z., Fan, X., Ozsolak, F. & Struhl, K. Global analysis of mRNA isoform half-lives reveals stabilizing and destabilizing elements in yeast. *Cell* **156**, 812-24 (2014).

78. Murata, T. et al. The Legionella pneumophila effector protein DrrA is a Rab1 guanine nucleotide-exchange factor. *Nat Cell Biol* **8**, 971-7 (2006).

79. Pan, X., Eathiraj, S., Munson, M. & Lambright, D.G. TBC-domain GAPs for Rab GTPases accelerate GTP hydrolysis by a dual-finger mechanism. *Nature* **442**, 303-6 (2006).

80. Ullrich, O., Horiuchi, H., Bucci, C. & Zerial, M. Membrane association of Rab5 mediated by GDP-dissociation inhibitor and accompanied by GDP/GTP exchange. *Nature* **368**, 157-60 (1994).

81. Soldati, T., Shapiro, A.D., Svejstrup, A.B. & Pfeffer, S.R. Membrane targeting of the small GTPase Rab9 is accompanied by nucleotide exchange. *Nature* **369**, 76-8 (1994).

82. Fukuda, M., Kanno, E., Ishibashi, K. & Itoh, T. Large scale screening for novel rab effectors reveals unexpected broad Rab binding specificity. *Mol Cell Proteomics* **7**, 1031-42 (2008).

83. Rai, A., Goody, R.S. & Muller, M.P. Multivalency in Rab effector interactions. *Small GTPases*, 1-7 (2017).

84. Gillingham, A.K., Sinka, R., Torres, I.L., Lilley, K.S. & Munro, S. Toward a comprehensive map of the effectors of rab GTPases. *Dev Cell* **31**, 358-73 (2014).

85. Seaman, M.N., McCaffery, J.M. & Emr, S.D. A membrane coat complex essential for endosome-to-Golgi retrograde transport in yeast. *J Cell Biol* **142**, 665-81 (1998).

86. Rojas, R. et al. Regulation of retromer recruitment to endosomes by sequential action of Rab5 and Rab7. *J Cell Biol* **183**, 513-26 (2008).

87. Diaz, E. & Pfeffer, S.R. TIP47: a cargo selection device for mannose 6-phosphate receptor trafficking. *Cell* **93**, 433-43 (1998).

88. Carroll, K.S. et al. Role of Rab9 GTPase in facilitating receptor recruitment by TIP47. *Science* **292**, 1373-6 (2001).

89. Martinez, O. et al. The small GTP-binding protein rab6 functions in intra-Golgi transport. *J Cell Biol* **127**, 1575-88 (1994).

90. Echard, A. et al. Interaction of a Golgi-associated kinesin-like protein with Rab6. *Science* **279**, 580-5 (1998).

91. Jordens, I. et al. The Rab7 effector protein RILP controls lysosomal transport by inducing the recruitment of dynein-dynactin motors. *Curr Biol* **11**, 1680-5 (2001).

92. Johansson, M. et al. Activation of endosomal dynein motors by stepwise assembly of Rab7-RILP-p150Glued, ORP1L, and the receptor betalll spectrin. *J Cell Biol* **176**, 459-71 (2007).

93. An, Y. et al. Structural and functional analysis of the globular head domain of p115 provides insight into membrane tethering. *J Mol Biol* **391**, 26-41 (2009).

94. Moyer, B.D., Allan, B.B. & Balch, W.E. Rab1 interaction with a GM130 effector complex regulates COPII vesicle cis--Golgi tethering. *Traffic* **2**, 268-76 (2001).

95. Sonnichsen, B. et al. A role for giantin in docking COPI vesicles to Golgi membranes. *J Cell Biol* **140**, 1013-21 (1998).

96. Barr, F.A., Nakamura, N. & Warren, G. Mapping the interaction between GRASP65 and GM130, components of a protein complex involved in the stacking of Golgi cisternae. *EMBO J* **17**, 3258-68 (1998).

97. Allan, B.B., Moyer, B.D. & Balch, W.E. Rab1 recruitment of p115 into a cis-SNARE complex: programming budding COPII vesicles for fusion. *Science* **289**, 444-8 (2000).

98. Diao, A., Frost, L., Morohashi, Y. & Lowe, M. Coordination of golgin tethering and SNARE assembly: GM130 binds syntaxin 5 in a p115-regulated manner. *J Biol Chem* **283**, 6957-67 (2008).

99. Cai, H. et al. TRAPPI tethers COPII vesicles by binding the coat subunit Sec23. *Nature* **445**, 941-4 (2007).

100. Rossi, G., Kolstad, K., Stone, S., Palluault, F. & Ferro-Novick, S. BET3 encodes a novel hydrophilic protein that acts in conjunction with yeast SNAREs. *Mol Biol Cell* **6**, 1769-80 (1995).

101. Whyte, J.R. & Munro, S. Vesicle tethering complexes in membrane traffic. *J Cell Sci* **115**, 2627-37 (2002).

102. Cai, H., Reinisch, K. & Ferro-Novick, S. Coats, tethers, Rabs, and SNAREs work together to mediate the intracellular destination of a transport vesicle. *Dev Cell* **12**, 671-82 (2007).

103. Grosshans, B.L. et al. The yeast lgl family member Sro7p is an effector of the secretory Rab GTPase Sec4p. *J Cell Biol* **172**, 55-66 (2006).

104. Nielsen, E. et al. Rabenosyn-5, a novel Rab5 effector, is complexed with hVPS45 and recruited to endosomes through a FYVE finger domain. *J Cell Biol* **151**, 601-12 (2000).

105. Simonsen, A., Gaullier, J.M., D'Arrigo, A. & Stenmark, H. The Rab5 effector EEA1 interacts directly with syntaxin-6. *J Biol Chem* **274**, 28857-60 (1999).

106. Harvey, J.J. An Unidentified Virus Which Causes the Rapid Production of Tumours in Mice. *Nature* **204**, 1104-5 (1964).

107. Kirsten, W.H., Schauf, V. & McCoy, J. Properties of a murine sarcoma virus. *Bibl Haematol*, 246-9 (1970).

108. Marshall, C.J., Hall, A. & Weiss, R.A. A transforming gene present in human sarcoma cell lines. *Nature* **299**, 171-3 (1982).

109. Shimizu, K., Goldfarb, M., Perucho, M. & Wigler, M. Isolation and preliminary characterization of the transforming gene of a human neuroblastoma cell line. *Proc Natl Acad Sci U S A* **80**, 383-7 (1983).

110. Wood, K.W., Sarnecki, C., Roberts, T.M. & Blenis, J. ras mediates nerve growth factor receptor modulation of three signal-transducing protein kinases: MAP kinase, Raf-1, and RSK. *Cell* **68**, 1041-50 (1992).

111. Howe, L.R. et al. Activation of the MAP kinase pathway by the protein kinase raf. *Cell* **71**, 335-42 (1992).

112. Vojtek, A.B., Hollenberg, S.M. & Cooper, J.A. Mammalian Ras interacts directly with the serine/threonine kinase Raf. *Cell* **74**, 205-14 (1993).

113. Sjolander, A., Yamamoto, K., Huber, B.E. & Lapetina, E.G. Association of p21ras with phosphatidylinositol 3-kinase. *Proc Natl Acad Sci U S A* **88**, 7908-12 (1991).

114. Rodriguez-Viciana, P. et al. Phosphatidylinositol-3-OH kinase as a direct target of Ras. *Nature* **370**, 527-32 (1994).

115. Jorissen, R.N. et al. Epidermal growth factor receptor: mechanisms of activation and signalling. *Exp Cell Res* **284**, 31-53 (2003).

116. Mayer, B.J. The discovery of modular binding domains: building blocks of cell signalling. *Nature Reviews Molecular Cell Biology* **16**, 691-698 (2015).

117. Buhrman, G., Holzapfel, G., Fetics, S. & Mattos, C. Allosteric modulation of Ras positions Q61 for a direct role in catalysis. *Proc Natl Acad Sci U S A* **107**, 4931-6 (2010).

118. Spiegel, J., Cromm, P.M., Zimmermann, G., Grossmann, T.N. & Waldmann, H. Small-molecule modulation of Ras signaling. *Nat Chem Biol* **10**, 613-22 (2014).

119. Malumbres, M. & Barbacid, M. RAS oncogenes: the first 30 years. *Nat Rev Cancer* **3**, 459-65 (2003).

120. Bos, J.L. ras oncogenes in human cancer: a review. *Cancer Res* **49**, 4682-9 (1989).

121. Cox, A.D., Fesik, S.W., Kimmelman, A.C., Luo, J. & Der, C.J. Drugging the undruggable RAS: Mission possible? *Nat Rev Drug Discov* **13**, 828-51 (2014).

122. Ostrem, J.M. & Shokat, K.M. Direct small-molecule inhibitors of KRAS: from structural insights to mechanism-based design. *Nat Rev Drug Discov* **15**, 771-785 (2016).

123. Ledford, H. Cancer: The Ras renaissance. *Nature* **520**, 278-80 (2015).

124. Ostrem, J.M., Peters, U., Sos, M.L., Wells, J.A. & Shokat, K.M. K-Ras(G12C) inhibitors allosterically control GTP affinity and effector interactions. *Nature* **503**, 548-51 (2013).

125. Lim, S.M. et al. Therapeutic targeting of oncogenic K-Ras by a covalent catalytic site inhibitor. *Angew Chem Int Ed Engl* **53**, 199-204 (2014).

126. Zimmermann, G. et al. Small molecule inhibition of the KRAS-PDEdelta interaction impairs oncogenic KRAS signalling. *Nature* **497**, 638-42 (2013).

127. Spiegel, J. et al. Direct targeting of Rab-GTPase-effector interactions. *Angew Chem Int Ed Engl* **53**, 2498-503 (2014).

128. Stokes, G.G. On the Change of Refrangibility of Light. *Philosophical Transactions of the Royal Society of London* **142**, 463-562 (1852).

129. Förster, T. Zwischenmolekulare Energiewanderung und Fluoreszenz. *Annalen der Physik* **437**, 55-75 (1948).

130. Piston, D.W. & Kremers, G.J. Fluorescent protein FRET: the good, the bad and the ugly. *Trends Biochem Sci* **32**, 407-14 (2007).

131. Strickler, S.J. & Berg, R.A. Relationship between Absorption Intensity and Fluorescence Lifetime of Molecules. *The Journal of Chemical Physics* **37**, 814-822 (1962).

132. Axelrod, D., Koppel, D.E., Schlessinger, J., Elson, E. & Webb, W.W. Mobility measurement by analysis of fluorescence photobleaching recovery kinetics. *Biophys J* **16**, 1055-69 (1976).

133. Elson, E.L., Schlessinger, J., Koppel, D.E., Axelrod, D. & Webb, W.W. Measurement of lateral transport on cell surfaces. *Prog Clin Biol Res* **9**, 137-47 (1976).

134. Jacobson, K., Derzko, Z., Wu, E.S., Hou, Y. & Poste, G. Measurement of the lateral mobility of cell surface components in single, living cells by fluorescence recovery after photobleaching. *J Supramol Struct* **5**, 565(417)-576(428) (1976).

135. Schlessinger, J. et al. Lateral transport on cell membranes: mobility of concanavalin A receptors on myoblasts. *Proc Natl Acad Sci U S A* **73**, 2409-13 (1976).

136. Lippincott-Schwartz, J., Altan-Bonnet, N. & Patterson, G.H. Photobleaching and photoactivation: following protein dynamics in living cells. *Nat Cell Biol* **Suppl**, S7-14 (2003).

137. Presley, J.F. et al. Dissection of COPI and Arf1 dynamics in vivo and role in Golgi membrane transport. *Nature* **417**, 187-93 (2002).

138. Stephens, D.J., Lin-Marq, N., Pagano, A., Pepperkok, R. & Paccaud, J.P. COPI-coated ER-to-Golgi transport complexes segregate from COPII in close proximity to ER exit sites. *J Cell Sci* **113 (Pt 12)**, 2177-85 (2000).

139. Storrie, B. et al. Recycling of golgi-resident glycosyltransferases through the ER reveals a novel pathway and provides an explanation for nocodazole-induced Golgi scattering. *J Cell Biol* **143**, 1505-21 (1998).

140. Presley, J.F. et al. ER-to-Golgi transport visualized in living cells. *Nature* **389**, 81-5 (1997).

141. Patterson, G.H. & Lippincott-Schwartz, J. A photoactivatable GFP for selective photolabeling of proteins and cells. *Science* **297**, 1873-7 (2002).

142. Ellen C. O'Shaughnessy, J.j.Y., Klaus M. Hahn. Biosensors of Small GTPase proteins for Use in Living cells and Animals. in *Optical Probes in Biology* (ed. Jin Zhang, S.M., Carsten Schultz) (2015).

143. Kraynov, V.S. et al. Localized Rac activation dynamics visualized in living cells. *Science* **290**, 333-7 (2000).

144. Benard, V., Bohl, B.P. & Bokoch, G.M. Characterization of rac and cdc42 activation in chemoattractant-stimulated human neutrophils using a novel assay for active GTPases. *J Biol Chem* **274**, 13198-204 (1999).

145. Bondeva, T., Balla, A., Varnai, P. & Balla, T. Structural determinants of Ras-Raf interaction analyzed in live cells. *Mol Biol Cell* **13**, 2323-33 (2002).

146. Caloca, M.J., Zugaza, J.L. & Bustelo, X.R. Exchange factors of the RasGRP family mediate Ras activation in the Golgi. *J Biol Chem* **278**, 33465-73 (2003).

147. Bivona, T.G. et al. Rap1 up-regulation and activation on plasma membrane regulates T cell adhesion. *J Cell Biol* **164**, 461-70 (2004).

148. Augsten, M. et al. Live-cell imaging of endogenous Ras-GTP illustrates predominant Ras activation at the plasma membrane. *Embo Reports* **7**, 46-51 (2006).

149. Mochizuki, N. et al. Spatio-temporal images of growth-factor-induced activation of Ras and Rap1. *Nature* **411**, 1065-8 (2001).

150. Kamiyama, D. & Chiba, A. Endogenous activation patterns of Cdc42 GTPase within Drosophila embryos. *Science* **324**, 1338-40 (2009).

151. Yoshizaki, H. et al. Activity of Rho-family GTPases during cell division as visualized with FRET-based probes. *J Cell Biol* **162**, 223-32 (2003).

152. Itoh, R.E. et al. Activation of rac and cdc42 video imaged by fluorescent resonance energy transfer-based single-molecule probes in the membrane of living cells. *Mol Cell Biol* **22**, 6582-91 (2002).

153. Pertz, O., Hodgson, L., Klemke, R.L. & Hahn, K.M. Spatiotemporal dynamics of RhoA activity in migrating cells. *Nature* **440**, 1069-72 (2006).

154. Kawase, K. et al. GTP hydrolysis by the Rho family GTPase TC10 promotes exocytic vesicle fusion. *Dev Cell* **11**, 411-21 (2006).

155. Takaya, A. et al. R-Ras regulates exocytosis by Rgl2/Rlf-mediated activation of RalA on endosomes. *Mol Biol Cell* **18**, 1850-60 (2007).

156. Kitano, M., Nakaya, M., Nakamura, T., Nagata, S. & Matsuda, M. Imaging of Rab5 activity identifies essential regulators for phagosome maturation. *Nature* **453**, 241-5 (2008).

157. Ishido, H.K., Yasushi Sako, Takao Arai, Mistunori Fukuda and Takeshi Nakamura. How to make FRET biosensors for Rab family GTPases. (2011).

158. Kalab, P., Weis, K. & Heald, R. Visualization of a Ran-GTP gradient in interphase and mitotic Xenopus egg extracts. *Science* **295**, 2452-6 (2002).

159. Komatsu, N. et al. Development of an optimized backbone of FRET biosensors for kinases and GTPases. *Mol Biol Cell* **22**, 4647-56 (2011).

160. Hodgson, L., Pertz, O. & Hahn, K.M. Design and optimization of genetically encoded fluorescent biosensors: GTPase biosensors. *Methods Cell Biol* **85**, 63-81 (2008).

161. Kardash, E. et al. A role for Rho GTPases and cell-cell adhesion in single-cell motility in vivo. *Nat Cell Biol* **12**, 47-53; sup pp 1-11 (2010).

162. Lorenz, M., Yamaguchi, H., Wang, Y., Singer, R.H. & Condeelis, J. Imaging sites of N-wasp activity in lamellipodia and invadopodia of carcinoma cells. *Curr Biol* **14**, 697-703 (2004).

163. Graham, D.L., Lowe, P.N. & Chalk, P.A. A method to measure the interaction of Rac/Cdc42 with their binding partners using fluorescence resonance energy transfer between mutants of green fluorescent protein. *Anal Biochem* **296**, 208-17 (2001).

164. Nalbant, P., Hodgson, L., Kraynov, V., Toutchkine, A. & Hahn, K.M. Activation of endogenous Cdc42 visualized in living cells. *Science* **305**, 1615-9 (2004).

165. Goguen, B.N., Loving, G.S. & Imperiali, B. Development of a fluorogenic sensor for activated Cdc42. *Bioorg Med Chem Lett* **21**, 5058-61 (2011).

166. MacNevin, C.J. et al. Ratiometric Imaging Using a Single Dye Enables Simultaneous Visualization of Rac1 and Cdc42 Activation. *J Am Chem Soc* (2016).

167. Hodgson, L. et al. FRET binding antenna reports spatiotemporal dynamics of GDI-Cdc42 GTPase interactions. *Nat Chem Biol* **12**, 802-9 (2016).

168. Toutchkine, A., Kraynov, V. & Hahn, K. Solvent-sensitive dyes to report protein conformational changes in living cells. *J Am Chem Soc* **125**, 4132-45 (2003).

169. Wilkins, M.R. et al. Protein identification and analysis tools in the ExPASy server. *Methods Mol Biol* **112**, 531-52 (1999).

170. Wissner, R.F., Batjargal, S., Fadzen, C.M. & Petersson, E.J. Labeling proteins with fluorophore/thioamide Forster resonant energy transfer pairs by combining unnatural amino acid mutagenesis and native chemical ligation. *J Am Chem Soc* **135**, 6529-40 (2013).

171. Grecco, H.E., Roda-Navarro, P. & Verveer, P.J. Global analysis of time correlated single photon counting FRET-FLIM data. *Opt Express* **17**, 6493-508 (2009).

172. Evers, T.H., van Dongen, E.M., Faesen, A.C., Meijer, E.W. & Merkx, M. Quantitative understanding of the energy transfer between fluorescent proteins connected via flexible peptide linkers. *Biochemistry* **45**, 13183-92 (2006).

173. Li, X. et al. Deletions of the Aequorea victoria green fluorescent protein define the minimal domain required for fluorescence. *J Biol Chem* **272**, 28545-9 (1997).

174. Kim, Y. et al. Efficient site-specific labeling of proteins via cysteines. *Bioconjug Chem* **19**, 786-91 (2008).

175. Marino, S.M. & Gladyshev, V.N. Cysteine function governs its conservation and degeneration and restricts its utilization on protein surfaces. *J Mol Biol* **404**, 902-16 (2010).

176. Chen, X., Muthoosamy, K., Pfisterer, A., Neumann, B. & Weil, T. Site-selective lysine modification of native proteins and peptides via kinetically controlled labeling. *Bioconjug Chem* **23**, 500-8 (2012).

177. Voss, S., Zhao, L., Chen, X., Gerhard, F. & Wu, Y.W. Generation of an intramolecular three-color fluorescence resonance energy transfer probe by site-specific protein labeling. *J Pept Sci* **20**, 115-20 (2014).

178. Cormack, B.P., Valdivia, R.H. & Falkow, S. FACS-optimized mutants of the green fluorescent protein (GFP). *Gene* **173**, 33-8 (1996).

179. Griesbeck, O., Baird, G.S., Campbell, R.E., Zacharias, D.A. & Tsien, R.Y. Reducing the environmental sensitivity of yellow fluorescent protein. Mechanism and applications. *J Biol Chem* **276**, 29188-94 (2001).

180. Seabra, M.C. Membrane association and targeting of prenylated Ras-like GTPases. *Cell Signal* **10**, 167-72 (1998).

181. Dawson, P.E., Muir, T.W., Clark-Lewis, I. & Kent, S.B. Synthesis of proteins by native chemical ligation. *Science* **266**, 776-9 (1994).

182. Machner, M.P. & Isberg, R.R. A bifunctional bacterial protein links GDI displacement to Rab1 activation. *Science* **318**, 974-7 (2007).

183. Goody, P.R. et al. Reversible phosphocholination of Rab proteins by Legionella pneumophila effector proteins. *EMBO J* **31**, 1774-84 (2012).

184. Schoebel, S., Cichy, A.L., Goody, R.S. & Itzen, A. Protein LidA from Legionella is a Rab GTPase supereffector. *Proc Natl Acad Sci U S A* **108**, 17945-50 (2011).

185. Bergbrede, T. et al. Biophysical analysis of the interaction of Rab6a GTPase with its effector domains. *J Biol Chem* **284**, 2628-35 (2009).

186. Muller, M.P. et al. Characterization of enzymes from Legionella pneumophila involved in reversible adenylylation of Rab1 protein. *J Biol Chem* **287**, 35036-46 (2012).

187. Hou, X. et al. A structural basis for Lowe syndrome caused by mutations in the Rab-binding domain of OCRL1. *EMBO J* **30**, 1659-70 (2011).

188. Cheng, W. et al. Structural insights into a unique Legionella pneumophila effector LidA recognizing both GDP and GTP bound Rab1 in their active state. *PLoS Pathog* **8**, e1002528 (2012).

189. Muller, M.P. et al. The Legionella effector protein DrrA AMPylates the membrane traffic regulator Rab1b. *Science* **329**, 946-9 (2010).

190. Rai, A. et al. bMERB domains are bivalent Rab8 family effectors evolved by gene duplication. *Elife* **5**(2016).

191. Hinde, E., Digman, M.A., Welch, C., Hahn, K.M. & Gratton, E. Biosensor Forster resonance energy transfer detection by the phasor approach to fluorescence lifetime imaging microscopy. *Microsc Res Tech* **75**, 271-81 (2012).

192. Walther, K.A., Papke, B., Sinn, M.B., Michel, K. & Kinkhabwala, A. Precise measurement of protein interacting fractions with fluorescence lifetime imaging microscopy. *Mol Biosyst* **7**, 322-36 (2011).

193. Alvarez, C., Garcia-Mata, R., Brandon, E. & Sztul, E. COPI recruitment is modulated by a Rab1b-dependent mechanism. *Mol Biol Cell* **14**, 2116-27 (2003).

194. Plutner, H. et al. Rab1b regulates vesicular transport between the endoplasmic reticulum and successive Golgi compartments. *J Cell Biol* **115**, 31-43 (1991).

195. Tisdale, E.J., Bourne, J.R., Khosravi-Far, R., Der, C.J. & Balch, W.E. GTP-binding mutants of rab1 and rab2 are potent inhibitors of vesicular transport from the endoplasmic reticulum to the Golgi complex. *J Cell Biol* **119**, 749-61 (1992).

196. Peter, F., Nuoffer, C., Pind, S.N. & Balch, W.E. Guanine nucleotide dissociation inhibitor is essential for Rab1 function in budding from the endoplasmic reticulum and transport through the Golgi stack. *J Cell Biol* **126**, 1393-406 (1994).

197. Wu, S.K. et al. Molecular role for the Rab binding platform of guanine nucleotide dissociation inhibitor in endoplasmic reticulum to Golgi transport. *J Biol Chem* **273**, 26931-8 (1998).

198. Ortiz Sandoval, C. & Simmen, T. Rab proteins of the endoplasmic reticulum: functions and interactors. *Biochem Soc Trans* **40**, 1426-32 (2012).

199. Slavin, I. et al. Role of Rab1b in COPII dynamics and function. *Eur J Cell Biol* **90**, 301-11 (2011).

200. Beard, M., Satoh, A., Shorter, J. & Warren, G. A cryptic Rab1-binding site in the p115 tethering protein. *J Biol Chem* **280**, 25840-8 (2005).

201. Choudhury, R. et al. Lowe syndrome protein OCRL1 interacts with clathrin and regulates protein trafficking between endosomes and the trans-Golgi network. *Mol Biol Cell* **16**, 3467-79 (2005).

202. Boriack-Sjodin, P.A., Margarit, S.M., Bar-Sagi, D. & Kuriyan, J. The structural basis of the activation of Ras by Sos. *Nature* **394**, 337-43 (1998).

203. Margarit, S.M. et al. Structural evidence for feedback activation by Ras.GTP of the Ras-specific nucleotide exchange factor SOS. *Cell* **112**, 685-95 (2003).

204. Freedman, T.S. et al. A Ras-induced conformational switch in the Ras activator Son of sevenless. *Proc Natl Acad Sci U S A* **103**, 16692-7 (2006).

205. Sondermann, H. et al. Structural analysis of autoinhibition in the Ras activator Son of sevenless. *Cell* **119**, 393-405 (2004).

206. Vo, U. et al. Monitoring Ras Interactions with the Nucleotide Exchange Factor Son of Sevenless (Sos) Using Site-specific NMR Reporter Signals and Intrinsic Fluorescence. *J Biol Chem* **291**, 1703-18 (2016).

207. Hancock, J.F., Paterson, H. & Marshall, C.J. A polybasic domain or palmitoylation is required in addition to the CAAX motif to localize p21ras to the plasma membrane. *Cell* **63**, 133-9 (1990).

208. Foster, J.M. et al. Clinical implications of novel activating EGFR mutations in malignant peritoneal mesothelioma. *World J Surg Oncol* **8**, 88 (2010).

209. Tang, Z. et al. Disruption of the EGFR E884-R958 ion pair conserved in the human kinome differentially alters signaling and inhibitor sensitivity. *Oncogene* **28**, 518-33 (2009).

210. Murakoshi, H., Shibata, A.C., Nakahata, Y. & Nabekura, J. A dark green fluorescent protein as an acceptor for measurement of Forster resonance energy transfer. *Sci Rep* **5**, 15334 (2015).

211. Giehl, K., Skripczynski, B., Mansard, A., Menke, A. & Gierschik, P. Growth factor-dependent activation of the Ras-Raf-MEK-MAPK pathway in the human pancreatic carcinoma cell line PANC-1 carrying activated K-ras: implications for cell proliferation and cell migration. *Oncogene* **19**, 2930-42 (2000).

212. Wilson, A.L., Erdman, R.A. & Maltese, W.A. Association of Rab1B with GDP-dissociation inhibitor (GDI) is required for recycling but not initial membrane targeting of the Rab protein. *J Biol Chem* **271**, 10932-40 (1996).

213. Ullrich, O. et al. Rab GDP dissociation inhibitor as a general regulator for the membrane association of rab proteins. *J Biol Chem* **268**, 18143-50 (1993).

214. Martinez, H., Garcia, I.A., Sampieri, L. & Alvarez, C. Spatial-Temporal Study of Rab1b Dynamics and Function at the ER-Golgi Interface. *PLoS One* **11**, e0160838 (2016).

215. Hutt, D.M., Da-Silva, L.F., Chang, L.H., Prosser, D.C. & Ngsee, J.K. PRA1 inhibits the extraction of membrane-bound rab GTPase by GDI1. *J Biol Chem* **275**, 18511-9 (2000).

216. Haas, A.K. et al. Analysis of GTPase-activating proteins: Rab1 and Rab43 are key Rabs required to maintain a functional Golgi complex in human cells. *J Cell Sci* **120**, 2997-3010 (2007).

217. Overmeyer, J.H., Wilson, A.L., Erdman, R.A. & Maltese, W.A. The putative "switch 2" domain of the Ras-related GTPase, Rab1B, plays an essential role in the interaction with Rab escort protein. *Mol Biol Cell* **9**, 223-35 (1998).

218. Bannykh, S.I., Nishimura, N. & Balch, W.E. Getting into the Golgi. *Trends Cell Biol* **8**, 21-5 (1998).

219. Saraste, J. & Svensson, K. Distribution of the intermediate elements operating in ER to Golgi transport. *J Cell Sci* **100 (Pt 3)**, 415-30 (1991).

220. Aridor, M., Bannykh, S.I., Rowe, T. & Balch, W.E. Sequential coupling between COPII and COPI vesicle coats in endoplasmic reticulum to Golgi transport. *J Cell Biol* **131**, 875-93 (1995).

221. Davidson, H.W. & Balch, W.E. Differential inhibition of multiple vesicular transport steps between the endoplasmic reticulum and trans Golgi network. *J Biol Chem* **268**, 4216-26 (1993).

222. Yasuda, R. et al. Supersensitive Ras activation in dendrites and spines revealed by two-photon fluorescence lifetime imaging. *Nat Neurosci* **9**, 283-91 (2006).

223. Oliveira, A.F. & Yasuda, R. Imaging the activity of Ras superfamily GTPase proteins in small subcellular compartments in neurons. *Methods Mol Biol* **1071**, 109-28 (2014).

224. Benink, H.A. & Bement, W.M. Concentric zones of active RhoA and Cdc42 around single cell wounds. *J Cell Biol* **168**, 429-39 (2005).

225. Park, T.J., Mitchell, B.J., Abitua, P.B., Kintner, C. & Wallingford, J.B. Dishevelled controls apical docking and planar polarization of basal bodies in ciliated epithelial cells. *Nat Genet* **40**, 871-9 (2008).

226. Hemsath, L., Dvorsky, R., Fiegen, D., Carlier, M.F. & Ahmadian, M.R. An electrostatic steering mechanism of Cdc42 recognition by Wiskott-Aldrich syndrome proteins. *Mol Cell* **20**, 313-24 (2005).

227. Ren, X.D., Kiosses, W.B. & Schwartz, M.A. Regulation of the small GTP-binding protein Rho by cell adhesion and the cytoskeleton. *EMBO J* **18**, 578-85 (1999).

228. Kuriyan, J. & Eisenberg, D. The origin of protein interactions and allostery in colocalization. *Nature* **450**, 983-90 (2007).

229. Chandra, A. et al. The GDI-like solubilizing factor PDEdelta sustains the spatial organization and signalling of Ras family proteins. *Nat Cell Biol* **14**, 148-58 (2011).

230. Brunsveld, L. et al. Lipidated ras and rab peptides and proteins--synthesis, structure, and function. *Angew Chem Int Ed Engl* **45**, 6622-46 (2006).

231. Chen, Y.X. et al. Synthesis of the Rheb and K-Ras4B GTPases. *Angew Chem Int Ed Engl* **49**, 6090-5 (2010).

232. Seabra, M.C. & James, G.L. Prenylation assays for small GTPases. *Methods Mol Biol* **84**, 251-60 (1998).

233. Gillette, W.K. et al. Farnesylated and methylated KRAS4b: high yield production of protein suitable for biophysical studies of prenylated protein-lipid interactions. *Sci Rep* **5**, 15916 (2015).

234. Nuoffer, C., Peter, F. & Balch, W.E. Purification of His6-tagged Rab1 proteins using bacterial and insect cell expression systems. *Methods Enzymol* **257**, 3-9 (1995).

235. Dharmaiah, S. et al. Structural basis of recognition of farnesylated and methylated KRAS4b by PDEdelta. *Proc Natl Acad Sci U S A* (2016).

236. Pylypenko, O. et al. Structure of doubly prenylated Ypt1:GDI complex and the mechanism of GDI-mediated Rab recycling. *EMBO J* **25**, 13-23 (2006).

237. Rimmele, S., Gierschik, P., Joos, T.O. & Schneiderhan-Marra, N. Bead-based protein-protein interaction assays for the analysis of Rho GTPase signaling. *J Mol Recognit* **23**, 543-50 (2010).

238. Surviladze, Z. et al. Identification of a small GTPase inhibitor using a high-throughput flow cytometry bead-based multiplex assay. *J Biomol Screen* **15**, 10-20 (2010).

239. Coyle, S.M. & Lim, W.A. Mapping the functional versatility and fragility of Ras GTPase signaling circuits through in vitro network reconstitution. *Elife* **5**(2016).

240. Theillet, F.X. et al. Structural disorder of monomeric alpha-synuclein persists in mammalian cells. *Nature* **530**, 45-50 (2016).

241. Sharei, A. et al. A vector-free microfluidic platform for intracellular delivery. *Proc Natl Acad Sci U S A* **110**, 2082-7 (2013).

242. Kollmannsperger, A. et al. Live-cell protein labelling with nanometre precision by cell squeezing. *Nat Commun* **7**, 10372 (2016).

243. Lang, K. & Chin, J.W. Cellular incorporation of unnatural amino acids and bioorthogonal labeling of proteins. *Chem Rev* **114**, 4764-806 (2014).

244. Chen, X. & Wu, Y.W. Selective chemical labeling of proteins. *Org Biomol Chem* (2016).

245. Ye, S. et al. Site-specific incorporation of keto amino acids into functional G protein-coupled receptors using unnatural amino acid mutagenesis. *J Biol Chem* **283**, 1525-33 (2008).

246. Lang, K. et al. Genetic Encoding of bicyclononynes and trans-cyclooctenes for site-specific protein labeling in vitro and in live mammalian cells via rapid fluorogenic Diels-Alder reactions. *J Am Chem Soc* **134**, 10317-20 (2012).

247. Hoffman, G.R., Nassar, N. & Cerione, R.A. Structure of the Rho family GTP-binding protein Cdc42 in complex with the multifunctional regulator RhoGDI. *Cell* **100**, 345-56 (2000).

248. Beemiller, P., Hoppe, A.D. & Swanson, J.A. A phosphatidylinositol-3-kinase-dependent signal transition regulates ARF1 and ARF6 during Fcgamma receptor-mediated phagocytosis. *PLoS Biol* **4**, e162 (2006).

249. Hall, B. et al. A fluorescence resonance energy transfer activation sensor for Arf6. *Anal Biochem* **374**, 243-9 (2008).

250. Donnelly, S.K., Bravo-Cordero, J.J. & Hodgson, L. Rho GTPase isoforms in cell motility: Don't fret, we have FRET. *Cell Adh Migr* **8**, 526-34 (2014).

251. Aoki, K. & Matsuda, M. Visualization of small GTPase activity with fluorescence resonance energy transfer-based biosensors. *Nat Protoc* **4**, 1623-31 (2009).

252. Oliveira, A.F. & Yasuda, R. An improved Ras sensor for highly sensitive and quantitative FRET-FLIM imaging. *PLoS One* **8**, e52874 (2013).

253. Berezin, M.Y. & Achilefu, S. Fluorescence lifetime measurements and biological imaging. *Chem Rev* **110**, 2641-84 (2010).

254. Fritz, R.D. et al. A versatile toolkit to produce sensitive FRET biosensors to visualize signaling in time and space. *Sci Signal* **6**, rs12 (2013).

255. George Abraham, B. et al. Fluorescent Protein Based FRET Pairs with Improved Dynamic Range for Fluorescence Lifetime Measurements. *PLoS One* **10**, e0134436 (2015).

256. Lam, A.J. et al. Improving FRET dynamic range with bright green and red fluorescent proteins. *Nat Methods* **9**, 1005-12 (2012).

257. Baird, G.S., Zacharias, D.A. & Tsien, R.Y. Circular permutation and receptor insertion within green fluorescent proteins. *Proc Natl Acad Sci U S A* **96**, 11241-6 (1999).

258. Nagai, T., Yamada, S., Tominaga, T., Ichikawa, M. & Miyawaki, A. Expanded dynamic range of fluorescent indicators for Ca(2+) by circularly permuted yellow fluorescent proteins. *Proc Natl Acad Sci U S A* **101**, 10554-9 (2004).

259. Shaner, N.C., Steinbach, P.A. & Tsien, R.Y. A guide to choosing fluorescent proteins. *Nat Methods* **2**, 905-9 (2005).

260. Day, R.N. & Davidson, M.W. The fluorescent protein palette: tools for cellular imaging. *Chem Soc Rev* **38**, 2887-921 (2009).

261. Kneen, M., Farinas, J., Li, Y. & Verkman, A.S. Green fluorescent protein as a noninvasive intracellular pH indicator. *Biophys J* **74**, 1591-9 (1998).

262. Sabet, O. et al. Ubiquitination switches EphA2 vesicular traffic from a continuous safeguard to a finite signalling mode. *Nat Commun* **6**, 8047 (2015).

263. Day, R.N. & Davidson, M.W. Fluorescent proteins for FRET microscopy: monitoring protein interactions in living cells. *Bioessays* **34**, 341-50 (2012).

264. Goedhart, J. et al. Bright cyan fluorescent protein variants identified by fluorescence lifetime screening. *Nat Methods* **7**, 137-9 (2010).

265. Klarenbeek, J.B., Goedhart, J., Hink, M.A., Gadella, T.W. & Jalink, K. A mTurquoise-based cAMP sensor for both FLIM and ratiometric read-out has improved dynamic range. *PLoS One* **6**, e19170 (2011).

266. Hoffmann, C., Zurn, A., Bunemann, M. & Lohse, M.J. Conformational changes in G-protein-coupled receptors-the quest for functionally selective conformations is open. *Br J Pharmacol* **153 Suppl 1**, S358-66 (2008).

267. Klarenbeek, J., Goedhart, J., van Batenburg, A., Groenewald, D. & Jalink, K. Fourth-generation epac-based FRET sensors for cAMP feature exceptional brightness, photostability and dynamic range: characterization of dedicated sensors for FLIM, for ratiometry and with high affinity. *PLoS One* **10**, e0122513 (2015).

268. Toseland, C.P. Fluorescent labeling and modification of proteins. *J Chem Biol* **6**, 85-95 (2013).

269. Gaietta, G. et al. Multicolor and electron microscopic imaging of connexin trafficking. *Science* **296**, 503-7 (2002).

270. Los, G.V. et al. HaloTag: a novel protein labeling technology for cell imaging and protein analysis. *ACS Chem Biol* **3**, 373-82 (2008).

271. Keppler, A. et al. A general method for the covalent labeling of fusion proteins with small molecules in vivo. *Nat Biotechnol* **21**, 86-9 (2003).

272. Gautier, A. et al. An engineered protein tag for multiprotein labeling in living cells. *Chem Biol* **15**, 128-36 (2008).

273. Zheng, Q., Xu, G. & Prasad, P.N. Conformationally restricted dipyrromethene boron difluoride (BODIPY) dyes: highly fluorescent, multicolored probes for cellular imaging. *Chemistry* **14**, 5812-9 (2008).

274. Lewis, F.D., Zhang, L. & Zuo, X. Orientation control of fluorescence resonance energy transfer using DNA as a helical scaffold. *J Am Chem Soc* **127**, 10002-3 (2005).

275. Iqbal, A. et al. Orientation dependence in fluorescent energy transfer between Cy3 and Cy5 terminally attached to double-stranded nucleic acids. *Proc Natl Acad Sci U S A* **105**, 11176-81 (2008).

Eidesstattliche Erklärung (Affidavit)

_____ _____

Name, Vorname
(Surname, first name)

Matrikel-Nr.
(Enrolment number)

Belehrung:

Wer vorsätzlich gegen eine die Täuschung über Prüfungsleistungen betreffende Regelung einer Hochschulprüfungsordnung verstößt, handelt ordnungswidrig. Die Ordnungswidrigkeit kann mit einer Geldbuße von bis zu 50.000,00 € geahndet werden. Zuständige Verwaltungsbehörde für die Verfolgung und Ahndung von Ordnungs-widrigkeiten ist der Kanzler/die Kanzlerin der Technischen Universität Dortmund. Im Falle eines mehrfachen oder sonstigen schwerwiegenden Täuschungsversuches kann der Prüfling zudem exmatrikuliert werden, § 63 Abs. 5 Hochschulgesetz NRW. Die Abgabe einer falschen Versicherung an Eides statt ist strafbar. Wer vorsätzlich eine falsche Versicherung an Eides statt abgibt, kann mit einer Freiheitsstrafe bis zu drei Jahren oder mit Geldstrafe bestraft werden, § 156 StGB. Die fahrlässige Abgabe einer falschen Versicherung an Eides statt kann mit einer Freiheitsstrafe bis zu einem Jahr oder Geldstrafe bestraft werden, § 161 StGB

Die oben stehende Belehrung habe ich zur Kenntnis genommen.

Official notification:

Any person who intentionally breaches any regulation of university examination regulations relating to deception in examination performance is acting improperly. This offence can be punished with a fine of up to EUR 50,000.00. The competent administrative authority for the pursuit and prosecution of offences of this type is the chancellor of the TU Dortmund University. In the case of multiple or other serious attempts at deception, the candidate can also be unenrolled, Section 63, paragraph 5 of the Universities Act of North Rhine-Westphalia.
The submission of a false affidavit is punishable.
Any person who intentionally submits a false affidavit can be punished with a prison sentence of up to three years or a fine, Section 156 of the Criminal Code. The negligent submission of a false affidavit can be punished with a prison sentence of up to one year or a fine, Section 161 of the Criminal Code.

I have taken note of the above official notification.

_____ _____

Ort, Datum
(Place, date)

Unterschrift
(Signature)

Titel der Dissertation:
(Title of the thesis):

_____

Ich versichere hiermit an Eides statt, dass ich die vorliegende Dissertation mit dem Titel selbstständig und ohne unzulässige fremde Hilfe angefertigt habe. Ich habe keine anderen als die angegebenen Quellen und Hilfsmittel benutzt sowie wörtliche und sinngemäße Zitate kenntlich gemacht.
Die Arbeit hat in gegenwärtiger oder in einer anderen Fassung weder der TU Dortmund noch einer anderen Hochschule im Zusammenhang mit einer staatlichen oder akademischen Prüfung vorgelegen.

I hereby swear that I have completed the present dissertation independently and without inadmissible external support. I have not used any sources or tools other than those indicated and have identified literal and analogous quotations.

The thesis in its current version or another version has not been presented to the TU Dortmund University or another university in connection with a state or academic examination.

_____ _____

Ort, Datum
(Place, date)

Unterschrift
(Signature)

Acknowledgements

I would like to express my gratitude to Dr. Yaowen Wu for the opportunity to join his group, for his continuous support and for giving me the time and space to learn and try new things.

I would like to thank Prof. Dr. Roger S. Goody for allowing me to be part of his department in the very beginning of this work and accepting to be the first referee.
I would like to thank Prof. Dr. Roland Winter for kindly accepting to be the second referee of this dissertation.

I wish to thank all past and present members of the Wu group for rewarding scientific discussions, shared reagents, technical expertise and the great working atmosphere.

Special thanks to Petra Geue and Nathalie Bleimling for their excellent (technical) assistance and support.

My sincere thanks to Christa Hornemann and the IMPRS for outstanding support and countless opportunities for scientific and personal growth.

All current and former members of the climbing crew, I would like to thank for providing superb distractions and challenges in the vertical dimension.

I am immensely grateful for the diversion and friendship the “Rugby Divas Dortmund” provided me throughout the time spent on and off the pitch.

Especially, I would like to thank my friends and family for their unwavering support and the precious time spend together throughout the years.